

Faculty of Engineering

Investigations of Innovative Biomass Materials for Low Carbon Buildings

Thesis by

Yixin WANG (BEng, MSc)

ID: 14342120

Supervisors: Prof. Saffa Riffat, Prof. Yuehong Su

Thesis submitted to the University of Nottingham

For the degree of Doctor of Philosophy

2022

ABSTRACT

The energy shortage, excessive consumption of oil resources and environmental pollution are the major problems worldwide, and there is an urgent need to improve and solve these problems. This thesis aims to develop novel, environmentally friendly biomass aerogels as thermal insulating, sound absorbing and filtering materials for low-carbon buildings. The biomass aerogels are made of natural materials and prepared through sol-gel, ageing and freeze drying methods to have advantageous properties of low density, high specific surface area and high porosity. The work will be divided into seven sections as follows: 1) Overview of the current status of biomass aerogels; 2) Selection of the starting materials and evaluate the characteristics of composite biomass mixtures/gels; 3) Preparation of sound absorbing biomass aerogels and the performance testing; 4) Preparation of thermal insulating biomass aerogels and properties measurement; 5) Production of biomass aerogels with promising filtration performance; 6) Simulation and evaluation of the energy saving of a retrofitted house with biomass aerogel as the insulator; 7) Economic and environmental assessment of biomass aerogels.

This research selected Konjac glucomannan, starch, gelatin and wheat straw as the starting materials. The biomass mixtures/gels were prepared through sol-gel and ageing processes. Meanwhile, the biomass aerogels were produced by the freeze drying method. In these initial experiments, systems' pasting properties, rheological properties and microstructure were tested and observed to explore the influence of process parameters and different addition ranges of raw materials on the biomass mixtures/gels. Based on the results, raw materials dissolution temperature was chosen as 95°C, the recommended amount of KGM is about 1% (w/v), and the ageing process must be carried out under 37°C.

The characteristic experiments were conducted on three types of biomass aerogels with different compositions for three applications: sound absorption, thermal insulation and filtration. KGM, gelatin and wheat straw were selected to produce sound absorbing biomass aerogels. Results show that gelatin addition can significantly improve sound absorption performance at medium/high frequencies and mechanical strength. The small amount of wheat straw addition improves sound absorption property, but it is reduced with more content added. Better sound absorption performance is achieved than sound absorption cotton, while the best result is obtained with an average noise reduction coefficient of 0.38, and the coefficient reaches 0.88 at 4500 Hz. Wheat straw addition also leads to strength reduction but enhancement when the addition is more than 1%, where fine wheat straw bars form nest structures for strengthening. For thermal insulation, test results show that the appropriate wheat straw length and pre-freeze temperature greatly influence thermal insulation properties of biomass aerogels. With wheat straw sieved through 120 mesh, K1G0.5S2WS1.5 aerogel had a thermal conductivity of 0.0420 $Wm^{-1}K^{-1}$. When the pre-freeze temperature further decreased to -30°C and -40°C, the thermal conductivities of K1G0.5S2WS1.5 aerogels were reduced to 0.0375 and 0.0327 $Wm^{-1}K^{-1}$, respectively. For filtration properties, the biomass aerogel K0.9G1.8S3.6WS1.8 shows excellent performance in removing particulate matter 2.5 (PM 2.5) (99.50%) and PM 10 (99.40%) from the environment in an actual room with small thickness.

Numerical modelling was conducted to investigate the energy saving of a retrofitted E.ON house with biomass aerogel as insulation layers. Meanwhile, the economic and environmental analysis results show that applying these novel biomass aerogels in low carbon buildings is valuable.

LIST OF PUBLICATIONS

JOURNAL PAPER:

(1) **Yixin Wang**, Yuehong Su, Weiling Wang, Ying Fang, Saffa Riffat, and Fatang Jiang. The advances of polysaccharide-based aerogels: Preparation and potential application. Carbohydrate polymers 226 (2019): 115242.

(2) **Yixin Wang**, Fei Xiang, Wei Wang, Weiling Wang, Yuehong Su, Fatang Jiang, Sheng Chen, and Saffa Riffat. Sound absorption characteristics of KGM-based aerogel. International Journal of Low-Carbon Technologies 15, no. 3 (2020): 450-457.

(3) **Yixin Wang**, Rizwan Rasheed, Fatang Jiang, Asfra Rizwan, Hajra Javed, Yuehong Su, and Saffa Riffat. Life cycle assessment of a novel biomass-based aerogel material for building insulation. Journal of Building Engineering 44 (2021): 102988.

(4) **Yixin Wang**, Emmanuel Tapia-Brito, James Riffat, Ziwei Chen, Fatang Jiang, and Saffa Riffat. Investigation on the Efficient Removal of Particulate Matter (PM) with Biomass-Based Aerogel. Future Cities and Environment 7, no. 1 (2021).

(5) **Yixin Wang**, Hui Zhu, Wenyao Tu, Yuehong Su, Fatang Jiang, Saffa Riffat. Sound absorption, structure and material modelling of konjac glucomannan-based aerogel with addition of gelatin and wheat straw. Construction and building materials, 352 (2022): 129052.

(6) Ke Qu, Xiangjie Chen, **Yixin Wang**, John Calautit, Saffa Riffat, and Xin Cui. Comprehensive energy, economic and thermal comfort assessments for the passive energy retrofit of historical buildings-A case study of a late nineteenth-century Victorian house renovation in the UK. Energy 220 (2021): 119646.

(7) Wenyao Tu, Wenjuan Shi, Hao Li, **Yixin Wang**, Dongling Qiao, Fatang Jiang, and Binjia Zhang. Xanthan gum inclusion optimizes the sol-gel and mechanical properties of

agar/konjac glucomannan system for designing core-shell structural capsules. Food Hydrocolloids 122 (2022): 107101.

(8) Fei Xiang, Yuting Xia, Yan Wang, **Yixin Wang**, Kao Wu, and Xuewen Ni. Preparation of konjac glucomannan based films reinforced with nanoparticles and its effect on cherry tomatoes preservation. Food Packaging and Shelf Life 29 (2021): 100701.

(9) Emmanuel Tapia-Brito, James Riffat, **Yixin Wang**, Amir M. Ghaemmaghami, Christopher M. Coleman, and Saffa Riffat. Experimental Investigation of a MopFan-Based Photocatalytic Air Purification Device. Future Cities and Environment 8, no. 1 (2022).

CONFERENCE PAPER:

(1) **Yixin Wang**, Yuehong Su, Fatang Jiang, Saffa Riffat. (2019). *Sound Absorption Properties of Biomass Aerogels for Building Application*, SET2019–18th International Conference on Sustainable Energy Technologies, Kuala Lumpur, Malaysia.

(2) Ke Qu, **Yixin Wang**, John Kaiser Calautit, Saffa Riffat. (2020). *Retrofit selection criteria for interior facade insulation integrated with solar assisted heat pump based on specified dwelling types*, ECOS 2020 - 33rd International Conference on Efficiency, Cost, Optimization, Simulation and Environmental Impact of Energy Systems. Osaka, Japan.

(3) Hasila Jarimi and **Yixin Wang**. (2020). *An affordable calibrated hot box- heat flow meter suitable for thermal performance measurement of an insulation panel*. IAPE'20 - International Conference on Innovative Applied Energy. Cambridge, United Kingdom.

ACKNOWLEDGEMENT

Firstly and foremost, I would like to express my warmest gratitude to my supervisor, Professor Saffa Riffat, for supporting my study and research at the University of Nottingham.

I will never forget the day in February 2019 that Prof. Riffat and I did a small experiment of wrapping cucumbers with biomass materials in his office. His considerable knowledge, motivation and patience have deeply inspired me. It is a great privilege and honour to study under his guidance. My sincere thanks also go to Prof. Yuehong Su, my additional supervisor. His guidance and expert advice carried me through all the stages of my study.

I would like to thank Prof. Fatang Jiang and Dr Siddig Omer for their advice, help, guidance and valuable comments on my research. Further thanks to my colleagues and friends, Dr Yate Ding, Dr Hasila Jarimi, Dr Hang Zhou, Dr Ziwei Chen, Dr Yanan Zhang, Dr Qi Xu, Dr Shihao Zhang, Dr Weihan Zhao, Dr Yun-Sheng Hsu, Dr Xiao Li, Dr Ke Qu, Mr Emmanuel Tapia Brito, Mr James Riffat and Miss Tianhong Zheng who were always helpful and accommodating. It is a great pleasure to show my special thanks to Ms Zeny Amante Roberts and Ms Celia Berry for their sincere help.

Last but not least, I would like to express my love and gratitude to my family for their continued support and encouragement. They always quietly support all of my decisions. Without the help from my family members, I could not conquer all the difficulties and problems I met. I want to thank my boyfriend, Hui Zhu, for his encouragement and support. I will never become who I am today if he is not there motivating me with his kindness and inspiring me with his strengths. I hope he will also complete his PhD study successfully.

TABLE OF CONTENTS

ABSTRACT I

LIST OF PUBLICATIONS III

ACKNOWLEDGEMENT IV

TABLE OF CONTENTS VI

NOMENCLATURE XII

LIST OF FIGURES XVI

LIST OF TABLES XXII

1 INTRODUCTION 1

1.1 BACKGROUND INFORMATION 1

1.2 NARRATIVE OF AEROGELS 4

1.3 TOPIC OF THE STUDY 5

1.4 AIMS AND OBJECTIVES OF THE RESEARCH 6

1.5 NOVELTY OF THE RESEARCH 7

1.6 THESIS STRUCTURE 8

1.7 RESEARCH METHODOLOGY 11

1.7.1 Raw materials 11

1.7.2 Raw materials selection strategy 13

1.7.3 General presentation of biomass solutions/mixtures/gels preparation 14

1.7.4 Freeze drying for the preparation of biomass aerogels 16

2 LITERATURE REVIEW 17

2.1 INTRODUCTION 17

2.2 RAW MATERIALS SELECTION AND PREPARATION TECHNOLOGY FOR BIOMASS AEROGELS 19

2.2.1 Pore structure design 19

2.2.2 Raw materials for the preparation of aerogels with different pore structures 23

2.2.3 Drying methods in preparation of biomass aerogels 33

2.3 POTENTIAL APPLICATIONS OF BIOMASS AEROGELS WITH PERFORMANCE ASSESSMENT 39

2.3.1 Sound absorption 39
2.3.2 Thermal insulation 41
2.3.3 Fire resistant 43
2.3.4 Air filtration 43
2.4 CONCLUSION, CHALLENGES AND PERSPECTIVES 45
3 EXPERIMENTS FOR CHARACTERISTICS ANALYSIS OF BIOMASS MIXTURES/GELS 48
3.1 INTRODUCTION 48
3.2 SYNTHESIS OF BIOMASS SOLUTION THROUGH SOL-GEL METHOD 48
3.2.1 Materials 48
3.2.2 Preparation of biomass solution/mixtues/gels and aerogels 49
3.2.3 Procedures for formula determination 49
3.3 METHODS FOR STUDIES OF SOLUTIONS AND GELS 50
3.3.1 Pasting properties 50
3.3.2 Rheology of biomass solutions and mixtures 51
3.3.3 Confocal laser scanning microscopy (CLSM) 52
3.4 RESULTS AND DISCUSSION 53
3.4.1 Influence of KGM concentrations on the pasting properties of KGM/starch mixtures 53
3.4.2 Influence of starch concentrations on the rheology properties of KGM/starch mixtures 57
3.4.3 The macro and micro-network changes of KGM-gelatin mixtures 60
3.4.4 Impact of gelatin concentration on the rheological properties 61
3.4.5 The macroscopic characterization of KGM/wheat straw mixtures 63
3.4.6 Influence of different raw materials on the biomass aerogels 64
3.5 CONCLUSION 65
4 EXPERIMENTAL INVESTIGATION ON SOUND ABSORPTION, STRUCTURE AND MATERIAL MODELLING OF BIOMASS AEROGELS 67
4.1 INTRODUCTION 67
4.2 KGM/GELATIN/WHEAT STRAW AEROGEL PREPARATION 68
4.2.1 Materials 68
4.2.2 Preparation of KGM/gelatin/wheat straw aerogel 69

4.2.3 Procedures for formula determination 69
4.3 CHARACTERIZATION OF BIOMASS AEROGELS 70
4.3.1 Scanning electron microscopy (SEM) 70
4.3.2 Sound absorption coefficient measurement 70
4.3.3 Texture profile analysis 71
4.3.4 Fourier transform infrared spectroscopy (FTIR) 72
4.3.5 Thermogravimetric analysis (TGA) 72
4.4 ANALYSIS OF BIOMASS AEROGEL STRUCTURE AND MORPHOLOGY 73
4.4.1 Impact of gelatin on the microstructure of KGM aerogels 73
4.4.2 Impact of gelatin on the KGM/wheat straw mixtures 75
4.4.3 Impact of wheat straw on the microstructure of KGM/gelatin aerogels 76
4.5 SOUND ABSORPTION TEST OF BIOMASS AEROGELS 78
4.5.1 General acoustic absorption performance analysis for biomass aerogels 78
4.5.2 The sound absorption coefficient of KGM/wheat straw aerogels 79
4.5.3 Sound absorption coefficient of KGM/gelatin aerogels 81
4.5.4 The sound absorption coefficient of KGM/gelatin/wheat straw composite aerogels 84
4.6 INFRARED REFLECTANCE SPECTROSCOPY (FTIR) OF BIOMASS AEROGELS 86
4.7 MECHANICAL PROPERTY OF BIOMASS AEROGELS 88
4.8 MATERIAL MODELLING OF THE COMPRESSIVE BEHAVIOUR 90
4.8.1 Function to describe stress–strain relationship 91
4.8.2 Effect of gelatin addition 94
4.8.3 Effect of wheat straw addition 95
4.8.4 Material model and prediction results 96
4.9 THERMAL PROPERTY OF BIOMASS AEROGELS 98
4.10 CONCLUSION 100
5 EXPERIMENTAL INVESTIGATION ON THE THERMAL INSULATION PERFORMANCE OF BIOMASS AEROGELS 102
5.1 INTRODUCTION 102
5.2 KGM/GELATIN/STARCH/WHEAT STRAW AEROGEL PREPARATION 103
5.2.1 Materials 103

5.2.2 Preparation of KGM/gelatin/starch/wheat straw aerogel 103
5.2.3 Flowchart of experiments in Chapter 5 104
5.3 PREPARATION OF COMPARISON PANELS 104
5.4 CHARACTERIZATION OF K1S2G0.5W1.5 105
5.4.1 Thermal conductivity measurement 105
5.4.2 Microscale Combustion Calorimeter (MCC) Measurement 106
5.4.3 Thermal transmittance measurements through the hot box method 107
5.5 INFLUENCE OF RAW MATERIAL ON THE MORPHOLOGY 109
5.5.1 Impact of starch on the microstructure of KGM aerogels 109
5.5.2 Impact of gelatin on the KGM/starch/wheat straw mixtures 110
5.5.3 Impact of wheat straw on the microstructure of KGM/gelatin/starch composite aerogels 111
5.6 EFFECT OF WHEAT STRAW SIZE AND PRE-FREEZING TEMPERATURE ON THE THERMAL INSULATION PROPERTY OF BIOMASS AEROGELS 112
5.6.1 General heat transfer analysis for biomass aerogels 112
5.6.2 Impact of raw materials on thermal conductivity of biomass aerogels 113
5.6.3 Impact of wheat straw size on pore structure and thermal conductivity of K1G0.5S2WS1.5 aerogels 114
5.6.4 Impact of pre-freezing temperature on pore structure and thermal conductivity of K1G0.5S2WS1.5 aerogels 119
5.7 THERMAL PROPERTY OF K1G0.5S2WS1.5 AEROGELS 122
5.7.1 Thermal transmittance and thermal insulation test through the real small box 122
5.7.2 TG test results 123
5.7.3 Heat release behaviour of K1G0.5S2WS1.5 aerogels 124
5.8 CONCLUSION 126
6 EXPERIMENTAL INVESTIGATION ON THE EFFICIENT REMOVAL OF PARTICULATE MATTER WITH BIOMASS AEROGELS 128
6.1 INTRODUCTION 128
6.2 BRIEF SUMMARY OF KGM/GELATIN/STARCH/WHEAT STRAW AEROGEL PREPARATION 129
6.2.1 Materials 129
6.2.2 Preparation of KGM/gelatin/starch/wheat straw aerogel 129

6.2.3 Flowchart of experiments in Chapter 6 129
6.3 CHARACTERIZATION OF BIOMASS AEROGELS 130
6.3.1 Microstructure observation with a digital microscope 130
6.3.2 PM generation and filtration measurements 131
6.3.3 Real room filtration tests 133
6.4 MICROSTRUCTURE CHARACTERIZATION OF DIFFERENT FILTERS 134
6.5 PM FILTRATION PERFORMANCE TEST IN THE TRANSPARENT CHAMBER 138
6.6 MONITORING OF INDOOR AMBIENT AIR QUALITY WITH DIFFERENT FILTERS 141
6.7 CONCLUSION 143
7 COMPUTER SIMULATION FOR ENERGY DEMAND OF E.ON HOUSE WITH BIOMASS AEROGEL INSULATION PANELS 145
7.1 INTRODUCTION 145
7.2 THE CONSTRUCTION AND MATERIALS OF THE ORIGINAL E.ON HOUSE 146
7.3 MODELLING OF NOTTINGHAM E.ON HOUSE 148
7.3.1 Simulation target statement 148
7.3.2 Simulation setting 148
7.4 SIMULATION RESULTS OF THE ORIGINAL E.ON HOUSE 153
7.5 EXTERIOR WALL RETROFIT MEASURES AND SIMULATION MODELLING RESULTS OF E.ON HOUSE WITH A WALL INSULATION 154
7.6 CONCLUSION 157
8 ECONOMIC AND ENVIRONMENTAL ANALYSIS 158
8.1 INTRODUCTION 158
8.2 ECONOMIC ANALYSIS 158
8.2.1 Declared unit 159
8.2.2 System boundaries 159
8.2.3 Cost of energy and Cumulative Net Present Value (NPV) Calculation 160
8.2.4 Economic assessment results 161
8.2.5 Comparison between common insulation materials and biomass aerogels in an industrial scale 166
8.3 ENVIRONMENTAL ANALYSIS 167

8.4 CONCLUSION 168

9 CONCLUSIONS AND FUTURE WORK 169

9.1 GENERAL CONCLUSIONS 169

9.2 RECOMMENDATION AND FUTURE WORK 170

REFERENCES 173

NOMENCLATURE

Symbol	**Term**	**Unit**
C	The energy cost to produce 1 m^2·cm of aerogel	£
C1	PM mass concentration before the start of air purifier	μg/m^3
C2	PM mass concentration after the start of air purifier	μg/m^3
CFi	The cost of gas saving fee	£
C_{i0}	Parameters of Yeoh model	
C_{ij}, D_i	Parameters of polynomial model	
E	The total energy consumption of an instrument	kWh
F	Deformation gradient	
F0	Force	N
G'	Storage modulus	Pa
G"	Loss modulus	Pa
I	The initial investment cost	£
I_1, I_2	Two strain invariants	
J	Determinant of deformation gradient	
k	Model parameter to predict effect of gelatin addition	
Ka	Acid Dissociation Constant	
Mw	molecular weight	
m, n	model parameters to predict effect of wheat straw addition	
pKa	-log Ka	
R	market interest	%
Ri	inflation rate	%
r1	natural gas increase rate	

r2	The real discount rate	
rpm	Revolutions Per Minute	
S0	The initial cross-sectional area	mm^2
T	the cost of 1 kWh of electricity in UK	£ / kWh
W	Strain energy density	

Greek Letter	**Term**	**Unit**
ε	Strain	
$\lambda, \lambda_1, \lambda_2, \lambda_3$	stretch ratios	
λeff	The effective total thermal conductivity	$Wm^{-1}K^{-1}$
λg	Effective thermal conductivity of the gaseous phase	$Wm^{-1}K^{-1}$
λr	The radiative conductivity	$Wm^{-1}K^{-1}$
λs	Solid thermal conductivity of the solid backbone	$Wm^{-1}K^{-1}$
μ_1, α_i, D_i	Parameters of Ogden model	
ρ_{G}	the addition of gelatin	
$\rho_{\mathrm{G}}^{\mathrm{Ref}}$	The selected reference addition of gelatin	
ρ_{WS}	the addition of wheat straw	
$\rho_{\mathrm{WS}}^{\mathrm{Ref}}$	the selected reference addition of wheat straw	
σ	Stress	KPa
$\sigma_{\mathrm{G}}^{\mathrm{Ref}}$	The engineering stress of biomass aerogel with reference gelatin addition	
$\sigma_{\mathrm{WS}}^{\mathrm{Ref}}$	the engineering stress of biomass aerogel with the reference wheat straw addition	

Subscripts and Superscripts	
i	The period to which the cash inflow relates

n	The year when the negative cumulative NPV becomes positive

Abbreviation	**Term**
BC	Bacterial cellulose
CLSM	Confocal laser scanning microscopy
CNC	Cellulose nanocrystal
CNT	Carbon nanotube
EPS	Expanded polystyrene
FTIR	Fourier transform infrared spectroscopy
G	Gelatin (the number after G indicates the weight volume percent of origin biomass solutions)
GHG	Greenhouse gas
GPC-MALLS	Gelpermeation chromatography-multiangle laser light scattering
HEPA	High-efficiency particulate air
HPSF	High-pressure shift freezing
HRR	Heat release rate
HVAC	Heating ventilation and air conditioning
LT-SEM	Low temperature scanning microscopy
K	KGM (the number after K indicates the weight volume percent of origin biomass solutions)
KGM	Konjac glucomannan
MCAs	Magnetite carbon aerogel
MCC	Microscale Combustion Calorimeter
MOF	Metal organic framework
NFC	Nanofibrillated cellulose
NPV	Net Present Value

NRC	Noise reduction coefficient
NTs	Nanotubes
PHRR	The peak heat release rate
PIR	Polyisocyanurate
PM	Particulate matter
R^2	Coefficient of determination
RMSE	root mean square error
RVA	Rapid Visco Analyzer
S	Starch (the number after S indicates the weight volume percent of origin biomass solutions)
SAP	Standard Assessment Procedure
SEM	Scanning electron microscopy
SH	Sulfhydryl
TGA	Thermogravimetric analysis
THR	Total heat release
WS	Wheat straw (the number after WS indicates the weight volume percent of origin biomass solutions)

LIST OF FIGURES

Figure 1-1. Flowchart of this research work......11

Figure 1-2. SEM image of wheat straw. 12

Figure 1-3. General preparation of biomass solutions/mixtures/gels/. 14

Figure 1-4. Image of freeze dryer and vacuum pump. 16

Figure 2-1. Simplified schematic of aerogels preparation and application......19

Figure 2-2. SEM observations of relatively closed[59] and opened pores [83]......20

Figure 2-3. Gelatin and polysaccharide mixture molecular mechanism [85]......21

Figure 2-4. Optical images of biopolymeric porous matrix samples. (a) solution with 3% alginate, (b) 10% gelatin, (c) 3% alginate and 10% gelatin, (d) calcium alginate gel [83]. 22

Figure 2-5. SEM images of pectin aerogels. [86]. 23

Figure 2-6. Molecular structure of cellulose [103]......25

Figure 2-7. Hierarchical structure of NFC, CNC and BC; molecular structure of sugar unit; and SEM of BC ribbons, nata-de-coco and pellicle [104]. 25

Figure 2-8. Mechanism of three drying methods on a phase diagram [71]......33

Figure 2-9. Schematic of aerogel formation [161]. 36

Figure 2-10. Temperature influences on nucleation rate and ice crystal growth rate [164]. 37

Figure 3-1. Flowchart of formula determination. 50

Figure 3-2. Image of Rapid Visco Analyzer......51

Figure 3-3. Image of Rheometer. 52

Figure 3-4. Pasting curves of KGM/starch hybrid system......56

Figure 3-5. Influence of frequency on the elastic modulus (G') and viscous (G'') modulus of different KGM/starch system 59

Figure 3-6. Images of KGM–gelatin mixtures. 60

Figure 3-7. Fluorescence micrographs of KGM-gelatin mixtures......61

Figure 3-8. Changes of G' and G'' during the cooling process (70°C to 10°C) of the KGM/gelatin mixtures. 63

Figure 3-9. Digital photograph of KGM/Wheat straw biomass mixtures......64

Figure 3-10. The images of biomass aerogels (K1S1, K1G1 and K1WS1)......65

Figure 4-1. Flowchart of formula determination. 69

Figure 4-2. Image of scanning electron microscopy. 70

Figure 4-3. Image of the (a) impedance tube and the principle drawing of impedance tubes (b) L tube for the frequency from 50Hz-1000Hz; (c) S tube for the frequency from 500Hz-6500Hz......71

Figure 4-4. Image of a Texture analyzer. 72

Figure 4-5. Image of the TGA instruments......73

Figure 4-6. SEM observation of KGM and KGM/gelatin aerogels. 74

Figure 4-7. Size distribution (a: 0–450 μm; b: 0–100 μm) of KGM/gelatin aerogels pores with different gelatin concentrations. 75

Figure 4-8. Digital photograph of KGM/gelatin/wheat straw biomass mixtures (K1G1.5WS0.5, K1G1.5WS1, K1G1.5WS1.5 and K1G1.5WS2). 76

Figure 4-9. Schematic representation of gelatin structure in heating and cooling status......76

Figure 4-10. SEM observation of KGM/gelatin/wheat straw aerogels. 77

Figure 4-11. Size distribution (A: 0–450 μm; B: 0–100 μm) of KGM/gelatin/wheat straw aerogels pores with different wheat straw concentrations. 78

Figure 4-12 Image of KGM aerogel and KGM/wheat straw aerogels. 80

Figure 4-13. Sound absorption efficiency of KGM/wheat straw aerogels (K1WS1, K1WS2, K1WS3). 81

Figure 4-14. Sound absorption efficiency of composite aerogels (K1G0.5, K1G1, K1G1.5 and K1WS3). 83

Figure 4-15. Illustration of sound absorption by (a) K1G0.5 and (b) K1G1.5. 84

Figure 4-16. Illustration of sound absorption by K1G1.5WS1. 85

Figure 4-17. Sound absorption efficiency of composite aerogels (K1G1.5, K1G1.5WS0.5, K1G1.5WS1, K1G1.5WS1.5, K1G1.5WS2 and sound absorption cotton). 86

Figure 4-18. FTIR spectra of KGM aerogel, gelatin aerogel and KGM/gelatin aerogel. 87

Figure 4-19. FTIR spectra of wheat straw aerogel, KGM/gelatin aerogel and KGM/gelatin/wheat straw aerogel. 88

Figure 4-20. Compressive testing results of biomass aerogels with different additions of (a) gelatin and (b) wheat straw; SEM observation of wheat straw distribution in (c) K1G1.5WS0.5 and (d) K1G1.5WS2. 90

Figure 4-21. Comparison between different models: (a) predicted stress–strain curves and (b) calculated $R2$ and $RMSE$; Experimental and predicted effects of (c) gelatin addition and (d) wheat straw addition on engineering stress. 94

Figure 4-22. Prediction and evaluation results of the material model for compressive behaviour of biomass aerogels with different additions of (a), (b) gelatin, (c) and (d) wheat straw. 98

Figure 4-23. TGA of KGM, gelatin, wheat straw and K1G1.5WS1 aerogel. 99

Figure 5-1. Image of Tyler screens. 103

Figure 5-2. Flowchart of experiments in Chapter 5. 104

Figure 5-3. Images of testing panels. 105

Figure 5-4. Thermal conductivity analyzer for small size specimens. 106

Figure 5-5. Images of Microscale Combustion Calorimeter device......106

Figure 5-6. Images of the original panel box, the small heating fan and the data logger. 108

Figure 5-7. Details of installation position. 108

Figure 5-8. SEM observation of KGM and KGM/starch aerogels. 110

Figure 5-9. Size distribution (a: 0–450 μm; b: 0–100 μm) of KGM/starch aerogels pores with different starch concentrations. 110

Figure 5-10. Digital photograph of KGM/gelatin/starch/wheat straw biomass mixtures (K1G0.5S2WS0.5, K1G0.5S2WS1, K1G0.5S2WS1.5 and K1G0.5S2WS2)......111

Figure 5-11. SEM observation of KGM/starch aerogel and KGM/gelatin/starch aerogel and KGM/gelatin/starch/wheat straw aerogels......112

Figure 5-12. Illustration of heat transfer mechanism in biomass aerogels. 115

Figure 5-13. SEM observation of K1G0.5S2WS1.5 aerogel with different wheat straw sizes......117

Figure 5-14. Microstructure of K1G0.5S2WS1.5 aerogels formed under different pre-freezing temperature: (-15, -25, -30, -40°C) and image of frozen sample K1G0.5S2WS1.5. 121

Figure 5-15. Experimental results for the normal panel surface temperature, environmental temperature and U value in a small box......123

Figure 5-16. TGA of starch and K1G0.5S2WS1.5 aerogel......124

Figure 5-17. Heat release rate (HRR) curves of PU and EPS [241]......125

Figure 6-1. Flowchart of experiments in Chapter 6. 130

Figure 6-2. Image of a digital compound microscope......131

Figure 6-3. Schematic illustration of lab-built PM adsorption test system. 132

Figure 6-4. Images of all filter samples (a) surgical mask; (b) biomass aerogel; (c) HEPA; (d) silica aerogel and (e) cotton cloth......133

Figure 6-5. Photos of the actual room experiment setup. 134

Figure 6-6 Micro-images of biomass aerogels before the filtration test (a) and after the filtration test (b)......135

Figure 6-7. SEM-images of biomass aerogels before the filtration test......136

Figure 6-8. Micro-image of melt-blown fabric and non-woven fabric after the filtration test......137

Figure 6-9. SEM-images of melt-blown fabric, non-woven fabric, biomass aerogel, regular cloth and silica aerogel after the filtration test. 138

Figure 6-10. The PM 2.5 removal efficiency of (a) different filters from 0 min to 30 min, (b) HEPA, surgical mask and biomass aerogel K0.9G1.8S3.6WS1 from 26min to 30 min. 140

Figure 6-11. The PM 10 removal efficiency of (a) different filters from 0 min to 30 min, (b) HEPA, surgical mask and biomass aerogel K0.9G1.8S3.6WS1 from 26 min to 30 min......141

Figure 6-12. Measured (a) PM 2.5 concentration in the actual room; and (b) the PM 2.5 removal efficiency with HEPA, K0.9G1.8S3.6WS1.8 and K0.7G1.4S2.8WS1.4......142

Figure 6-13. Measured (a)PM 10 concentration in the actual room; and (b) the PM 10 removal efficiency with HEPA, K0.9G1.8S3.6WS1.8 and K0.7G1.4S2.8WS1.4......143

Figure 7-1. Images of E.ON house......146

Figure 7-2. The model of E.ON house. 149

Figure 7-3. The average monthly rainfall and average air temperature in the UK. 150

Figure 7-4. Schematic of zoning on the ground floor (left) and 1st floor (right). ..151

Figure 7-5. Specification of the overall energy consumption of the original E.ON house. 154

Figure 7-6. Heating gas demand of the E.ON house comparison between original E.ON house and the E.ON house with biomass aerogel wall insulation. 156

Figure 7-7. Specification of the overall energy consumption of the E.ON house with wall insulation......157

Figure 8-1. System boundary of biomass aerogel production process (gate to gate). 159

Figure 8-2. The Net Present Value of E.ON house with K1G0.5S2WS1.5 aerogel wall insulation in lab scale and industrial scale. 166

Figure 9-1. The macro images of biomass aerogels with and without hydrophobic treatment......172

LIST OF TABLES

Table 2-1 Summary of biomass modification influence on performance......31

Table 2-2 Basic difference between three kinds of celluloses: NFC, CNC and BC..32

Table 2-3 Physical properties of different types of polysaccharide aerogels......34

Table 2-4 Polysaccharide aerogels pore size under different freeze-drying conditions. 38

Table 3-1 Aerogel sample formula. 49

Table 3-2 Effect of Konjac glucomannan (KGM) on the pasting properties of potato starch and KGM-starch mixtures. 55

Table 4-1 Sound absorbing aerogel sample formula. 68

Table 4-2 Parameters of the polynomial, Ogden and Yeoh models......93

Table 4-3 Parameters of the material model for compressive behaviour of biomass aerogels with different additions of gelatin and wheat straw. 96

Table 5-1 The formula of the samples and their raw materials. 104

Table 5-2 Thermal conductivity of K1G0.5S2WS1.5 aerogels made from different sizes of wheat straw......118

Table 5-3 Thermal conductivity of K1G0.5S2WS1.5 (wheat straw sieved from 120 mesh) aerogels made under different pre-freezing temperatures: (-15, -25, -30, -40°C)......122

Table 6-1 The formula of the samples and their raw materials. 129

Table 7-1 The original building construction materials of the E.ON research house. 147

Table 7-2 Dimensions of zones of E.ON research house. 151

Table 7-3 Detailed information about appliances, natural gas, people and zone infiltration. 152

Table 7-4 The new exterior wall construction materials of E.ON research house with wall insulation......155

Table 8-1 Economic indicators and natural gas increase rate 161

Table 8-2 Cost of the raw materials for the production in a lab scale......162

Table 8-3 Economic assessment of the biomass aerogel Life Cycle in large batches. 164

Table 8-4 Total cost of the biomass aerogel used in E.ON house renovation......165

Table 8-5 The cost of common insulation materials and biomass aerogels......166

1 INTRODUCTION

1.1 BACKGROUND INFORMATION

Energy conservation, rapidly diminishing oil resources and environmental protection have received growing attention as global energy demand increases. Increasing environmental problems and a growing awareness of environmental protection have led to a consensus on reducing fossil fuel consumption. The European Union has aimed to reduce energy use and flue gas emissions [1]. Therefore, energy conservation policies can be enforced and implemented by the development of buildings. According to a Worldwatch Institute study, buildings are the largest energy consumer of any sector, accounting for 40% of the world's total annual energy consumption and about one-third of total CO_2 emissions [2]. To reduce CO_2 emissions, many low-energy buildings and passive houses have been built in German [3]. On the other hand, a large amount of energy is used for space heating and air conditioning, especially in extremely hot and cold climate regions, and real estate has great potential for energy saving by rational use of resources. Considerable effort has been made over the past 20 years to develop low/zero carbon buildings by improving energy efficiency and developing environmentally friendly materials using renewable resources. Thermal insulation helps buildings minimize energy consumption to maintain thermal comfort by preventing unwanted heat loss or gain [4]. Commonly, thermal insulation materials are composed of organic polymers, such as polyurethane foam, polystyrene foam and glass wool. Polyurethane foam can be divided into two categories: flexible polyurethane foam and rigid polyurethane foam [5], and is often used as thermal insulation materials in the building envelope and domestic refrigerators [6]. However, polyurethane foam production relies on unsustainable petroleum sources, as its two main components are isocyanates and polyether. Moreover, the

widespread use of polyurethane has produced considerable amounts of waste, and these wastes usually go into landfills, which need a long time to be degraded.

Noise is considered as the most widespread and hardest controlled environmental pollution [7, 8]. In 1972, the World Health Organization announced that noise is a pollutant. Noise can cause negative health effects and has become a significant pollution problem worldwide. It will affect the human hearing system and cause health problems such as high blood pressure [9] and increased physiologic stress [10, 11]. Apart from the influence on human health [12], noise can accelerate the ageing of buildings and machinery, affecting the accuracy of the equipment. Therefore, acoustic absorption materials are used in different fields [13-16], especially in buildings, to reduce the impact of noise on residents. Currently, there are many types of sound absorbing materials, such as glass fiber [17], metal fiber [18], polyethene foam [19], ceramic [20], rock [21] and glass wool [18]. The structure can be divided into two categories: porous sound absorbing materials [22-24] and resonant sound absorbing materials [25, 26]. Porous sound absorption materials have many tiny, porous structures, which penetrate each other and communicate with the outside through the surface pores, called open porous [27]. Currently, the sound absorbing materials commonly used in the market have some defects. For example, sponges have excellent sound-absorbing properties often used in recording studios. However, it has a poor damping effect and easy to absorb dust; Glass fibers commonly used as sound absorption materials have good sound insulation properties as well as fragile performance, which will cause damage to the lungs if inhaled by the human.

At the same time, air pollution is one of the leading environmental problems in the world and is among the critical challenges facing modern societies. It refers to the contamination of the atmosphere by a mix of hazardous substances, particulate matter (PM) from natural sources and human activities. Natural forms of pollution result from naturally occurring phenomena, such as volcanic eruptions, forest fires, ocean waves and soil dust. However, the most

significant contributor to pollution is human activities, including industrial waste exhaust gas, fossil-fuel emissions, and motor vehicle emissions. Inhalable PM particles can be roughly divided into two size fractions PM 2.5 (aerodynamic diameter below 2.5 μm) and PM 10 (aerodynamic diameter between 2.5 μm and 10 μm) [28, 29], both of those are fine inhalable particles and cannot be detected by naked eyes so that they are easily inhaled into human lung contributing to serious health problems [30]. Between them, particles with a diameter less than 2.5 μm, which is only 3% of the diameter of a human hair, are also known as PM 2.5. They are easier to penetrate deep into the human lungs; some may even enter the bloodstream and circulatory system, causing cough, asthma, or morbidity and mortality. To solve this serious problem, researchers worldwide are dedicated to studying various techniques to reduce air pollution. In the early period, the filter materials were mainly made of cotton, wool, jute, and various synthetic cellulose fabrics and other porous fabrics. Mandal and Srimani [31] used jute fiber as the filter in the microbiological experiment. In the 1940s, the high-efficiency particulate air (HEPA) filter was invented in the USA [32], and then it was introduced into commercial applications in the following decade, such as air purification in particular rooms. Since then, filter materials have developed rapidly and grown in popularity and necessity. In recent years, many novel air filter materials appeared in succession. Filtration materials are widely used in many applications, including the typical heating ventilation and air conditioning (HVAC) systems. Hui Liu et al. [33] created a nanoscale polyacrylonitrile fiber filter using an innovative electro netting technique. It has been verified that the PM 0.3 was reduced by 99.996% with the novel nanonet filter. Abdul Rajak et al. [34] used expanded polystyrene (EPS) waste as the raw material to make a nanofibrous membranes filter through the electrospinning method. Nanofibrous membranes with low density and high Young's modulus can achieve high-efficiency PM 2.5 removal of 99.99% and a high-quality factor of 0.15 Pa^{-1}. Chao Jia et al. [35] developed a kind of Al_2O_3-

stabilized ZrO_2 submicron fiber air filter paper, which has high filtration efficiency (99.56%) and a low-pressure drop (108 Pa). At the same time, this material also shows excellent flexibility and thermal stability. Using the electrostatic induction-assisted solution blowing method, Shengnan Lv et al. [36] fabricated PLA/PMMA composite nanofibers with 99.5% PM 2.5 removal. In the research of Wallace Woon FongLeung and Qiangqiang Sun, the improved nanofiber filter with charged fibers was invented for capturing 100 nm aerosols [37].

1.2 NARRATIVE OF AEROGELS

Aerogel is a synthetic three-dimensional porous material produced by specific drying methods to replace the liquid part in gel with air [38]. Aerogels have a unique structure possessing low density, high porosity and large interior surface area, which contributes to specific functional properties. Kistler first studied silicon aerogels in 1931, and their special functional properties gained great attention in academia [39]. Since their inception, various aerogels have been researched, developed and applied in various fields [40, 41]. Raw materials of conventional aerogels come from inorganic or petrochemical-based materials such as those used in silica aerogels, graphene aerogels [42] and titanium aerogels [43], or their oxides aerogels. In response to the environmentally friendly requirement, developing biomass aerogels has attracted extensive interest from researchers [44-46]. Biomass aerogels are made from natural ingredients. They have an excellent eco-friendly biodegradable feature, so maximizing the biomass ingredients in aerogels has become a tendency. With abundant sources, polysaccharides and proteins including cellulose [47, 48], chitosan [49, 50], starch [51], alginate [52], agar [53], gelatin [54] and whey protein [55] have been adopted to prepare aerogels. These biomass materials are abundantly resourced, low-cost, environmentally friendly, and key to producing multifunctional materials.

As a promising polysaccharide, Konjac glucomannan (KGM) is an edible polysaccharide found in the tuber of the amorphophallus konjac plant [56] with a high molecular weight [57] (6.8×10^5~9×10^6) and high viscous property (30000 mPa·s, 1%, w/v). As reported, it has the potential to be a skeletal material in gel due to its macromolecular chain structures [58], and KGM-based aerogels exhibit three-dimensional network structures [59, 60]. Gelatin [61, 62] is a collagen peptide derived from the skin, bone and cartilage of animals and is widely used as a bionic scaffold in tissue culture engineering because of its biocompatible and porous properties. Starch, an edible, renewable agricultural product is usually used in food or other industrial products [63]. Wheat is cultivated in over 115 nations of the world and can be used as sound absorption material [64, 65]. Wheat straw is a kind of agricultural waste, the main components of which are cellulose, hemicellulose and lignin [66]. Currently, the typical way to dispose of wheat straw is by burning, which causes severe air pollution to the environment. In this study, a new approach to utilize it and improve its economic and environmental values is explored by adopting wheat straw as a raw material to prepare biomass aerogel.

1.3 TOPIC OF THE STUDY

This study focuses on developing alternative novel, low carbon and sustainable biomass aerogels applied in buildings to solve energy shortages, sound/environmental pollution and other global crises. The biomass aerogels were produced via the sol-gel process and freeze drying method using natural materials. Natural biomass and its derivatives are widely used because of its non-toxicity, sustainability and biodegradability. Using renewable resources is a way to reduce greenhouse gas emissions at the source. In this study, different polysaccharides and proteins were selected to investigate the effect of different formulations on the microstructure morphology and properties of biomass aerogels. This study also evaluated the thermal insulation, sound absorption and filtration performance of biomass

aerogels as construction materials. The environmental and economic assessment verified that biomass aerogel is an ideal material used in low-carbon buildings.

1.4 AIMS AND OBJECTIVES OF THE RESEARCH

This research aims to develop novel biomass aerogels as thermal insulating, sound-absorbing and filtering materials for low-carbon buildings, which are produced using natural biomass materials. Compared to conventional building materials, the biomass aerogel studied in this research is 100% degradable, environmental-friendly and easy to dispose of after use, while it also has a three-dimensional structure, low density, high porosity and excellent properties. Biomass aerogels have a broad prospect in construction applications, saving energy and reducing noise and environmental pollution. Few studies have reported on the physicochemical changes that occur during the preparation of biomass aerogels and the effects of raw materials and components on the porous structure and properties of aerogels. In this study, these will be explored. The environmental impacts of manufacturing a novel biomass aerogel at a lab scale are also evaluated. Biomass aerogels could replace the traditional petroleum-based materials to reduce the use of fossil energy and achieve low carbon emissions. Therefore, the study on the preparation and application of biomass aerogels has essential theoretical significance.

The specific objectives of the research are presented below:

(1) To conduct a comprehensive literature review on the status of biomass aerogels from three aspects: raw materials, preparation methods and potential applications.
(2) To evaluate the characteristic of raw materials, biomass mixtures and gels. The influence of each component and process parameters on biomass gel and aerogel was investigated.
(3) To develop biomass aerogels with excellent sound absorption performance. The correlations of biomass aerogel performance (i.e., sound absorption and mechanical

performances) and its microstructure (i.e., micro-pore structure, the size distribution of micro-pore) were explored.

(4) To optimize the thermal insulation property of biomass aerogels by regulating the growth of ice crystal and wheat straw length. The thermal conductivity of different insulation materials was compared through long-term monitoring by a heat flux sensor and temperature sensors in a small box.

(5) To develop biomass aerogels with excellent PM filtration performance. The correlation between filtration performance and its microstructure was explored.

(6) To evaluate the heating energy saving after retrofitting the house wall with biomass aerogel insulation layer using energy plus.

(7) To analyze the economic and environmental impact of producing biomass aerogel, enabling continuous production suitable for industrial scale.

1.5 NOVELTY OF THE RESEARCH

This research has uniquely developed a novel biomass aerogel with effective performance. To overcome the common drawback of the commercial building materials, the biomass aerogels were produced from natural biomass, which will not harm our environment and pose a threat to wildlife after use. Its unique performance could be used as insulation and filtration materials. The detailed novel aspects of this research are shown as the following:

- This research will develop an innovative biomass aerogel produced from natural biomass, safe and sustainable raw materials.
- It aims to employ KGM as a skeleton micro-pore structure, use starch and gelatin to enhance the mechanical performance of the aerogel and offer good sound absorption, thermal insulation and air pollutant filtration performance.

- The agricultural waste, wheat straw, has been converted into valuable raw material for producing biomass aerogel.
- It effectively controls the pore structure and pore size distribution of the aerogels by regulating the ratio of raw materials in the sol-gel process and the growth of ice crystals in freeze drying process.
- Low cost: it has an economically viable and comparatively simple manufacturing process with low environmental impact; it is easy to mass-produce.
- 100% biodegradable, environmental-friendly, and easy to dispose of after use.

The innovative biomass aerogels were developed and assessed. The raw materials and preparation methods for producing biomass aerogels are relatively simple, economical and environmentally friendly. The freeze drying method consumes relatively less energy and thus has a lesser CO_2 burden. In addition, the aerogel can be used as insulation material in buildings to reduce energy demand for heating. Therefore, this material can offer opportunities for saving energy and reducing the amount of CO_2 released into the environment.

1.6 THESIS STRUCTURE

The thesis consists of eight chapters. The overall structure and the brief description of the research are shown below:

Chapter 1 introduces the background generally and states the current problems and challenges. The aims, objectives and the novelties of this research are introduced in detail. A brief methodology introduction of starting materials and experimental methods for preparing biomass mixtures/gels and aerogels is presented.

This research starts with a literature review in **Chapter 2** based on the current development and status of biomass aerogels. A review of pore structure design, raw materials selection,

existing preparation technologie and application fields has been carried out to provide a background for starting this research.

In Chapter 3 Some initial experiments are carried out to select the optimal raw biomass materials for the preparation and investigate the characteristics of different binary composite mixtures/gels. The initial test analysis determined ranges of raw materials addition and process parameters (preparation temperature, stirring time and gel ageing temperature).

In **Chapter 4,** the physical and chemical properties will be investigated, including microstructure, sound absorption properties, thermal stability and mechanical properties. The influence of gelatin and wheat straw addition on the microstructure and chemical properties will be studied and compared. The sound absorption performance of biomass aerogels will be measured and compared with sound absorption cotton. A material model of KGM aerogels with gelatin and wheat straw addition will be presented.

Chapter 5 focuses on the thermal insulation property of biomass aerogels. The impact of wheat straw length and pre-freeze temperature on the thermal insulation property of biomass aerogels will be studied. The microstructure, thermal stability and mechanical properties will be investigated. An actual small box will be built to test and verify the thermal insulation property of biomass aerogels in reality. These results will also be compared with the commercial materials. The flame retardant properties of biomass aerogels will be presented.

Chapter 6 is dedicated to testing the particulate matter (PM) filtration ability of biomass aerogels over a long period. The microstructure of biomass aerogels before and after the filtration test will be investigated. The PM removal ability of biomass aerogels will be compared with common commercial filtration materials, including HEPA, surgical masks, regular cloth and silica/glass fiber aerogel.

Chapter 7 explores the applicability of biomass aerogel as an insulation material in buildings. A representative exemplary research E.ON house will be used to simulate the energy consumption using Energy Plus. The simulation will study and compare the heating energy consumption of E.ON house with and without the retrofitting of biomass aerogel as the insulation layer.

The economic and environmental analysis of biomass aerogels will be presented in **Chapter 8**, which indicates the sustainability and great future market potential of these novel biomass aerogels.

Chapter 9 will present the main conclusions and limitations of this work. Discussing the recommendations for future works will provide a reference for the future development of biomass aerogels. A flow chart of this thesis will be demonstrated in the following figure.

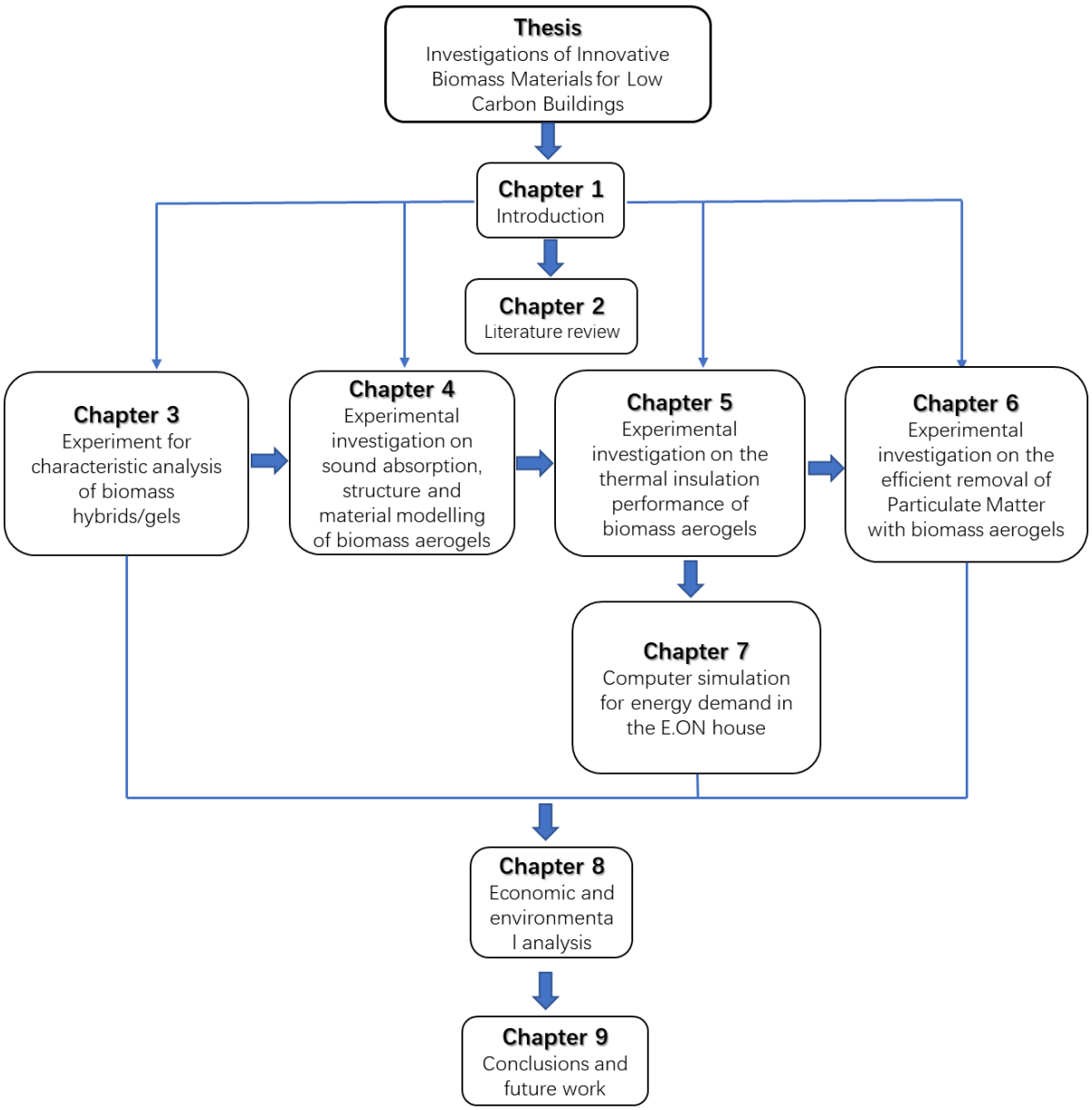


Figure 1-1. Flowchart of this research work.

1.7 RESEARCH METHODOLOGY

1.7.1 Raw materials

KGM: KGM was purchased from Hubei Konson Konjac Gum Co., Ltd (Wuhan, China). The weight average molecular weight (Mw) of KGM powder was characterized by the gel permeation chromatography-multiangle laser light scattering (GPC-MALLS) of 911.5 KDa with a molar ratio of mannose: glucose of 1.6:1 and a degree of acetylation of 1.85%. With

high molecular weight and high viscous, it has potential to be used as a thickener for the solutions [67]. Additionally, KGM is also known to interact synergistically with other polysaccharide, enhanced their rheological properties. It can be a good skeleton material for aerogel preparation.

Potato starch: It was purchased from Wuhan Lin He Ji Food Co., Ltd. (Wuhan, China). The potato starch was characterized by an Mw of 79.8 KDa. As a very refined starch, potato starch contains minimal protein [68]. In order to reduce the influence of protein in starch on experimental results, potato starch was selected.

Wheat straw: The dry wheat straw was obtained from a local farm in Wuhan. After being cut into small segments and washed more than five times, raw wheat straw was completely dried in an oven at 90°C. The dried straw segments were mechanically milled into particles by a cereal pulverizer. The wheat straw powder was sieved through the Tyler screen before being used. The microstructure of wheat straw is presented in Figure 1-2. To increase the amount of the small pores in aerogels, wheat straw was used in this research as it can also provide many micron-scale pores due to its multi-cavity and hollow structure.

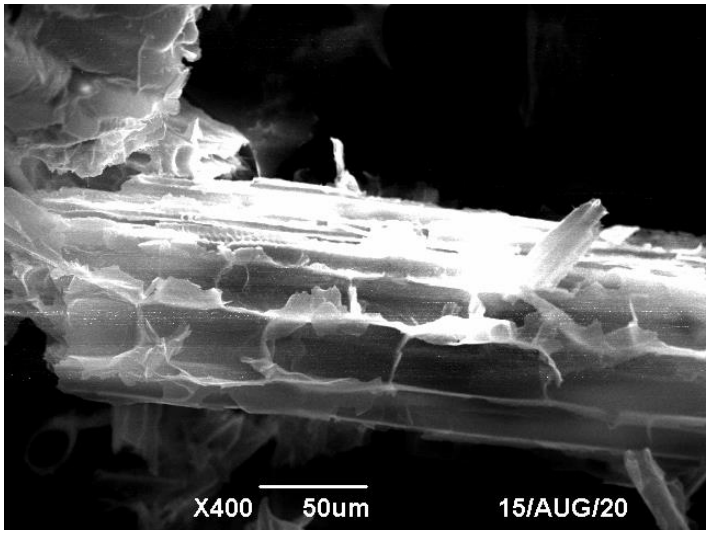


Figure 1-2. SEM image of wheat straw.

Gelatin: Gelatin was purchased from Sinopharm Chemical Reagent Co., Ltd. (Shanghai, China). The gelatin was characterized by an Mw of 245.2 KDa. Gelatin can convert into gel rapidly when the temperature is lower 37°C. Based on this property, it could be used for preventing the subsidence of wheat straw in the gels. Furthermore, gelatin could contribute to produce interconnecting pores in aerogels.

1.7.2 Raw materials selection strategy

For sound absorption study in Chapter 4, KGM, gelatin and wheat straw have been selected. KGM has large molecular chain, could be considered as the good skeleton material for aerogel preparation. With the combination of gelatin, it could help to decrease the pore size and increase the pore amounts. In addition, gelatin could contribute to produce interconnecting pores in aerogels as it has been verified and been widely used as a bionic scaffold in tissue culture engineering [69]. For sound absorption, this property is very necessary as it can provide the chances for the sound wave enter the interior of pores. With multi-cavity and hollow structure, wheat straw leads to form complicated aerogel pore structure to dissipate the energy of sound waves. Meanwhile, gelatin can prevent the subsidence of wheat straw as it can be converted into gel rapidly below 37°C.

For thermal insulation study in Chapter 5, it is different from the sound absorption. Closed-pore structure is good for thermal insulation. Different from gelatin, starch addition contributes to the form of more micron-sized close pores, improving thermal insulation property. After adding wheat straw, the biomass aerogel structure became complex, and the gaseous flow path was changed to be more complicated, leading to the lower thermal conductivity. The introduction of gelatin is not conducive to improving thermal insulation performance, but a small amount of gelatin is needed for preventing wheat straw subsidence.

For particle filtration study in Chapter 6, KGM, glelatin, starch and wheat straw were selected. For the filtration, both open and close pores are needed. The particles can enter aerogels through open pores in the surface and they will be intercepted by close pores in aerogels. As explained above, these four raw materials have great influence on the aerogel structure.

1.7.3 General presentation of biomass solutions/mixtures/gels preparation

Biomass solutions and biomass gels preparation are described in the following steps: dissolution of polysaccharides and gelatin in the distilled water, gel casting and gel-ageing in a 4°C refrigerator.

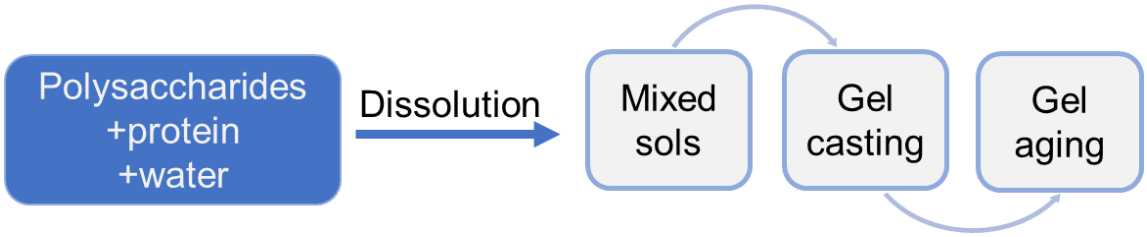


Figure 1-3. General preparation of biomass solutions/mixtures/gels/.

(1) Synthesis of KGM solution and gel: The KGM powder was slowly added to the 100 mL water and mixed homogeneously with the 95°C water bath heating under constant stirring at 600 rpm. After stirring the mixture for 1 h, KGM solution was poured into a mould and placed in a 4°C refrigerator as gel-ageing for 2 h to obtain the KGM stocking solution.

(2) Synthesis of KGM/starch mixtures and gels: The starch powder was added to the beaker with 100 mL of distilled water at room temperature (22°C) and mixed homogeneously with the glass rod. After the starch powder was completely soaked, the beaker was put into a water bath at 95°C. Before the temperature rises, the KGM powder was gradually added to the beaker under constant stirring at 600 revolutions Per Minute (rpm). After stirring for 1 h,

the KGM/starch mixtures were poured into a mould and placed in a 4°C refrigerator as gel-ageing for 2 h to obtain the KGM/starch stocking solutions.

(3) Synthesis of KGM/gelatin mixtures and gels: Gelatin was first dissolved in a beaker with 20 mL of water for half an hour, heating in a water bath at 60°C. After the gelatin dissolved completely, 80 mL of double-distilled water was then added. Meanwhile, the KGM powder was slowly added under constant stirring at 600 rpm, and the water bath temperature was increased to 95°C. After stirring for 1 h, the KGM/gelatin mixtures were poured into a mould and placed in a 4°C refrigerator as gel-ageing for 2 h to obtain the KGM/gelatin gels.

(4) Synthesis of KGM/ wheat straw solutions: The wheat straw powder was added to the beaker with 100 mL distilled water under room temperature and mixed homogeneously with the glass rod. After the wheat straw powder was completely soaked, the beaker was put into a water bath at 95°C. Before the temperature rises, the KGM powder was gradually added to the beaker under constant stirring at 600 rpm. After stirring for 1 h, the KGM/wheat straw mixtures were poured into a mould.

(5) Synthesis of KGM/gelatin/wheat straw solution, mixtures and gels

Gelatin was first dissolved in a beaker with 20 mL of double-distilled water for half an hour of heating in a water bath at 60°C. After the gelatin dissolved completely, 80 mL of double-distilled water and wheat straw were then added. Meanwhile, the KGM powder was slowly added under constant stirring at 600 rpm, and the water bath temperature was increased to 95°C. After stirring for 1 h, the KGM/gelatin/wheat straw mixtures were poured into a mould and placed in a 4°C refrigerator as gel-ageing for 2 h to obtain the KGM/gelatin/wheat straw gel.

(6) Synthesis of KGM/ gelatin/ starch/wheat straw solutions, gels and mixtures:

Gelatin was first dissolved following the same procedure introduced in Section 4.2.2.1. Then starch and wheat straw were added. Meanwhile, the KGM powder was slowly added under constant stirring at 600 rpm, and the water bath temperature was increased to 95°C. After stirring for 1 h, the KGM/gelatin/wheat straw mixtures were poured into a mould and placed in a 4°C refrigerator as gel-ageing for 2 h to obtain the KGM/gelatin/starch/wheat straw gel.

1.7.4 Freeze drying for the preparation of biomass aerogels

After the ageing process in the refrigerator at 4°C, the samples were immediately frozen in an ultra-low temperature freezer (LGT2325, German-Swiss) at −25 °C for 10 h. The frozen sample was dried in a freeze dryer (FD-1A-50, Boyikang, China) at −55 °C under a vacuum of 1 Pa for approximately 24 h as shown in Figure 1-4, and aerogels were formed and obtained.

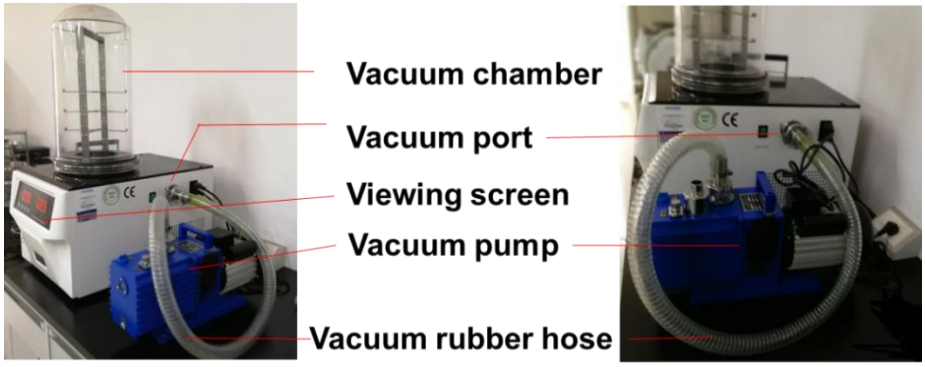


Figure 1-4. Image of freeze dryer and vacuum pump.

2 LITERATURE REVIEW

2.1 INTRODUCTION

Aerogels were firstly fabricated by Kistler. He obtained it from gels, where the liquid was replaced by gas. Some other practitioners believe that only the materials with meso- and macropores with diameters up to a few hundred nanometres and porosity of more than 95% can be called aerogels [70]. João P. Vareda [71] reconsidered the definition of aerogels and presented the view that aerogels need to be redefined as the recent development of aerogels with multiple drying methods. With the widening of the definition, more and more studies on aerogels have been conducted.

By summarizing research with three drying methods, this review is inclined to the view that aerogels have high porosity, high surface area and low density, and pore size distribution is mainly from nano to micro-scale. One kind of new sustainable biomass aerogels stood out and attracted much interest from researchers.

Raw materials of conventional aerogels come from inorganic or petrochemical-based materials such as those used in silica aerogels, graphene aerogels [42], titanium aerogels [43], or their oxides aerogels. In response to the environmentally friendly requirement, developing biomass-derived aerogels has attracted extensive interest from researchers in the past decades [72, 73]. The biomass-derived aerogels are formulated from natural ingredients, so they have an excellent eco-friendly biodegradable feature; hence, maximizing the biomass ingredients in aerogels has become a tendency.

According to their ingredients, biomass-derived aerogels (or called biomass aerogels) can be divided into three categories: polysaccharide aerogels, protein aerogels and lignin aerogels [74]. Among them, polysaccharide aerogel as the precursor has abundant natural sources, such as cellulose, starch, chitosan, alginate, carrageenan and pectin. As one of the most

abundant natural polymers, cellulose widely exists in wood [75], bamboo [76], cotton [77], banana peel fiber [78] and coconut husk [79]. Biomass may become a key ingredient in novel functional materials because of their unique properties, including biocompatibility, sustainability, low toxicity and renewability. Polysaccharide aerogel has been a research focus in recent years due to European Union rules for reducing the use of plastic film and foam materials. As for the application as packaging foam, biomass aerogels have overwhelming superiority to accelerate the promotion of this ban. The functional biocompatibility and low toxicity properties of biomass aerogels can also be applied in health and medicine to overcome the stability problem of drugs and some limitations of drug delivery to benefit humankind. Apart from polysaccharide, protein has also been used in aerogels such as gelatin and whey protein. Protein has attracted attention as a functional material in many fields with many outstanding characteristics, such as digestibility, biocompatibility, thermo-/pH-sensitivity and gelation ability.

This review aims to describe and discuss the structure design, raw materials selection, preparation and application of biodegradable biomass aerogels, focusing on polysaccharide aerogels and protein aerogels. In Section 2.2, three drying methods of aerogels are compared, especially on the aspect of pore structure, to provide a reference for aerogels structure design. Then with excellent advantages of natural raw materials, biomass aerogels have attracted wide interest in many fields, such as environmental engineering, buildings, medicines, electrochemical components and food packages. The applications of biomass aerogels are discussed in Section 2.3. Finally, the challenges, perspectives and concluding marks are presented in Section 2.4. Hopefully, this review could help explore biomass aerogels' formulation, preparation and application, as shown in Figure 2-1. It also provides clear guidance for the future development of biomass aerogels.

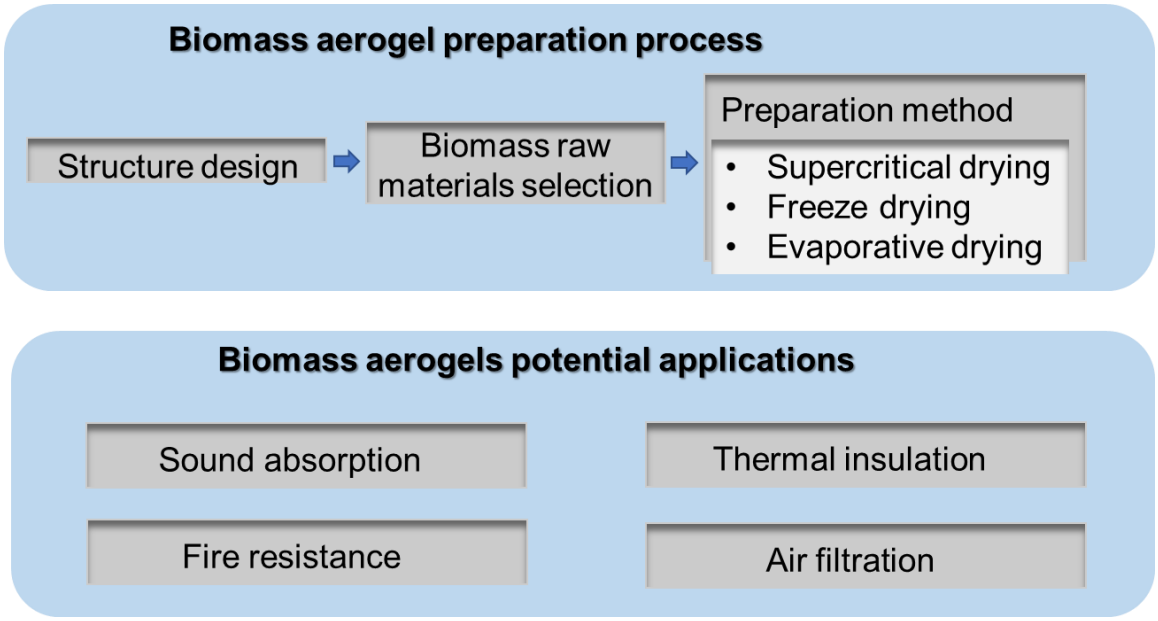


Figure 2-1. Simplified schematic of aerogels preparation and application.

2.2 RAW MATERIALS SELECTION AND PREPARATION TECHNOLOGY FOR BIOMASS AEROGELS

2.2.1 Pore structure design

In all porous solid materials, various channels and cavities exist, which are regarded as pores. Aerogel materials stand out from porous materials due to their unique pore structure, high specific surface area and low density, which could be used in many applications [80]. Depending on the application requirements, the meaningful functional properties affected by pore structures could be introduced in different aerogels. The shape of aerogel pores could be divided into open and close pores according to the gas fluid flow property presented in the theory of Rouquerol, et al [81]. In the previous studies, relatively close and open pores could be observed in SEM images, as shown in Figure 2-2. Open pores have the opportunity to communicate with others and the external surface of the materials. The close pore is the relatively independent one separating from any nearby pores. For example, aerogels are often used in different fields, such as drug encapsulation, generative medicine and water pollutants

adsorption. In these application fields, the requirement of the material structure is quite different. When the drug is being carried, the drug needs to be encapsulated by the carrier, porous aerogels with relatively closed pores [82], and then released under specific conditions. In regenerative medicine, aerogels as the scaffold structure, require uniform open pores [69]. As an adsorbent material, aerogels require a certain amount of open pore structure to inhale pollutants and close pore structure to store the pollutants. Therefore, the significance of aerogels structure design is to be better adapted to the different application requirements.

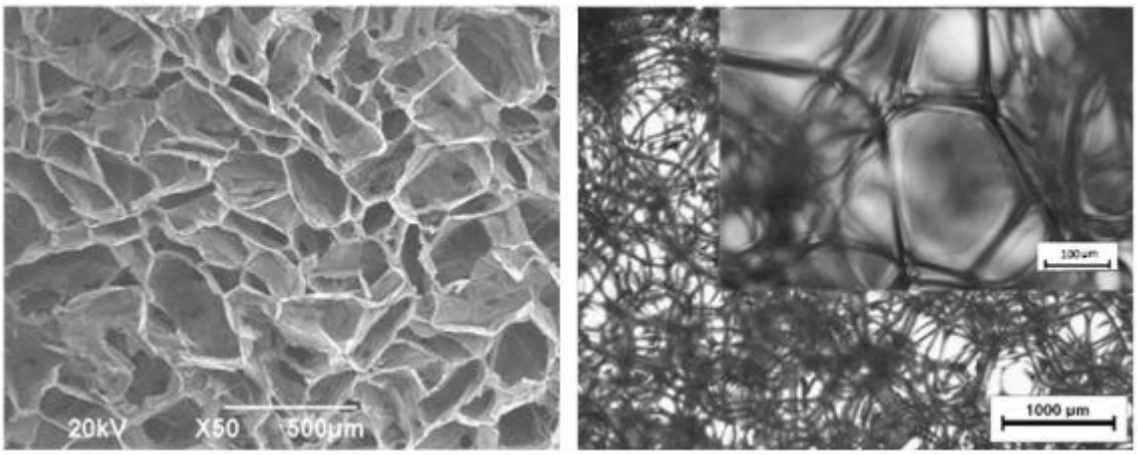


Figure 2-2. SEM observations of relatively closed[59] and opened pores [83].

Previous studies [81, 82] show that different preparation technologies, including raw materials, gel process and drying methods, lead to different aerogel pore structures. With different unique molecule chain structures, polysaccharide could directly affect aerogels' physical properties, which will be given a detailed introduction in Section 2.2.2. Meanwhile, physical properties could also be changed by adjusting the aerogels pore structure. Raw materials could affect the pore structure due to their unique properties. As presented in the previous work [59], with a high concentration of starch, the pore wall becomes thicker, which benefits the formation of close pores in aerogels. With the thicker wall, it can bear certain pressure to protect the pores in aerogels forming as the close pores. Oppositely, gelatin with a special triple helix structure (Figure 2-3), sucrose and paraffin wax has been confirmed to be

used as porogens to increase the porosity of materials [83, 84]. From the optical microscopy images comparison of a biopolymeric porous matrix (as shown in Figure 2-4) with three different solutions (alginate solution, gelatin solution and mixture solution), more interconnected pores will be formed with the addition of gelatin [83]. Gelatin, sucrose and paraffin wax have been confirmed to be used as porogens to increase the porosity of materials.

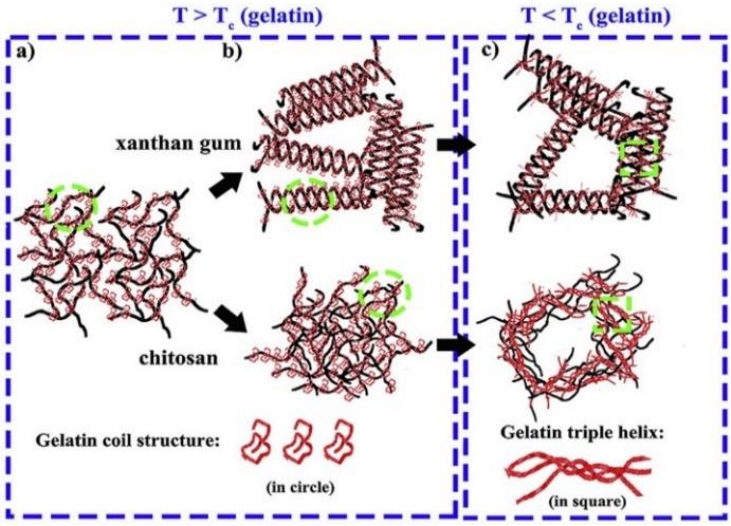


Figure 2-3. Gelatin and polysaccharide mixture molecular mechanism [85].

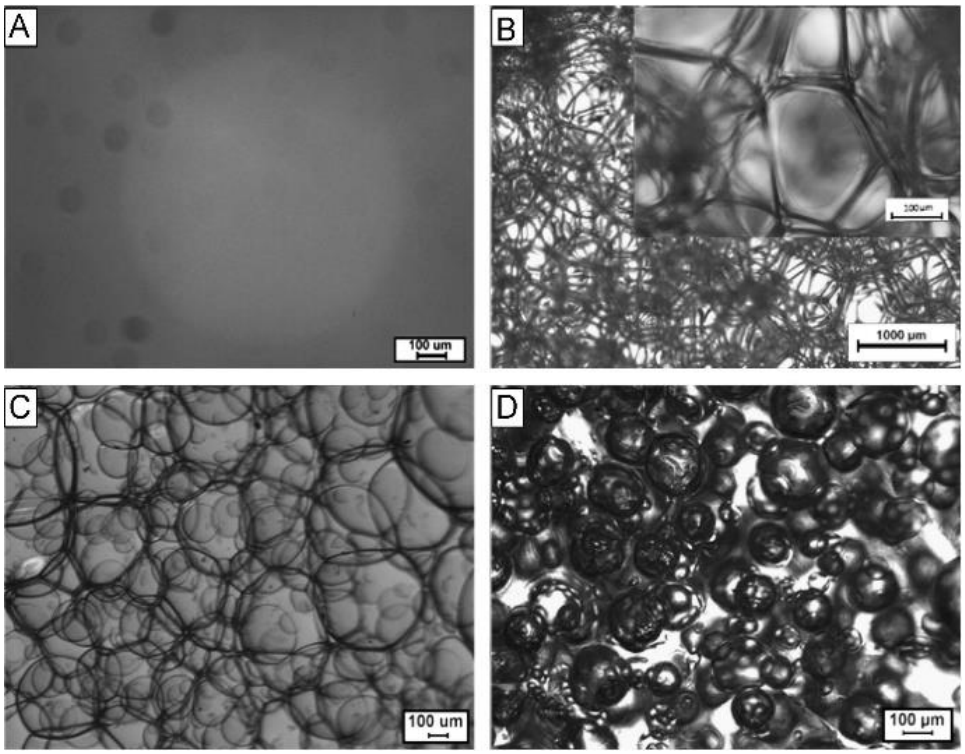


Figure 2-4. Optical images of biopolymeric porous matrix samples. (a) solution with 3% alginate, (b) 10% gelatin, (c) 3% alginate and 10% gelatin, (d) calcium alginate gel [83].

On the other hand, drying methods of aerogels can control the pore structure of aerogels. Supercritical drying produces pores dominantly at the nanoscale. Sophie Groult, et al. [86] have studied the various effect of external conditions on the pore structure of aerogel. With the supercritical drying method, it can be seen from Figure 2-5 that many cylindrical rods are crossed together as the skeleton to form a three dimension network. The pore size and network intensive degree can be tuned with two different non-solvents during the supercritical drying method. In recent years, the freeze drying method has been commonly used due to its safety, convince and low cost. Choosing a different way to pre-freeze samples will lead to different ice crystal-sized pores in aerogels.

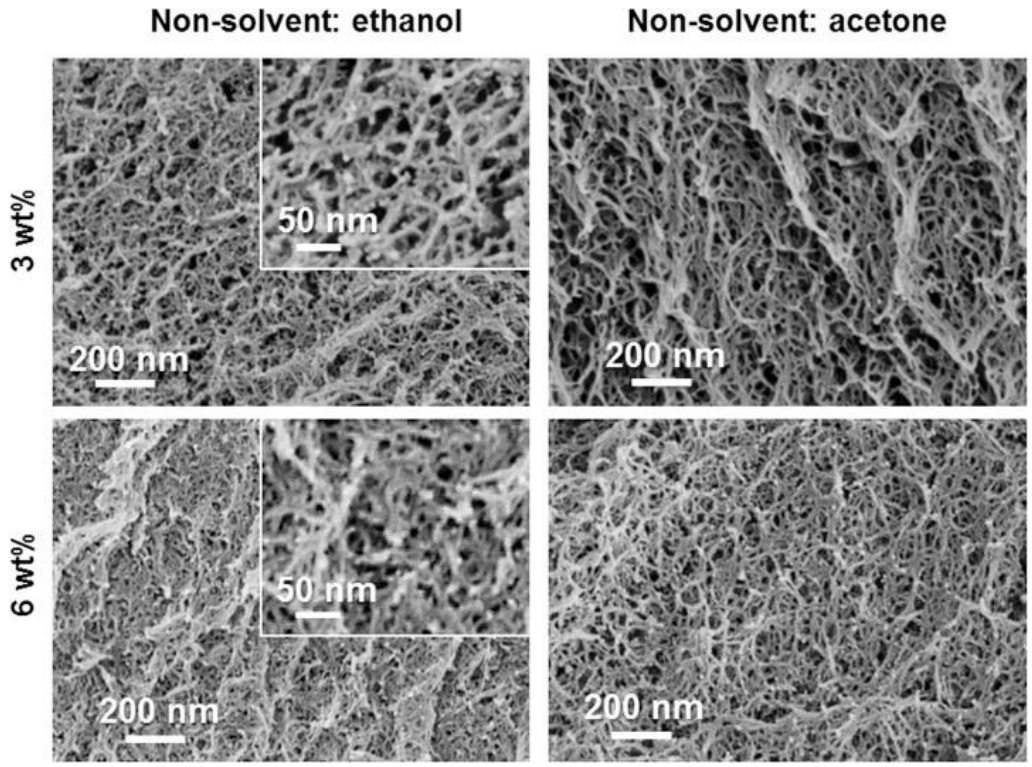


Figure 2-5. SEM images of pectin aerogels. [86].

2.2.2 Raw materials for the preparation of aerogels with different pore structures

Initially, the primary attention was on silica aerogels. In recent research, polysaccharide and protein are widely used in aerogels due to their bio-sustainable and biocompatible features. Described below are the molecular structural features with or without modification (as summarised in Table 2-1) of various natural materials and the characteristics of sample biomass aerogels:

2.2.2.1 Polysaccharide

Cellulose: As one of the most abundant organic resources on the earth, cellulose has been transformed into aerogels with excellent performance and value in industrial field applications during the last decades. It is commonly obtained from plants [87] and microorganisms [87, 88]. Cellulose is a biopolymer composed of D-glucose and β-1, 4-glucosidic bond, as shown in Figure 2-6. Three cellulose aerogels, including nano-fibrillated cellulose aerogels, bacterial cellulose aerogels and cellulose nanocrystal aerogels [89], are

distinguished through different ingredient and synthetic methods. These three general types of cellulose are divided depending on the different resources, processes and morphology (as shown in Table 2-2) [90]. The hierarchical structure of NFC, CNC and BC is presented in Figure 2-7. After the fibrillated process, cellulose fiber reached microfibril units that can be considered as nanofibrillated cellulose (NFC) with 5-70 nm diameter [91]. Commonly, the characteristics of NFC are usually presented as both amorphous and crystalline. Thus, after forming as aerogels, NFC presents a network structure of about 10-100 nm. Some researchers use this particular structure to construct the properties of aerogel. Shaoliang Xiao et al. [92] were reported to fabricate NFC from natural pine needles. Nano-level NFCs interconnecting with each other (diameter range from 30 to 70 nm), NFC aerogel fabricated with three dimensional polymeric networks has been introduced to increase the surface area. Cellulose nanocrystal (CNC) aerogels are also known as nanowhiskers. After hydrolysis reaction and mechanical treatment, lignocellulose fibers were disposed into a few nanometers in length with strong acids [93, 94]. Quan Yong Cheng et al. [95] reported that a super hydrophobicity CNC coated cotton fabric was fabricated to separate oil and water. Unlike NFC and CNC, bacterial cellulose (BC) is produced by acetobacter xylinum, which plays a vital role in this preparation process [95, 96]. However, a common point between BC and NFC is that the length is lower than 100 nm with similar morphologies. Compared with plant cellulose, BC has typical characteristics with high crystalline (>80%), a high degree of polymerization (8000) and nontoxicity [96], and thus is suitable for many specific applications. Hadi Hosseini [97] took full advantage of entangled BC nanofibers to fabricate a new class of BC/reduced graphene oxide nanocomposite aerogels to be used as a sensor in some components and parts. With high stimulative epithelialization ability, and anti-infective properties [98], BC is commonly used in medical science, such as skin care [99, 100], topological wound healing [101] and drug delivery [102].

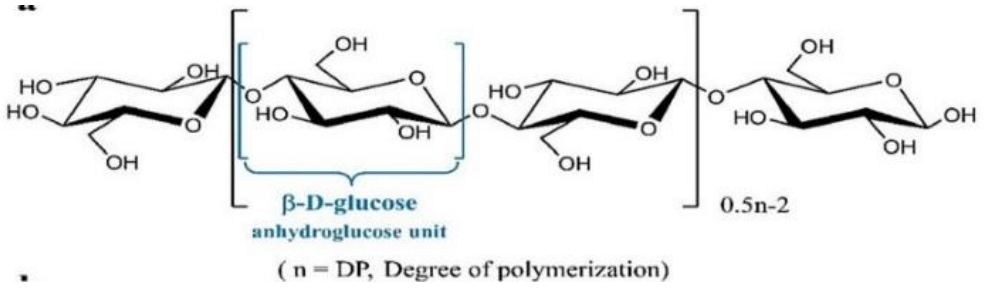


Figure 2-6. Molecular structure of cellulose [103].

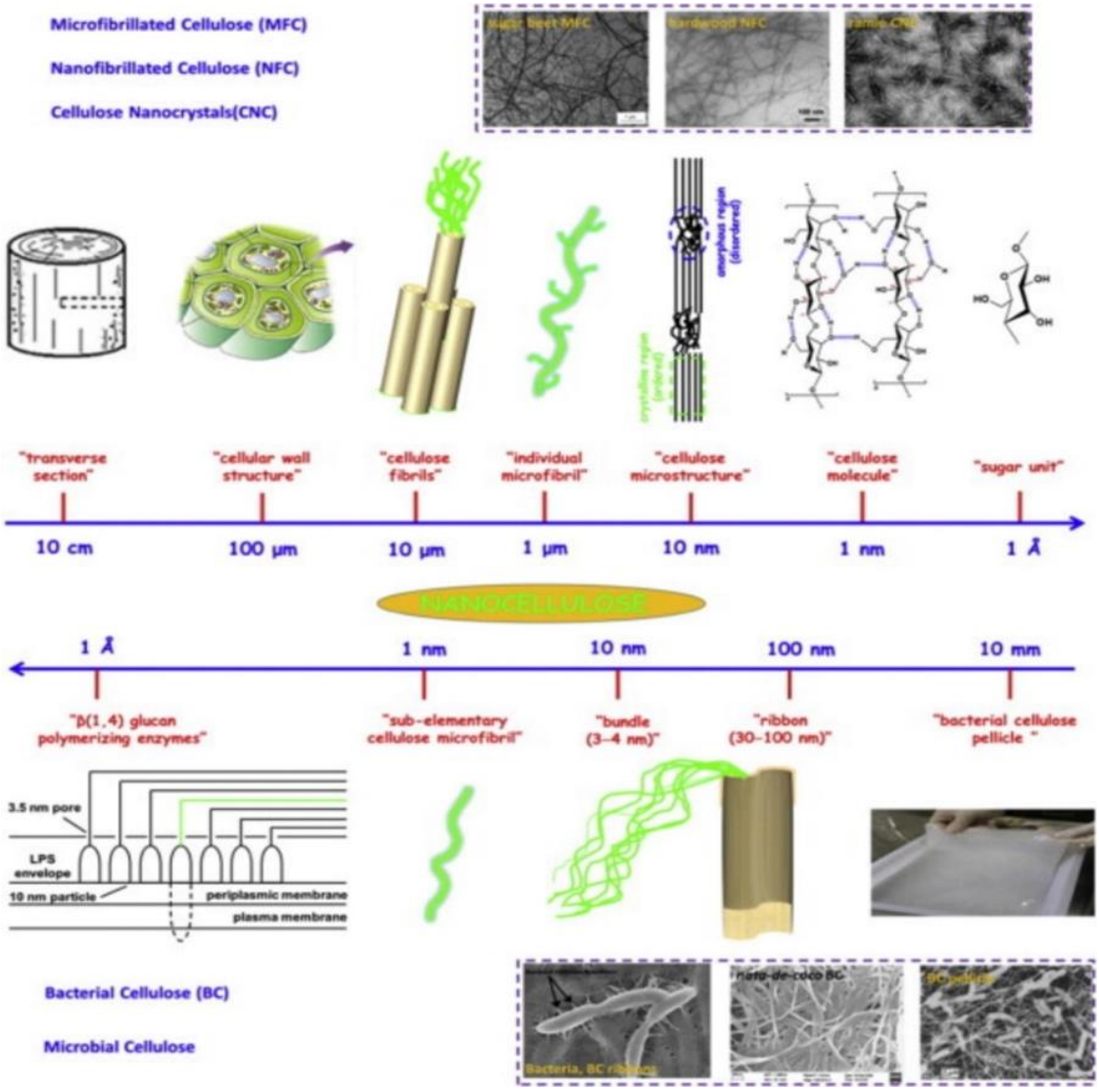


Figure 2-7. Hierarchical structure of NFC, CNC and BC; molecular structure of sugar unit; and SEM of BC ribbons, nata-de-coco and pellicle [104].

Starch: Starch is the primary storage carbohydrate in higher plants. Starch contains two D-glucan biopolymers, i.e., amylose, a relatively linear 1,4-α-D-glucan with a small number of long branches; and amylopectin, mainly a 1,4-α-D-glucan containing high-density branches (ca. 5% of glycosidic bonds are α-1,6) [105]. With a mass of the starch branched structure, it is easy to stretch into three dimensional network forming as starch hydrogel when the chains of starch meet water [106]. According to the diverse constitution of amylose and amylopectin, starch performance is different. Pure amylose could not form as aerogels because the heterogeneous structure could not stand the pressure during the freezing process [107]. However, the appropriate addition of amylose can increase the specific surface area of the aerogel but reduce the density.

Moreover, the type of starch and ratio of amylose and amylopectin are essential for the microstructure of aerogels, resulting in different properties. For example, the amylose content of starch could determine the mechanical properties of aerogels [108]. Despite the outstanding advantages of starch aerogel, some drawbacks remain, such as low hardness. However, the mechanical property can be improved through start materials modified in the preparation process of aerogels [109, 110]. Negar Abhari et al. [109] fabricated trisodium citrate cross-linked starch aerogels to improve the hardness and decrease the adhesiveness.

Chitosan: Extracted from various organisms commonly found in arthropod shells, chitin has β-linked N-acetyl-D-glucosamine carbohydrate polymer presenting insoluble performance [111]. To have a specific extent solubility of chitin, chitosan can be obtained through deacetylate treatment [112]. The properties of chitosan can be enhanced by chemical modification, such as grafting reaction [113], monomethyl-modification [112], and O-alkylated reaction. In the research of Takeshita & Yoda [114], the comparison between cellulose aerogels and chitosan aerogels with the same density shows that chitosan aerogels have a more random orientation pore structure contributes to the good thermal insulation

properties. Meanwhile, formed in chitosan aerogels, three dimension hierarchical porous scaffold benefits the improvement of electrochemical cyclability and rate capability [115, 116].

Konjac glucomannan: KGM is an edible and soluble dietary fiber polysaccharide found in the tube of amorphophallus konjac plant. KGM is a β-1, 4 glycosidic bonds linked polysaccharide composed of D- mannose and D- glucose with the molar ratio of 1.5:1-1.6:1 and 5–10 % acetyl substitution. KGM has abundant free carboxyl and hydroxyl groups in the skeleton unit, contributing to its excellent ability to attract the multivalent cations and form a desirable cross-linking structure. It has high viscous property (30,000 mPa s, 1%, w/v) and molecular weight ($6.8 \times 10^5 – 9 \times 10^6$ Da) [117, 118], making it easier to be considered as a framework material in aerogels [119]. In our previous studies [59], KGM molecular chain as a skeleton can be composited with gelatin and starch, which could promote the formation of open and close pores, respectively. Currently, some physical and chemical methods are commonly used to modify the native konjac glucomannan due to their functional limitation. Chen Xin et al. [120] studied the effect of different deacetylation interaction degrees on intramolecular and intermolecular forces in KGM system. The deacetylation reaction is carried out under alkaline conditions, which will result in the formation of an irreversible gel differing from the native KGM thermal reversible gels. Meanwhile, Active hydroxyl groups exist in KGM structure in favour of some other chemical reactions, including grafting [121, 122], cross-linking [123] and oxidation [124].

Alginate: Having free carboxyl and hydroxyl groups in the alginate linear structure and the G-blocks, alginate has an excellent capacity to attract the multivalent cations and then form a novel “egg-box” structure. The block content of β-d-mannuronic acid or α-l-guluronic acid impacts the structure of hydrogel and the aerogels pore structures, including porosity percentages and pore size [125]. Sodium alginate possesses the characteristic of pH

sensitivity with different solubility. At pH < 4, the sodium alginate is insoluble while it has a viscous and stable characteristic when pH increases to 6-9. Chemical modification is a universal method to introduce functional groups into molecules. Lin Shao et al. [126] have obtained a thermos-responsiveness and pH-responsiveness alginate composite aerogel by grafting with N-isopropylacrylamide (hydrophobic block) and N-hydroxymethylacrylamide (hydrophilic block).

Carrageenan: 3-linked-β-d-galactopyranoses and 4-linked-α-d-galactopyranoses constitute the carrageenan alternatively and repetitively. According to different sulfation degrees and positions, carrageenan can be distinguished from different variants and is mainly divided into κ-carrageenan, ι -carrageenan and λ-carrageenan [127]. The difference between these three types of carrageenan is the binding ions forming helical structures. κ-, ι-, and λ-carrageenan are easier to strengthen with the presence of K^+, Ca^{2+} and no need for sodium salts, respectively [128]. Located out the double helix, the sulfonate groups of κ-carrageenan interacted with the cations (K^+, Ca^{2+}, Co^{2+} and Fe^{3+}) by ionic force. This specific binding could contribute to dope the conductive polymer, which promotes the aggregation to junction areas and the cross-linking of conductive polymer with the carrageenan-cation, resulting in improved mechanical properties of aerogels [129]. Chemical modification of carrageenan is considered as an effective route to improving properties. The carboxymethylation process has been used in kappa-carrageenan to produce carrageenan derivatives which have promising potential to apply in drug delivery [130].

Pectin: Pectin is composed of different degrees of esterified residues of galacturonic acid [131]. Depending on various degrees of pectin esterification, it can be classified into two categories: high-methoxy pectin and low-methoxy pectin. Victor J. Morris et al. [133] verified that pectin-based materials present various biological and chemical properties with diverse chemical structures. In some specific aerogels, pectin was used as a stabilizer due to

its high solution viscosity and gel speed. Moreover, it is promising to use pectin aerogels in oral drug delivery because of their gastro-resistant properties [86]. When the pH is near or higher than PK_a (3–3.5), pectin can combine with divalent cations, also known as the "egg-box" structure, to form an intermolecular junction zone mainly through the connection of ionic bonds. An affinity with alginate has been compared and ranked as follows: Pb (II) > Cu (II) > Cd (II) > Ba (II) > Sr (II) > Ca (II) > Co (II) , Ni (II) , Zn (II) > Mn (II) [132]. Commonly, other direct chemical modifications have been introduced into pectin, including oxidation [133], functional copolymerization [134] and carboxymethylation [135].

2.2.2.2 Protein

Gelatin: According to different degrees of hydrolysate and various extraction parameters (temperature, pH, time and storage humidity level), gelatin structure is easily influenced. Gelatin is a mixture of peptide molecules with wide molecular weight distribution formed by amino acids. When the temperature is under 40°C [136], polypeptide chain tends to curl irregularly, resulting in the formation of triple helixes called 'renaturation'. With good biocompatibility [137], intrinsic bioactivity [138] and cell affinity, gelatin has been regarded as a promising candidate for drug delivery materials. [139]. As the drug deliverer, Péter Veres et al. [140] studied the drug release model kinetics of silica – gelatin aerogels by 1 s time resolution method contributing to future drug delivery system design.

Whey protein: whey protein is a kind of globular protein derived from milk processing and by-products of cheese. The main components of whey protein are α-lactalbumin and β-lactoglobulin, identified as essential factors in manipulating structure change as denaturation behaviour during heating [141-143]. From the molecular aspect, a single monomer of α-lactalbumin does not contain any free sulfhydryl (SH) groups, whereas there are two disulfide bonds with a buried free SH group existing in the β-lactoglobulin monomer [142]. These functional SH groups will be exposed and interacted with other β-lactoglobulin monomers

through the formation of disulfide bonds, causing the generating of another SH group. In another situation, two β-lactoglobulin monomers react with each other and form a disulfide bond through the SH group. This reaction will be terminated because there is no existing of SH group. This chemical reaction is a kind of irreversible aggregation when the SH group or disulfide bond reaction appears. Therefore, α-lactalbumin monomers can only react with each other through the unstable noncovalent interactions, including van der Waals interactions and the hydrophobic effect [144], which can be reversed when the temperature is raised. Aoife K. Buggy et al. [141] have reported that pH and protein concentration greatly influence the whey protein stability of heat treated. With the specific pH condition and protein concentration increase from 1% to 12%, the turbidity, protein precipitation and particle size concomitant change in thermal stabilities.

Table 2-1 Summary of biomass modification influence on performance.

Name	Modification methods	Performance improvement	Reference
Starch	Acids, hybrid	Improvement of aerogel hardness, anti-fungal propertysurface area, thermal insulation property	[109, 110] and [59]
Chitosan	Grafting, monomethyl-modification	Improvement of solubility coagulation	[113] and [112]
Konjac glucomannan	Grafting, oxidation	Hydrophobic interactions ability, good swelling ability and appropriate water retention capacity	[121] and [124]
Alginate	Grafting and targeted modification	Thermos-responsiveness, pH-responsiveness and hydrophobicity	[126]
K-Carrageenan	Carboxymethylation	Targeted release in the intestine.	[130]
Pectin	Oxidation, carboxymethylation,	Intrinsic viscosity decrease, thermo-sensitive	[133] and [134]
Gelatin	Cross link	High elasticity and strong adhesion	[145]
Whey protein	pH	Stability	[141]

Table 2-2 Basic difference between three kinds of celluloses: NFC, CNC and BC.

Type	Typical sources	Treating process	Morphology	Reference
Nanofibrillated cellulose (NFC)	Native cellulose	Homogenization with strong mechanical (shear) forces	Network (Diameter: 5-60nm; Length: several μm)	[146]
Cellulose nanocrystal (CNC)	Native cellulose	Strong acid with extraction process	Rod-like nanoparticles (Diameter: 5-70nm, Length: 100-250nm, from plant cellulose; 100-several μm, from tunicates, algae and bacteria)	[147]
Bacterial cellulose (BC)	Low-molecular-weight sugars and alcohols	Biosynthesis of BC	Ribbon shaped (Diameter: 20-100 nm)	[148]

2.2.3 Drying methods in preparation of biomass aerogels

Many raw materials with flawed structure will be modified using some specific pretreatment to pursue the excellent performance of aerogels. After refitting, the inherent drawbacks of biomass source will be overcome, contributing to the development of biomass application, as introduced in Section 2.3. Under certain conditions, the modified raw materials mix with water or other liquid phases, during which the molecular chain stretchers to a full extent. And then, some experiments would be conducted with or without an ageing period before forming a gel.

In 1931, Kistler first invented and defined aerogels as the pore liquid of gels that were replaced by air without severe structure shrinkage. With the development of aerogels, many other definitions came out. Some of them are inaccurate and have been overturned. However, it has been commonly considered that aerogels should be obtained by supercritical drying rather than other drying methods. Recently, a researcher João P. Vareda [71] from the University of Coimbra published a paper to reconsider the definition of aerogels and presents the view that aerogels need to be redefined as the recent development of aerogels with multiple drying methods. According to this theory, there are three drying methods to prepare aerogels with different mechanisms, as shown in Figure 2-8.

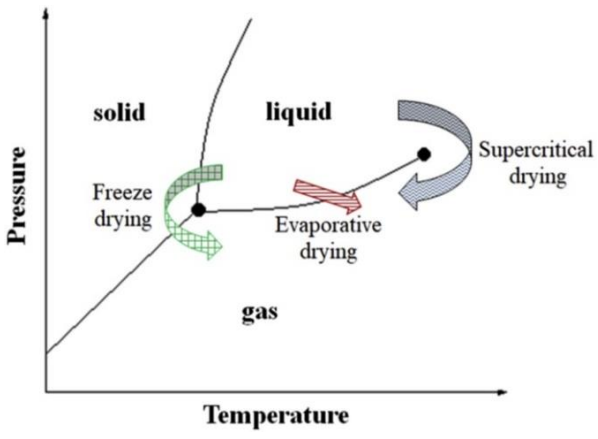


Figure 2-8. Mechanism of three drying methods on a phase diagram [71].

2.2.3.1 Supercritical drying method

The supercritical drying method can eliminate capillary pressure and maintain the original shape of materials because that pressure and temperature can be controlled to get a critical point–at which gas and liquid co-exist with the same density and the interface disappears to achieve phase transfer [39]. This high efficient hydrogel drying method has the advantage that surface tensions in pores can be avoided to maintain the pore structure of aerogels. In transforming gels to aerogels in the supercritical drying method, the hydrogel aqueous phase will be substituted by ethanol to reduce surface tension and thereby eliminate capillary pressure to prevent pore collapse [149]. Finding suitable and safe supercritical fluid was considered as a challenge in the previous research work until CO_2 was used as a drying medium for its relatively high security, temperature condition and mild pressure [150] during the preparation process in the industry. After ethanol substituting (the preparation of alcogels), the supercritical extraction of ethanol assisted by supercritical fluids (such as CO_2, CH_4) was carried out, and then aerogels could be collected. Table 2-3 showed a microstructure comparison between different ingredient aerogels with the same supercritical drying methods. It can be found that the pore size is concentrated on the range of nano level with the lengths in the range of several to several tens nanometers with high porosity. This is the typical characteristic of supercritical drying method.

Table 2-3 Physical properties of different types of polysaccharide aerogels.

Samples	Density (g/cm^{-3})	Surface area (m^2/g)	Pore size (nm)	Porosity (%)	Country	Reference
Pectin aerogel	0.04-0.05	270-350	-	-	Serbia	[151]
barley and yeast β-glucan aerogels	0.03-0.12	89.4-173.1	23.7-16.1	-	Spain	[152]

Alginate aerogel	0.15-0.17	126.9-173.3	15.48-17.34	-	Slovenia	[153]
Ag nanoparticle/cellulose nanofiber aerogel	0.021	31.5		98.6	Japan	[154]
Nano-cellulose aerogels	-	260.87-353.83	7.81-9.38	-	China	[155]
starch aerogels	-	93	24-25	87.7	Spain	[156]
Chitosan aerogels	-	257-479	12.6-15.0	96.8	Spain	[157]
Tungsten/alginate aerogels	-	381	31	96	Greece	[158]
chitosan/lanthanum hydroxide aerogel	-	172.74	19.79	-	China	[159]

2.2.3.2 Freeze drying method

Because of its low cost and high safety, it is a tendency that freeze drying is extensively applied for aerogel preparation. First, gel sol is frozen, and then ice is sublimated, during which the liquid in gels is replaced by gas to generate pores under a high vacuum. [160]. Aerogel structure is determined by the ice crystal growth process of the gel solution. Shunli Liu et al. [149] fabricated gum/graphene oxide aerogels and found that there is a force pushing and flocking the solute (XG/GO hybrid) together between two ice blocks during ice crystalizing, and then after sublimation, the aerogel walls formed (schematic diagram as shown in Figure 2-9). Therefore, the structure of pores is directly determined by the ice crystal frame. Using low temperature polarizing microscopy, Xuewen Ni et al. [160] observed the ice crystal growing

process with different temperature conditions and ingredient concentrations. The SEM images and figures of pore size distribution show that temperature and ingredient concentration can significantly affect the growth of ice crystals and further the pore structure. Under different freeze drying conditions, aerogel pore size can be adjusted (as summarized in Table 2-4).

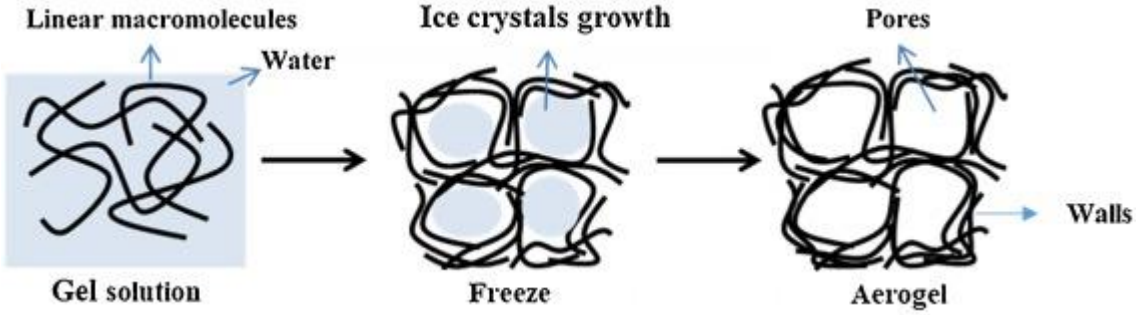


Figure 2-9. Schematic of aerogel formation [161].

2.2.3.2.1. Ice crystal growth theory

From the freezing profile provided by Dimitris Zaragotas et al. [162], who studied ice nucleation and crystal, it can be seen that there are two phases of crystallization: nucleation and crystal growth. The first short step of crystallization is nucleation. During this period, when the solvent cools down to reach supercooling status, the crystal centre and crystal nucleus form with some specific stimulus. As previous studies [163] have suggested, it is vital to control the ice nucleus because the initial nucleation temperature and crystallization rate depend on it, so the ice crystal size is determined. The second step is the growth of ice crystals. There is a competitive relationship between the growth of ice nucleus and ice crystal (as shown in Figure 2-10). Under the condition that ice nucleus are easy to form, it will grow rapidly, condense into a block and finally decrease the growth chance of ice crystal contributing to form relatively small and uniform crystal. However, if the temperature lower down slowly, the ice nucleus near cold side have the tendency to derive to other regions resulting in the formation of large size ice crystal.

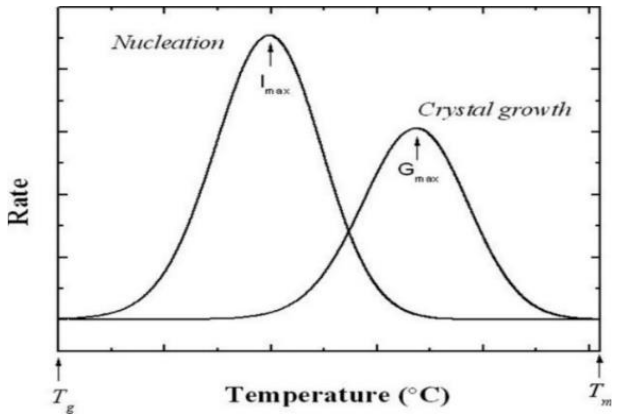


Figure 2-10. Temperature influences on nucleation rate and ice crystal growth rate [164].

2.2.3.2.2. The influential factor of ice crystal growth

Temperature: Generally, temperature and slurry concentration are significant factors affecting ice crystal growth [165]. By low temperature polarizing microscopy, ice crystal morphology was observed under different temperatures, and the results showed a high correlation between temperature and the ice crystal structure. When decreasing temperature, the mean diameter of pore size distribution moved to a low value significantly, while the aerogel pores had the same tendency. An extreme lower temperature freezing can be achieved by liquid nitrogen freezing.

Pressure: During freezing process, high pressure can shorten the time of cooling and form small and regular ice. According to the theory, some researchers [166] have studied the high-pressure shift freezing (HPSF). The stable structure of H_2O molecules will be destroyed at high pressure, and the broken bonds tend to be more compact [167]. Under high pressure, the freezing point will be decreased, inducing the super-cooling and rapid ice nucleation rates producing tiny ice crystals. M.T. Kalichevsky-Dong et al. [168] found that the HPSF technique can produce smaller and more uniform ice only under −15 °C. It has been applied in some food products to promote the formation of more regular ice crystals [169, 170].

Concentration: According to the simulation of sugar solutions, single and multiply crystals which can also be applied as the freezing model in other aqueous solutions, such as biomass

[171], it can be concluded that ice crystal sizes depend on solute concentration. During the crystal growing process, the concentration will be continuously increased while the solute is pushed to the higher concentration area, inhibiting further ice crystal growth. The three dimensional ice crystals growing in trehalose solution with different concentrations can be obtained by the Mach-Zehnder interferometer. With the rise of trehalose concentration (8 wt%), the growth rate of ice crystal increases to a top point (2 wt%) and then decreases [172]. Additionally, the existence of suspension solids also dramatically influences the shape of ice crystals. During the freezing process of locust bean and xanthan gums solution, LT-SEM micrographs have been used to verify that ice crystal growth has been limited by suspension solids [173].

Table 2-4 Polysaccharide aerogels pore size under different freeze-drying conditions.

Aerogel type	Pore size	Freezing temperature	Freezing pressure	Concentration	Reference
Nanofibrillated cellulose aerogel	2-50nm	liquid nitrogen bath (-196°C)	< 5 Pa	0.10wt%	[174]
cellulose aerogel	20-600 μm	-80℃	20 Pa	2wt%	[175]
nanofibrillated cellulose aerogel	50.6-74.3 μm	-18°C (liquid nitrogen)	< 20 Pa	3wt%	[176]
nanofibrillated cellulose aerogel	47.3-68.1 μm 11.8-19.2 μm	-55°C (dry ice) -196°C (certified freezer)	< 20 Pa	3wt%	[176]

2.2.3.3 Evaporative drying method

Evaporative drying, which is performed at atmospheric pressure, is a simple, cheap and safe drying method without potential risk and is more suitable for large-scale industrial production than several other methods. However, the primary internal solvent is water and ethanol solution with large surface tension, contributing to structuring collapse. To overcome the solvent surface tension and capillary pressure under atmospheric drying, the hydrogel must be pre-treated while the solvent needs to be replaced with a small surface tension one or the surface characteristics of the wet gels to be modified from hydrophilic to hydrophobic using reagents with hydrophobic reactive agents [177]. Because the uncertain degree of collapse [178, 179] will still appear, the development of this drying method is limited in some fields. If the collapse phenomenon could be ignored, this drying method with the advantage of less cost of equipment and low energy consumption, has been industrialized.

2.3 POTENTIAL APPLICATIONS OF BIOMASS AEROGELS WITH PERFORMANCE ASSESSMENT

2.3.1 Sound absorption

With the development of society, new words appeared: noise pollution, which has been recently introduced into the university curriculum, was led by industrial machines, home appliances, vehicles and buildings [13, 180]. The noise was considered the most widespread and hardest controlled environmental pollution [7, 181]. Noise can cause harmful effects on health and has become one of the three major pollution problems in the world. It will affect the human hearing system and cause health problems such as high blood pressure [9] and increased physiologic stress [11, 182]. Apart from the influence on human health, noise can accelerate the ageing of buildings and machinery, affecting the accuracy of the equipment. Therefore, acoustic insulation materials used in sonar exploration and the aerospace field are urgently needed. Currently, a range of acoustic insulation or absorption materials are used in the

construction industry to reduce the impact of noise on people's life. The common sound absorption materials are sound-absorbing cotton, sound-absorbing felt, sound-absorbing board and other sound-absorbing materials. However, the traditional sound-absorbing materials on the market have a number of disadvantages: environmentally harmful, low compression and bending strength [183]. For example, the glass fiber and mineral are easy to be inhaled and will cause irritation and deposition in alveoli of the lungs [184]. Some synthetic polyurethane foam, polyester fiber and aluminum silicate cotton and other petrochemical-type sound-absorbing materials are easy to increase the burden on the environment.

Porous materials have a large number of porous structures on the surface and inside contribute to the good sound absorption performance of porous materials. When sound waves pass through the material, a part of sound energy is reflected. The rest enters porous material and is converted into heat energy by the vibration or friction of material. Many studies have been carried out to develop and investigate the sound absorption performance of difference natural porous materials [185-188]. As porous cement-based materials are acknowledged to be useful in pavement sound absorption, Yoon et al. [189] successfully improved the performance by enhancing the pore structure with addition of natural fibers and aluminum powder into cement. Wang and Du [190] developed recycled aggregate crumb rubber concrete with recycled aggregate and rubber particles from waste tire mixture and rubber pad. The authors found this material could be qualifying in sound absorption application and proposed to use it in building partition walls. Inorganic porous materials have also been widely investigated in many studies, which were focused on the preparation by use of fly ash, coal gangue, blast furnace slag and other industrial solid wastes. In the research of Wu et al. [191], ammonium hydrogen carbonate was used as pore former to reveal the effect of pore former and other process parameters on the apparent porosity, pore size and sound absorption property of the developed ceramsites. Furthermore, porous aerogels are also commonly used in the acoustic design of buildings and

aircraft with unique open pore structures to absorb the sound wave. At the National University of Singapore, Jingduo Feng et al. [192] carried out silica/cellulose hybrid aerogels for thermal and acoustic insulation with recycled cellulose fibers and methoxytrimethylsilane (MTMS) silica. The sound absorption coefficients represented the acoustic performance of 0.39-0.50 with 10 mm thickness.

2.3.2 Thermal insulation

Commonly, thermal insulation materials are composed of organic polymers, such as polyurethane foam, polystyrene foam, glass wool, etc. Polyurethane foam can be divided into two categories: flexible polyurethane foam and rigid polyurethane foam [193], and is often used as thermal insulation materials in the building envelop and domestic refrigerators [194]. However, the production of polyurethane foam relies on the unsustainable petroleum sources, as its two main components are isocyanates and polyether. Moreover, the widely use of polyurethane has produced considerable number of wastes, and these wastes usually go into landfill, which need quite long time to be degraded. Since the advent of aerogels, NASA's Kennedy Space Center and NASA's Glenn Research Center have focused on aerogels' thermal insulating function to be applied to the space industry, such as space radiators and space suits [195]. With the improvement of technologies and cost reduction, the civilization of natural aerogels in buildings has been widely achieved, contributing to the improvement of energy-saving. Currently, to avoid drawbacks of traditional aerogels including environment pollution during the preparation process and degradation period after being abandoned, biomass ingredients are being introduced into aerogel insulation materials. Inventing advanced biomass aerogels have drawn significant interest within the scientific community during the rapid development of novel aerogels. The most popular building application is the wall-filling materials, especially aerogels, due to their excellent mechanical and thermal properties. For instance, Yanwen Zhao et al. [196] showed the possibility of using starch, clay and cellulose

nanofibrils (CNFs) to synthesize the aerogel with good thermal insulation properties. By reducing starch content and incorporation of CNFs, the density and thermal conductivity of the optimal aerogel in this study are 0.05 g/cm^3 and 41.5 mWm^{-1}K^{-1}, respectively. Furthermore, the CNFs have abundant hydroxyl groups, a high aspect ratio and excellent mechanical strength, which contributes to the high crack resistance under stress and enhanced compressive strength. A kind of urea-modified chitosan aerogels was reported by Natalia Guerrero-Alburquerque et al. [197] that these aerogels have high surface area and promising mechanical properties and thermal insulation performance. In this study, two preparation methods have been compared, including supercritical CO_2 drying (SCD) and ambient pressure drying (APD) methods, and it could be found that aerogels have a thermal conductivity of ∼24 and ∼31 mWm^{-1}K^{-1} for SCD and APD, respectively. The fire resistance has been investigated that the aerogel can self-extinguish after direct exposure to flame. In the author's previous research [59], konjac glucomannan (KGM)/starch based aerogels have been invented with natural raw materials, even the waste of agriculture (wheat straw) and the environmental-friendly preparation method (freeze drying) presenting good thermal insulation and mechanical properties. An optimized thermal conductivity of 0.04641Wm^{-1}K^{-1} and compression modulus of 67.5 kPa was measured to assess potential application prospect in thermal insulation. The main goal and advantage of this konjac glucomannan (KGM)/starch based aerogels are the biodegradable performance after being abandoned, which will not increase the burden on the environment. In another work, Pragya Gupta et al. [174] invented nanofibrillated cellulose aerogels based on pinewood cell wall with freeze drying method for thermal insulation application. This research developed in the combination with purification and fibrillation of pinewood cell wall to obtain nanofibrillated cellulose. The cellulose aerogels were synthesized at the concentration varied from 0.75 to 1.75 wt% with the lowest thermal conductivity of 0.025 Wm^{-1}K^{-1}, and could be applied in various practical application particularly in building thermal insulation field.

2.3.3 Fire resistant

In June 2017, one of the worst building fires, the Grenfell Tower Fire, happened in London and caused 72 deaths. This conflagration at an English-style villa was spread rapidly upwards and across the tower, which was attributable to several flammable materials, including polyurethane polymer foam insulation board used on building walls. It is urgent to enhance the fire resistance of the building insulation materials. Bio-based gum arabic/clay aerogels were fabricated by freeze drying method with thermal stability and flame retardancy by Liang Wang et al. [198]. In this research, biomass aerogels offered attractive, superior and sustainable features with the preparation of gum Arabic (GA) and sodium montmorillonite (Na^+-MMT) clay. Acted as a physical barrier, the fire can be resisted by clay determining the fire flame retardation efficiency with different concentrations. In another work, this functional clay has also been fabricated with cross-linked alginate via the adjustment of pH. The fire combustion behaviour was tested with a cone calorimeter, which presented that alginate/clay aerogels with the addition of p-toluenesulfonic acid can reduce the total heat release of aerogels and toxic combustion. Melamine-formaldehyde resins have flame retardant characteristics, always used as fire retardant. At Sichuan University, Hong Bing Chen et al. [199] have fabricated self-cross-linked melamine-formaldehyde-pectin aerogels with good thermal stability, excellent water resistance and low flammability. Pectin, a kind of polysaccharide, acts as the structure materials during the cross-linking reaction of melamine-formaldehyde. After freeze drying, composite aerogels were fabricated and tested using cone calorimetry. The results showed that composite aerogels have a time to ignition of 24-27 s, and the heat release rate peak of 80.1-116.6 kW/m^2.

2.3.4 Air filtration

Air pollution is a severe problem in the world. Indoor air pollution is linked to many adverse health outcomes, and many people suffer from respiratory illnesses due to air pollution. Tiny

air pollutants break through the defence of the human body and penetrate deep into our respiratory and circulatory systems, damaging our lungs, hearts and brains. Since indoor particulate matter (PM) is still a severe environmental problem, more and more people are using air purifiers to reduce indoor PM pollution. Even in special places, such as hospitals and many other buildings, air filtration systems are installed to protect people from PM. Mandal and Srimani [200] have used jute fiber as the filter in the microbiological experiment. In the 1940s, the high-efficiency particulate air (HEPA) filter was invented in the USA [32]. Since then, filter materials have developed rapidly and grown in popularity and necessity. There are many novel air filter materials appeared in succession. Filtration materials are widely used in many applications including the typical heating ventilation and air conditioning (HVAC) systems. Hui Liu et al. [33] created a kind of nanoscale polyacrylonitrile fiber filter using an innovative electronetting technique. It has been verified that the PM 0.3 was reduced by 99.996% with the novel nanonet filter. Abdul Rajak et al. [34] used expanded polystyrene (EPS) waste as the raw material to make a nanofibrous membranes filter through the electrospinning method. Such nanofibrous membranes with low density and high Young's modulus can achieve high-efficiency PM 2.5 removal of 99.99% and a high-quality factor of 0.15 Pa^{-1}. Chao Jia et al. [35] developed a kind of Al_2O_3-stabilized ZrO_2 submicron fiber air filter paper, which has high filtration efficiency (99.56%) and a low-pressure drop (108 Pa). At the same time, this material also shows excellent flexibility and thermal stability. Using the electrostatic induction-assisted solution blowing method, Shengnan Lv et al. [201] fabricated PLA/PMMA composite nanofibers with 99.5% PM 2.5 removal. In the research of Wallace Woon FongLeung and Qiangqiang Sun, the improved nanofiber filter with charged fibers has been invented for capturing 100 nm aerosols, which are similar to that of the COVID- 19 [37]. Currently, some research has been devoted to studying environmentally friendly air filtration materials. It is well known that air filter cartridges (filter materials) must be replaced periodically, and most of

these materials are non-biodegradable. Xusheng Xie et al. [202] prepared a silk nanofibrous aerogels with an excellent ability to absorb PM 2.5 particles and residual oil using filament nanofibers naturally as raw materials. Bionic technology has become popular in recent years. Inspired by the abundant tube channels inside natural wood, Zhihui Zeng et al. [203] introduced a cross-linked lignin-based aerogel prepared using a simple unidirectional ice-crystal-induced self-assembly method followed by low-temperature annealing. The internal functional groups and pore channels of lignin and the addition of graphene enhanced the filtration efficiency as well as the mechanical stiffness and thermal stability of the aerogel, respectively. A comparison between commercial HEPA and lignin-based aerogel shows that the filtration efficiency of lignin-based aerogel for particles is significantly better than commercial HEPA filters.

2.4 CONCLUSION, CHALLENGES AND PERSPECTIVES

Biomass aerogels belong to the new generation of porous materials and have been regarded as the most sustainable aerogel material because of their advantages of sustainability, low toxicity, biocompatibility and renewability. The preparation methods include extraction of raw materials (polysaccharide and protein), modification of raw materials, preparation of hydrogel and three main drying methods (supercritical drying method, freeze drying method and evaporative drying method). Biomass aerogels have significant application prospects in five fields, including environmental engineering, buildings, medicine, electrochemistry components, and packaging.

By summarizing the research on biomass aerogels in recent years, it can be seen that low-density, high specific surface area biomass aerogels are widely used in various fields due to their excellent characteristics. Optimizing the performance of aerogels and biomass aerogels that meet the needs of the current society will be a hot spot for future research. With the

increased environmental pollution, biomass aerogels can also exert their specific advantages, replacing traditional materials to benefit humanity. At present, there is still improvement space for further research on biomass aerogels. Based on the literature above, several recommendations can be put forward which may provide clear guidance for the future development of biomass aerogels:

(1) Use of natural waste as raw materials and improving preparation. Regarding raw materials, the preparation and selection of ingredients need to be improved in future research. Most of the current researchers use the extraction and modification methods to produce raw materials of biomass aerogels, so a large number of organic reagents will be introduced during this preparation process, causing environmental pollution. Furthermore, most of these extracted and modified biomasses are combined with some conventional inorganic and organic materials to prepare aerogels with the advantages of both natural and synthetic materials. However, we should promote the use of waste in nature to prepare biomass aerogels. In recent years, this concept has been reflected in some publications, such as using discarded banana peels and straws to prepare biomass aerogels.

(2) Extend the selection range for raw materials. In recent studies, a large proportion of the current research is focused on cellulose-based aerogels, which is almost several or even tens of times the number of studies on other polysaccharide/protein aerogels. Researches on protein aerogels are relatively fewer than that on polysaccharide aerogels. With the unique performance of temperature and pH sensitivity, protein aerogels can be used in some specific fields (medicine and sensor). It is urgent to amplify the application fields of protein aerogels. Therefore, researchers need to pay attention to broad the selection range of raw materials.

(3) Expansion of industrial production. In terms of preparation methods, some researchers tend to adopt the freeze drying method to save energy. Either freeze-drying or supercritical drying

needs to be simplified, manufacturing costs reduced to achieve mass production in industry and application in broad fields.

3 EXPERIMENTS FOR CHARACTERISTICS ANALYSIS OF BIOMASS MIXTURES/GELS

3.1 INTRODUCTION

Biomass aerogels are produced by freeze drying of biomass gels. The micro/macro-network and intermolecular interactions of the gels have great influence on the performance of aerogels. Therefore, it is important to study the microstructure, pasting and rheological properties of biomass gels. While pasting property and rheology will be practical tools to describe and access samples in their fluid state.

Four starting materials were selected, including KGM, starch, gelatin and wheat straw. The essential structure information, such as the molecular weight of the KGM, starch and gelatin, will be given, which will affect their behaviour in the subsequent work. The biomass mixtures and gels are prepared through two main steps: raw materials dissolution in the distilled water and gel-ageing in a 4°C refrigerator. For biomass aerogels, an additional freeze drying process is required. In this study, in order to investigate the effect of different raw materials on the system, the optimal amount of KGM addition was first determined by the viscosity properties of KGM/starch mixtures, and then different raw materials were mixed with KGM to prepare binary systems. The pasting viscosity, rheological properties, and microstructure of systems were tested and observed to explore the effect of process parameters and different addition ranges of raw materials on biomass mixtures microstructure. The preparation temperature, stirring time and gel ageing temperature are determined based on the experimental results.

3.2 Synthesis of biomass solution through sol-gel method

3.2.1 Materials

To simplify the description of biomass aerogels, all samples were coded in the form of K0S0G0WS0 (K, S, G, WS represent KGM, potato starch, gelatin and wheat straw), and the

number after K, S, G, WS indicate the concentration of raw materials. The detailed sample formula and sample codes are shown in Table 3-1.

Table 3-1 Aerogel sample formula.

	Main raw materials				Staining material
Sample code	K (KGM)	S (starch)	G (Gelatin)	WS (Wheat straw)	Rhodamine B
	Unit (g/100 mL)				
S2	0	2	0	0	Rhodamine B is used for staining protein in the confocal laser scanning microscopy
K1S1/K1S2/K1S3	1	1/2/3	0	0	
K1G1/K1G1.2	1	0	1/1.2	0	
K1G1.4/ K1G1.6	1	0	1.4/1.5	0	
K1G1.8/K1G2	1	0	1.6/2	0	
K1WS1/K1WS2	1	0	0	1/2	

3.2.2 Preparation of biomass solution/mixtues/gels and aerogels

The KGM/starch, KGM/gelatin, KGM/wheat straw solution/mixtures and aerogels preparation method are the same as Section 1.7.3 (1-4) and 1.7.4.

3.2.3 Procedures for formula determination

The flowchart to determine the addition amount of different raw materials in the biomass gels is shown in Figure 3-1. In this chapter, the optimal amount of KGM addition and preparation parameters were firstly determined by the viscosity properties of KGM/starch mixtures, and then different raw materials were mixed with 1% KGM to prepare binary systems. The pasting viscosity, rheological properties, and microstructure of binary systems were tested and

observed to determine recommended starch and gelatin amount ranges and gelatin ageing process temperature. In the test, wheat straw subsidence appeared, which need to be solved by adding gelatin.

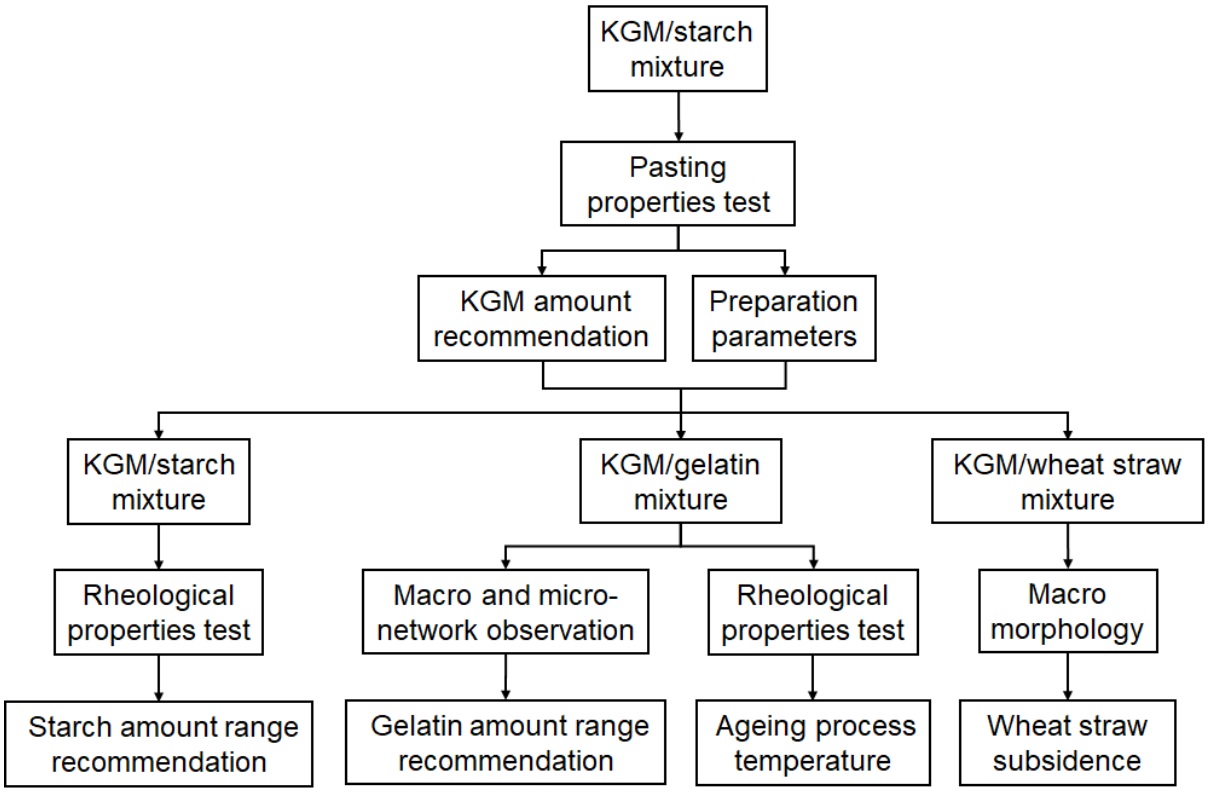


Figure 3-1. Flowchart of formula determination.

3.3 METHODS FOR STUDIES OF SOLUTIONS AND GELS

3.3.1 Pasting properties

Pasting properties of the starch with and without KGM were determined by a Rapid Visco Analyzer, as shown in Figure 3-2 (RVA 4500, Perten Ruihua Scientific Instrument Co., Ltd., Sweden). With the magnetic stirring, KGM was dispersed in 25 mL reverse osmosis (RO) water in an aluminium vessel, and then the starch (3.5 g) was added slowly to the vessel based on the method No.76-21 as described in AACC (2000). The pasting properties were analyzed using the following temperature profiles according to Ma et al. (2019) [204]. The starting temperature was set at 50°C. After holding for 1 min, the samples were heated at the rate of

12°C/min to 95°C maintaining the holding temperature for 2.5 min. Finally, the cooling process was set at 12°C/min, and the hot samples were cooled to 50°C and held for 2 min. The agitation speed of the paddle was started at 960 rpm for the initial 10 s and 160 rpm for the remaining test period. In this test, RVA characteristics, including pasting temperature, peak temperature, peak viscosity, breakdown, setback and final viscosity, will be presented from RVA curves. All tests were performed at least in triplicate.

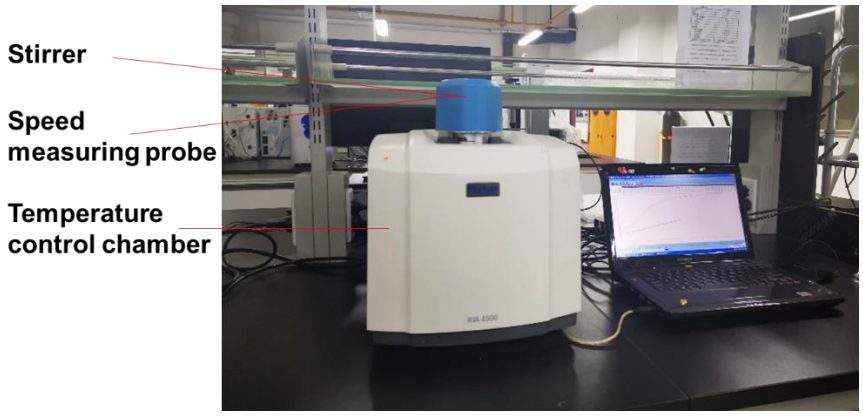


Figure 3-2. Image of Rapid Visco Analyzer.

3.3.2 Rheology of biomass solutions and mixtures

The rheological properties of the biomass solutions and mixtures were carried out with a rheometer (RS6000, Hake Ltd., Germany) equipped with a parallel plate of 35 mm in diameter, and the geometry gap was set at 1 mm. The rheometer is presented in Figure 3-3. The hot sample solutions and mixtures were placed on the plate and were kept at the set temperature.

3.3.2.1 Frequency Sweep

Dynamic rheological properties of biomass solutions and mixtures were measured under 25°C. Before the frequency sweep tests, the stress sweep tests were carried out to ensure all samples were in the linear viscoelastic deformation region (stress = 1 Pa). The frequency sweep tests were measured from 0.1 to 10 Hz at 1 Pa to record the storage modulus (G') and loss modulus (G") as the function of angular frequency. All tests were performed at least in triplicate.

3.3.2.2 Temperature sweep

For the temperature sweep measurements, all samples were tested at the constant stress and frequency of 1 Pa and 1 Hz, respectively. 0.5 mL of solutions or mixtures were poured on sample stage, which had been kept at 5℃ and then adjusted to 70℃. To prevent the water evaporation of the mixtures in high temperatures, the exposed surface of the sample was covered with a thin layer of silicone oil. In this test, the cooling process was observed with the temperature decreasing from 70℃ to 10℃ with a rate of 0.5℃/min. All the G' and G'' data were measured.

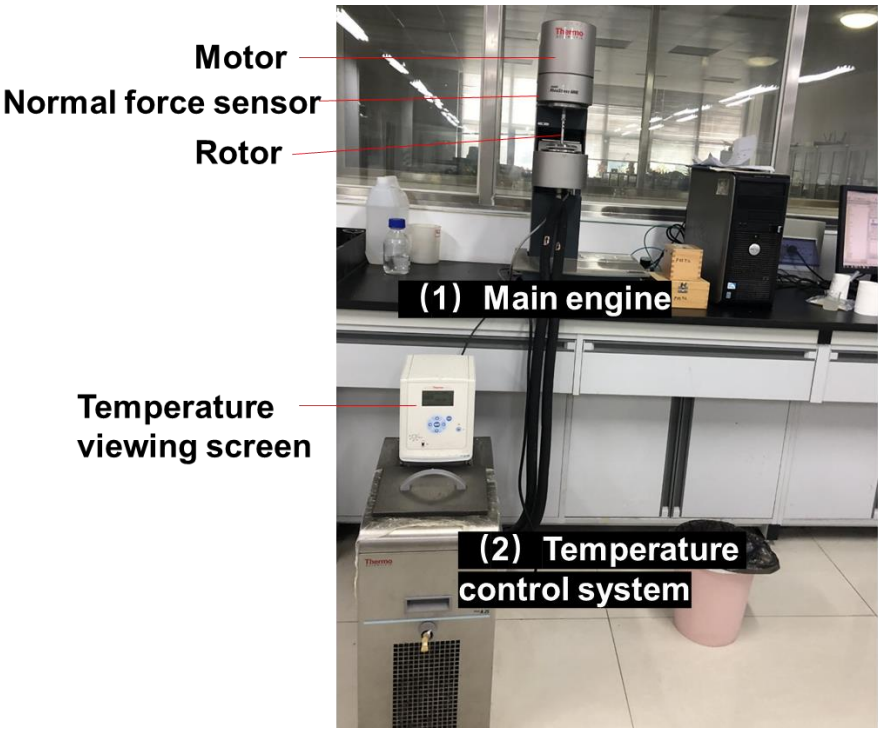


Figure 3-3. Image of Rheometer.

3.3.3 Confocal laser scanning microscopy (CLSM)

The morphology and distribution of KGM-gelatin composite gels were observed by the Confocal Laser Scanning Microscopy (LEICA SP8, German). Mixtures were stained with the rhodamine B solution that binds strongly to proteins. An aliquot of mixtures (10 mL) was stained with 20 μL of dye solution containing 0.4 wt% rhodamine B. After adding rhodamine

B solution, the mixtures were mixed by magnetic stirrer at 150 rpm for 15 min at room temperature to ensure sufficient protein staining. All the preparation process should be carried out in a dark room. A drop of dyed mixtures was observed using a coverslip and a confocal plate. Mixtures were excited by a red laser beam at 552 nm.

3.4 RESULTS AND DISCUSSION

3.4.1 Influence of KGM concentrations on the pasting properties of KGM/starch mixtures

The specific molecular structure of KGM contributes to the unique high viscosity of KGM solution and high molecular weight of KGM. With the macromolecular chains, KGM could be considered as a good skeleton material for biomass aerogel preparation. Due to the defects of pure KGM aerogels, an appropriate combination of different polymers could contribute to significant improvements in material properties [205].

To evaluate the quality of starch, pasting viscosity is an important characteristic widely used in the food field [206]. For the hybrid system (starch with different amounts of KGM), pasting temperature, peak temperature, peak viscosity, breakdown viscosity, final viscosity, and setback viscosity were determined and are shown in Table 3-2. The pasting temperature means that the starch granules are completely gelatinized before the viscosity of the starch begins to rise. In the whole heating process, the peak viscosity is the highest indicating the water-holding capacity of mixtures. The breakdown viscosity is the difference between the peak and lowest viscosity during the holding stages. As presented in Table 3-2 and Figure 3-4, the pasting temperature of pure potato starch was 68.65°C, the peak temperature was 82.3°C, the peak viscosity was 7822 CP, the breakdown viscosity was 4894 CP, the final viscosity was 4894 CP and the setback viscosity was 1084 CP. It could be found that the peak temperature and all viscosities of the pure starch system were the lowest when compared with the starch system with the addition of KGM. These results showed that the peak temperature, peak viscosity,

breakdown viscosity, final viscosity, and setback viscosity tended to be increased with the increase of KGM concentrations. In Figure 3-4, the increase of KGM concentration resulted in the gradual enhancement of final and peak viscosity, indicating the intermolecular forces. To be more specific, compared with the pure starch system, KGM addition of 0.2%, 0.4%, 0.6%, 0.8%, 1% and 1.5% can bring improvement of peak viscosity by 5.87%, 7.31%, 17.96%, 25.31%, 28.28%, 43.95%, respectively. Two factors contribute to this phenomenon. At the beginning of the pasting process, starch granules swelled and absorbed water in the KGM solution during the heating process, leading to an increase in hydrocolloid concentration and an increase in the system's viscosity. On the other hand, significant synergisms appeared between KGM and potato starch, which is consistent with the report of Guo et al. [206]. KGM addition could accelerate the rate of starch swelling and increase starch swelling at low temperature contributing to the easier gelatinization of starch. This phenomenon may be caused by the reaction between KGM molecular and leached amylose leading to the increase in compound system viscosity. However, the pasting temperature has the opposite tendency of other parameters. Without KGM addition, the pasting temperature of the pure starch system was 68.65°C, and after KGM addition, the pasting temperature was gradually decreased with the increase of KGM concentration, which has similar research results to Guo et al. [206]. The pasting temperature seemed to be certainly influenced by variation in KGM contents. As the starch granules break up during the pasting process, the amylose is the first to spread in all directions, dissolve out of granules, and then interact with hydrocolloid KGM so it can easily separate from starch granule crystals, resulting in the decrease of starch pasting temperature. Breakdown viscosity is the difference between the peak viscosity and the lowest viscosity, which indicates the decomposition degree of starch granules during the gelatinization process. Significant breakdown viscosity differences were observed among different samples. Pure starch showed the lowest breakdown viscosity (4894 CP), and the starch-1.5% KGM had the

highest (7314 CP). This is probably ascribed to the viscosity increase as more KGM exists in the system. With the increase of viscosity, the higher shear force is generated and acts on starch granules, resulting in further disruption of starch granule integrity and then increasing the breakdown viscosity of systems. In the cooling stage, the retrogradation phenomenon occurs, which is always happened in food processing. An increase in setback viscosity was observed as more KGM addition. A similar phenomenon has been reported by Keyu Tao [207], which explained that the amylose molecule mainly influenced the increase of setback viscosity as it could react with hydrophilic colloids and the amylose molecules themselves. With the addition of KGM, the retrogradation of starch-KGM mixture systems could be promoted in the short storage and conversely could be retarded slightly in the long-term storage (14 days), which was verified by Yoshimura et al. [208] in 1996.

Based on the RVA results of KGM/starch mixtures, it could be found that the peak and final viscosities of starch-KGM mixture systems are enhanced with the increase of KGM concentration. The recommended amount of KGM is 1% to prevent the mixtures from becoming too viscous and not easy to be stirred, as well as prevent excessive regeneration when adding KGM. In addition, the preparation temperature of all mixtures or solutions in this study has been selected as 95°C, which is higher than the pasting temperature and peak temperature among all samples based on RVA results.

Table 3-2 Effect of Konjac glucomannan (KGM) on the pasting properties of potato starch and KGM-starch mixtures.

Sample	Peak temperature (°C)	Pasting Temperature (°C)	Peak viscosity (CP)	Break down (CP)	Final viscosity (CP)	Set back (CP)
Starch	82.3±0.93	68.65±0.52	7822±115	4894±66	4012±19	1084±59

Starch-0.2%KGM	85.45±0.53	68.6±0.60	8281±90	5187±53	4284±90	1190±147
Starch-0.4%KGM	87.9±0.82	67.8±0.48	8394±149	5200±198	4416±135	1222 ± 94
Starch-0.6%KGM	87.95±0.85	66.9±0.48	9227±74	5849±17	4559±28	1181±63
Starch-0.8%KGM	91.15±0.42	62.55±0.41	9802±160	6232±90	4805±51	1235±41
Starch-1.0%KGM	92.05±0.78	53.9±0.94	10034±273	6356±252	5218±28	1540±158
Starch-1.5%KGM	91.2±0.46	50.3±0.15	11260±343	7314±302	5813±178	1867±208

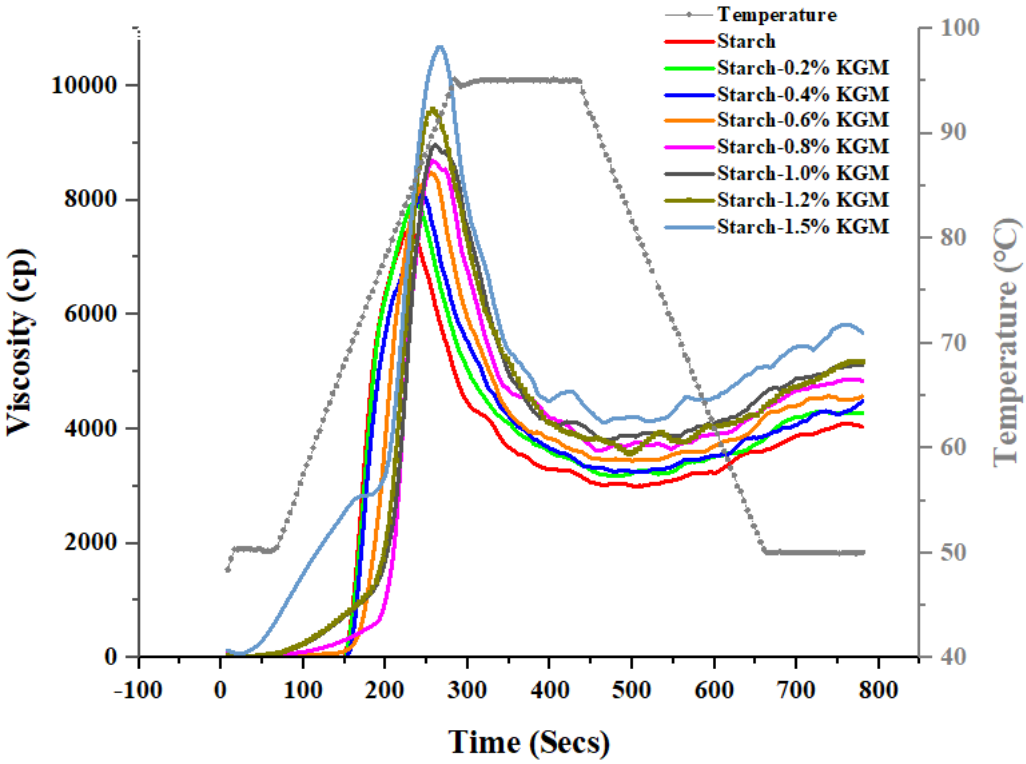


Figure 3-4. Pasting curves of KGM/starch hybrid system.

3.4.2 Influence of starch concentrations on the rheology properties of KGM/starch mixtures

As introduced in section 3.4.1, 1% content of KGM has been selected. In this section, five KGM/starch mixtures with different starch concentrations (0-4%) have been produced, and the influence of starch concentration on the rheology properties of mixtures has been studied. The dynamic rheology was used to clarify the molecular entanglement, molecular network and viscoelasticity of KGM/starch mixtures. Figure 3-5 presents the storage modulus (G') and loss modulus (G'') of pure KGM and KGM/starch mixtures. The G' and G'' are related to the elastic energy stored in viscoelastic material and dissipated energy during deformation. When G' value is higher than G'', the system shows a typical solid/gel-like behaviour, but when the G' value is smaller than G'', the system is expected to be dominated by liquid-like properties [209]. As shown in Figure 3-5, it could be found that both G' and G'' values of all samples display growth with the increase of frequency. G' value of K1, K1S1 and K1S2 is smaller than G'' at low frequency, reflecting the liquid-like behaviour. However, at high frequency, the G' values became larger than G'', and it shows a cross-over point. The changes in G' and G'' values were contributed by the molecular chain entanglement and disentanglement. At low frequency, it is easier for molecular chains to relax and disentangle. Therefore, the G'' values are higher than G'. In contrast, by increasing the frequency, the molecular chains became aggregated, associated, and a temporary three-dimensional network structure was formed [210], exhibiting the elastic solid-like state; therefore, the G' value exceeded G'' [211]. With starch addition of 0, 1% and 2%, the frequency at the cross-over point occurred at 0.6 Hz, 0.48 Hz and 0.36Hz, respectively. It could be found that the cross-over frequency of G' and G'' shifted to a lower value, indicating the stronger entanglement and hydrogen bonding of molecular chains. However, when the starch concentration reached 3%, the G'' was higher than G' during the entire frequency range, and both values of G' and G'' was increased with the increase of frequency, maintaining the dilute solution behaviour [212]. Furthermore, compared with the

pure KGM system, K1S3 system has smaller G’ and G’’ values. Because of the relatively low KGM content, there is less macromolecular chain structure in the system, which reduces the possibility of chain entanglements. Overall, the dynamic rheological results suggest that the stronger entanglement and hydrogen bonding of molecular chains were produced with a small amount of starch addition. When the starch content increases to 3%, the system will present a liquid-like behaviour, similar to the pure starch system.

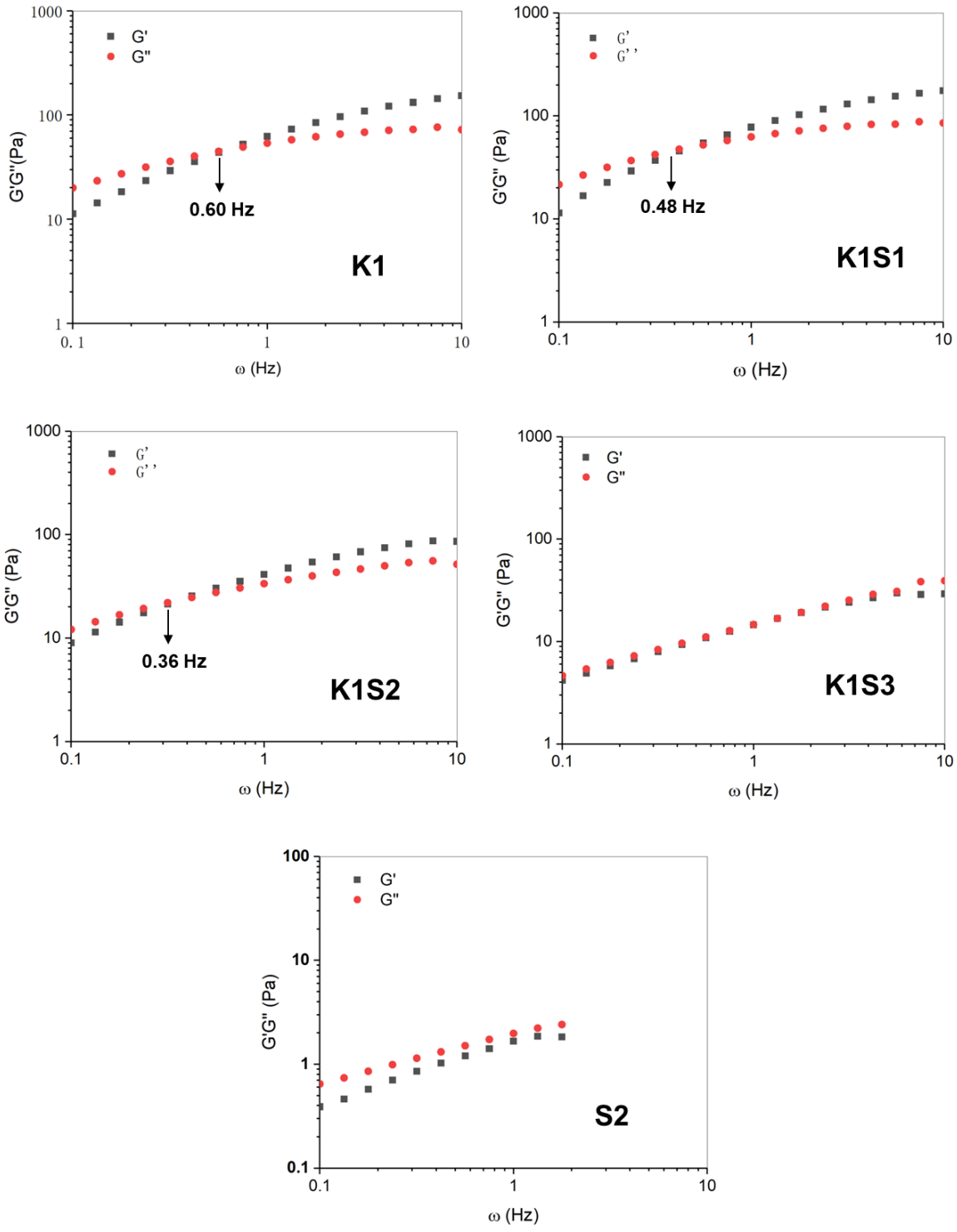


Figure 3-5. Influence of frequency on the elastic modulus (G') and viscous (G'') modulus of different KGM/starch system

3.4.3 The macro and micro-network changes of KGM-gelatin mixtures

Biomass mixtures containing 1% (w/v) KGM and 1-2% (w/v) gelatin were produced and then stored in the glass sample bottle at room temperature. After being stored for 10 h, these bottles are recorded as presented in Figure 3-6, which shows two regions, a phase separation mixture region and a stable mixture region. As reported, phase separation was a common phenomenon between gelatin and non-adsorption polysaccharides and it is more likely to appear at higher concentrations [117, 213]. The thermodynamic incompatibility between KGM and gelatin molecular was the leading cause of phase separation. As can be seen in Figure 3-6, the homogeneous phenomenon can be observed with low gelatin concentration. It can be found that the mixtures of K1G1 to K1G1.5 shows the homogeneous phase. However, the slight phase separation phenomenon appeared when the addition of gelatin increased to 1.6% (w/v). When the gelatin addition increases, the phase separation of the mixtures becomes more serious. The sample K1G2 shows significant phase separation, and two layers can be observed in the mixture: the upper layer is the turbid konjac-rich phase, and the lower layer is the transparent gelatin-rich phase.

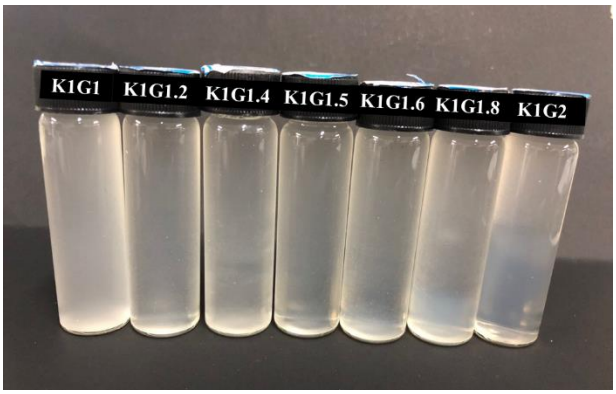


Figure 3-6. Images of KGM–gelatin mixtures.

Figure 3-7 shows images of rhodamine B stained KGM-gelatin mixtures to observe their microstructure network. The CLSM images confirm that gelatin was stained with rhodamine B and then excited by red fluorescent emission, which is depicted as a red area. The K1G1 to

K1G1.5 solutions exhibit a uniform fluorescence that gelatin was homogeneously distributed in the mixtures. It shows that KGM was combined with gelatin evenly without phase separation. However, with further increased gelatin concentration (reaches 1.6 wt%, K1G1.6), the small red cluster appeared in the CLSM images, demonstrating a slight phase separation. This phenomenon is more obvious with the increase of gelatin addition. As expected, a large red cluster is presented in the CLSM image of K1G2.

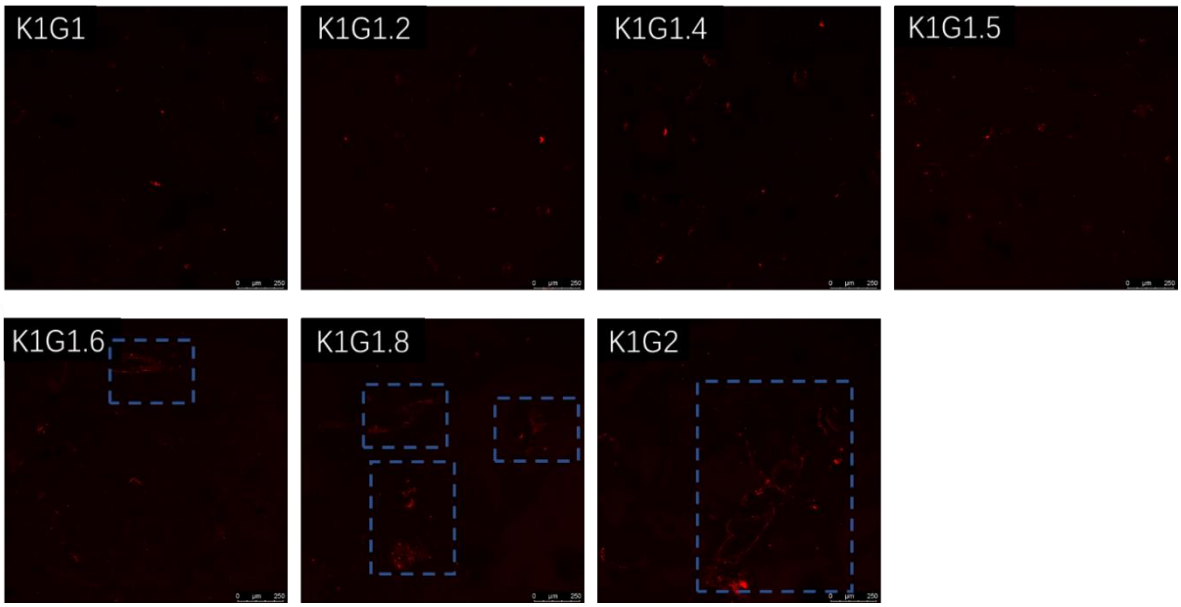


Figure 3-7. Fluorescence micrographs of KGM-gelatin mixtures.

3.4.4 Impact of gelatin concentration on the rheological properties

The storage modulus (G') relates to the ability of materials to store energy elastically, representing the elastic portion. Similarly, the loss modulus (G'') of a material is related to the material's ability to dissipate stress through heat, representing the viscous portion. Therefore, G' and G'' reflect the viscoelastic ratio of materials. In the cooling process (from 70°C to 10°C), G' and G'' of mixtures are presented in Figure 3-8. During the initial cooling process, both G' and G'' of the different KGM/gelatin composite systems were gradually increased with the decrease of temperature, and the value of G' is lower than that of G''. At this point, the viscoelasticity of the mixtures is in a low level contributing to the active movement

between the molecules with relatively high temperature, revealing the predominant viscous liquid behaviour [214]. With the further decrease of temperature, the value of G' and G'' have a significant increase until the temperature decreases around 20°C. The increase rate of G' becomes higher than that of G'', and G' value will be greater than G'' at a point, which is called a cross point, indicating that conformation has been transformed from random coils to helix structures [215] and gel properties dominated to form a gelation network in different KGM/gelatin mixtures. At this point, the molecular movements are limited, which eventually causes the rearrangement of molecules, the formation of stable bonds and a strong gel network structure. It could be observed from Figure 3-8 that the pure KGM sample gel point of G' and G'' is at about 32°C, which showed higher crossover point values than other samples. As seen in figure, samples with more gelatin content have a much higher growth rate of G' than pure KGM sample from 25 to 15°C. That means the mixtures with a high KGM ratio have slower gelation kinetics, but increasing the gelatin concentration could accelerate gelation during the dynamic cooling process [214]. With the addition of 1% gelatin, the gel point temperature has decreased to 23°C. And then, it continues to decline until reaching a low point at 19°C, the cross point of sample K1G1.6, which has the lowest gel temperature of all samples. This may be due to the reduced proportion of KGM in the hybrid system, where KGM cannot provide many hydrogen bonds [210] resulting in less opportunity for macromolecular chain entanglement and intermolecular interactions. However, when gelatin content increased to 1.8%, gel point temperature slightly increased. It could be explained that the strong KGM molecular entangled network may not be enough to inhibit gelatin random chain motion and then the gelatin tends to form the triple helix structure entangled with itself when the concentration of gelatin increased to a certain level. At this point, the KGM/gelatin mixture system phase separation appeared.

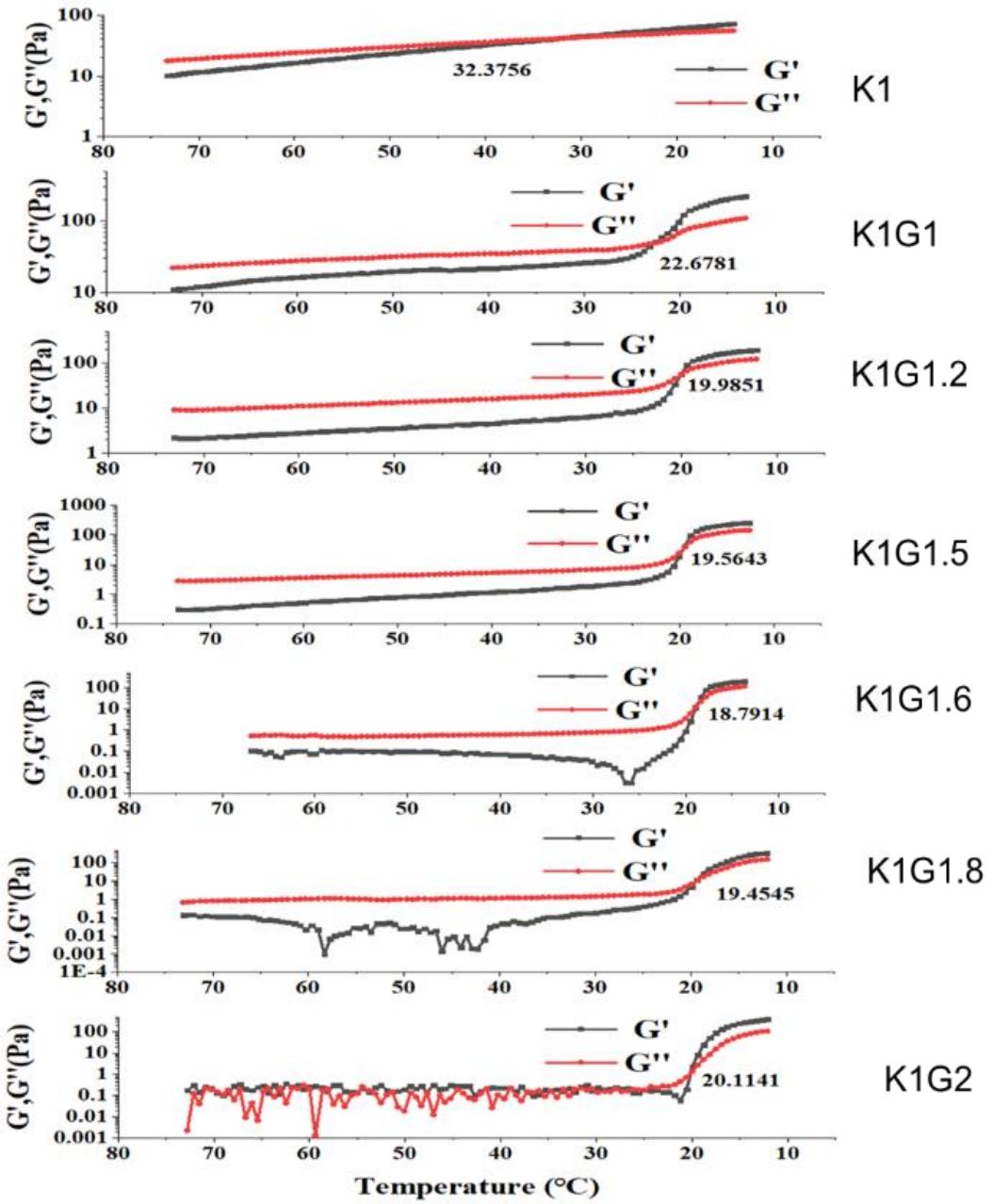


Figure 3-8. Changes of G' and G'' during the cooling process (70°C to 10°C) of the KGM/gelatin mixtures.

3.4.5 The macroscopic characterization of KGM/wheat straw mixtures

The macro morphology of KGM/wheat straw solutions with various wheat straw contents was prepared and compared in Figure 3-9. After the gel-ageing process in a refrigerator at 4°C, it can be observed that wheat straw began to subside, and the delamination phenomenon occurred after storing for a long time. The upper layer of the mixtures is light green-brown, which is the

color of the gel formed by KGM and a small amount of fine wheat straw particles, while most of the wheat straw was mainly gathered on the bottom of bottles.



Figure 3-9. Digital photograph of KGM/Wheat straw biomass mixtures.

3.4.6 Influence of different raw materials on the biomass aerogels

Macroscopic pictures of KGM/starch, KGM/gelatin and KGM/wheat straw composite aerogels are shown in Figure 3-10. The ratio of different raw materials, 1% (w/v), has been selected to produce biomass aerogels with freeze drying method. From the following comparison images, it could be found K1S1 presenthomogeneous appearance in white colour as starch and KGM are white. Finely processed KGM powder is virtually free of impurities and the particles are uniform and white. Gelatin is partially degraded by collagen in connective tissues such as animal skin, bone, muscle membrane, muscle charm and other connective tissues and becomes white or yellowish, translucent, microlustrous flakes or powder. Therefore, KIG1 is slightly yellowish in color compared to K1S1, and has a slightly shiny sequin on the surface. When KGM mixed with wheat straw, the obtained K1WS1 shows a greenish-brown appearance, while the wheat straw particles could be clearly observed at the aerogel bottom. This phenomenon is mainly caused by the wheat straw sedimentation due to the reduced viscosity of solution.



Figure 3-10. The images of biomass aerogels (K1S1, K1G1 and K1WS1).

3.5 CONCLUSION

Four biomass polymers, konjac glucomannan, starch, gelatin and wheat straw were chosen as raw materials to prepare biomass mixtures/gels or aerogels. In this chapter, the characteristics of different binary composite mixtures/gels were investigated to explore the optimal process parameters and addition ranges of raw materials for biomass aerogel preparation in the next step.

At first, the influence of KGM addition amounts on the pasting property of KGM/starch mixtures was investigated using the RVA. Compared with the pure starch system, the peak, final viscosities and break down viscosities of KGM/starch systems gradually increase, while the starch pasting temperature gradually decreases when increasing KGM content in KGM/starch mixtures. KGM addition could accelerate the rate of starch swelling and increase the level of starch swelling at low temperature contributing to the easier gelatinization of starch. Based on the results of RVA testing, the raw materials dissolution temperature in this study was selected to be 95°C, which is higher than the paste and peak temperature of all samples to ensure adequate starch pasting. Meanwhile, the recommended amount of KGM is 1% to prevent the mixtures from becoming too viscous and not easy to be stirred, as well as prevent excessive regeneration when adding KGM.

The internal molecular properties of 1% KGM mixed with different starch concentrations were investigated by using a rheometer. The dynamic rheological results showed that the molecular chains produced strong entanglement and hydrogen bonding with small amounts of starch. However, when the starch content increases to 3%, the KGM/starch system will show a liquid-like behaviour, with fewer chain entanglements similar to the pure starch system.

The micro-network of KGM/gelatin mixture systems was investigated with dynamic rheological measurements and fluorescence microscopy observations. With low gelatin content, the system is compatible, but when gelatin content is increased to a certain level, the system shows a phase separation transition. Gelling point decreases significantly and then gradually increases with increasing gelatin content. In compatible phase status, gelatin addition contributes to the acceleration of the gelling process. However, when the gelatin content reaches 1.6%, it tends to form a triple helix structure entangled with itself, resulting in slight phase separation of KGM/gelatin mixtures. To avoid this phenomenon, high gelatin content is not recommended in KGM/gelatin mixtures. Meanwhile, it could be observed from rheological curves that G' and G" of KGM/gelatin mixtures have significant changes when the temperature is lower than 20°C, where the gelling point appears. At this point, the triple-helix structure formed by gelatin molecules makes it difficult for KGM molecules to move. Therefore, it is necessary to put mixtures in a low-temperature refrigerator to accelerate gelling as called the ageing process.

When KGM is mixed with wheat straw, KGM solution changes from viscous to thin, and wheat straw is easy to subside in the mixtures and could be gathered at the bottom of bottles. This problem needs to be solved in the next chapter.

4 EXPERIMENTAL INVESTIGATION ON SOUND ABSORPTION, STRUCTURE AND MATERIAL MODELLING OF BIOMASS AEROGELS

4.1 INTRODUCTION

Currently, a range of acoustic insulation or absorption materials are used in the construction industry to reduce the impact of noise on people's life. Porous materials are most commonly used in the building field, such as organic fibers (natural and plant fibers), inorganic fibers (glass fibers), polymeric, inorganic and metallic foams. Among them, aerogels have a unique pore structure, which could be helpful in absorbing sound energy. This chapter is to propose biomass aerogels for noise absorption by adopting KGM, gelatin and wheat straw as raw materials. With large molecular chain, KGM could be considered as the good skeleton materials for aerogels preparation. For sound absorption, the tiny and complex pore structure is necessary as it can provide the chances for the sound wave enter the interior of pores and dissipate the energy of sound waves. Wheat straw, a kind of farm waste, it has multi-cavity and hollow structure, which has been used as the raw materials in preparing biomass aerogels. As shown in Section 3.4.5, wheat straw is easy to gather at the bottom of the samples. Gelatin can prevent the subsidence of wheat straw as it can be converted into gel rapidly below 37°C. In addition, gelatin could produce interconnecting pores in aerogels, which facilitate the entry of sound waves into the aerogels and the loss of sound energy to achieve noise reduction. Based on the study in Chapter 3, the appropriate gelatin and wheat straw addition concentration have been investigated in this Chapter. The physical and chemical properties, including microstructure, sound absorption properties, thermal stability and mechanical properties are studied. The influence of each component on sound absorption property is discussed. Based on the compressive testing results, a material model is proposed and used to predict the stress-strain behaviour of biomass aerogels with considering the effects of gelatin and wheat straw

additions. It has a guiding value for the material design, selection, and practical application aspects of biomass composite aerogels.

4.2 KGM/GELATIN/WHEAT STRAW AEROGEL PREPARATION

4.2.1 Materials

In this chapter, KGM, gelatin and wheat straw were selected to produce sound absorbing biomass aerogels. The reason for the selection of these three raw materials has been described in Section 1.7.2. Starch is not considered in this Chapter because it contributes to the form of micron-sized close pores, which is not conducive to sound absorption.

Table 4-1 Sound absorbing aerogel sample formula.

	Main raw materials			
Sample code	**K (KG**M)	S (starch)	G (Gelatin)	WS (Wheat straw)
	Unit (g/100 mL)			
K1G0.5	1	0	0.5	0
K1G0.75	1	0	0.75	0
K1G1	1	0	1	0
K1G1.25	1	0	1.25	0
K1G1.5	1	0	1.5	0
K1G1.5WS0.5	1	0	1.5	0.5
K1G1.5WS1	1	0	1.5	1
K1G1.5WS1.5	1	0	1.5	1.5
K1G1.5WS2	1	0	1.5	2

4.2.2 Preparation of KGM/gelatin/wheat straw aerogel

The KGM/gelatin/wheat straw aerogels preparation method is the same as Section 1.7.3 (5) and 1.7.4.

4.2.3 Procedures for formula determination

The flowchart to determine the formula of the biomass aerogel for sound absorption is shown in Figure 4-1. Firstly, the sound absorption property of KGM/wheat straw and KGM/gelatin aerogels with different formulas were tested. According to the testing results, recommended addition of gelatin is suggested to improve the poor sound absorption performance of KGM/wheat straw aerogel by avoiding the wheat straw subsidence. By performing microstructure observations and sound absorption tests, the optimal formula of KGM/gelatin/wheat straw aerogel can be obtained.

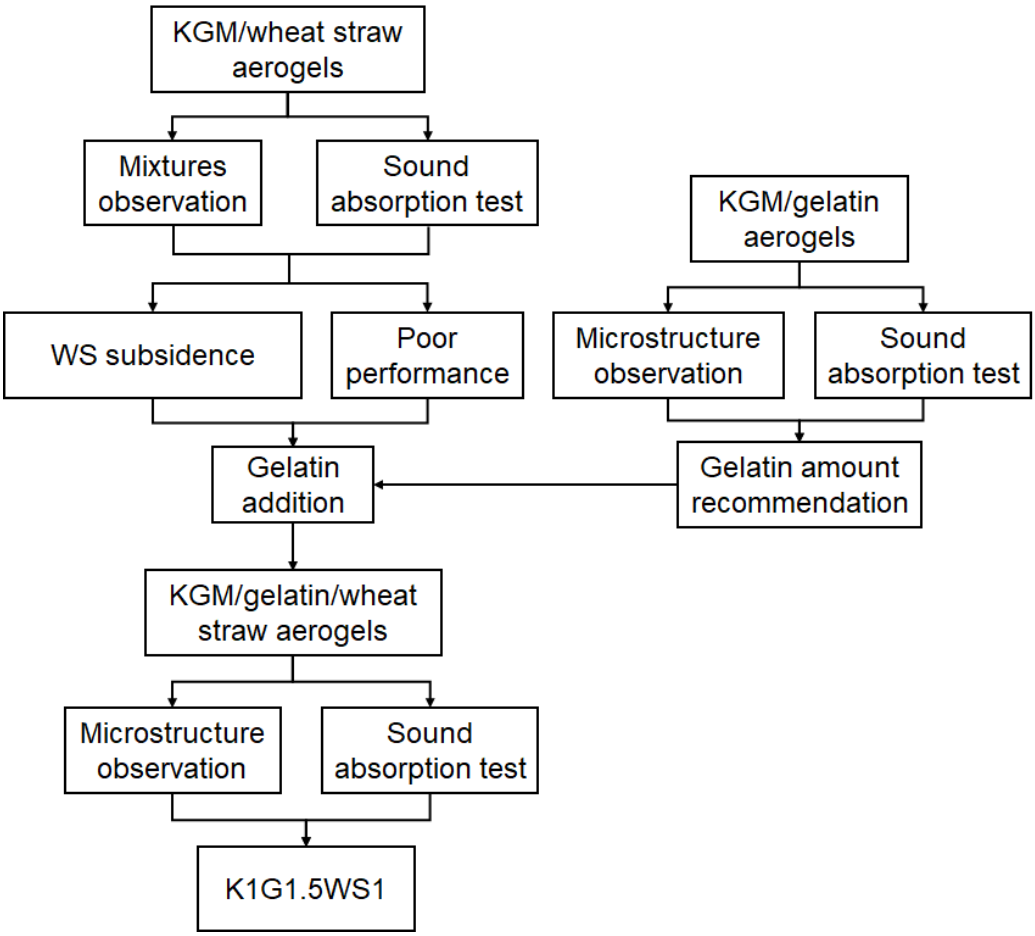


Figure 4-1. Flowchart of formula determination.

4.3 CHARACTERIZATION OF BIOMASS AEROGELS

4.3.1 Scanning electron microscopy (SEM)

The microstructure was observed with SEM (JSM6390LV, JEOL, Tokyo, Japan), as shown in Figure 4-2. Before all the tests, aerogels were cut into 5 mm × 5 mm × 1 mm cubical pieces coated with gold particles using a Gold and Platinum Sputter Coater. Specimens were observed at magnifications of 50×, 100× and the pore size distribution was counted and analyzed by Image Pro Plus software based on 3 representative SEM images.

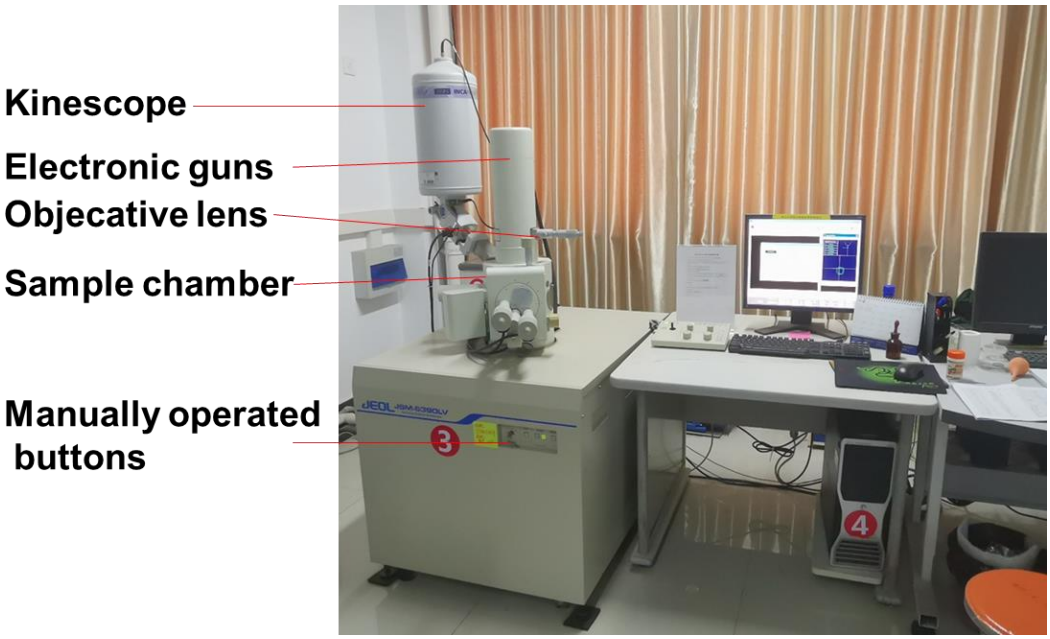


Figure 4-2. Image of scanning electron microscopy.

4.3.2 Sound absorption coefficient measurement

Aerogel samples were cut into two different sizes: the diameter of 30 mm, the height of 10 mm and the diameter of 96 mm, the height of 10 mm, respectively. The sound absorption coefficient was tested by the Impedance Tube AWA6122A (Hangzhou Aihua Instruments, China) at room temperature. All tests were performed in triplicate. The average noise reduction coefficient (NRC) value is the average value of the individual sound absorption coefficients at 125, 250, 500, 1000, 2000 and 4000 Hz, which is used to compare the sound absorption

capacity of different samples. The schematic diagram of the impedance tube device is shown in Figure 4-3.

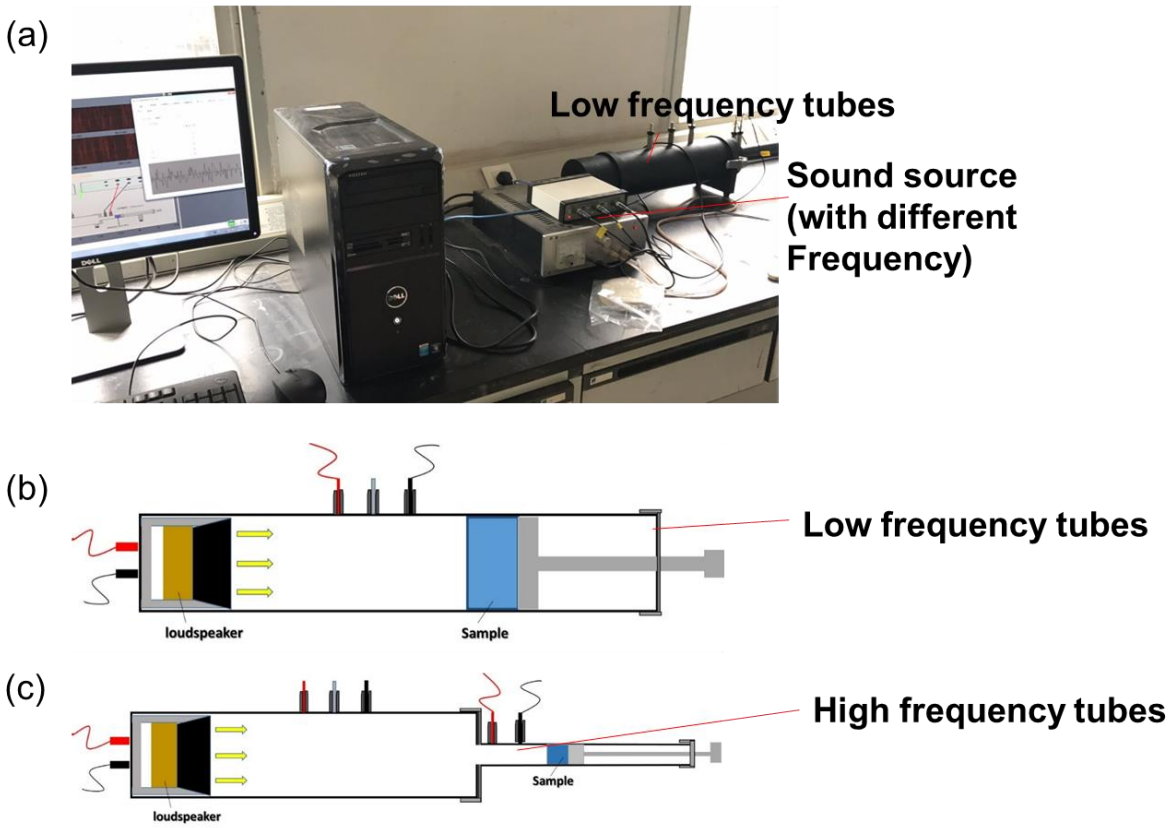


Figure 4-3. Image of the (a) impedance tube and the principle drawing of impedance tubes (b) L tube for the frequency from 50Hz-1000Hz; (c) S tube for the frequency from 500Hz-6500Hz.

4.3.3 Texture profile analysis

The mechanical property of samples was tested by a Texture analyzer (TA.XT Plus, Stable Micro Systems, Surrey, UK) equipped with a 5 kg load cell and a discoidal probe P/36R through single compressive tests. The test compression rate and ratio were 0.5 mm/sec and 45%, respectively. All tests were performed at least in triplicate. The compressive strength of specimens is defined as the maximum stress during the test. Stress (σ) was calculated by the following standard equations:

$$\sigma = \frac{F0}{S0} \quad (4\text{-}1)$$

where F0 is the force (in N) applied on the sample surface, S0 in mm^2, the initial cross-sectional area of the sample. All tests were performed in triplicate.

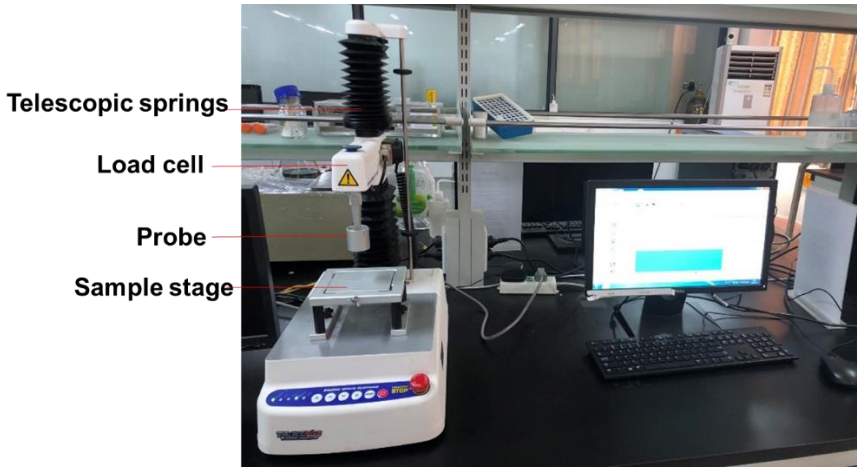


Figure 4-4. Image of a Texture analyzer.

4.3.4 Fourier transform infrared spectroscopy (FTIR)

The biomass aerogels were tested by a Fourier transform infrared spectroscopy (FTIR) spectrometer (VERTEX 70, Bruker Co., Ltd Germany) with attenuated total reflection in the range of 4000-650 cm^{-1}. Prior to tests, all samples were dried for 48 h in a dryer. Data were collected in 32 scans at a resolution of 4 cm^{-1}.

4.3.5 Thermogravimetric analysis (TGA)

Thermogravimetric analysis of biomass aerogels was characterized by a Netzsch SDT Q600 (Netzsch, Selb, Germany), reflecting the thermostability by weight loss in relation to temperature. After being pulverized, samples were heated from 25°C to 600°C with a heating rate of 20°C/min in the N_2 atmosphere and the weight loss curve was recorded.

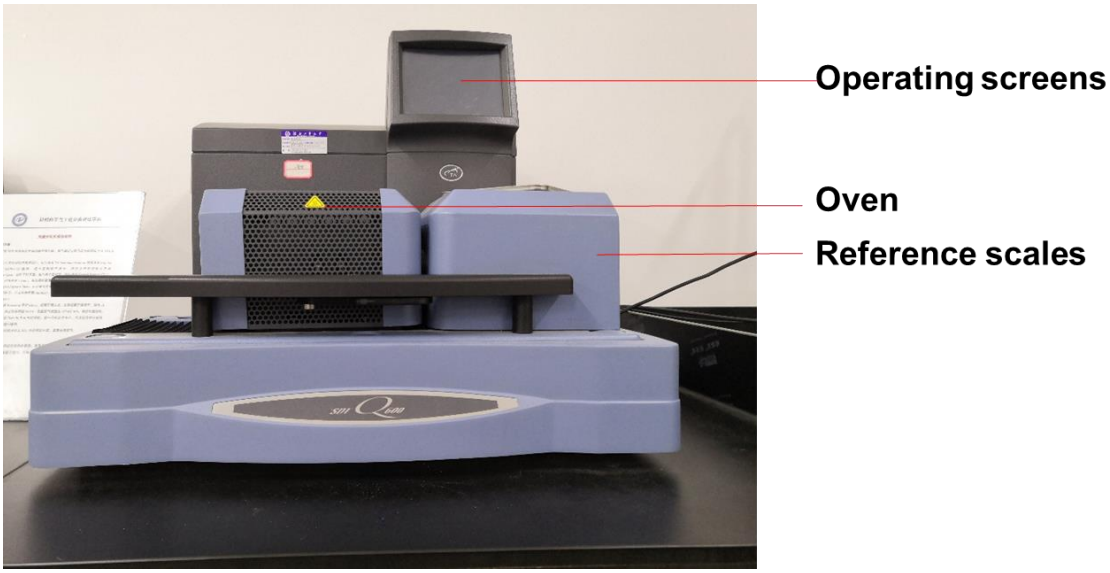


Figure 4-5. Image of the TGA instruments.

4.4 ANALYSIS OF BIOMASS AEROGEL STRUCTURE AND MORPHOLOGY

4.4.1 Impact of gelatin on the microstructure of KGM aerogels

The pore structure is formed during the freeze drying process. First, the ice nuclei forms and then grows into large ice crystal with the aggregation of water molecules when temperature decreases [160]. At last, water ice crystals sublimate directly when the pressure reaches to vacuum, which causes the formation of pores in the biomass aerogels. These pore sizes depend on the size of original ice crystals [160, 216]. The pure KGM aerogels show a relatively spherical porous structure, as shown in Figure 4-6. As known, gelatin was commonly employed as the porogen in tissue engineering to fabricate porous scaffolds [217]. When increasing the gelatin contents in pure KGM aerogels, it can be found that the pore sizes of KGM/gelatin aerogels are gradually decreased, and aerogel pore walls are thickened because of the increase of total solid concentrations. In addition, pore structures of KGM/gelatin aerogels are interconnected with one another and present as open pores when gelatin is added.

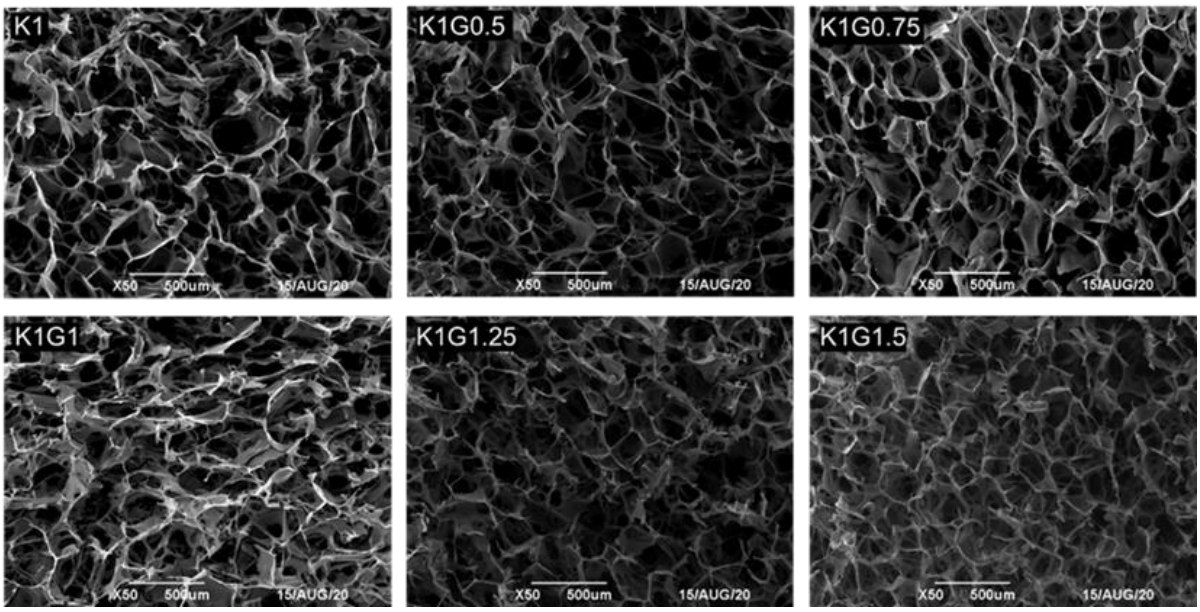


Figure 4-6. SEM observation of KGM and KGM/gelatin aerogels.

To further investigate the effect of gelatin content on the aerogel pore structure, the pore size distribution of KGM/gelatin aerogels was statistically analyzed. As presented in Figure 4-7 (a and b), the pore sizes of all composite KGM/gelatin aerogels mainly range from 1 to 100 μm. With gelatin content increasing from 0.5% to 1.5% (w/v), the total pore numbers in aerogel with pore sizes of 0–50 μm are gradually increased, which is consistent with the observation from SEM images. With more gelatin addition, more small size hole cavities were formed. Gelatin is always used to provide intermediate structural support in composite constituents. Meanwhile, it can also act as a porogenic agent [218]. The numbers of small size pores of K1G1.25 and K1G1.5 are more than that of other KGM/gelatin aerogels. This could explain that the increasing amount of gelatin influences the growth space of ice crystals, leading to the occurrence of more small pores. In addition, the increase in total solid concentration also leads to the reduction of pore channel sizes.

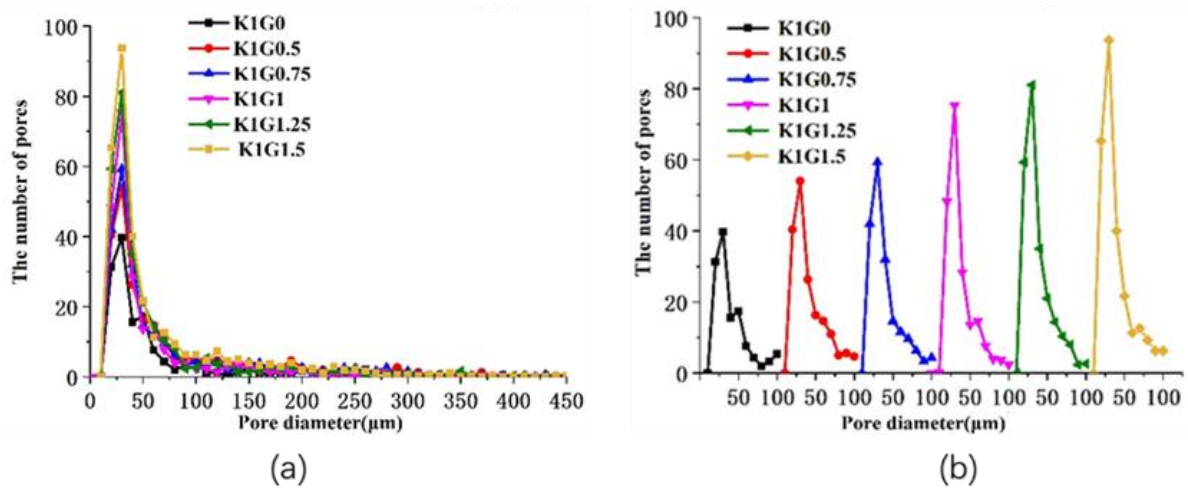


Figure 4-7. Size distribution (a: 0–450 μm; b: 0–100 μm) of KGM/gelatin aerogels pores with different gelatin concentrations.

4.4.2 Impact of gelatin on the KGM/wheat straw mixtures

In the food industry, gelatin is a kind of functional protein to be utilized as the drug delivery carrier and tissue engineering material in medical applications because gelatin can convert into gel rapidly when the temperature is lower 37°C [219]. According to this characteristic, gelatin was introduced in this study to stop wheat straw from subsiding [59], and it could be observed from Figure 4-8 that the addition of gelatin does work. This is because of the gelatin peculiarity. Its polypeptide chains aggregate and attempt to regain their secondary structure in the solution at low temperature, known as the ageing process. After this process, water molecules in the solution were trapped within the gelatin network, as shown in Figure 4-9. The ageing process also contributes to the maximum degree of gelatin helical structure formation.



Figure 4-8. Digital photograph of KGM/gelatin/wheat straw biomass mixtures (K1G1.5WS0.5, K1G1.5WS1, K1G1.5WS1.5 and K1G1.5WS2).

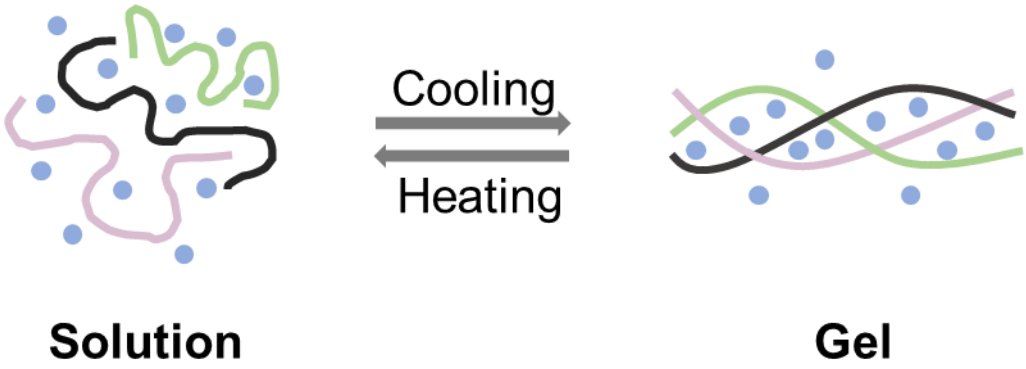


Figure 4-9. Schematic representation of gelatin structure in heating and cooling status.

4.4.3 Impact of wheat straw on the microstructure of KGM/gelatin aerogels

Figure 4-10 shows SEM micrographs of KGM/gelatin/wheat straw aerogels with different wheat straw contents. After adding wheat straw, the aerogel pores become smaller and more complex from polygons into irregular shapes. The reason is that wheat straw addition may increase the resistance against the growth from water to ice crystals [220] and cause shape changes of ice crystals during the freezing process, which could affect the pore size distribution, the shape and the connectivity of the porous network [221]. As supported by the aerogel pore size distribution results (Figure 4-11), wheat straw can also provide many micron-scale pores due to its multi-cavity structure. The wheat straw unique structure could be observed using

SEM, as presented in Figure 4-10. By analyzing the pore size distribution of KGM/gelatin/wheat straw aerogels, most pores have a size from 1 to 100 μm, and the peak number appears at a pore diameter of 20-30 μm. There is a significant increase in peak value when wheat straw addition reaches 1% or 2%. The reason is that wheat straw with a multi-cavity structure is randomly hugged in KGM/gelatin pore wall, displaying an open-cell geometry and contributing to the appearance of small pores.

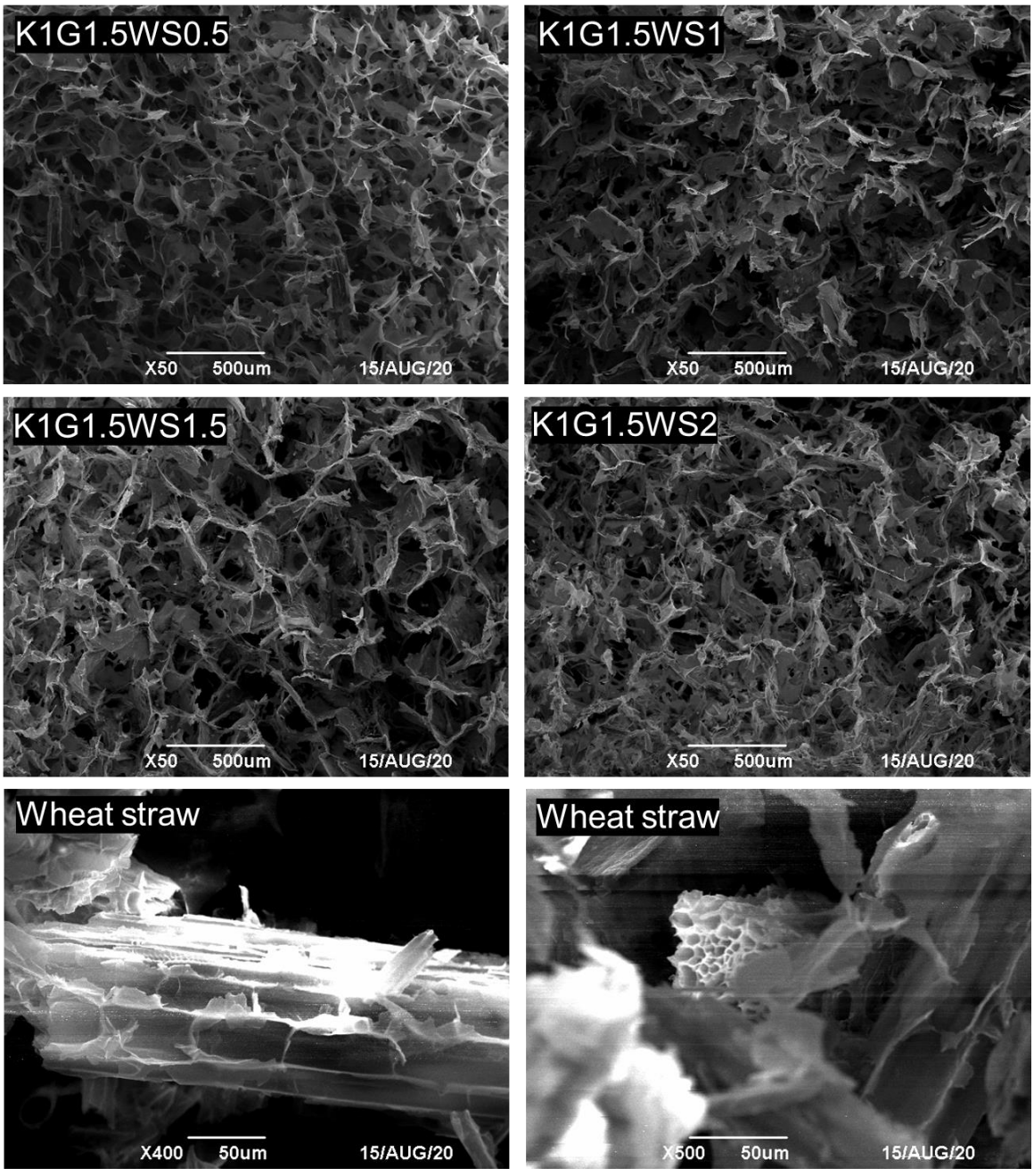


Figure 4-10. SEM observation of KGM/gelatin/wheat straw aerogels.

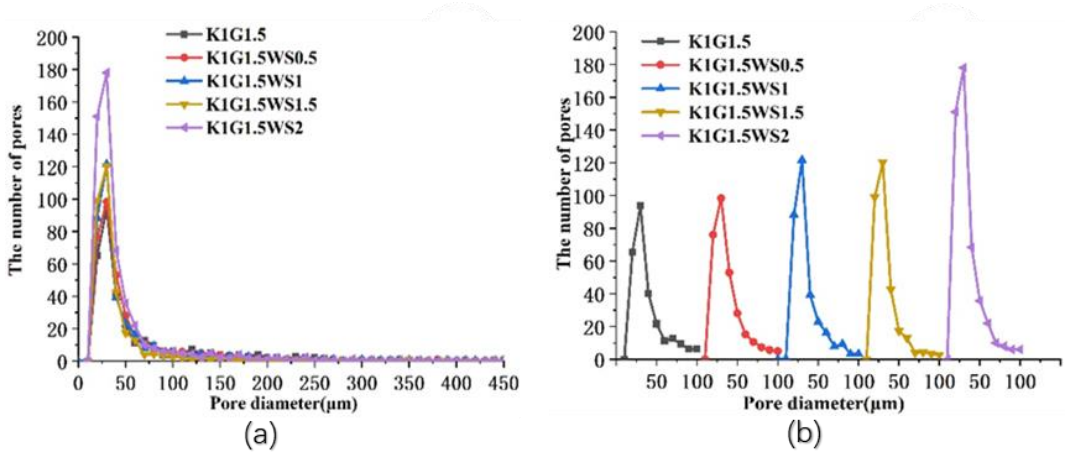


Figure 4-11. Size distribution (A: 0–450 μm; B: 0–100 μm) of KGM/gelatin/wheat straw aerogels pores with different wheat straw concentrations.

4.5 SOUND ABSORPTION TEST OF BIOMASS AEROGELS

4.5.1 General acoustic absorption performance analysis for biomass aerogels

KGM/gelatin aerogel is composed of many holes and tiny cracks, and it has many continuous cavities, which penetrate each other and communicate with the outside through surface pores [27]. When sound waves reach the aerogel surface, part of the sound wave is reflected, and the other part is transmitted, which travels into the aerogel inner structure. The consumption of sound energy in porous aerogels can be divided into three parts. First, sound wave vibration causes air movement in tiny holes and cracks. The air molecular close to the pore wall or wheat straw surface is not easy to move and air molecules would rub with pore walls. During this friction process, the sound energy will be converted to heat and dissipated [24]. Second, when longitudinal sound waves enter the aerogel, the passive compression and release of the internal air will also contribute to sound energy loss. Third, sound waves can produce the resonance of the pore wall, which converts sound energy to mechanical and heat energy. These endow porous aerogels with good high-frequency sound absorption ability.

The sound absorbing property of porous materials is dependent on different factors, including airflow resistivity, material thickness, porosity, bulk density, tortuosity and fiber diameter [222]. For porous aerogels, optimal airflow resistivity is crucial to achieving better acoustic insulation performance. When the airflow resistivity is too high, the sound wave cannot easily enter the inner structure of aerogels, resulting in poor sound absorption. On the other hand, if the airflow resistivity is insufficient, it will lead to low energy conversing efficiency. As indicated by R Dunne et. [222], materials tortuosity directly impacts the airflow resistivity, resulting in a direct impact on sound absorption. In Mamtaz's opinion, the more tortuous the material, the greater its ability to absorb sound. [223]. It has been verified that increasing thickness can improve sound absorption, especially at the middle and low frequencies. Various sizes or porosities have different effects on sound absorption characteristics. When sound waves enter the large holes, there are few chances for sound waves to have a repetitious collision with pore walls, so the sound energy loss is relatively less. After entering many tiny pores of aerogels, sound waves are prone to colliding with pore walls and consuming the sound energy. In conclusion, porous materials with good absorption performance always have the following three characteristics [24]: 1) there are a considerable number of pores with proper size evenly distributed in materials; 2) these pores should be connected and are not independent; 3) there are a large number of continuous channels, which penetrate each other and more important is that it could communicate with the outside through the surface pores.

4.5.2 The sound absorption coefficient of KGM/wheat straw aerogels

The presence of wheat straw could affect the distribution of pore size, shape and the connectivity of the porous network due to their multi-cavities. However, without the addition of gelatin, wheat straw subsidence occurred due to the shear-thinning phenomenon in KGM/wheat straw solution, as discussed in Section 4.4.2. After the freeze drying method, KGM/wheat straw aerogels were obtained, as shown in Figure 4-12.

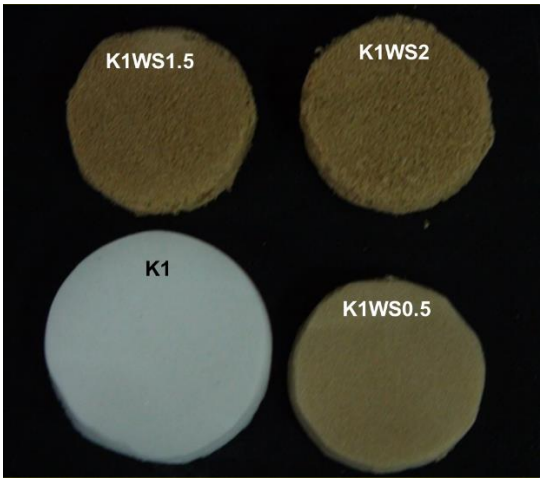


Figure 4-12 Image of KGM aerogel and KGM/wheat straw aerogels.

Sound absorption performance was carried out using impedance tubes. As presented in Figure 4-13, the NRC values of K1WS1 and K1WS2 are the same (0.17). When wheat straw concentration increased to 3% (w/v), the NRC value of K1WS3 was 0.19. With different wheat straw additions, KGM/wheat straw aerogels have similar NRC values around 0.17, which are uncompetitive compared to traditional sound insulation materials. Generally, a material with an NRC value greater than 0.2 can be considered as a sound-absorbing material [224]. The KGM/wheat straw aerogels have the following drawbacks. First, the wheat straw was prone to be settled at the bottom of aerogels, which may clog the gas flow in the aerogels. Second, the low density of KGM/wheat straw aerogels will also cause poor sound absorption properties as the sound waves are easily transmitted. In addition, it could be found that there was no significant influence on sound absorption coefficient at the low frequency when the wheat straw addition changed. At high frequency, the sound absorption coefficient only slightly improved with the increase of wheat straw concentration. The K1WS3 has a denser structure, resulting in slightly higher sound absorption performance in the middle and high frequency. Overall, the distinct stratification and non-uniform structure is the crucial factor contributing to the poor sound absorption performance of KGM/wheat straw aerogels.

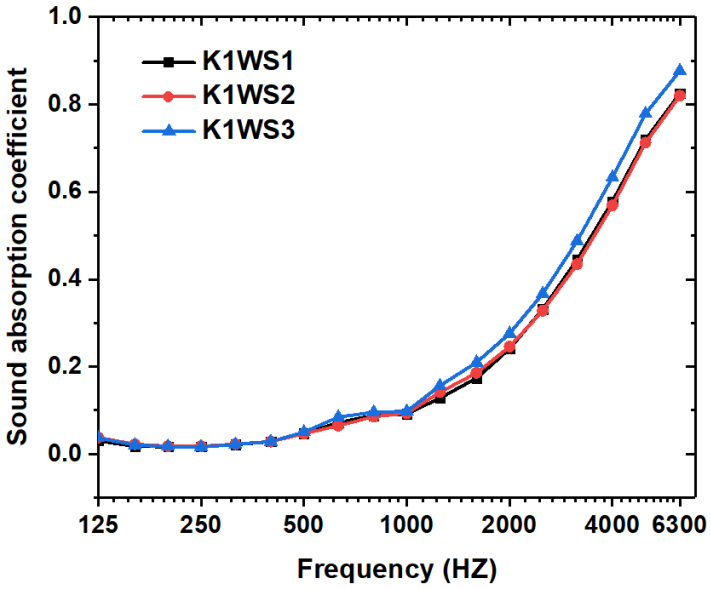


Figure 4-13. Sound absorption efficiency of KGM/wheat straw aerogels (K1WS1, K1WS2, K1WS3).

4.5.3 Sound absorption coefficient of KGM/gelatin aerogels

Referring to the study in Section 4.4.1, gelatin concentrations significantly affect the microstructure and density of KGM/gelatin aerogels. The aerogel size, density and type of pores are essential for sound absorption performance. Compared with K1WS3, the sound absorption performance of KGM/gelatin aerogels has a significant improvement with higher values of NRC, as shown in Figure 4-14. The significant enhancement of sound absorption performance in high frequency range is correlated well with bulk density and structure of KGM/gelatin aerogels. The average densities of K1G0.5, K1G1 and K1G1.5 were 0.01976±0.00422, 0.02276±0.0050, and 0.02979±0.0030 $g \cdot cm^{-3}$, respectively. As mentioned in 4.5.2, the upper part of K1WS3 has many large pores while lots of wheat straw powder gathers at the bottom. Different from KGM/wheat straw aerogels, the pores inside KGM/gelatin aerogels are hierarchically maze-like and distributed evenly. As presented in Figure 4-6, many fine pores exist on the surface and inside of the KGM/gelatin aerogels. As illustrated in Figure 4-15 (a), pores are connected and communicate with the outside, so aerogel is air permeable and easy for

sound waves to enter. With the repeated propagation, the friction is generated between sound waves and the internal complex pore structures of aerogels, resulting in viscosity and heat conduction effects, and the sound energy is gradually turned into heat dissipation after a long path. Therefore, KGM/gelatin aerogels have better sound absorption performance. As shown in Figure 4-13 (b), it is observed to exhibit an improvement in sound absorption performance with the increase of gelatin concentrations. With frequencies ranging from 125 to 6300 Hz, the NRC values of K1G0.5, K1G1 and K1G1.5 are 0.29, 0.30 and 0.36, respectively. It could be found in Figure 4-14 that the sound absorption coefficient of all biomass aerogels shows a relatively lesser sound absorption coefficient at low frequency, but after 500 Hz, a significant increase occurs. It shows an increasing trend of sound absorption coefficient with the increase of frequency, which may be due to the continuous high frequency collision and friction between sound waves and porous structure inside the biomass aerogels. This is a common characteristic of porous materials. Porous sound-absorbing materials generally have good sound absorption ability for medium and high frequency sound waves. The sound absorption coefficients show no significant difference at low frequency with different addition of gelatin. The slight enhancement of sound absorption performance at the middle frequency can be explained by the influence of density. With a specific thickness, the sound absorption coefficient at low and medium frequencies will be increased when the material density increases. This enhancement is much smaller than the increase caused by the thickness. A significant difference in sound absorption coefficient is observed when the frequency rises to 500 Hz. In the frequency range from 500 Hz to 3150 Hz, sound absorption coefficient of K1G1.5 is much higher than that of K1G1 and K1G2. At 1250Hz, the average sound absorption coefficient values of K1G0.5, K1G1 and K1G1.5 are 0.29, 0.28 and 0.66, respectively. The improvement is caused by the increasing number and proportion of small size pores, as shown in Figure 4-6 and 4-7, which enhance the complexity of pore structure and cause more reflection and friction between the

pore walls and sound waves. This increases the energy loss during the propagation of sound waves, as illustrated in Figure 4-15 (b). It is noteworthy that although the NRC of K1G1.5 is the highest among the three KGM/gelatin aerogels, there is an apparent decrease in the absorption coefficient at 4000 Hz. It may be explained by increased flow resistance inside K1G1.5 aerogel with the increase in total solid content. The flow resistance for sound absorption characteristics of materials can be summarized as follows. With low internal flow resistance, the materials sound absorption coefficient value is small at low frequencies, but when the frequency is raised to middle and high frequency ranges, the sound absorption coefficient will increase steeply. Compared to materials with low internal flow resistance, the sound absorption coefficients of materials with high internal flow resistance will be improved in the low and middle frequency bands. However, the sound absorption coefficient decreases significantly in the high frequency range. Therefore, it is necessary to find a way to change the internal flow resistance of K1G1.5 aerogels.

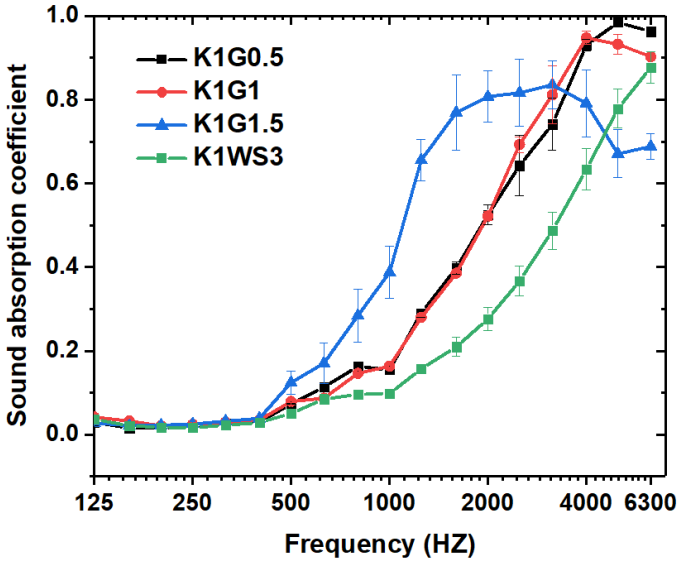


Figure 4-14. Sound absorption efficiency of composite aerogels (K1G0.5, K1G1, K1G1.5 and K1WS3).

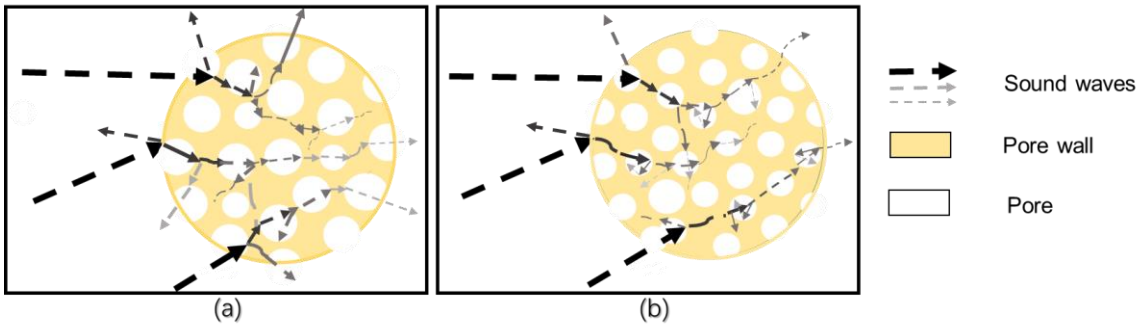


Figure 4-15. Illustration of sound absorption by (a) K1G0.5 and (b) K1G1.5.

4.5.4 The sound absorption coefficient of KGM/gelatin/wheat straw composite aerogels

To further improve the sound absorption performance of KGM/gelatin aerogels, it is necessary to reduce the internal flow resistance of K1G1.5 aerogels. As verified in a previous study [225], the resistance of KGM-based aerogels shows a significant reduction with the addition of wheat straw as it has multi-cavity and hollow structure, which could help dissipate the energy of sound waves, as illustrated in Figure 4-16. Meanwhile, gelatin can prevent the subsidence of wheat straw as it can be converted into gel rapidly below 37°C. It can be observed from Figure 4-17 that the introduced wheat straw influences the sound absorption coefficient, which is reflected in the NRC values. The NRC values of the KGM/gelatin/wheat straw aerogels with wheat straw addition from 0 to 2% are 0.36, 0.34, 0.38, 0.37 and 0.29, respectively. To have a comparison, a sound-absorbing cotton board was tested, and its sound absorption coefficient (NRC 0.22) is shown in Figure 4-17. Below 4000 Hz, the sound absorption coefficient of sound-absorbing cotton is much lower than that of biomass aerogels, which shows excellent sound absorption characteristics. At low and medium frequencies, it can be found that the sound absorption coefficient of KGM/gelatin/wheat straw aerogels is raised when the wheat straw content increases from 0 to 2%. This follows the rule: increasing material density can improve the sound absorption coefficient at low and medium frequencies when the material's thickness is maintained at a certain level. When the wheat straw addition increases from 0 to 0.5%, the sound absorption values at high frequency present a slight decrease, which may be

explained by the fact that a very small amount of wheat straw addition is insufficient to achieve the function of reducing the flow resistance inside biomass aerogel. As can be seen in Figure 4-17, the sound absorption coefficient of K1G1.5WS1 in the high frequency range is the highest among all KGM/gelatin/wheat straw aerogels. Since the wheat straw content continues to rise, especially when the wheat straw concentration reaches 2%, the sound absorption coefficient decreases significantly at high frequencies as a large amount of wheat straw causes high flow resistance. Therefore, an appropriately small amount of wheat straw addition contributes to the improvement of sound absorption performance.

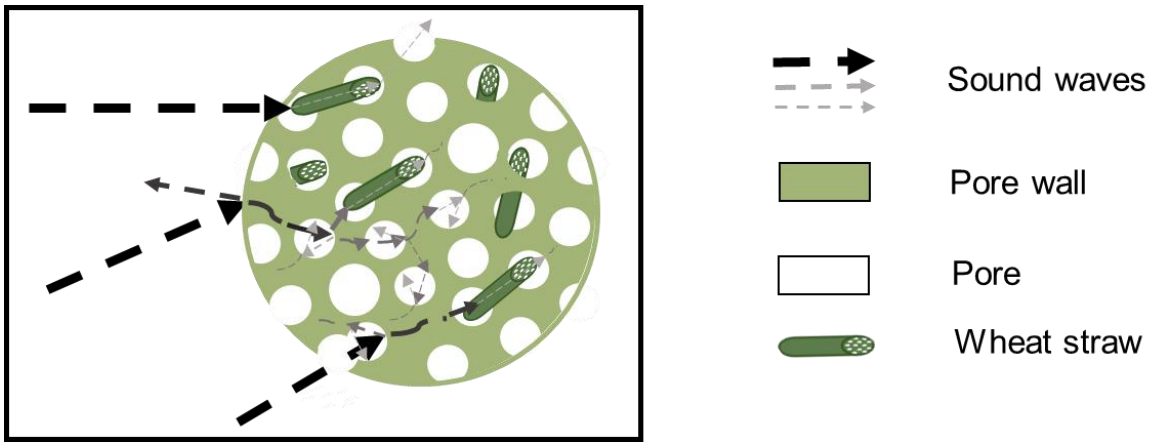


Figure 4-16. Illustration of sound absorption by K1G1.5WS1.

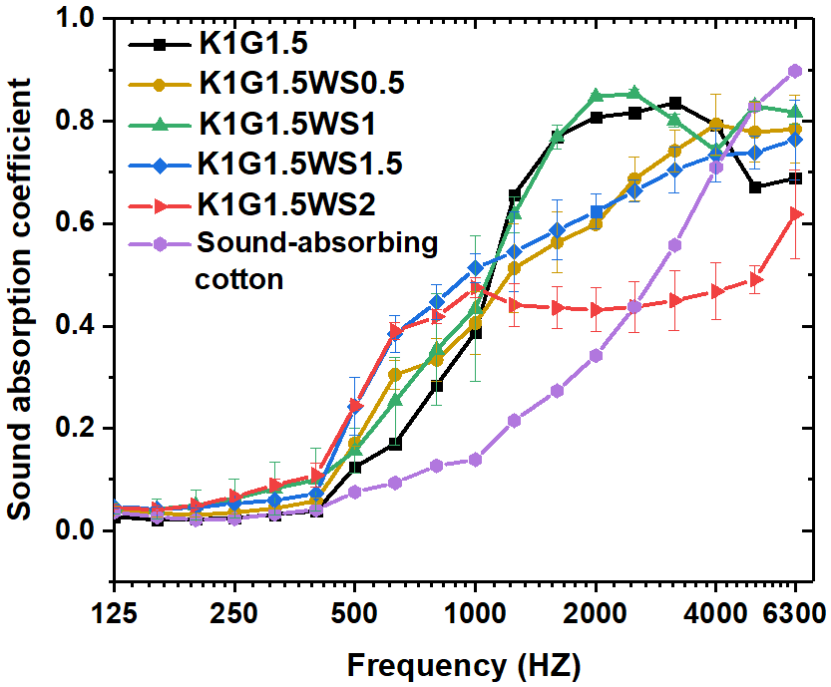


Figure 4-17. Sound absorption efficiency of composite aerogels (K1G1.5, K1G1.5WS0.5, K1G1.5WS1, K1G1.5WS1.5, K1G1.5WS2 and sound absorption cotton).

4.6 INFRARED REFLECTANCE SPECTROSCOPY (FTIR) OF BIOMASS AEROGELS

As shown in Figure 4-18, KGM FTIR spectral features can be observed at 874 cm^{-1} and 805 cm-1, and the peak at around 894 cm^{-1} is associated with the β-glucosidic bonds in KGM. These characteristic absorption bands are also exhibited in KGM/gelatin aerogels, which indicates that the characteristic structure of KGM is not impaired. KGM aerogel also shows peaks at 1636 $cm^{-1,}$ corresponding to the C–O stretching of the hydroxyl group [226]. The peak at 2886 cm^{-1} could be described as the stretching of methyl C–H, and another broad peak at 3346 cm^{-1} is mainly related to the stretching vibration of O-H groups. For gelatin aerogel, the characteristic peak at 1632 cm^{-1} is attributed to the amide I extension of C=O and the peak situated at 1538 cm^{-1} can be assigned to the amide II stretching of C–N and bending of the N–H ligation. A spectral peak at 1236 cm^{-1} results from the amide III (the plane vibration of C-N and N-H bond) [227]. Compared with the spectrum of gelatin aerogels, some peaks of KGM/gelatin aerogels become slightly stronger, and the peaks for amide I, II, and III of

KGM/gelatin aerogels shift to the higher wavenumbers due to the addition of KGM. Generally, intermolecular interactions of chemical groups are reflected in FTIR spectra, such as the absorption bands shifts, which may represent hydrogen bond interactions between KGM and gelatin chains. In addition, for KGM/gelatin composite aerogels, the infrared peak at 873 cm^{-1} were the characteristic absorption band of KGM attributed to the mannose of KGM. Generally, intermolecular interactions of chemical groups are reflected in FT-IR spectra, such as the absorption bands shifts, which may represent good miscibility between polymers. The above results verify the interaction between KGM and gelatin.

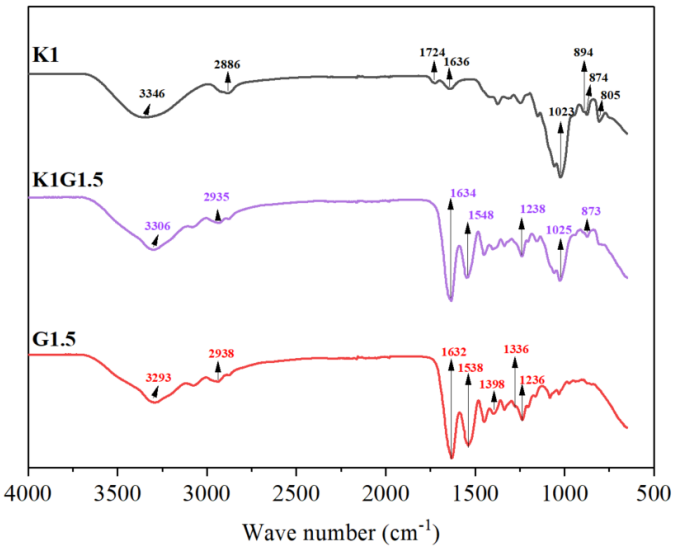


Figure 4-18. FTIR spectra of KGM aerogel, gelatin aerogel and KGM/gelatin aerogel.

FTIR spectra of wheat straw, KGM/gelatin aerogels and KGM/gelatin/wheat straw aerogels are shown in Figure 4-19. Two dominant absorption peaks of wheat straw are distributed around 3415, and 1050 cm^{-1}, which are due to the stretching vibrations of OH and CO, respectively [228]. The peak at 1616 cm^{-1} is a characteristic absorption band of lignin caused by the vibration of the aromatic backbone [229]. This proves the presence of lignin in wheat straw. It could be observed in the area around 1504 cm^{-1} typical chemical bonding behaviours of aromatic rings C=C stretch of lignin. The peak at 1161 cm^{-1} was characterized by the deformation of C-O-C antisymmetric bridge (from hemicellulose and cellobiose) and the

aromatic C-H (eugenyl and guaiacyl units in lignin). In the case of wheat straw addition, a broad peak at 3325 cm^{-1} can be seen and it has been shifted to a lower wave number when compared with wheat straw. At the same time, an 'redshift' phenomenon also appeared at 1031 cm^{-1} of KGM/gelatin/wheat straw composite aerogels when compared with wheat straw, which may be caused by the formation of hydrogen bond. In addition, KGM/gelatin/wheat straw aerogel also showed peak at 1549 cm^{-1} characteristics vibrational modes of N–H bending and C–N stretching assigned to the amide II, known as the characteristic peak of gelatin. These results indicate the good miscibility between polymers.

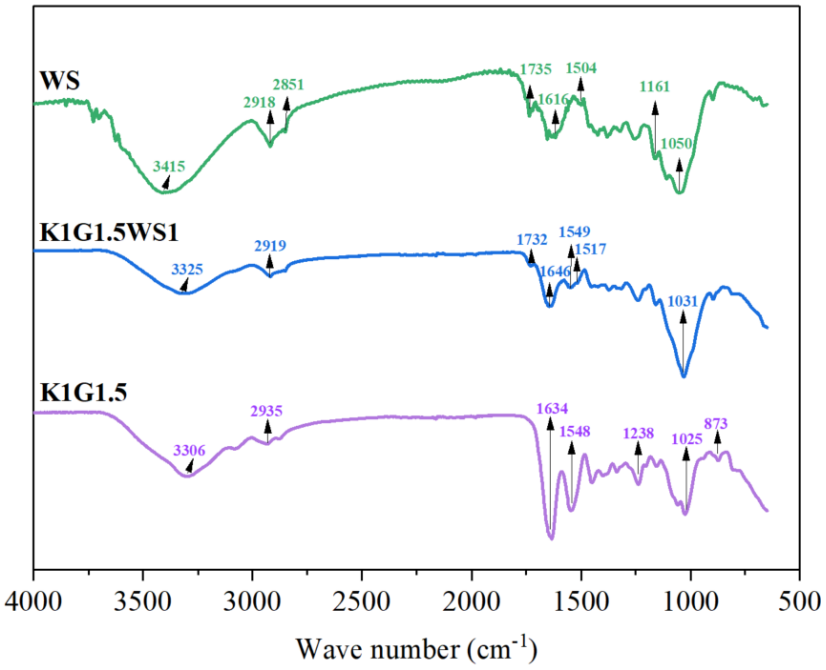


Figure 4-19. FTIR spectra of wheat straw aerogel, KGM/gelatin aerogel and KGM/gelatin/wheat straw aerogel.

4.7 MECHANICAL PROPERTY OF BIOMASS AEROGELS

To be used in building partition walls for sound absorption, the novel sound absorption material should have acceptable loading capacity to external mechanical forces. Therefore, the mechanical property of the developed KGM aerogel with the addition of gelatin and wheat straw is of great value to be investigated. This study tested the compressive behaviours of

biomass aerogels with different additions of gelatin and wheat straw. As shown in Figure 4-20 (a and b), the compressive behaviour presents a nonlinear stress–strain relationship with different stages: linear elastic, plateau, and densification stages, although the latter two stages are not significantly obvious. It can also be observed that the additions of gelatin and wheat straw have different effects on the strength of biomass aerogels. Between them, the gelatin plays a positive role in strengthening biomass aerogel. With the increase of gelatin addition, the pore size of biomass aerogels becomes smaller, and the wall thickness becomes slightly larger, which is revealed in Figures 4-6 and 4-10 in Section 4.4.1. Meanwhile, the strength of biomass aerogel presents to decrease first and then increase with the addition of wheat straw. As shown in Figure 4-20 (c), a small number of wheat straws are hugged by pore walls, and this unique combination may have a negative effect on the structural stability, which causes the worse mechanical property. With more wheat straw addition, the interaction effect among wheat straws becomes more evident and tiny wheat straw bars support one another to form nest structures, which are more stable than the original structures. Although the inherent negative influence of wheat straw still exists, the nest structure can lead to the strengthening effect when a large number of wheat straws are added. This explains the unique mechanical behaviour variation when different wheat straw additions are used.

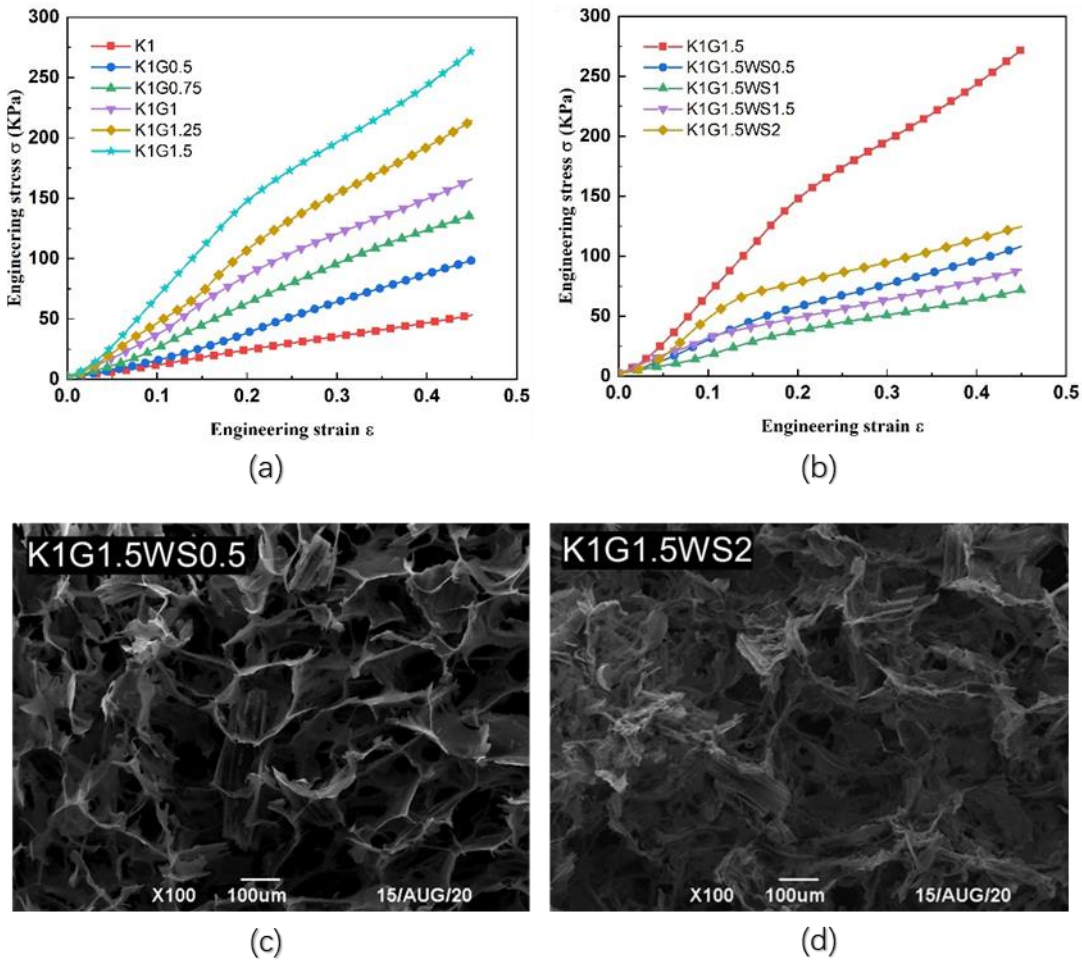


Figure 4-20. Compressive testing results of biomass aerogels with different additions of (a) gelatin and (b) wheat straw; SEM observation of wheat straw distribution in (c) K1G1.5WS0.5 and (d) K1G1.5WS2.

4.8 MATERIAL MODELLING OF THE COMPRESSIVE BEHAVIOUR

To predict the compressive behaviour for loading capacity evaluation in the sandwich structure of building partition walls, a material model is proposed for biomass aerogels with different additions of gelatin and wheat straw. This model is comprised of three parts to describe stress–strain relationship, the effects of gelatin addition and wheat straw addition. During the modelling process, the coefficient of determination (R^2) and root mean square error ($RMSE$) are used to evaluate the prediction accuracy, the calculation equations of which are given as below [230]:

$$R^2 = [\sum_{i=1}^{N}(E_i - E_{\mathrm{m}})^2 - \sum_{i=1}^{N}(E_i - P_i)^2]/\sum_{i=1}^{N}(E_i - E_{\mathrm{m}})^2 \quad (4\text{-}2)$$

$$RMSE = \sqrt{1/N \cdot \sum_{i=1}^{N}(E_i - P_i)^2} \quad (4\text{-}3)$$

where, E_i and E_{m} are experimental and mean values, respectively, P_i is predicted value, and N is total number of experimental cases used in the evaluation process. A higher level of R^2 value and/or a lower level of $RMSE$ value indicate better prediction accuracy of the material model.

4.8.1 Function to describe stress–strain relationship

Three different models are tested and compared in the current study: polynomial model [231], Ogden model [232] and Yeoh model [233]. Among them, the polynomial model is initially proposed to describe the elasticity of rubber-like incompressible materials and is dependent on two strain invariants I_1, I_2 of the left Cauchy-Green deformation tensor [231]. While, for compressible materials, such as biomass aerogel in this study, the strain energy density W can be expressed as follows [234]:

$$W = \sum_{i,j=0}^{n} C_{ij}(\bar{I}_1 - 3)^i (\bar{I}_2 - 3)^j + \sum_{i=1}^{n} D_i(J-1)^{2i} \quad (4\text{-}4)$$

where, $\bar{I}_1 = J^{-2/3}I_1$, $\bar{I}_2 = J^{-4/3}I_2$, $I_1 = \lambda_1^2 + \lambda_2^2 + \lambda_3^2$, $I_2 = \lambda_1^2\lambda_2^2 + \lambda_2^2\lambda_3^2 + \lambda_3^2\lambda_1^2$, $J = \det(F)$, F is the deformation gradient, C_{ij}, D_i are model parameters and $C_{00} = 0$. λ_1, λ_2 and λ_3 are stretch ratios, which are defined as the ratio between the lengths after and before deformation. For both uniaxial tensile and compressive tests, they can be expressed by the parallel stretch ratio λ as: $\lambda_1 = \lambda$ and $\lambda_2 = \lambda_3 = \lambda^{-1/2}$ [235]. As the strain energy density is defined as the strain energy per unit volume, the relationship between the engineering stress σ and the strain energy density W for uniaxial deformation state can be formulated as Eq. (4-5):

$$\sigma = \frac{\partial W}{\partial \lambda} \quad (4\text{-}5)$$

According to Eqs. (4-4) and (4-5), the relationship between the engineering stress σ and the stretch ratio λ is derived and can be finally expressed as the following equation [234]:

$$\sigma = 2(\lambda - \lambda^{-2})[C_{10} + C_{01}\lambda^{-1} + 2C_{20}(\lambda^2 + 2\lambda^{-1} - 3) + 2C_{20}(2\lambda + \lambda^{-2} - 3) + 3C_{11}(\lambda - 1 - \lambda^{-1} + \lambda^{-2})] \quad (4\text{-}6)$$

where, the conversion from stretch ratio λ to engineering strain ε can be easily achieved by using the relationship of $\lambda = 1 + \varepsilon$ for tensile testing condition and $\lambda = 1 - \varepsilon$ for compressive testing condition.

Ogden model also has a strain energy density function to describe the non-linear behaviour of materials such as rubbers, polymers and biological tissue [232]. For compressible materials, the strain energy density W is expressed as the following format [234]:

$$W = \sum_{i=1}^{n} \frac{\mu_i}{\alpha_i}\left(\lambda_1^{\alpha_i} + \lambda_2^{\alpha_i} + \lambda_3^{\alpha_i} - 3\right) + \sum_{i=1}^{n} D_i(J-1)^{2i} \quad (4\text{-}7)$$

The engineering stress – stretch ratio relationship under Ogden model can be derived and written as the following equation:

$$\sigma = \lambda^{-2}\left(\mu_1\lambda^{\alpha_1} + \mu_2\lambda^{\alpha_2} - \mu_1\lambda^{-1/2\alpha_1} - \mu_2\lambda^{-1/2\alpha_2}\right) \quad (4\text{-}8)$$

Yeoh model is a reduced polynomial model. The same to the above two models, Yeoh model also has the assumption that the material behaviour can be described by using a function of the strain energy density W [233], which can be expressed as follows for compressible materials [234]:

$$W = \sum_{i=1}^{n} C_{i0}(\bar{I}_1 - 3)^i + \sum_{i=1}^{n} D_i(J-1)^{2i} \quad (4\text{-}9)$$

where, $n = 3$, and C_{i0} is model parameter.

Therefore, the engineering stress can be predicted by Yeoh model using the following equation:

$$\sigma = 2C_{10}(\lambda - \lambda^{-2}) + 4C_{20}(\lambda - \lambda^{-2})(\lambda^2 + 2\lambda^{-1} - 3) + 6C_{30}(\lambda - \lambda^{-2})(\lambda^2 + 2\lambda^{-1} - 3)^2$$

(4-10)

To test and compare the applicability of the above three material models, the compressive testing result of K1G1.5 is used in this study. The parameters of the polynomial, Ogden and Yeoh models are calculated and given in Table 4-2.

Table 4-2 Parameters of the polynomial, Ogden and Yeoh models.

Model	Parameter	Value
Polynomial model	C_{10} (KPa)	-434.63
	C_{01} (KPa)	504.84
	C_{20} (KPa)	-1337.51
	C_{11} (KPa)	1202.39
	C_{02} (KPa)	-325.71
Ogden model	μ_1 (KPa)	1112.05
	α_1	-0.8962
	μ_2 (KPa)	-926.46
	α_2	-1.45
Yeoh model	C_{10} (KPa)	95.39
	C_{20} (KPa)	-31.37
	C_{30} (KPa)	3.63

Figure 4-21 (a and b) shows the prediction results and the comparison between different material models tested in this study. From Figure 4-21 (a), it is clearly shown that the polynomial model can give better prediction results than the other two models. From the quantitative aspect, the prediction result of the polynomial model has the highest R^2 and lowest $RMSE$ level of 0.9997 and 1.515 MPa, respectively, while Ogden and Yeoh models present

relatively worse prediction effects. Therefore, in the proposed material model, the polynomial model is considered to act as the part to describe the stress–strain relationship.

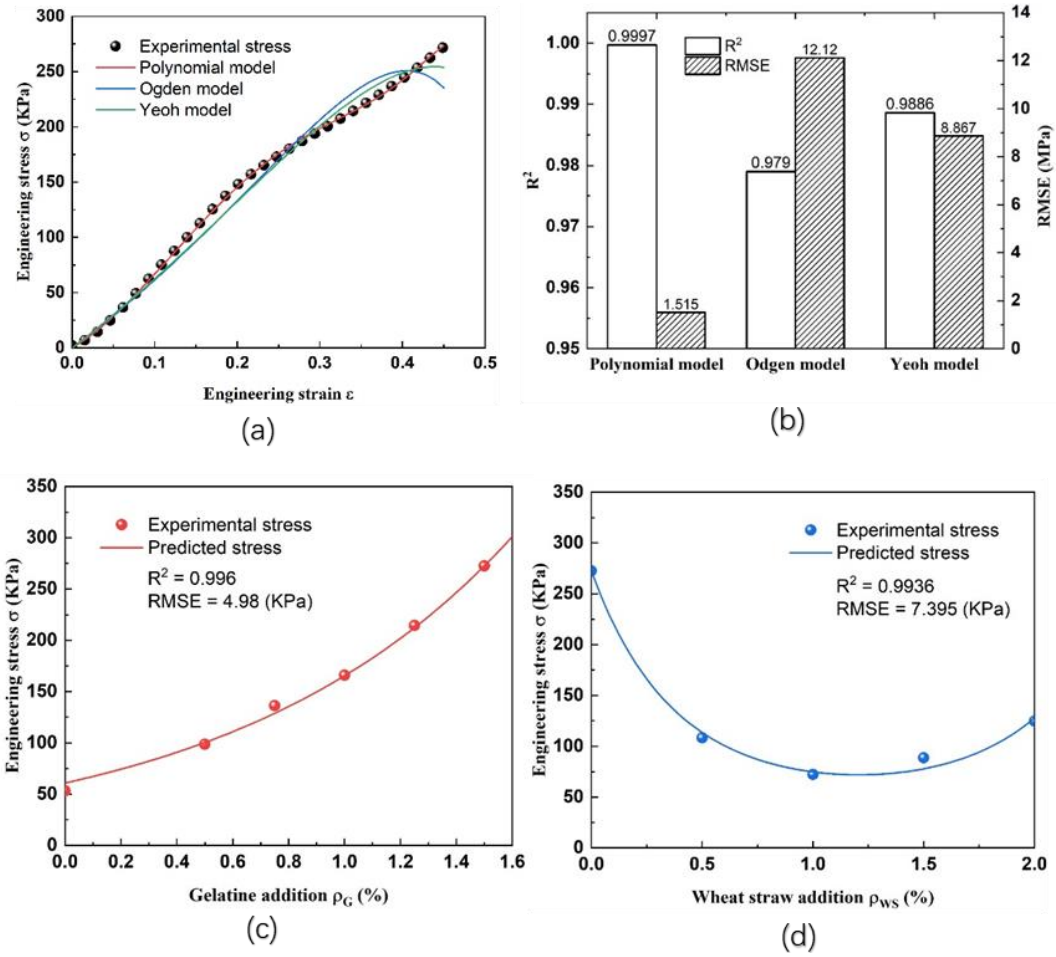


Figure 4-21. Comparison between different models: (a) predicted stress–strain curves and (b) calculated R^2 and $RMSE$; Experimental and predicted effects of (c) gelatin addition and (d) wheat straw addition on engineering stress.

4.8.2 Effect of gelatin addition

As shown in Figure 4-21 (c), the engineering stress for different addition of gelatin at the same engineering strain of 0.45 is extracted from Figure 4-20 (a), and the experimental results indicate that the addition of gelatin has an enhancement effect on the strength of biomass aerogels. Moreover, with the increase in gelatin concentration, the enhancement effect is observed to be more obvious. Based on the above experimental observation, the following

phenomenological equation is proposed to predict the effect of gelatin addition on the engineering stress σ of biomass aerogel:

$$\sigma = \sigma_{\mathrm{G}}^{\mathrm{Ref}} \exp\left[k\left(\rho_{\mathrm{G}} - \rho_{\mathrm{G}}^{\mathrm{Ref}}\right)\right] \quad (4\text{-}11)$$

where, ρ_{G} is the addition of gelatin, $\rho_{\mathrm{G}}^{\mathrm{Ref}}$ is the selected reference addition of gelatin, $\sigma_{\mathrm{G}}^{\mathrm{Ref}}$ is the engineering stress of biomass aerogel with reference gelatin addition, and k is the model parameter. The gelatin addition of 1.5% is selected as the reference value before the parameter identification, and therefore $\sigma_{\mathrm{G}}^{\mathrm{Ref}}$ is observed to be 307.39 KPa. By fitting the experimental relationship between the engineering stress and the gelatin addition, the model parameter k is identified as 99.87 in the studied case.

As shown in Figure 4-21 (c), the red curve presents the predicted results with the use of Eq. (4-11). It is observed that the predicted results are in good agreement with the experimental results, and R^2 and $RMSE$ have values of 0.996 and 4.98 KPa, respectively, which indicate that an accurate prediction of the effect of gelatin addition is achieved.

4.8.3 Effect of wheat straw addition

In the experiment, the effect of wheat straw addition on the engineering stress of biomass aerogels is presented in Figure 4-21 (d). The engineering stress for different additions of wheat straw is extracted from Figure 4-20 (b) at the same strain of 0.45. Initially, adding wheat straw significantly reduces the strength of biomass aerogels. The worst strength is observed with the wheat straw addition of 1%. However, the strength tends to be enhanced when the addition of wheat straw continues to increase. After 1% addition of wheat straw and with an addition of 1.5%, an obvious increase of strength is reached. To predict the unique trend of the effect of wheat straw addition, the following equation is proposed:

$$\sigma = \sigma_{\mathrm{WS}}^{\mathrm{Ref}} \exp\left[m\left(\rho_{\mathrm{WS}} - \rho_{\mathrm{WS}}^{\mathrm{Ref}}\right) + n\left(\rho_{\mathrm{WS}} - \rho_{\mathrm{WS}}^{\mathrm{Ref}}\right)^2\right] \quad (4\text{-}12)$$

where, ρ_{WS} is the addition of wheat straw, $\rho_{\mathrm{WS}}^{\mathrm{Ref}}$ is the selected reference addition of wheat straw, $\sigma_{\mathrm{WS}}^{\mathrm{Ref}}$ is the engineering stress of biomass aerogel with the reference wheat straw addition, m and n are model parameters. The wheat straw addition of 0% is selected as the reference value, and therefore $\sigma_{\mathrm{WS}}^{\mathrm{Ref}}$ is observed to be 307.39 KPa, which is the same to $\sigma_{\mathrm{G}}^{\mathrm{Ref}}$. The experimental relationship between the engineering stress and the wheat straw addition gives the fitting results of model parameters m and n, which are identified as -220.7 and 9144, respectively.

With the above proposed Eq. (4-12) and identified model parameter values, the predicted effects of wheat straw addition are depicted as the blue curve in Figure 4-21 (d). Results show that the proposed equation can predict the effect of wheat straw addition and reflect the unique weakening trend followed by a hardening effect. The values of R^2 and $RMSE$ are calculated as 0.9936 and 7.395 KPa, respectively, which demonstrate the high accuracy of the proposed prediction equation.

4.8.4 Material model and prediction results

To summarize, the material model for the compressive behaviour of the studied biomass aerogels can be written as the following equation:

$$\sigma = 2(\lambda - \lambda^{-2})[C_{10} + C_{01}\lambda^{-1} + 2C_{20}(\lambda^2 + 2\lambda^{-1} - 3) + 2C_{20}(2\lambda + \lambda^{-2} - 3) + 3C_{11}(\lambda - 1 - \lambda^{-1} + \lambda^{-2})] \exp\left[k\left(\rho_{\mathrm{G}} - \rho_{\mathrm{G}}^{\mathrm{Ref}}\right) + m\left(\rho_{\mathrm{WS}} - \rho_{\mathrm{WS}}^{\mathrm{Ref}}\right) + n\left(\rho_{\mathrm{WS}} - \rho_{\mathrm{WS}}^{\mathrm{Ref}}\right)^2\right] \quad (4\text{-}13)$$

where, the model parameters are summarized in Table 4-3.

Table 4-3 Parameters of the material model for compressive behaviour of biomass aerogels with different additions of gelatin and wheat straw.

Parameter	Value
C_{10} (KPa)	-434.63

C_{01} (KPa)	504.84
C_{20} (KPa)	-1337.51
C_{11} (KPa)	1202.39
C_{02} (KPa)	-325.71
k	9987
m	-220.70
n	9144

Using the derived model parameters, the prediction results are presented in Figure 4-22 (a and c) for different gelatin and wheat straw additions. For the prediction results of different gelatin additions shown in Figure 4-22 (a), although it shows a slight degree of difference from the experimental curve of K1G0.5 at a small strain range, all other predicted curves have a high agreement with the experimental ones. Meanwhile, for the prediction results of different wheat straw additions shown in Figure 4-22 (c), the ones of wheat straw addition of 1% and 2% are observed to be less accurate compared to the other three cases, but the unique effect of wheat straw addition on the compressive behaviour is presented successfully. The R^2 values of these two prediction parts are calculated as 0.992 and 0.9894, respectively, which means the material model can predict the compressive behaviour of biomass aerogels with different additions of gelatin and wheat straw with high accuracy.

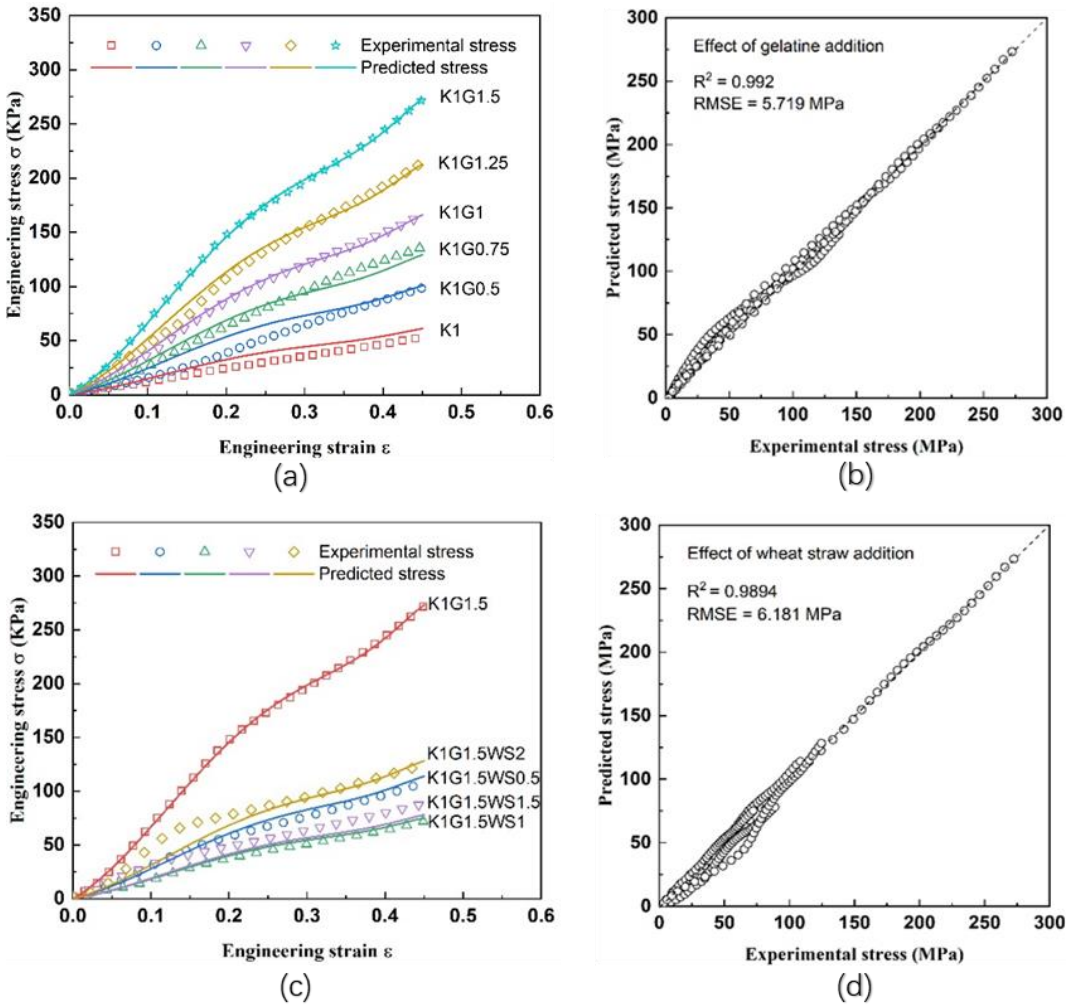


Figure 4-22. Prediction and evaluation results of the material model for compressive behaviour of biomass aerogels with different additions of (a), (b) gelatin, (c) and (d) wheat straw.

4.9 THERMAL PROPERTY OF BIOMASS AEROGELS

Figure 4-23 shows TGA results of biomass aerogels. The thermal decomposition of all aerogels has mainly two stages. The first degradation stage is from a temperature of 20°C to about 100°C, corresponding to the evaporation of free and bound water in samples. The mass loss in the second stage starts at around 100°C, mainly from the breakage of glycosidic bonds in the polysaccharides and the degradation of amino acids in the proteins. For KGM aerogels, the primary decomposition temperatures range from 265.69°C to 342.21°C, which is lower than

the ones of gelatin (298.82-375.05°C) and wheat straw (294.21-369.91°C). For wheat straw, the temperature where the maximum thermal decomposition rate appears is the highest (345.52°C) among all components, which may be attributed to its unique cavity structure that hinders heat transfer to some extent. After adding wheat straw, the mass loss of K1G1.5WS1 ranges from 280.02 to 352.28°C, where about 70.26% of the weight was lost due to the degradation of polysaccharides, gelatin, and wheat straw. As shown in Figure 4-23, the epitaxial initial decomposition temperature of K1G1.5WS1 is observed to be between the temperatures of three pure components. The results indicate that the thermal stability of KGM aerogels with the addition of gelatin and wheat straw could maintain a relatively good level compared to raw materials.

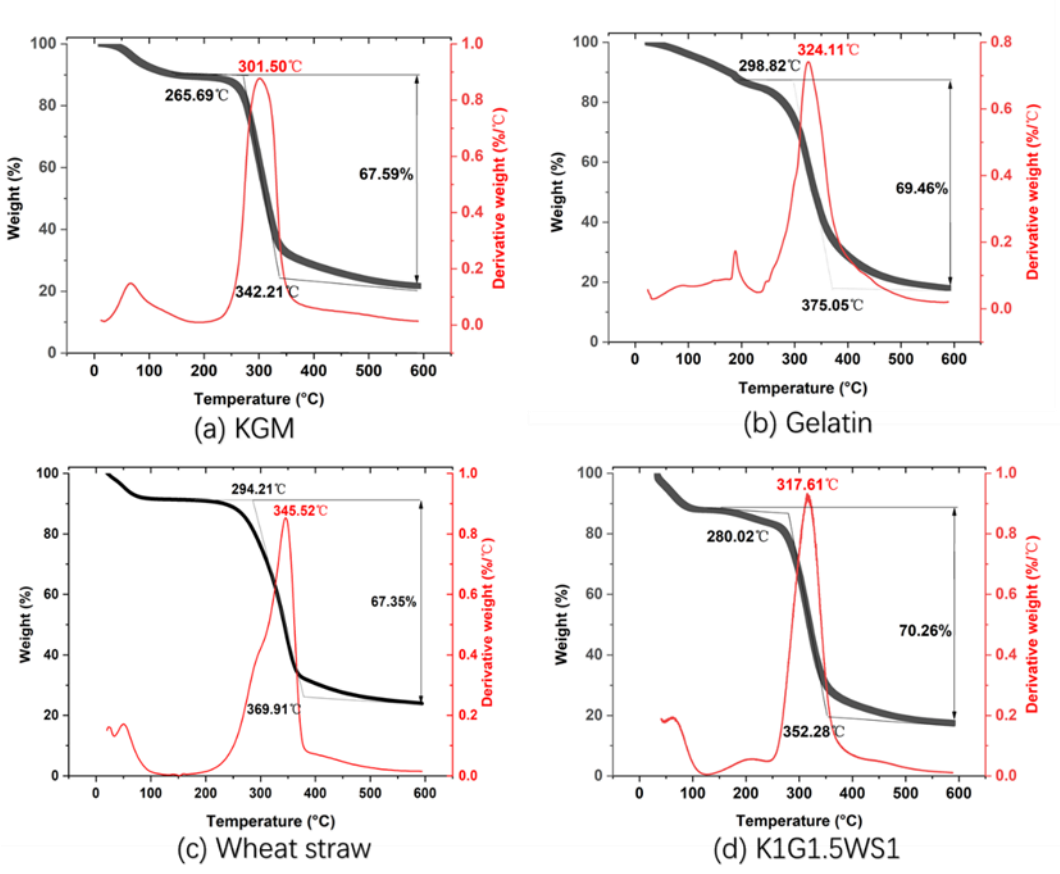


Figure 4-23. TGA of KGM, gelatin, wheat straw and K1G1.5WS1 aerogel.

4.10 CONCLUSION

This chapter demonstrates KGM/gelatin/wheat straw aerogels with good sound absorption properties. The pore structure, sound absorption property, infrared reflectance spectroscopy, thermal and mechanical properties of biomass aerogels are investigated and presented, followed by a material model to predict the compressive behaviour. The main conclusions can be drawn as follows:

(1) The NRC values of biomass aerogels are tested to be between 0.29 and 0.38. The additions of gelatin and wheat straw can improve the sound absorption performance of biomass aerogel because they contribute to the increase of open pores and more complicated pore structures. The optimized biomass aerogel specimen for sound absorption is identified to be K1G1.5WS1, with an NRC value of 0.38. Compared with sound absorption cotton, the developed biomass aerogels can achieve better sound absorption performance in most frequency ranges.

(2) The thermal decomposition property of biomass aerogels is similar to those of three raw materials. The initial decomposition temperature of the K1G1.5WS1 aerogel is identified to be moderate among the temperatures of KGM, gelatin and wheat straw. A relatively good level of thermal stability is maintained in the composite aerogels.

(3) Biomass aerogels have a nonlinear compressive behaviour with different stages. Gelatin has a positive influence on strengthening biomass aerogel and smaller pore size and larger wall thickness are induced by the increased addition of gelatin. With the addition of wheat straw, the strength of biomass aerogel is first weakened obviously and then increases when the addition is more than 1%. This results from the unstable structure due to the distribution of wheat straw hugged by pore walls, while with the increased addition, the high-intensity fine wheat straws interact and form a more stable nest structure to strengthen biomass aerogels.

(4) The proposed material model can predict the compressive stress–strain curves of biomass aerogels with high accuracy. The additions of gelatin and wheat straw are considered in this material model, and it is proven to be effective in predicting the effect of gelatin and wheat straw on compressive behaviour.

5 EXPERIMENTAL INVESTIGATION ON THE THERMAL INSULATION PERFORMANCE OF BIOMASS AEROGELS

5.1 INTRODUCTION

For thermal insulation, aerogels are commonly used because of their unique and superior properties. To reduce the use of organic polymers, this chapter produced a kind of biomass aerogel for thermal insulation using KGM, starch, gelatin and wheat straw. For thermal insulation, closed pore structure is necessary for insulating. Different from gelatin, starch addition contributes to the form of more micron-sized close pores, improving thermal insulation property. Therefore, starch is added in this chapter. Meanwhile, the gelatin concentration should be reduced as it contributes to the formation of open pores. Compared with Chapter 4, only small amount of gelatin is used for preventing wheat straw subsidence in this chapter. After adding wheat straw, the biomass aerogel structure became complex, and the gaseous flow path was changed to be more complicated, leading to the lower thermal conductivity. In this Chapter, all the experiments are based on the previous study [59], in which an L9(3^4) orthogonal array test was performed to analyze the impact of different components (KGM, gelatin, starch and wheat straw) and concentrations on the thermal conductivity and to obtain the optimized aerogel formula. The orthogonal Array Testing technique a scientific method for the study and treatment of multi-factorial experiments and is one of the larger branches of mathematical statistics, which is always used in biological and chemical experiments. Four factors (four raw materials) and three levels (three different concentrations) were applied, and 9 different biomass aerogel samples were selected to test thermal conductivity. Based on the testing results and analysis, it could be concluded that the optimized aerogel formula is K1G0.5S2WS1.5, and its thermal conductivity is 0.04641 $Wm^{-1}K^{-1}$. In this Chapter, the correlation between wheat straw length, pre-freeze temperature, microstructure and the thermal insulation performance is investigated. A series of studies on the microstructure,

thermal insulation, thermal stability and flame retardant properties of biomass aerogels are carried out. To better investigate the thermal insulation properties of biomass aerogels in real situations, this study measured the thermal insulation performance of a small box made of different insulation materials. This chapter will contribute to developing biomass materials in the thermal insulation field.

5.2 KGM/GELATIN/STARCH/WHEAT STRAW AEROGEL PREPARATION

5.2.1 Materials

In this chapter, KGM, gelatin, starch and wheat straw were selected to produce thermal insulation biomass aerogels. The reason for the selection of these four raw materials has been described in Section 1.7.2. Starch is added in this Chapter because it contributes to the form of micron-sized close pores, which is conducive to thermal insulation. In this chapter, the wheat straw powder was sieved through Tyler screen (60, 120, 140, 160 and 400 mesh) before being used.



Figure 5-1. Image of Tyler screens.

5.2.2 Preparation of KGM/gelatin/starch/wheat straw aerogel

The KGM/gelatin/starch/wheat straw aerogel preparation method is the same as Section 1.7.3 (6) and 1.7.4. The wheat straw size varies from 60 mesh to 400 mesh. The pre-freezing temperature was changed from -15 to -40°C.

Table 5-1 The formula of the samples and their raw materials.

Sample Code	KGM	Gelatin	Starch	Wheat straw
		(g/100 mL)		
K1G0.5S2WS1.5	1	0.5	2	1.5

5.2.3 Flowchart of experiments in Chapter 5

The flowchart for experimental investigation of biomass aerogels for thermal insulation is shown in Figure 5-2. Following the optimized aerogel formula K1G0.5S2WS1.5 determined by previous research [59], the effects of wheat straw size and pre-freezing temperature on the thermal conductivity and microstructure were investigated to obtain the recommended wheat straw size and pre-freezing temperature for improvement of thermal insulation property.

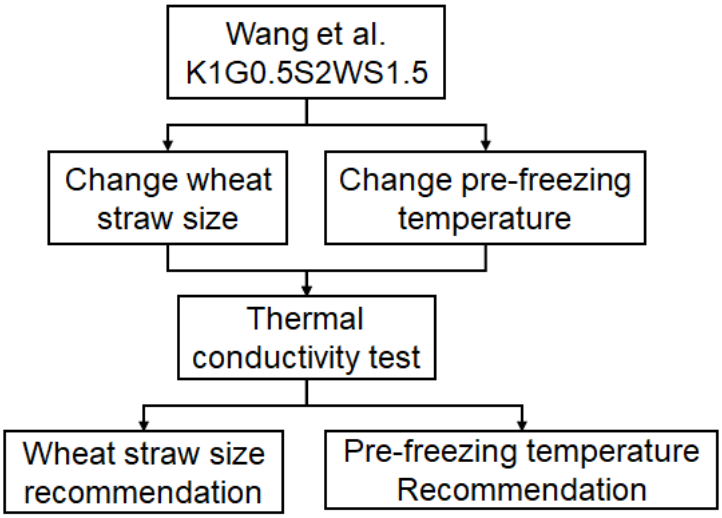


Figure 5-2. Flowchart of experiments in Chapter 5.

5.3 PREPARATION OF COMPARISON PANELS

The testing samples were selected from the common insulation materials, including cork panel (10 mm), biomass aerogel panels with wheat straw (10 mm) and PIR (polyisocyanurate) panel (10 mm). All samples have the same length and width (300mm × 300 mm). PIR panels are a

popular material for insulation applications. Due to its low thermal conductivity and excellent fire resistance properties, PIR were chosen for comparison in this section. Another traditional cork panels were also selected, which is harvested from cork forests. Cork panels are the natural choice for most construction insulation applications.

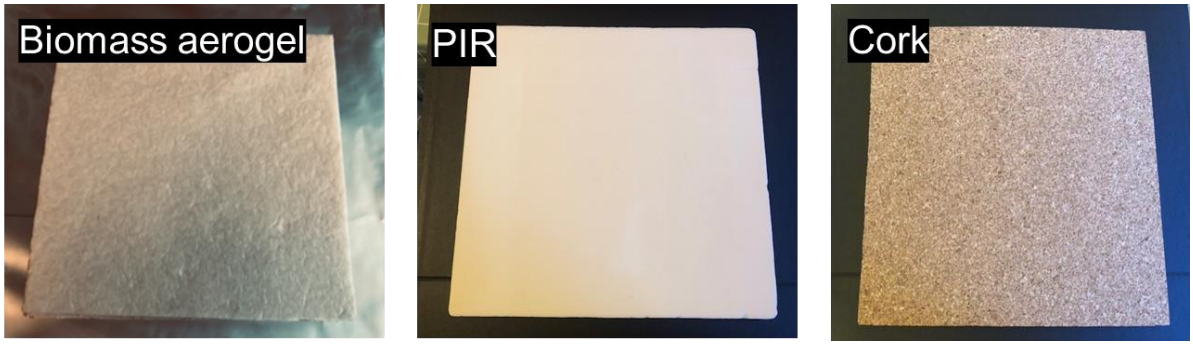


Figure 5-3. Images of testing panels.

5.4 CHARACTERIZATION OF K1S2G0.5W1.5

5.4.1 Thermal conductivity measurement

The thermal conductivity of biomass aerogels with different sizes was measured by a calibrated thermal conductivity analyzer (DRPL-2A, Xiangtan, China), comprised of sensors, temperature control systems, measurement modules and accessories. Small samples (diameter 6 cm) could be tested with this instrument. The tests were carried out with the sensor sandwiched between two biomass aerogel specimens. The specimens were surrounded by two insulating glass wool panels to prevent heat loss. After placing samples, the temperature setting for the hot plate is 50°C and for the cold side plate is 30°C. The ice water adjusts the temperature of the cold side in the holding tank. The testing equipment was put on a stable, flat table with a transparent plastic shield. All tests were performed at least in triplicate.

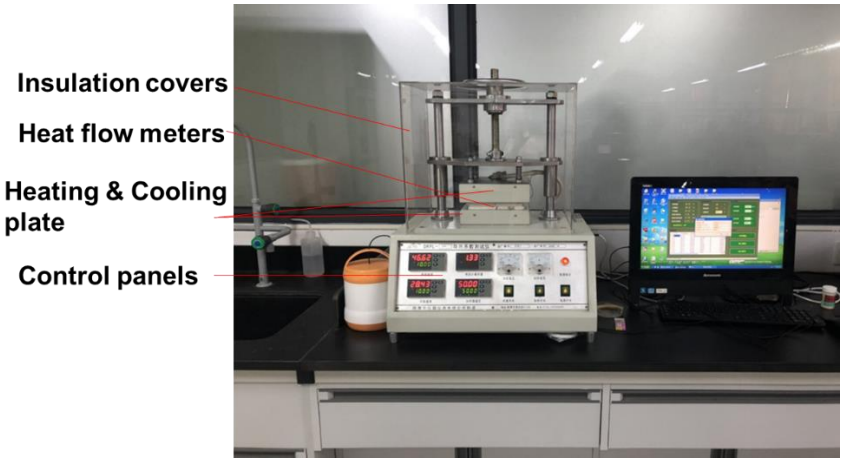


Figure 5-4. Thermal conductivity analyzer for small size specimens.

5.4.2 Microscale Combustion Calorimeter (MCC) Measurement

The flame retardancy tests were carried out with a Microscale Combustion Calorimeter (FTT0001, Fire Testing Technology Ltd., West Sussex, UK) based on the standard ASTM D7309-13. Specimens were cut by the blade into a small size of about 5 × 5 mm with a controlled mass of about 3.5 mg and placed in alumina ceramic crucibles. Specific Heat Release Rate (W/g) of different biomass aerogels can be determined with the specimens heated from 100°C to 380°C at a heating rate of 1°C/sec with a nitrogen flow rate of 80 cm^3/min and oxygen flow rate of 20 cm^3/min.

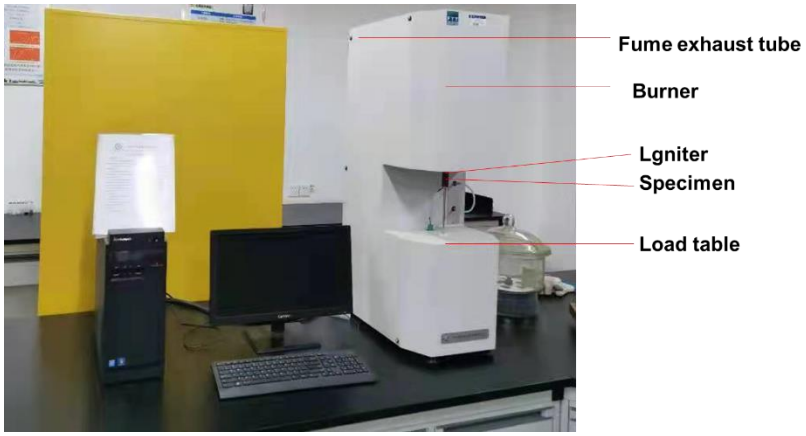


Figure 5-5. Images of Microscale Combustion Calorimeter device.

5.4.3 Thermal transmittance measurements through the hot box method

5.4.3.1 Design of the testing box

Two test boxes, which measured 300 × 300 × 300mm, were made in the winter of 2021. The thermal transmittance of different insulation panels was tested for 24 hours in this test. A box was constructed using original panels (cork panel, biomass aerogel panels and PIR panel). The inner and outer joints of insulation panels were sealed with 20 cm wide tape to prevent air leakage. As shown in Figure 5-6 (a), the front surface is covered by a 300 × 290 mm PIR board, which is also connected by aluminium tape. A 10 cm high hole is left to provide an air inlet for the small heating fan. For each panel test, the heating fan was placed at a 150 mm distance from the surface of the specimen panel, following the distance outlined in ISO 12567. As shown in Figure 5-6 (b), the original testing panel was placed on the right side and the fan was placed on the left corner. The test was carried out in two weeks when the temperature was relatively stable to control the temperature on the cool side. To ensure the inside temperature is at a stable level, there is a 100 mm-height hole reserved at the bottom of the front board.

5.4.3.2 Thermal transmittance measurements through the hot box method

Figure 5-7 shows the dimension of testing panels and the locations of constructional thermal couples and heat flux plate. Specifically, the thermal transmittance values of the tested specimens were measured using a heat flux sensor of hukesflux HP01 ($\pm$ 1.9 × 10^{-6}V/(W/m^2)), which is placed in the centre of the specimen panel's inner surface. Meanwhile, the inner surface temperature was measured with K-type thermocouples, which were placed on both sides of heat flux sensor at the same height. Before the test, all thermocouples were calibrated to ensure accuracy ($\pm$ 1.5°C). The data logger will record data every 10 minutes and each experiment will last 24 hours. On the opposite position outside, two thermocouples were installed to test the outer surface temperature of the panels. Both sides have a thermocouple to

test the environment temperature for inner and outer air. The temperature reading shall be taken at a 5 cm distance from the panels (shown in Figures 5-6 and 5-7). The exact installation position of heat flux sensor and thermocouples can be seen more clearly in the schematic diagrams, as shown in Figure 5-7 (b).

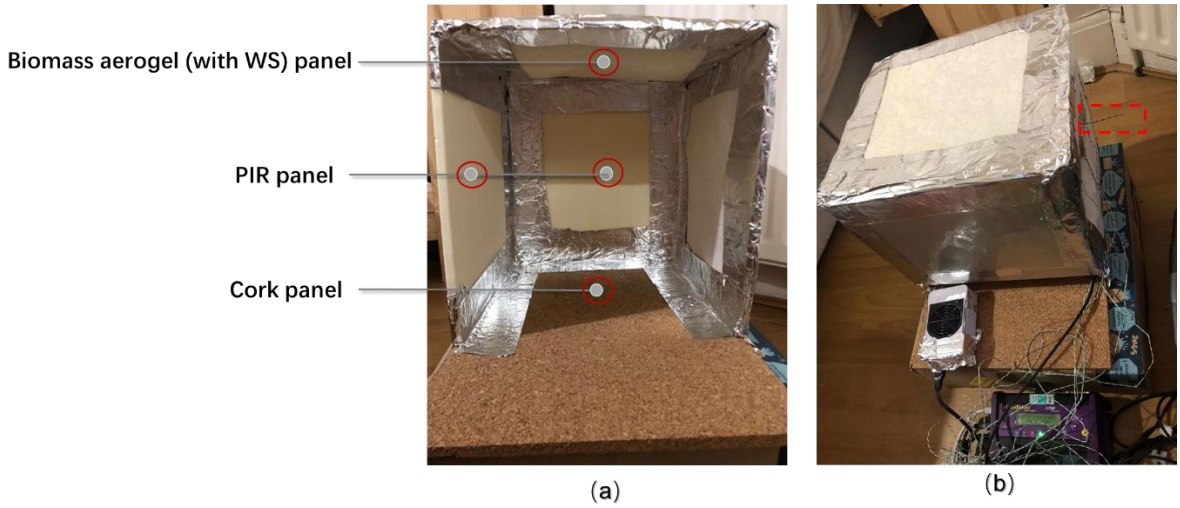


Figure 5-6. Images of the original panel box, the small heating fan and the data logger.

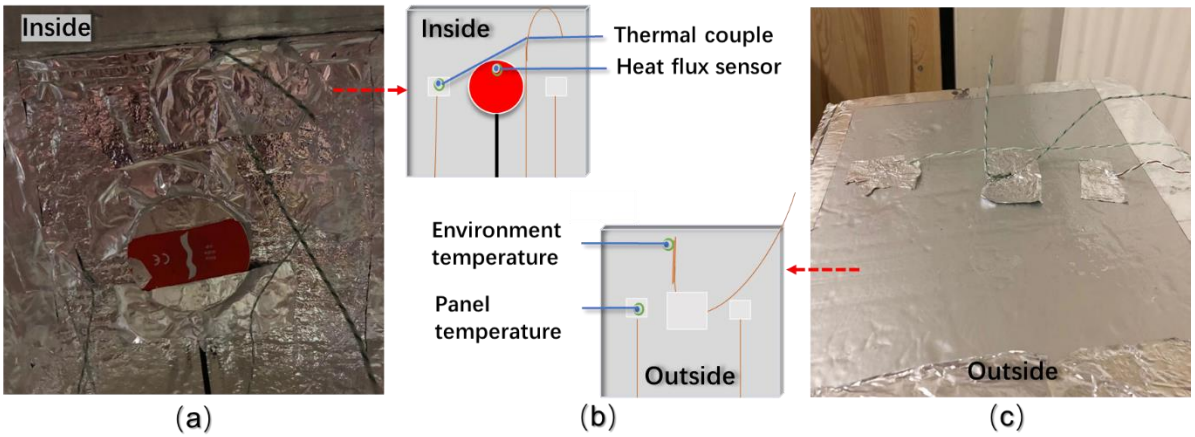


Figure 5-7. Details of installation position.

5.5 INFLUENCE OF RAW MATERIAL ON THE MORPHOLOGY

5.5.1 Impact of starch on the microstructure of KGM aerogels

The average density of KGM aerogel with starch has been investigated. The density of K1, K1S1, K1S2, K1S3 and K1S4 was 0.01313±0.00165, 0.02164±0.00284, 0.03608±0.00150, 0.04741±0.00100 and 0.05867±0.00144 $g \cdot cm^{-3}$, respectively. As the starch concentration increased from 0–4% (w/v), the average density of KGM/starch aerogels exhibited an increasing trend. SEM micrographs of KGM/starch aerogels with different starch contents are presented in Figure 5-8. KGM/starch aerogels show a homogeneous three-dimensional network structure and reveal the impact of starch concentration on the pore structure and micro-morphology of KGM aerogels. The formation of pores results from the ice crystal growth, which determines the size of pore structure. SEM results suggest that the pore size of KGM/starch aerogels was gradually decreased with starch concentration increased from 0 to 4% (w/v), which is consistent with the statistics of pore size distribution. As shown in Figure 5-9 (a, b), the pore size of all composite KGM/starch aerogels is also mainly in the range of 1-100 μm. With increased starch concentration, the number of small pore sizes gradually increased. Furthermore, the pore walls became thicker and the pore channel size decreased when starch concentrations increased. As shown in the following figures, it could be found that the addition of starch is a benefit for the formation of close pores in aerogels, which is an essential factor for thermal insulation property.

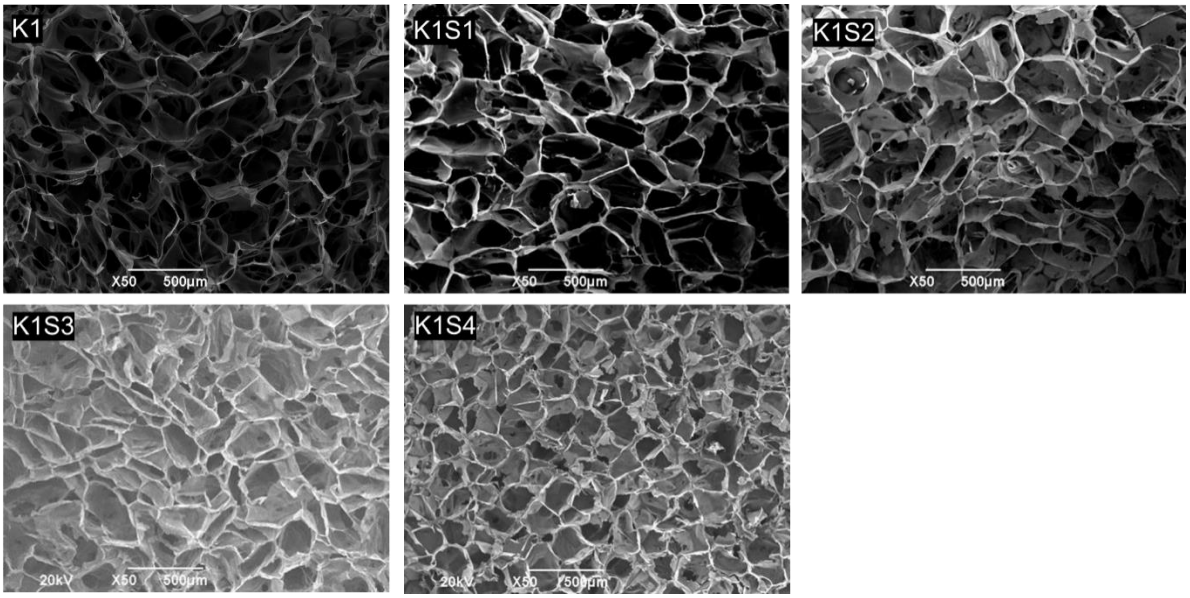


Figure 5-8. SEM observation of KGM and KGM/starch aerogels.

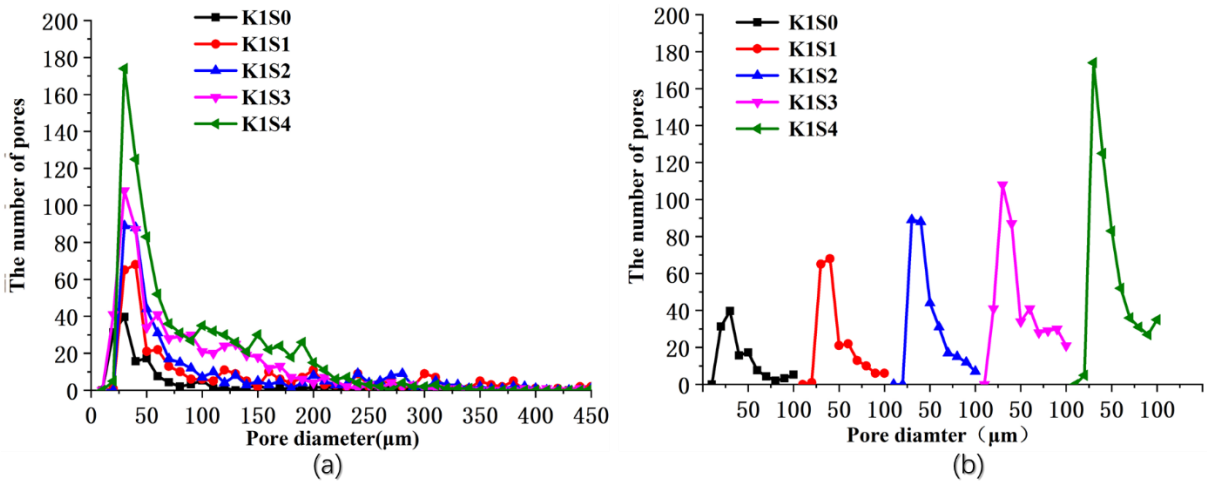


Figure 5-9. Size distribution (a: 0–450 μm; b: 0–100 μm) of KGM/starch aerogels pores with different starch concentrations.

5.5.2 Impact of gelatin on the KGM/starch/wheat straw mixtures

As introduced in Section 4.4.2, gelatin addition can prevent wheat straw from subsiding. The KGM/gelatin/starch/wheat straw biomass mixtures are shown in Figure 5-10. It could be found that there is no subsidence occurs after adding gelatin.



Figure 5-10. Digital photograph of KGM/gelatin/starch/wheat straw biomass mixtures (K1G0.5S2WS0.5, K1G0.5S2WS1, K1G0.5S2WS1.5 and K1G0.5S2WS2).

5.5.3 Impact of wheat straw on the microstructure of KGM/gelatin/starch composite aerogels

The addition of wheat straw significantly affects the pore structure and micro-morphology of final KGM/gelatin/starch composite aerogels. Compared with the biomass aerogels without wheat straw, the pore wall surface of KGM/gelatin/starch/wheat straw composite aerogels was unsmooth with some cavity structure which makes the connectivity of the porous network more complex (Figure 5-11). With the small amount of wheat straw addition, the major pores are formed by the ice crystal sublimation while the wheat straw was observed between pore cells, and there was full bonding between the wheat straw, polysaccharide and protein. When the wheat straw concentration increased, the aerogel pore shapes became irregular and the structure became denser. Similar to Section 4.4.3, this could be explained that the addition of rigid wheat straw increased the resistance of the biomass aerogels to the growth of ice crystals during the freeze drying process.

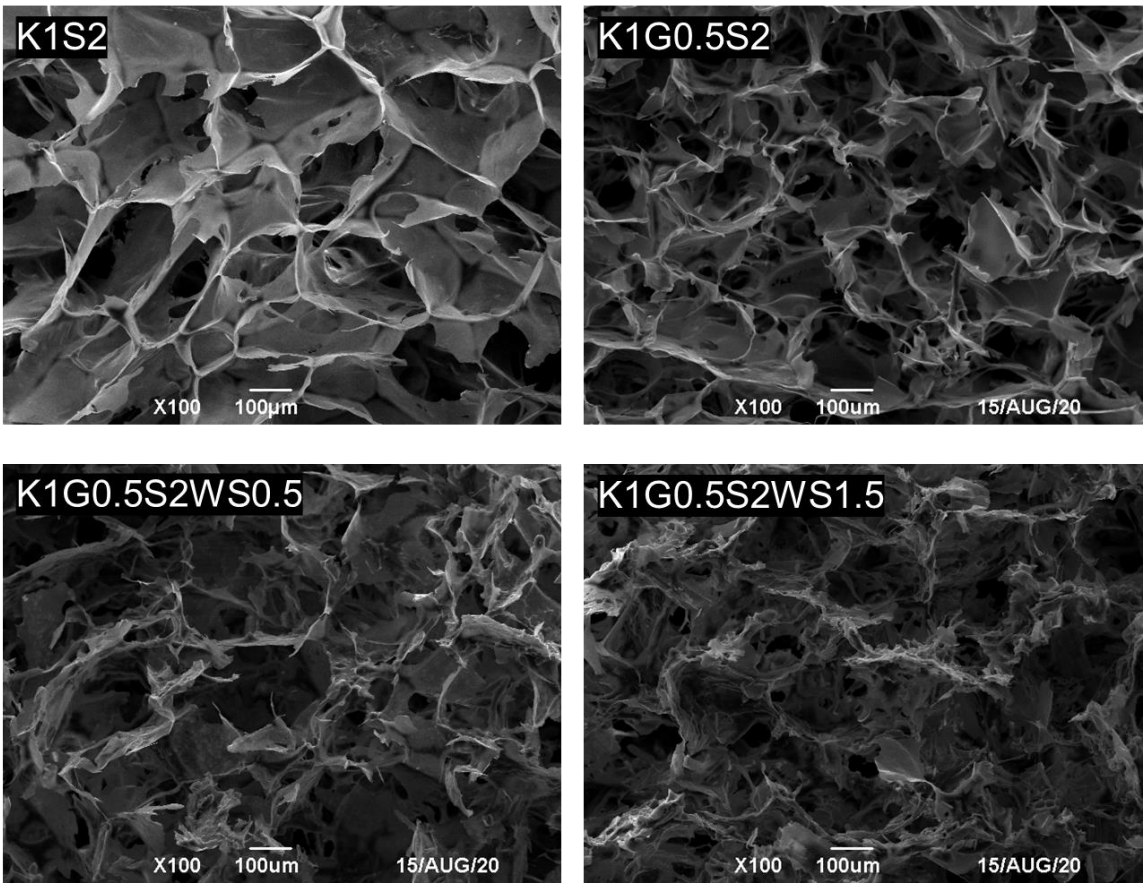


Figure 5-11. SEM observation of KGM/starch aerogel and KGM/gelatin/starch aerogel and KGM/gelatin/starch/wheat straw aerogels.

5.6 EFFECT OF WHEAT STRAW SIZE AND PRE-FREEZING TEMPERATURE ON THE THERMAL INSULATION PROPERTY OF BIOMASS AEROGELS

5.6.1 General heat transfer analysis for biomass aerogels

Thermal conductivity is the ratio of heat flow to temperature gradient. The effective total thermal conductivity (λeff) is defined as the sum of solid thermal conductivity of the solid backbone λs, the effective thermal conductivity of the gaseous phase λg, and finally, the radiative conductivity λr [236, 237]：λeff=λs+λg+λr. For biomass aerogels, In aerogels, heat is transferred mainly through solid conduction through the aerogel skeleton and gas conduction in the pores.

(1) Heat Transfer via the Solid Backbone

Heat transfer through the solid grain of composite aerogels is mainly through phonons or localized oscillations. In this study, the solid backbone of aerogels was composed of polysaccharides, protein and wheat straw whose volume heat capacity, frequency-averaged mean free path of phonons and average phonons velocity are invariable. Solid conduction correlates with density which can be changed by the concentration of raw materials, and the higher ρ, the higher solid heat conduction λs.

(2) Heat Transfer via the Gaseous Phase

Low-density porous materials can have super insulation properties due to the air confined in their pores when the pore size is below the free mean path of air molecules. To decrease the thermal conductivity of biomass aerogels, the average pore size should be decreased, especially to avoid the appearance of open pores simultaneously.

(3) Radiative Heat Transfer

The optical thickness is the main factor affecting radiative heat transfer, depending on temperature, density and effective specific extinction of the materials. For most organic aerogels, some infrared opacities are embedded into composite aerogels to decrease the λr. Since all prepared samples have the same composition and the heatwave amplitude is very small at room temperature, in this case, the radiative heat transfer could be neglected [174].

5.6.2 Impact of raw materials on thermal conductivity of biomass aerogels

In porous materials, solid conduction through aerogel skeleton and gas conduction in pores are the determining factors of effective thermal conductivity of biomass aerogels. Thermal conductivity is related to the density, pore size distribution, pore shape and pore wall of porous biomass aerogels. Based on the previous study [59], the optimized aerogel formula K1G0.5S2WS1.5 was used., and its thermal conductivity is 0.04641 $Wm^{-1} K^{-1}$. As verified in Section 4.6, the selected raw materials have a significant influence on biomass aerogels. After adding wheat straw, the biomass aerogel structure became more complicated, and the gaseous

flow path was changed to be more complicated, leading to the lower thermal conductivity. As introduced in Chapter 4, a small amount of gelatin addition is necessary to prevent wheat straw from subsiding during aerogel preparation. However, the introduction of gelatin is not conducive to improving thermal insulation performance. As can be seen in Figure 4-6, with high gelatin content, there are many open pore structures inside aerogels, and these pores are through to each other. This is due to the properties of gelatin, which is often used as the porogen in the field of tissue engineering as introduced in Section 4.4.1. Different from gelatin, starch addition contributes to the form of more micron-sized close pores, as verified by Figure 5-8. In addition, with the increase of starch concentration, the pore walls became thicker, the pore channel size decreased and the sum numbers of pores in aerogel with pore sizes 10–50 μm were gradually increased which has been verified in Section 5.6.1. This would benefit the formation of close pores in aerogels, improving thermal insulation property [238]. Based on the previous study, this research is expected to further reduce the thermal conductivity of biomass aerogels and improve thermal insulation performance.

5.6.3 Impact of wheat straw size on pore structure and thermal conductivity of K1G0.5S2WS1.5 aerogels

After a series of experiments, it was found that wheat straw length will also affect the thermal insulation performance of biomass aerogels. Based on the test results, the following conclusions were drawn. As introduced above, heat transfer in aerogels mainly occurs in two ways, aerogel solid skeleton and gas conduction. Therefore, the pore structure is a crucial factor, and the heat transfer mechanism depends on the pore structure, which is affected by wheat straw length, as shown in Figure 5-12. As wheat straw length increases, the pore structure of biomass aerogel becomes more complex and pleated pore walls appear. This significantly affects solid heat transfer that it will extend conduction paths, resulting in the reduction of thermal conductivity. As its length increases to a certain value, the wheat straw

can split the closed pore in half or more. Therefore, more irregular small size closed pore structures are formed due to the introduction of long wheat straws. Due to the special structure of wheat straw, there are many tiny porous cavities inside it, which will also provide more micropores.

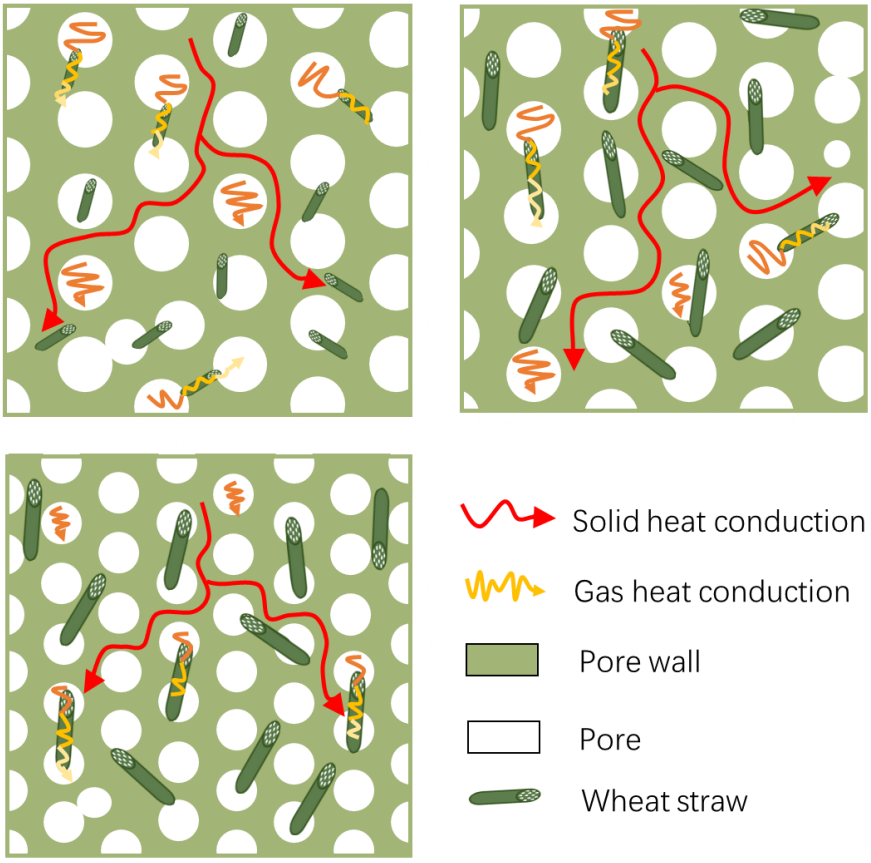


Figure 5-12. Illustration of heat transfer mechanism in biomass aerogels.

In this section, five Taylor sieves were used to separate different size wheat straw powders. Based on the previous optimal formula (lowest thermal conductivity 0.0467 $Wm^{-1}K^{-1}$), biomass aerogels (K1G0.5S2WS1.5) with different wheat straw lengths were produced. From the SEM images in Figure 5-13, it can be found that wheat straw sieved through a 400-mesh screen had a shorter length and the wheat straw cavity structure is broken. As presented in Figure 5-13 (a), wheat straw is attached to aerogel pore walls. Furthermore, the pore structure of biomass aerogel with small wheat straw is similar to those of aerogels without the addition of wheat

straw, and the pore sizes were relatively large, indicating that the addition of fine wheat straw has no significant influence on the complexity of biomass aerogel pore structure. Changes can be observed from SEM images with the gradual increase of wheat straw length. Longer-sized straws are interspersed between the closed pores. The pore structure of the biomass aerogel has also been changed significantly, becoming more complex and no longer has a flat smooth parallel surface due to the addition of long size wheat straw. SEM images presented that the size of wheat straw cavity is significantly smaller than the aerogel pores. When the aerogel was prepared using wheat straw sieved through a 60-mesh sieve, a large size of straw could be found across the aerogel, as shown in Figure 5-13 (e). The length of wheat straw is about the same or even larger than aerogel pores.

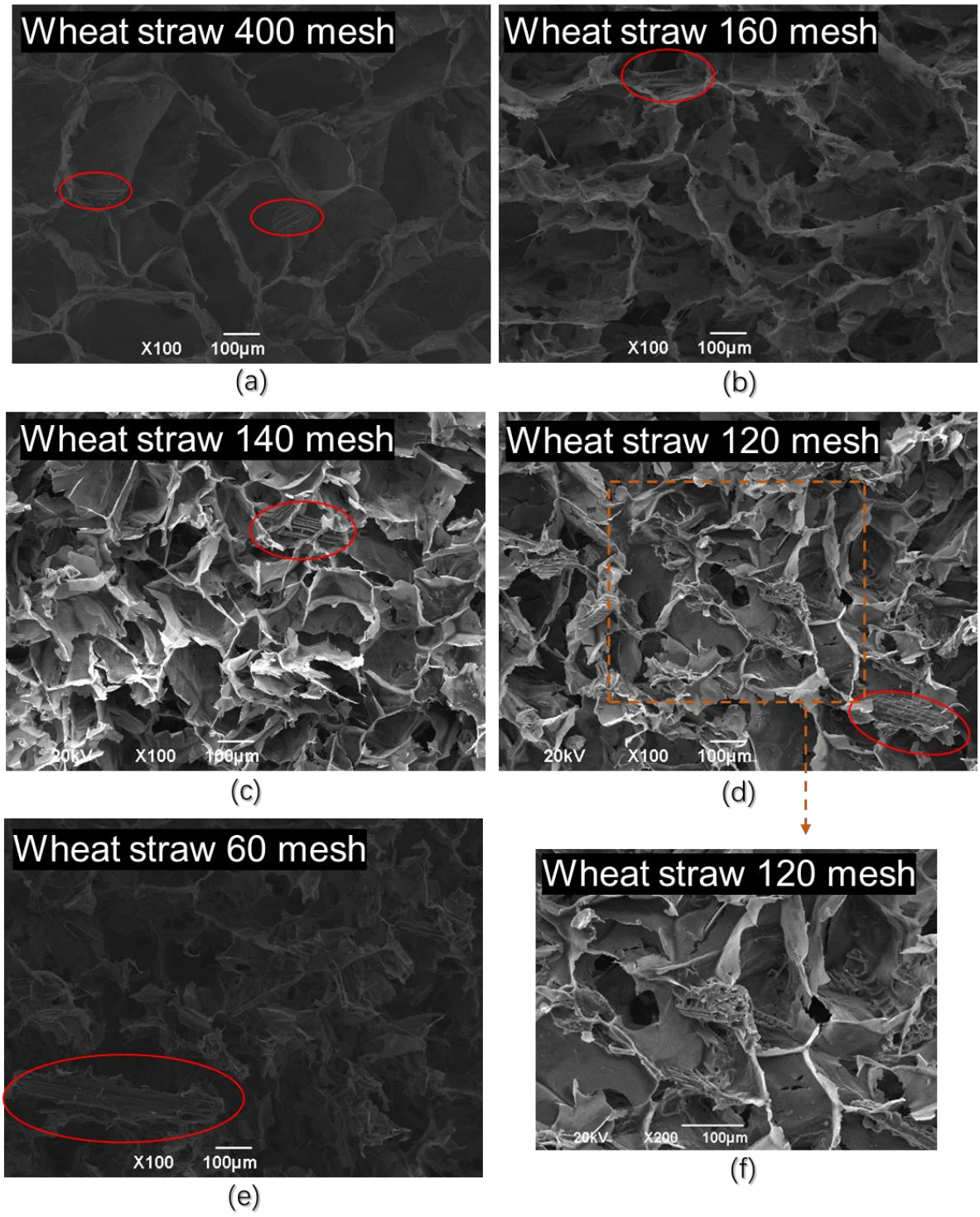


Figure 5-13. SEM observation of K1G0.5S2WS1.5 aerogel with different wheat straw sizes.

As a porous material, the pore structure of biomass aerogels plays a dominant role in controlling its properties. Especially for insulation, thermal conductivity of porous material

strongly correlates with the density and pore structure of the material. The density of biomass aerogel can be considered constant when controlling a certain amount of raw materials addition. The experimental results of thermal conductivity for K1G0.5S2WS1.5 aerogels with different wheat straw sizes are listed in Table 5-2. As expected, the K1G05S2WS1.5 aerogel using fine wheat straw (400 mesh) had the highest thermal conductivity (0.0496 $Wm^{-1}K^{-1}$). With the decrease of wheat straw length, thermal conductivity gradually decreased, but it started to increase when the aerogels added wheat straw that had been sieved through 60 mesh sieves. Combined with the analysis of SEM in the previous section, the aerogel pore size was decreased when using larger size wheat straw. These results support wheat straw length greatly influences biomass aerogel thermal conductivity. The shorter wheat straw is added, the less chance for aerogel to produce complex and tortuous structure since wheat straw porous cavities have been destroyed. Wheat straw is assembled on the polysaccharide and protein skeleton; therefore, the appropriate size of wheat straw will contribute to the interface heat transfer inhibition, thereby the reduction in gas-phase heat conduction. From Table 5-2, it can be concluded that for formulation K1G0.5S2WS1.5, the biomass aerogel prepared with the wheat straw sieved by a 120 mesh sieve has a relatively lower thermal conductivity.

Table 5-2 Thermal conductivity of K1G0.5S2WS1.5 aerogels made from different sizes of wheat straw.

Sample code (K1G0.5S2WS1.5)	Thermal conductivity ($Wm^{-1}K^{-1}$)
Wheat straw sieved from 60 mesh	0.0517±0.0004163332
Wheat straw sieved from 120 mesh	0.0420±0.0010148892
Wheat straw sieved from 140 mesh	0.0435±0.0011952820
Wheat straw sieved from 160 mesh	0.0462±0.0020881890
Wheat straw sieved from 400 mesh	0.0496±0.0012897030

5.6.4 Impact of pre-freezing temperature on pore structure and thermal conductivity of K1G0.5S2WS1.5 aerogels

There are a large number of hydroxyl groups in the polysaccharide and protein. The hydrogen bonding between water molecules in the hydrogel and the van der waals forces limited the thermal movement of water molecules, and at the same time, under the action of low temperature and hydrogen bonding, water molecules start to aggregate and form clusters. Ice nuclei start to form when the temperature is further reduced, and then ice crystals start to grow. The solute is pushed outward by the ice crystals and surrounds the ice crystals until completely frozen. In this process, pre-freeze temperature plays a vital role in nucleation, ice crystal growth rate, and finally, it significantly affects the final microstructure of biomass aerogels. In this section, different pre-freezing temperature (-15, -25, -30, -40°C) was employed to prepare K1G0.5S2WS1.5 composite aerogels. The disorderly arrangement of wheat straw under different pre-freeze temperatures makes the biomass aerogel structure disrupted and complicated. When using ultra-low temperature (-40°C), it was found during the experiments that microcracks were prone to appear in the pre-freezing process, as shown in Figure 5-14. After analysis, the main reason for crack generation was thermal stress during the freezing phase transition. The mixed system contains a large amount of water; when the temperature reaches zero degrees, it will turn into ice, and the volume will expand. Furthermore, the gel was cooled from outer to inside. Therefore, the edge of specimens froze first. After a short cooling period, the internal begins to freeze, but the outer ice limits the further volume expansion so that the internal stress will be generated. The greater temperature difference inside and outside specimen will produce larger thermal stress. In addition, wheat straw will contribute to the uneven internal stress distribution, further increasing the chance of cracking formation. These are the reasons for the appearance of cracks during pre-freezing process.

After selection, the homogeneous part without cracks was cut for SEM observation. SEM images are shown in Figure 5-14 (f), indicating that the pore size of biomass aerogel gradually decreased as the pre-freezing temperature reduced. With -40°C pre-freezing temperature, very fine dendritic pore structures appeared in aerogels. This may be explained that when the pre-freezing temperature is continuously reduced, the subcooling degree leads to more opportunities for nucleation and the continuous growth of ice crystals. In addition, at lower pre-freezing temperature, the nucleation rate exceeds the growth rate of ice crystals, so many small ice crystals are formed rapidly. Conversely, when the pre-freezing temperature is relatively high, the growth rate of ice crystals will be higher than the nucleation rate, and larger ice crystals will be formed.

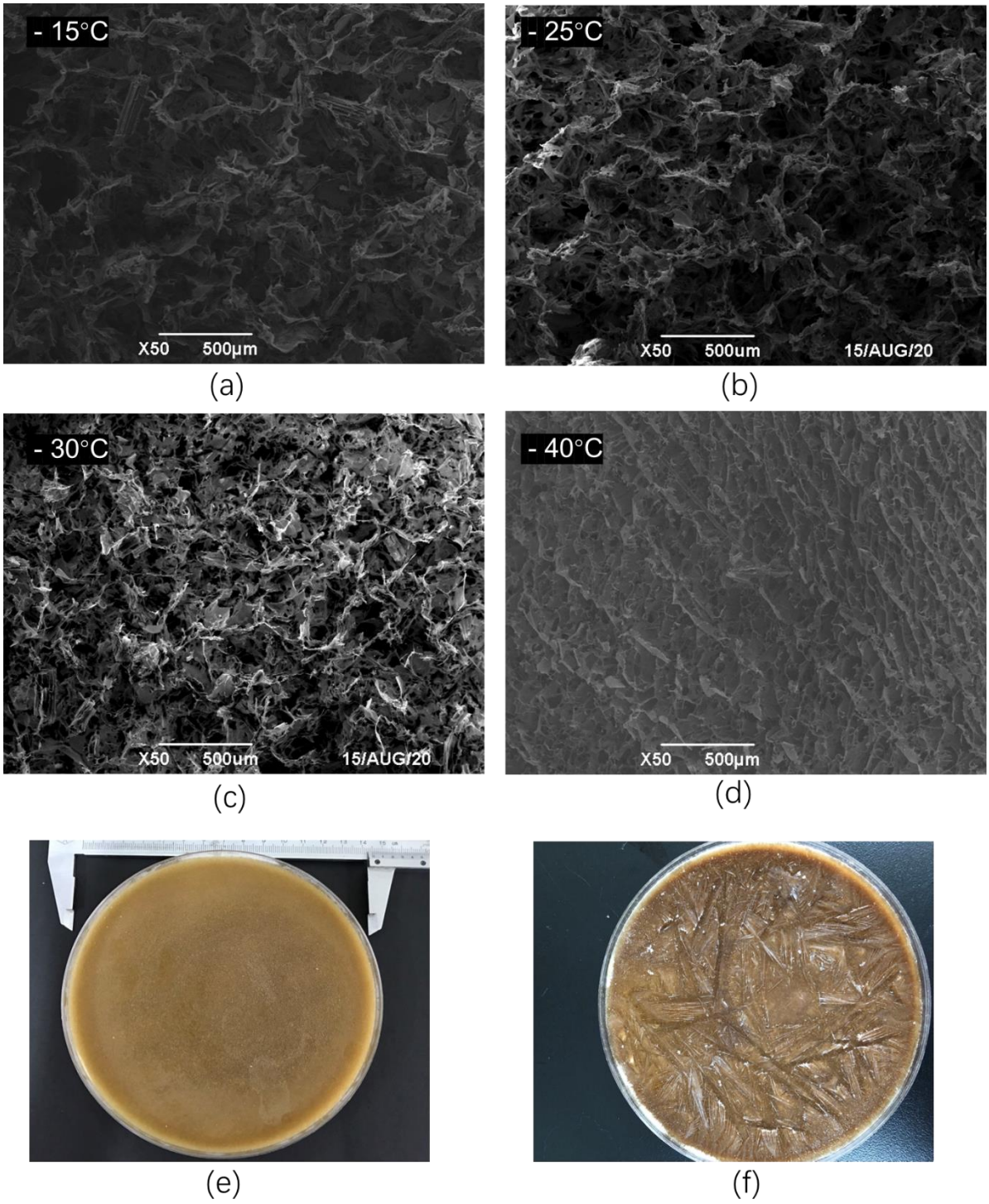


Figure 5-14. Microstructure of K1G0.5S2WS1.5 aerogels formed under different pre-freezing temperature: (-15, -25, -30, -40°C) and image of frozen sample K1G0.5S2WS1.5.

The thermal conductivity of K1G0.5S2WS1.5 aerogels formed under different pre-freezing temperatures has been tested, and the results are shown in Table 5-3. With the pre-freezing

temperature of -25°C and -30°C, the thermal conductivity of K1G0.5S2WS1.5 aerogels was recorded as 0.0420 $Wm^{-1}K^{-1}$ and 0.03755 $Wm^{-1}K^{-1}$, respectively. The thermal conductivity of aerogels with -15°C pre-freezing is the highest because the pore size of aerogels is largest at relatively high freezing temperatures.

Table 5-3 Thermal conductivity of K1G0.5S2WS1.5 (wheat straw sieved from 120 mesh) aerogels made under different pre-freezing temperatures: (-15, -25, -30, -40°C).

Sample code (K1G0.5S2WS1.5)	Thermal conductivity ($Wm^{-1}K^{-1}$)
Pre-freezing temperature (-15°C)	0.0478±0.001010885
Pre-freezing temperature (-25°C)	0.0420±0.0010148892
Pre-freezing temperature (-30°C)	0.0375±0.00170400
Pre-freezing temperature (-40°C)	0.0327±0.00078103

5.7 THERMAL PROPERTY OF K1G0.5S2WS1.5 AEROGELS

5.7.1 Thermal transmittance and thermal insulation test through the real small box

A small box with different insulation panels is made to investigate the thermal insulation properties of biomass aerogels in real situations and high temperature environments. After reaching the steady state, data was collected for around 24 h. Figure 5-15 shows the inner/outer air temperature, panel inner/outer surface temperature and the U value of different insulation panels. The ambient temperature in the box was controlled at around 70°C. To carry out the testing, the small box was installed and tested in February 2021. The room temperature was around 15°C, and no room heater was working to affect the indoor ambient temperature. It can be found from Figure 5-15 that the panel surface temperature and the ambient temperature have a similar change trend when the environmental temperature changes. The U values have been calculated, and the average U values are also shown in the figures. The cork panel shows the

highest U value of 6.39 $Wm^{-2}K^{-1}$, which was the worst thermal insulation performance, followed by the PIR panel with the U value of 3.65 $Wm^{-2}K^{-1}$. It can be comprehended from Figure 5-15 that the biomass aerogel has better thermal insulation performance when compared with cork and PIR panels. The U value of biomass aerogel with wheat straw is 3.20 $Wm^{-2}K^{-1}$. This test reveals that biomass aerogels can be introduced as environmentally promising alternatives for insulation materials.

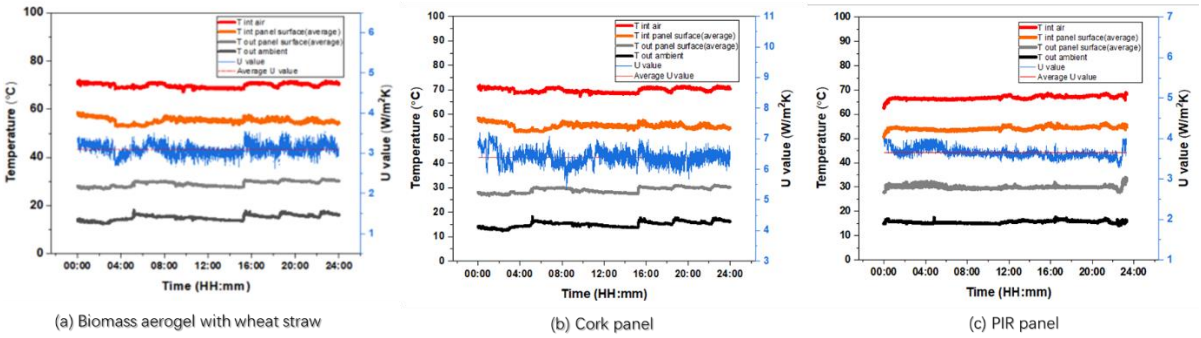


Figure 5-15. Experimental results for the normal panel surface temperature, environmental temperature and U value in a small box.

5.7.2 TG test results

Figure 5-16 presents TG curves of starch and K1G0.5S2WS1.5. It showed that the initial decomposition temperature of starch aerogel is around 301°C, and the second stage weight loss is 75.69% when the temperature increases to 600°C. As described in section 4.9, the initial decomposition temperature of KGM and gelatin is lower than that of starch. As for K1G0.5S2WS1.5 aerogel, it has a lower initial decomposition temperature than starch but higher than KGM. The red curves are the derivative thermogravimetric (DTG) of the biomass aerogels. The fastest weight loss rate of starch aerogel is achieved at a temperature of 311.78°C. Compared with starch aerogel, the derivative thermogravimetric peak of K1G0.5S2WS1.5 shifts to a higher temperature (320.63°C) due to the addition of wheat straw (DTG peak:

360.15°C). These suggest that its thermal stability is between the properties of four pure components.

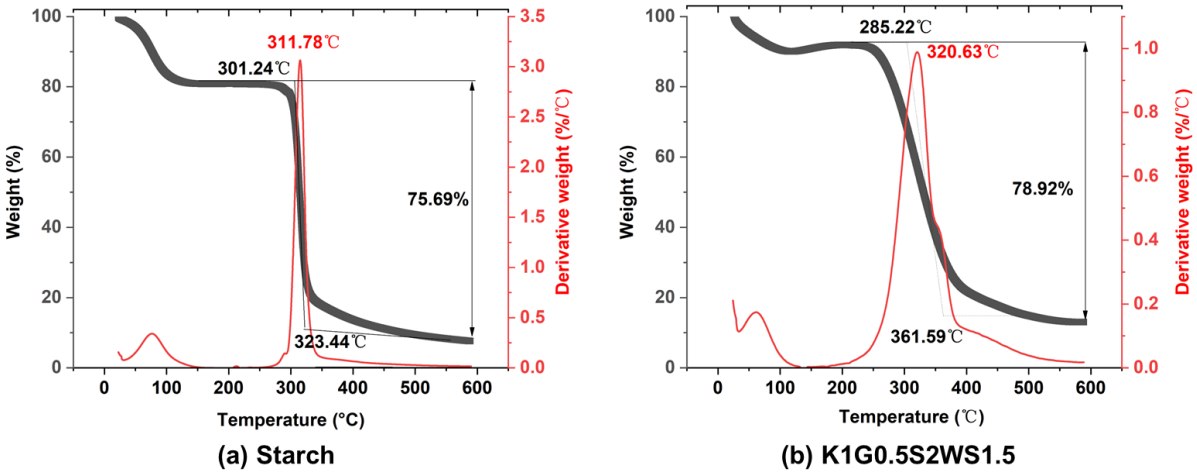


Figure 5-16. TGA of starch and K1G0.5S2WS1.5 aerogel.

5.7.3 Heat release behaviour of K1G0.5S2WS1.5 aerogels

MCC is adopted to investigate the combustion behaviour of biomass aerogels using two important fire-related parameters, including heat release rate (HRR) and total heat release (THR). The detailed results are displayed in Figure 5-17. Biomass aerogels have similar initial combustion behaviours, such as the HRR values starting to increase sharply at 200 s and reaching a peak at 250 s. Furthermore, the PHRR (300.31W/g) value of starch is the highest and is even about twice that of the other biomass aerogels, which is in accordance with TGA results. The peak heat release rate (PHRR) values for gelatin (175.22 W/g) and KGM (125.97 W/g) are close, while wheat straw has the lowest PHRR (96.75 W/g). In addition, the combustion properties of composite aerogels have been studied, where it can be found that the heat release behaviour of composite aerogels depends on the compositions and contents. After the inclusion of KGM, the HRR value of K1S2 has been reduced significantly. With the addition of wheat straw, heat release is further suppressed. By adding 1.5 wt% wheat straw, the PHRR value of K1G0.5S2WS1.5 (103.03 W/g) is similar to that of wheat straw, which is much

lower than starch, gelatin and KGM. The THR is also an important indicator, which is the total heat released per unit of materials from the beginning to the end of combustion. Generally, the higher the total heat release value, the more heat is released during combustion, which means that the more difficult to control the spread of flame when material burns and the more smoke is released to pollute the environment [239]. The THR values of starch, gelatin, KGM and wheat straw are 20.98,16.38,11.30 and 9.28 kJ/g, respectively. The trends in THR values for composite aerogels are similar to the HRR data. In previous research carried out by Kuang et al. [240], the flammability of EPS and PU foams was tested using the MCC. As the contrastive samples, these two foams displayed a relatively high peak heat release rate (PHRR) and THR compared to biomass aerogels (as shown in Figure 5-18). For PU, the PHRR and TRH values were 226.4 W/g and 24.3 kJ/g, indicating a high fire hazard.

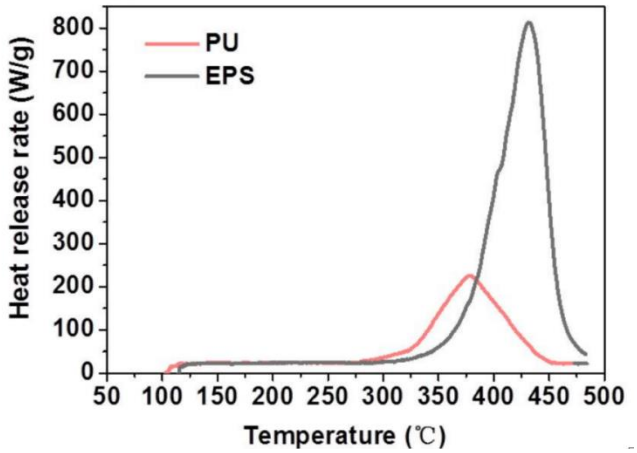


Figure 5-17. Heat release rate (HRR) curves of PU and EPS [241].

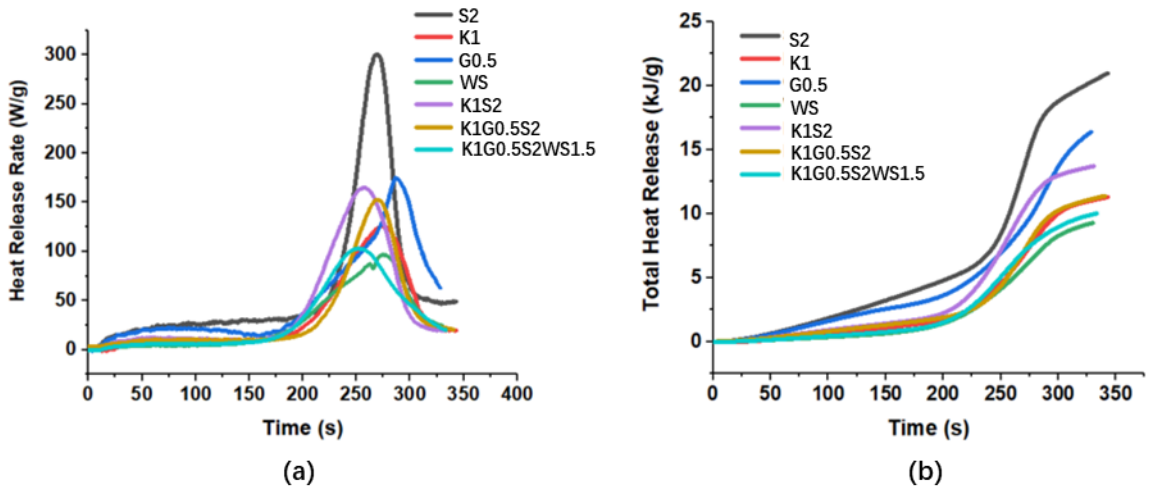


Figure 5-18. (a) Heat release rate (HRR) curves and (b) total heat release (THR) curves of the biomass aerogels.

5.8 CONCLUSION

This chapter demonstrates KGM/gelatin/starch/wheat straw aerogels with good thermal insulation properties. The pore structure, thermal insulation property and thermal properties of biomass aerogels are studied. The main conclusions can be drawn as follows:

(1) Adding starch contributes to many small pores, the thicker pore walls and more close pore formation. As introduced in the last chapter, the pore structure becomes complicated with the introduction of wheat straw.

(2) The impact of wheat straw length and pre-freeze temperature on the thermal insulation property of biomass aerogels has been investigated. When controlling the same density, the K1G05S2WS1.5 aerogel using wheat straw (120 mesh) had the lowest thermal conductivity (0.0420 $Wm^{-1}K^{-1}$), while the thermal conductivity of K1G05S2WS1.5 with 60 and 400 mesh wheat straw is 0.0517 and 0.0496 $Wm^{-1}K^{-1}$, respectively. The pre-freeze temperature is another crucial factor that affects biomass aerogel pore structure and thermal insulation property. With the pre-freezing temperature of -15°C, -25°C, -30°C and -40°C, the thermal

conductivity of K1G0.5S2WS1.5 aerogels was recorded as 0.0478, 0.0420, 0.0375 and 0.0327 $Wm^{-1}K^{-1}$, respectively.

(3) A small box was built to test the thermal insulation property of biomass aerogels in the real state, and it has been compared with the commercial PIR, cork panels. Biomass aerogel shows promising thermal insulation performance.

(4) The thermal decomposition property of biomass aerogels is similar to the raw materials. A relatively good level of thermal stability is maintained in the composite aerogels. The heat release behaviour of biomass aerogel has been studied, and results show it had good flame retardant properties.

6 EXPERIMENTAL INVESTIGATION ON THE EFFICIENT REMOVAL OF PARTICULATE MATTER WITH BIOMASS AEROGELS

6.1 INTRODUCTION

Recently, air pollution has been one of the main environmental problems in the world and is among the critical challenges facing modern societies. For particle matters filtration, both open and close pores are needed in the aerogels. The particles can enter aerogels through open pores in the surface and they will be intercepted by close pores in aerogels. Therefore, glelatin, starch and wheat straw were selected to prepare biomass aerogels. Different from Chapter 5, the gelatin concentration should be increased to produce more interconnecting structures. In the previous research, the best filtration formula (K1G2S4WS2) was determined through the test results [242]. Although the previous research investigated the impact of different components (KGM, gelatin, starch, and wheat straw) and concentrations on the filtration efficiency, the testing method has a limitation that the long-time filtration performance is not able to be reflected. In this Chapter, the K1G2S4WS2 aerogels with pore size distribution (total solid concentration from 50% to 90% of origin formula K1G2S4WS2) was selected to investigate the air filtration properties of biomass aerogels with different pore size distribution over a long period via tests in a transparent chamber and verification in an actual room with a burning smudge stick as the particle source. The microstructure observation is used to assist in verifying the filtration effect. The PM removal ability of biomass aerogels will be compared with other common commercial filtration materials, including HEPA, surgical masks, regular cloth and silica aerogel. Furthermore, the filtration performance of the biomass aerogels will be verified with an actual room test. The current work demonstrates the high potential of biomass aerogels for infiltration application in different fields and provides an avenue to reuse agricultural by-products.

6.2 BRIEF SUMMARY OF KGM/GELATIN/STARCH/WHEAT STRAW AEROGEL PREPARATION

6.2.1 Materials

In this chapter, KGM, gelatin, starch and wheat straw were selected to produce PM filtration biomass aerogels. The reason for the selection of these four raw materials has been described in Section 1.7.2. Large amount of starch and gelatin are added in this Chapter because they contribute to the formation of both micron-sized close and open pores, which is necessary in filtration. The detailed formula is shown in Table 6-1.

Table 6-1 The formula of the samples and their raw materials.

Sample Code	KGM	Gelatin	Starch	Wheat straw
		(g/100 mL)		
K0.5G1S2WS1	0.5	1	2	1
K0.7G1.4S2.8WS1.4	0.7	1.4	2.8	1.4
K0.9G1.8S3.6WS1.8	0.9	1.8	3.6	1.8

6.2.2 Preparation of KGM/gelatin/starch/wheat straw aerogel

The KGM/gelatin/starch/wheat straw aerogels preparation method is the same as Section 1.7.3 (6) and 1.7.4.

6.2.3 Flowchart of experiments in Chapter 6

The flowchart for experimental investigation of biomass aerogels for PM filtration is shown in Figure 6-1. Following the aerogel formula K1G2S4WS2 determined by previous research [242], total solid concentration from 50% to 90% of origin formula K1G2S4WS2) was selected to study the effect of pore size on the PM filtration performance. In this research, the filtration tests with PM2.5 and PM10 were carried out in both the chamber and the real room for more convincing results. Other materials including HEPA, surgical mask, cloth, and silica aerogel

were also tested for comparison to evaluate the PM filtration performance of the biomass aerogels.

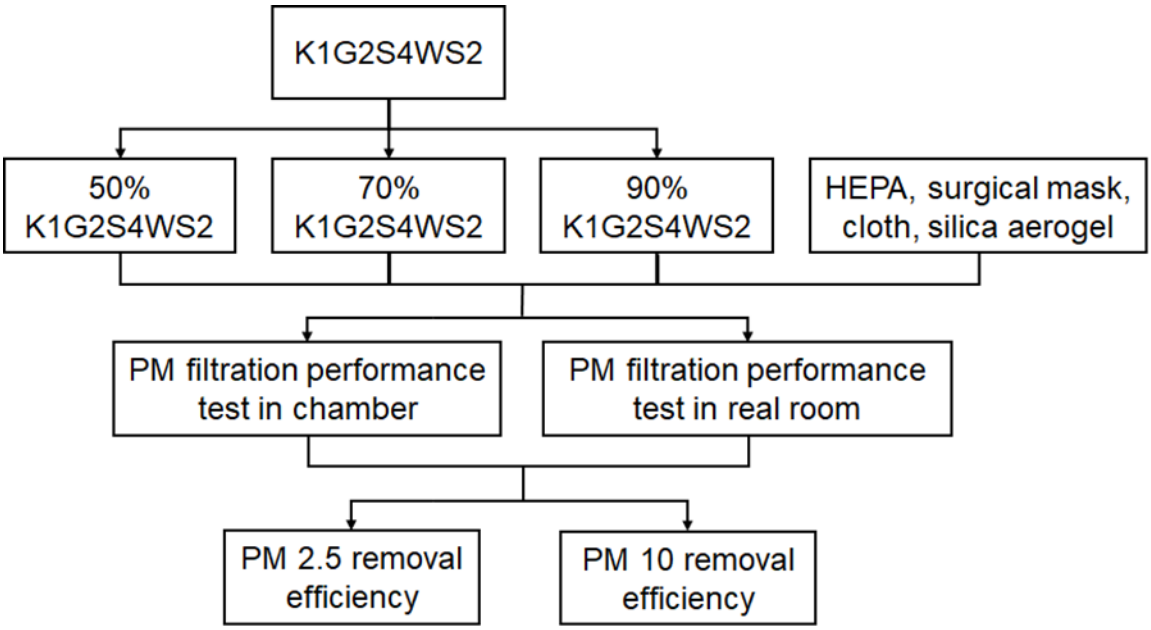


Figure 6-1. Flowchart of experiments in Chapter 6.

6.3 CHARACTERIZATION OF BIOMASS AEROGELS

6.3.1 Microstructure observation with a digital microscope

For the internal structure observation, the lab-scale KERN OBL 135C825 digital compound microscope with the adapted camera (ODC 825) has been used to observe the materials and take photos (as shown in Figure 6-2). All samples were cut into a small strip of 4 cm × 2 cm. The eyepiece lens magnification is 10 ×/⌀20 mm. The observation of different materials was carried out at the objective magnifications of 4 × and 10 ×.

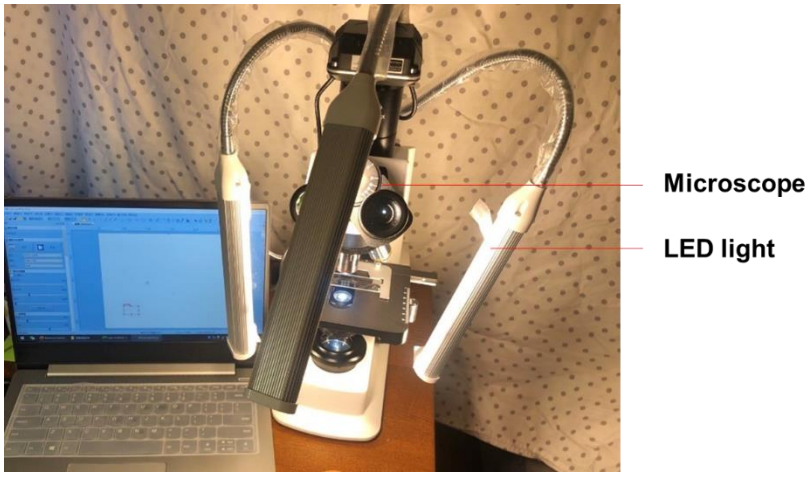


Figure 6-2. Image of a digital compound microscope.

6.3.2 PM generation and filtration measurements

A burning smudge stick was used as the source of PM particles to quantify the efficiency of PM filtration. With a continuous supply, different sizes of particles will be produced for the test. The filtration efficiency of PM is measured using the apparatus shown in Figure 6-3. All the tests were implemented in a transparent chamber. On one side, an access door was set for changing samples. A small fan was placed on the left of the chamber and next to the burning smudge stick to provide a steady smog source. Samples were cut as a disc with a diameter of 73 mm and used as the core of the air purifier (B-D01, Acekool Portable Air Purifier). All samples were inserted into the plastic ring groove, as shown in Figure 6-4. After passing through the purifier, most of the PM 2.5 and PM 10 particles were intercepted by filter materials, and the remaining particles with different sizes were captured and measured by a PM detector (LKC-1000S+, TEMTOP multifunctional air quality meter). This device has been calibrated uniformly from the factory in order to maintain its stability. To ensure the accuracy of the detector, it has been laced in a ventilated environment for at least 6 hours before used for the first time. The PM 2.5 and PM 10 mass concentrations were recorded by the detector. In addition, there are some limitations of equipment existing in this experiment, including the limitation of the maximum PM concentrations. All the filtration tests were repeated with 3

samples. As the PM removal curves were obtained from continuous tests, only one representative curve for each sample is presented, which is the intermediate one among results of three repeated tests. Before each test, the experimental cabin was fully ventilated. Both PM 2.5 and PM 10 removal efficiency of filter materials were calculated according to Yan et al. (2019) as below (Eq.6-1):

$$\text{Removal efficiency} = 1 - C2/C1 \times 100\% \quad (6\text{-}1)$$

where C1 represents the PM mass concentration before the start of air purifier and C2 represents the PM mass concentration after the start of air purifier.

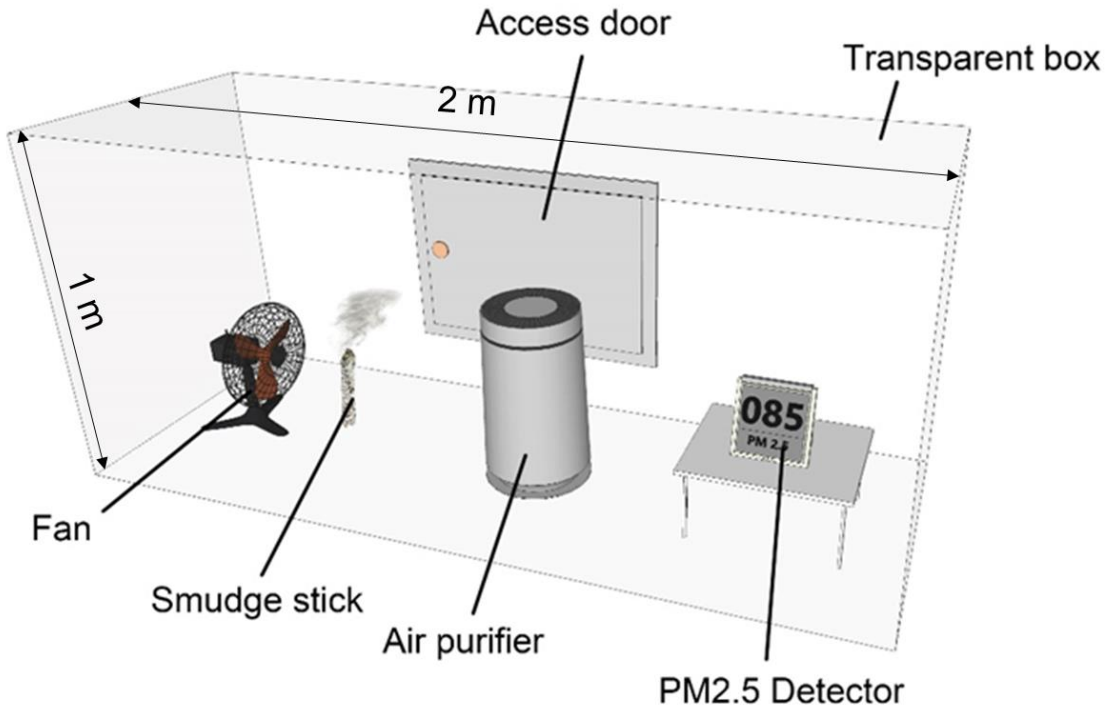


Figure 6-3. Schematic illustration of lab-built PM adsorption test system.

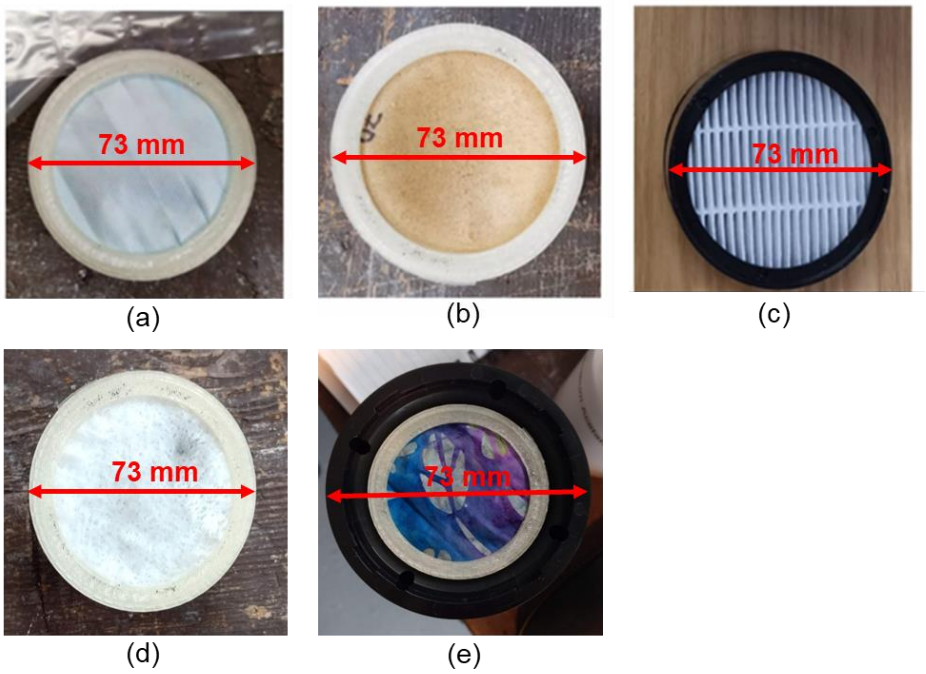


Figure 6-4. Images of all filter samples (a) surgical mask; (b) biomass aerogel; (c) HEPA; (d) silica aerogel and (e) cotton cloth.

6.3.3 Real room filtration tests

To further evaluate the PM filtration efficiency in practical applications, actual room filtration tests have been carried out in a small room, as shown in Figure 6-5. During the filtration test, the door and window in this room were closed to maintain the same test condition. After each test, the window and door will be opened to ventilate for the next test. Two smudge sticks and an air purifier (2415112EU, Leitz TruSens Z-1000 Air Purifier) with different filtration materials were placed on the table at the room corner. In this test, the entire process has been recorded, which could be divided into three stages: 1) the beginning stage of the smudge stick burning; 2) the stage when PM particles in the room reached the maximum; 3) the final stage after turning on the air purifier. Because of the similar properties to PMs, the burning smudge sticks were used to produce a large amount of smoke, which is representative of PM particles in this test. The Air purifier was placed next to the smudge stick to purify the air in the room. A PM detector was used to evaluate the gaseous pollutant removal performance of different

filtration materials. The removal efficiency of filters in the actual room was also calculated based on Eq. (6-1). Compared with the small transparent chamber filtration test, this real room experiment could represent practical air environment changes indoors.



Figure 6-5. Photos of the actual room experiment setup.

6.4 MICROSTRUCTURE CHARACTERIZATION OF DIFFERENT FILTERS

As introduced in chapter 5, the microstructure of KGM/gelatin/starch/wheat straw aerogels is a three-dimensional porous structure, as shown in Figure 6-6 (a). With the addition of wheat straw, biomass aerogels showed a greenish-brown appearance before the test. It could be observed that the wheat straw is randomly arranged in the pores of biomass aerogels. From Figure 6-7, it could be found that the pore sizes of biomass aerogels with three different solid concentrations (K0.5G1S2WS1, K0.7G1.4S2.8WS1.4 and K0.9G1.8S3.6WS1.8) are different. The pore size of biomass aerogels began to increase with the increase of total solid concentration significantly. The multi-cavities structure of wheat straw could be observed,

which contributes to the increase of tiny holes in the biomass aerogels and makes the biomass aerogel pore structure more complicated.

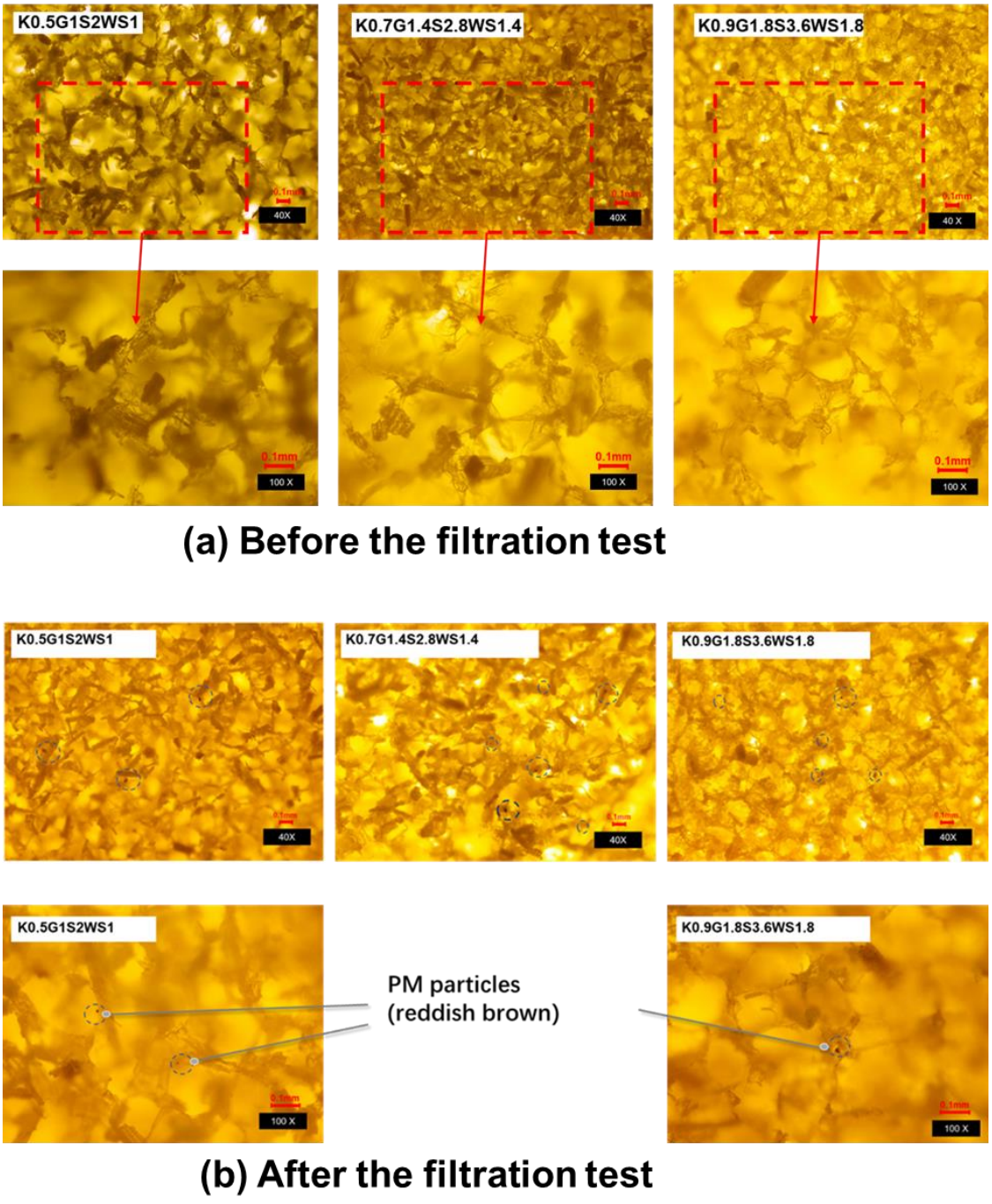


Figure 6-6 Micro-images of biomass aerogels before the filtration test (a) and after the filtration test (b).

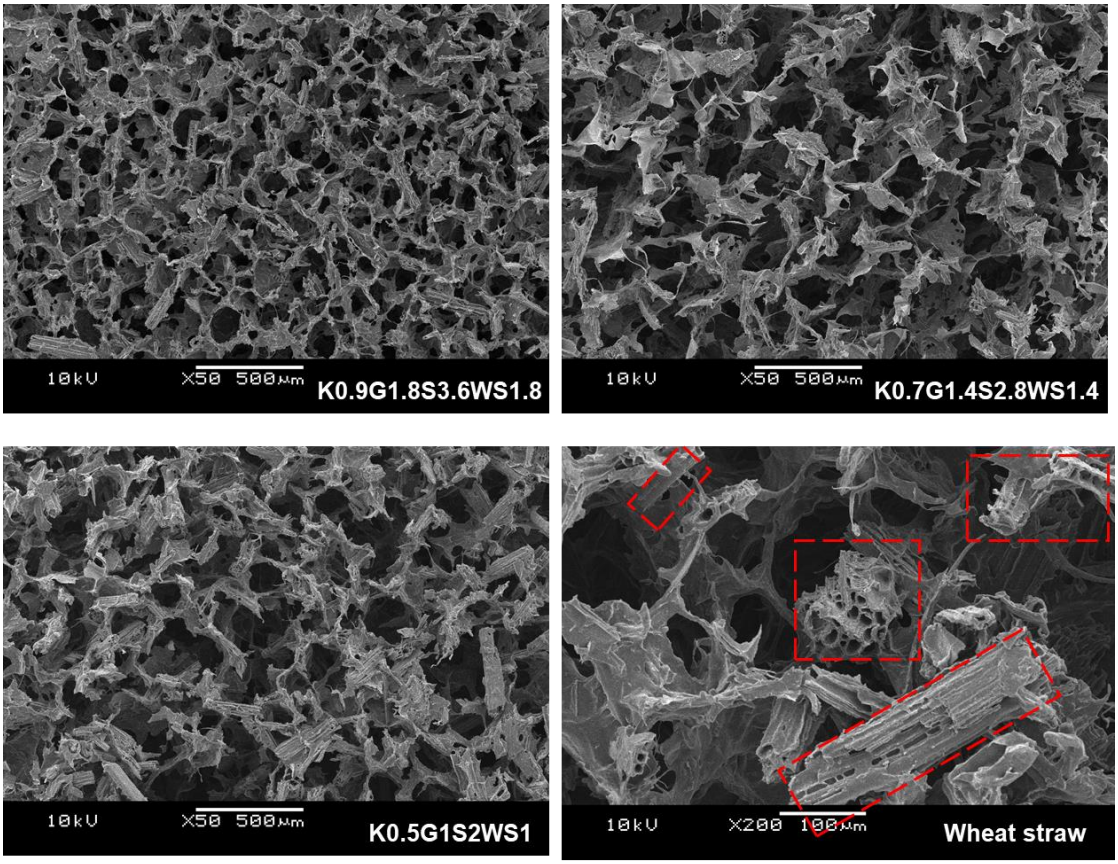


Figure 6-7. SEM-images of biomass aerogels before the filtration test.

After the filtration test, the colour of the biomass aerogels has been changed significantly, and it was stained red-brown by smoke. Due to the small size of particles, they cannot be fully observed. However, as illustrated in Figure 6-6 (b), the microscope can observe the intercepted large PM particles. In Figure 6-6 (b), the particle sizes were measured using Image-Pro Plus 6.0, and the diameters of particles range from 7.1 to 62.8 μm.

The same test has also been carried out with the melt-blown and non-woven fabrics; both are thin layers with a two-dimensional structure. As shown in Figure 6-8, the structure of the melt-blown cloth is dense, and few holes can be observed. However, too many open spaces in the fibers of non-woven fabric can allow particles to pass through. PM particles could be observed in these two fabrics, but the particles on the non-woven fabrics are relatively less than in melt-blown fabrics and biomass aerogels. The SEM images of different filters are presented in

Figure 6-9. As demonstrated, the pore size of non-woven fabric and silica aerogel is larger than that of melt-blown fabric, regular cloth and biomass aerogel K0.9G1.8S3.6WS1.8.

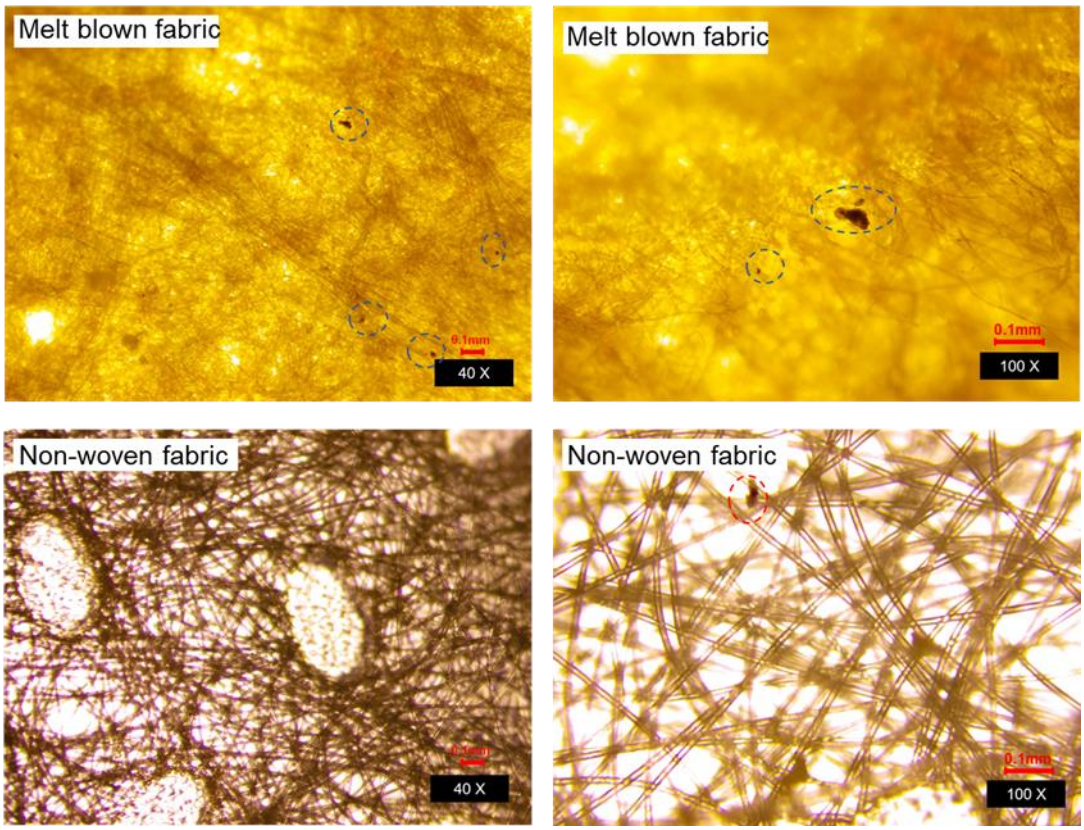


Figure 6-8. Micro-image of melt-blown fabric and non-woven fabric after the filtration test.

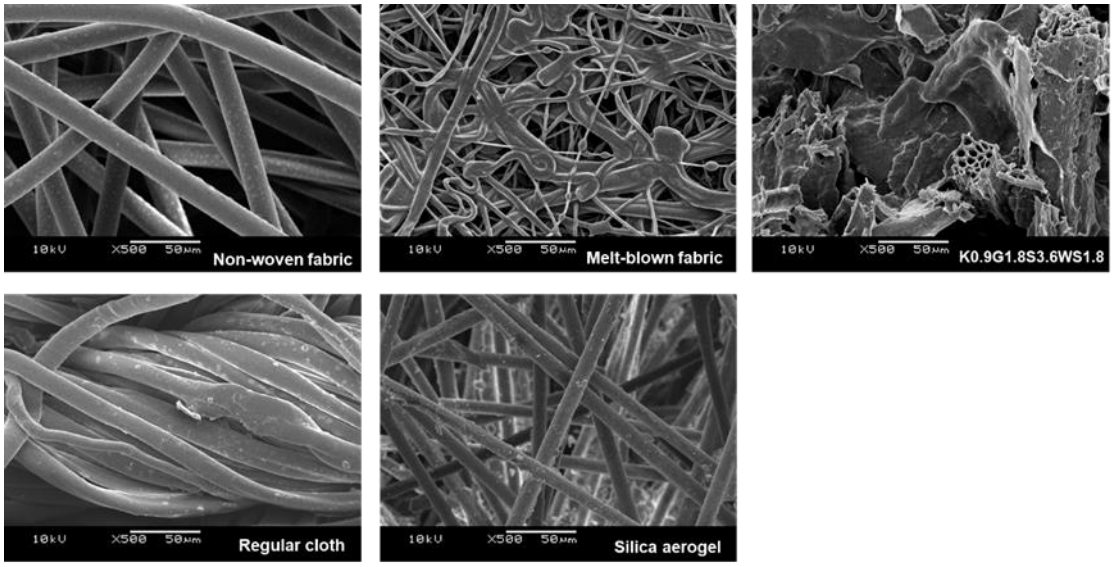


Figure 6-9. SEM-images of melt-blown fabric, non-woven fabric, biomass aerogel, regular cloth and silica aerogel after the filtration test.

6.5 PM FILTRATION PERFORMANCE TEST IN THE TRANSPARENT CHAMBER

As introduced in section 6.3.2, the PM filtration performance was measured using a handmade transparent chamber with a small fan, smudge stick, air purifier and PM detector. In this study, the PM 2.5 and PM 10 filtration efficiency of different filters was calculated by comparing the particle concentration before and after the start of the air purifier. Every test lasted one hour. During the first 30 minutes, the smudge stick was burned completely. In the next 30 minutes, the particle concentrations were measured, and the data was recorded every minute. With the work of different filters, the PM particles have been removed at different rates. Figure 6-10 shows that the filters have good filtration performance compared with regular cloth and silica aerogel. In the beginning, there is full of particles in the transparent chamber and the filtration efficiencies of all samples are zero in the first five minutes. At the fifth minute, the curve for HEPA starts to increase dramatically, converges gradually and finally reaches the highest filtration efficiency of 98.80% at the thirtieth minute. Compared with the HEPA filter, a one-minute delay can be observed for three types of biomass aerogels to start removing particles.

Biomass aerogel K0.9G1.8S3.6WS1.8 shows a similar growth rate to HEPA at the beginning, but its growth rate begins to exceed HEPA at around 15 minutes. At last, the removal efficiency of K0.9G1.8S3.6WS1.8 reaches 99.50% at the thirtieth minute, which is the highest among all filters. The particle removal efficient rates of three biomass aerogels are different. With a high density and relatively dense structure, the K0.9G1.8S3.6WS1.8 has the highest growth rate, followed by the K0.7G1.4S2.8WS1.4. In the beginning, there was a difference in their growth rate, which became more obvious as the experiment continued. At the end of the test, the PM 2.5 removal efficiency of K0.7G1.4S2.8WS1.4. is 89.79%. In the ninth minute, the surgical mask starts to work and has a similar growth rate of HEPA and K0.9G1.8S3.6WS1.8. At the end of the test, the removal efficiency of the surgical mask reached 97.90. Figure 6-10 (b) was used to magnify the details and compare the PM 2.5 removal efficiency of HEPA, surgical mask and biomass aerogel K0.9G1.8S3.6WS1 from 26 minutes to 30 minutes. It could be found that the filtration efficiency of HEPA decreases at the 30^{th} minute, while the filtration efficiency of biomass aerogel K0.9G1.8S3.6WS1.8 continuously increases and eventually higher than that of HEPA at the end. In this test, the two worst removal efficiencies were observed with silica aerogel (83.78%) and regular cloth (58.56%). To confirm the effect of particle sizes, the filtration tests of PM 10 were also studied, and the results are shown in Figure 6-11. Compared with the removal test of PM 2.5, the removal efficiency curve of PM 10 has a similar tendency, in which the filtration performance of HEPA and biomass aerogel K0.9G1.8S3.6WS1 (99.40%) is better than other filters with a relatively high growth rate. If removal efficiency of 97% is taken as the standard, the K0.9G1.8S3.6WS1, HEPA can meet the requirement. The removal efficiencies reach as high as 99% for both PM 2.5 and PM 10 for biomass aerogel with the formula K0.9G1.8S3.6WS1. The high promised removal efficiencies for PM 2.5 and PM 10 are attributed to the composite pore structure, the high specific surface area formed by the specific structure of wheat straw

and the freeze-drying method. In the freeze-drying process, the pores were formed by the ice crystal sublimation and the pore wall was composed of solid materials. The porous structure of biomass aerogel provides a good foundation for filtration performance. With the addition of the wheat straw, the internal structure becomes more complicated due to the unique multi-cavities structure of wheat straw (as shown in Figures 6-7, 6-9 and 6-9). When the particles enter the biomass aerogels, most of them will be intercepted inside the biomass aerogels because of the complicated 3D structure leading to higher filtration performance. Besides, for K0.7G1.4S2.8WS1.4, K0.5G1S2WS1, silica aerogel and regular cloth, there is a little difference in the filtration efficiency between PM 2.5 and PM 10. The efficiency of removing PM 2.5 with the regular cloth (58.56%) is higher than the efficiency of using it to remove PM 10 (25.33%), and this difference was significant, as shown in Figure 6-10 (a) and Figure 6-11 (a).

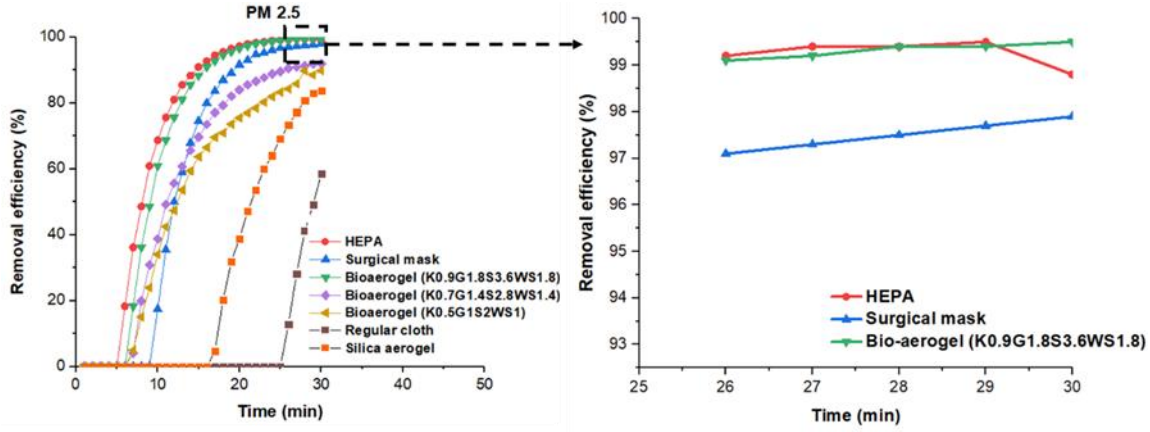


Figure 6-10. The PM 2.5 removal efficiency of (a) different filters from 0 min to 30 min, (b) HEPA, surgical mask and biomass aerogel K0.9G1.8S3.6WS1 from 26min to 30 min.

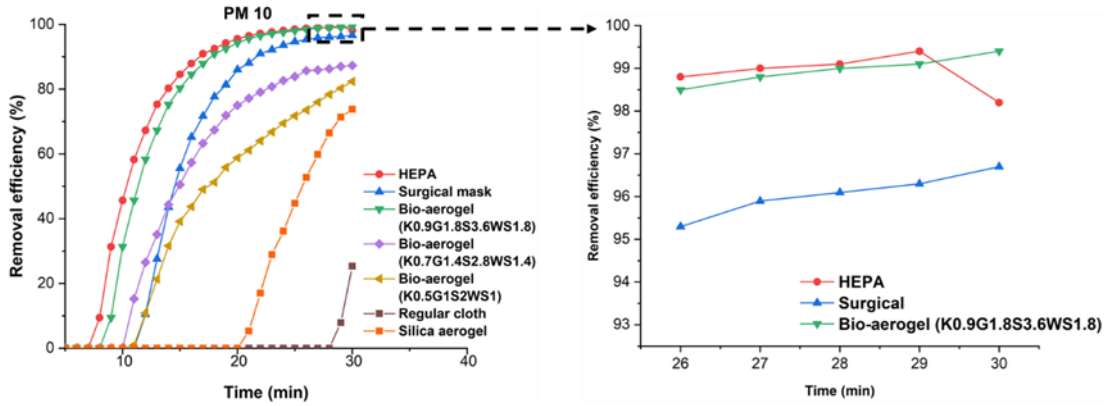


Figure 6-11. The PM 10 removal efficiency of (a) different filters from 0 min to 30 min, (b) HEPA, surgical mask and biomass aerogel K0.9G1.8S3.6WS1 from 26 min to 30 min.

6.6 MONITORING OF INDOOR AMBIENT AIR QUALITY WITH DIFFERENT FILTERS

The detailed PM 2.5 and PM 10 concentrations were recorded, removal efficiencies were calculated following the procedure above, and the results are shown in Figures. 6-12 and 6-13. As demonstrated by the purple curve in Figure 6-12 (a), the PM 2.5 concentration by biomass aerogel (K0.7G1.4S2.8WS1.4 and K0.9G1.8S3.6WS1.8) increases sharply in the first 14 minutes, followed by constant high values for 30 minutes, and then drops dramatically after the forty-fifth minute under the filtration effect of biomass aerogel K0.7G1.4S2.8WS1.4 and K0.9G1.8S3.6WS1.8. The reason for the constant high values from 15th min to 43rd min is the limitation of the detector that the maximum PM concentration it can measure is 999. On the other hand, the PM 2.5 concentration by HEPA shows a different trend, which increases to a peak value and decreases rapidly afterwards at the twenty-fifth minute. Figure 6-12 (b) shows the PM 2.5 removal efficiency of HEPA and two biomass aerogels. In the actual room test, the PM 2.5 removal efficiency of HEPA, biomass aerogel K0.9G1.8S3.6WS1.8 and K0.7G1.4S2.8WS1.4 exhibit a continuously increasing trend and the final reach 99.40%, 97.90% and 97.50%, respectively. These results are similar to filtration testing results in the transparent chamber, which shows an improvement for HEPA and biomass aerogel

K0.7G1.4S2.8WS1.4. However, biomass aerogel K0.9G1.8S3.6WS1.8 shows a slight reduction of filtration efficiency in the actual room compared with the transparent chamber. To be specific, the filtration test of biomass aerogel K0.7G1.4S2.8WS1.4 in the actual room can improve removal efficiency by 6.11%, and the biomass aerogel K0.9G1.8S3.6WS1.8 in the actual room can bring a slight reduction of removal efficiency by 1.61%. Compared with the HEPA filter, biomass aerogel K0.7G1.4S2.8WS1.4 and K0.9G1.8S3.6WS1.8 have a 16-minute and 17-minute delay in removing particles, respectively. After the start, biomass aerogel K0.9G1.8S3.6WS1.8 has a similar increase rate with HEPA, while the removal efficiency increases of biomass aerogel K0.7G1.4S2.8WS1.4 shows a much slower trend.

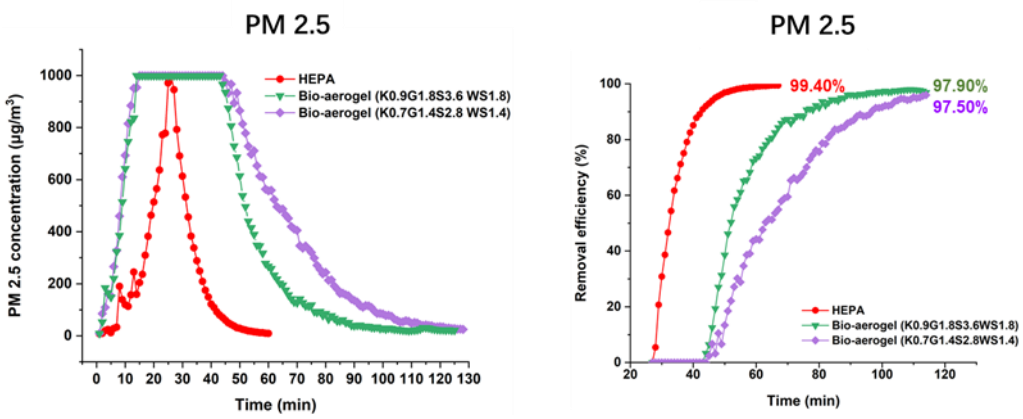


Figure 6-12. Measured (a) PM 2.5 concentration in the actual room; and (b) the PM 2.5 removal efficiency with HEPA, K0.9G1.8S3.6WS1.8 and K0.7G1.4S2.8WS1.4.

Meanwhile, Figure 6-13 shows the PM 10 concentration and removal efficiency during the testing process. The HEPA is usually made of chemical fibers or glass fibers, with a diameter of about 0.5 μm to 2 μm, smaller than the PM 10 particles. In general, the interception dominates in achieving the filtration efficiency when the particles are larger than the fiber diameter. It can be found in Figure 6-13 (a) that the PM 10 concentration in the actual room decreased rapidly when it started to use HEPA as the filter. Meanwhile, the filtration rate of the biomass aerogel K0.9G1.8S3.6WS1.8 and K0.7G1.4S2.8WS1.4 is slower than HEPA. This could explain that the biomass aerogel is a thin disc with a thickness of about 3 mm, much

thinner than HEPA. Besides, the pleated HEPA structure contributes to the maximum efficiency function. The filter core sample has a smaller volume and simple structure when using the biomass aerogel. The PM 10 removal efficiency of HEPA and biomass aerogel K0.7G1.4S2.8WS1.4 were 98.70% and 96.10%, respectively. Compared with the same test carried out in the transparent chamber, the filtration efficiency results of biomass aerogel K0.7G1.4S2.8WS1.4 in the actual room can improve removal efficiency by 10.09%, and K0.9G1.8S3.6WS1.8 in the actual room can bring a slight reduction of removal efficiency by 2.72%. The PM 2.5 and PM 10 removal efficiency results indicate that the biomass aerogels K0.9G1.8S3.6WS1.8 and K0.7G1.4S2.8WS1.4 show good particle filtration performance. Moreover, 3 mm thickness biomass aerogels K0.9G1.8S3.6WS1.8 shows similar PM removal performance to commercial HEPA (40 mm thickness).

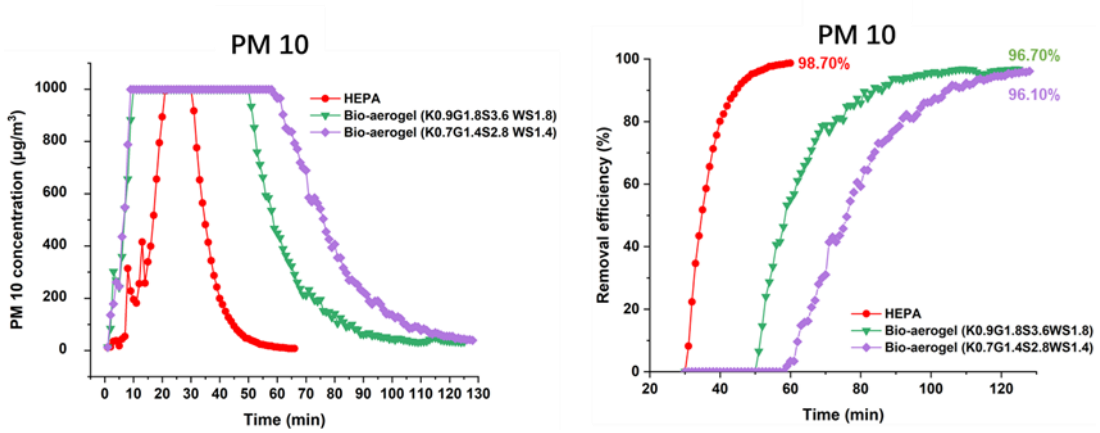


Figure 6-13. Measured (a)PM 10 concentration in the actual room; and (b) the PM 10 removal efficiency with HEPA, K0.9G1.8S3.6WS1.8 and K0.7G1.4S2.8WS1.4.

6.7 CONCLUSION

In this chapter, the filtration property of biomass aerogels in the actual environment has been investigated. The filtration performance comparison between biomass aerogels and some current commercial filters indicates the great potential of biomass aerogels as the filtration

materials for removing PM 2.5 and PM 10 in different fields. The main conclusions can be drawn as follows:

(1) The PM 2.5 and PM 10 removal efficiencies of biomass aerogel K0.9G1.8S3.6WS1.8 (thickness: 3 mm) in a small transparent chamber have been determined to be 99.50% and 99.40%, respectively. The PM 2.5 removal efficiency of biomass aerogels is better than surgical masks (97.90%), silica aerogel (83.78%) and regular cloth (58.56%). HEPA (thickness 40 mm) shows a similar effect having removal efficiencies of 98.80 for PM 2.5 and 98.20% for PM 10.

(2) The PM 2.5 removal efficiency of K0.7G1.4S2.8WS1.4. is 89.79% in the small transparent chamber. The filtration performance of K0.5G1S2WS1 (89.79%) is worse than the other two biomass aerogels because it has a low solid concentration, which results in a low density and a large number of open pores in the structure of biomass aerogels.

(3) In the actual room test, biomass aerogel K0.9G1.8S3.6WS1.8 shows a slight reduction of filtration efficiency in the actual room, the PM 2.5 removal efficiency is still higher than 97%.

7 COMPUTER SIMULATION FOR ENERGY DEMAND OF E.ON HOUSE WITH BIOMASS AEROGEL INSULATION PANELS

7.1 INTRODUCTION

Heating energy consumption accounts for a large proportion of all energy demand in buildings. Biomass aerogels have good thermal insulation performance, so adding insulation layers to improve the thermal performance of the building envelope will be considered. This chapter will use an E.ON house at the University of Nottingham as the modelling house. The E.ON house is a two-story semi-detached house with a small plant zone room built in 2007 [243]. The research house is located in the Department of Architecture and Built Environment, University of Nottingham, with a total construction area of E.ON house is 250.97m^2. This exemplary research house is divided into two parts, live laboratories and a plant zone. The plant zone is located on the left side of the whole building. The right section, residential laboratories, is comprised of 11 rooms: living room, kitchen, dining room, hall, store, three bedrooms, toilet, landing and attic room. In this research, similar to the previous research of M.C.Gillott [243], the floor area is about 110 m^2. However, there is a different division method about coal stores between M.C.Gillott and this research. In this research, the coal store is also treated as the floor area merged with the pantry. The total floor area comprises a living room, a kitchen and a store on the ground floor and three bedrooms, a toilet which contains a bathroom and a separate toilet on the first floor.



Figure 7-1. Images of E.ON house.

7.2 THE CONSTRUCTION AND MATERIALS OF THE ORIGINAL E.ON HOUSE

In this study, the original base-case condition, including fabric and ventilation characteristics (with poor thermal insulation), were used as the baseline according to previous research by M.C.Gillott [243]. Table 7-1 presents all the original building materials, constructions and thermal physical characters. The original ground floor and upper floor are mainly based on an uninsulated suspended timber floor with 920 mm, and the overall U-value is 0.72 $Wm^{-2}K^{-1}$. However, the kitchen is special, which has been decorated with an uninsulated concrete slab, overall U-value is 0.99 $Wm^{-2}K^{-1}$. The existing exterior wall is mainly based on the 50 mm uninsulated cavity and 100 mm solid block with lath and plaster finish, overall U-value is 1.29 $Wm^{-2}K^{-1}$. The exterior roof was used with an uninsulated pitched rafter and purlin roof with a breathable membrane (U-value of 1.63 $Wm^{-2}K^{-1}$). The single glazing windows and doors with timber framed with an overall U-value of 4.8 $Wm^{-2}K^{-1}$ and 3.8 $Wm^{-2}K^{-1}$, respectively.

Table 7-1 The original building construction materials of the E.ON research house.

	Materials	Thickness (mm)	Conductivity ($Wm^{-1}K^{-1}$)	Specific heat capacity (J/kg·K)	Overall U-value ($Wm^{-2}K^{-1}$)
Ground floor and upper floor	Uninsulated suspended timberfloor	200	0.14	2300	0.72
Kitchen floor	Uninsulated concrete slab	410	0.41	2300	0.99
Exterior wall	100 mm brick	100	0.24	800	1.29
	50mm uninsulated cavity	50	0.27	-	
	100 mm solid block with lath and plaster finish	100	0.56	1000	
Exterior roof	Uninsulated pitched rafter & purlin roof with breathable membrane	176	0.29	1380	1.63
Exterior window	Timber framed single glazed	20	0.096	-	4.80
Exterior door	Timber framed single glazed	40	0.152	2300	3.80

7.3 MODELLING OF NOTTINGHAM E.ON HOUSE

7.3.1 Simulation target statement

The original E.ON house was applied to test building performance treated as the baseline to provide a comparison with the interior passive retrofit measure, which used the original exterior wall combined with biomass aerogel.

In this section, the E.ON house with original construction characteristics will be designed, and heating energy and equipment energy consumption will be simulated and obtained by the software of Sketchup (Version 2017) and Energy plus (Version 8.8.0) to verify the veracity of the actual energy consumption in E.ON research house. Energy plus is a building energy dynamic simulation software to simulate the hourly load and energy consumption of buildings throughout the year, which helps architects and engineers to consider how to save energy from the whole architectural design process.

7.3.2 Simulation setting

As shown in Figure 7-2, the geometry of the E.ON research house is drawn in the Sketchup based on the architectural plan.

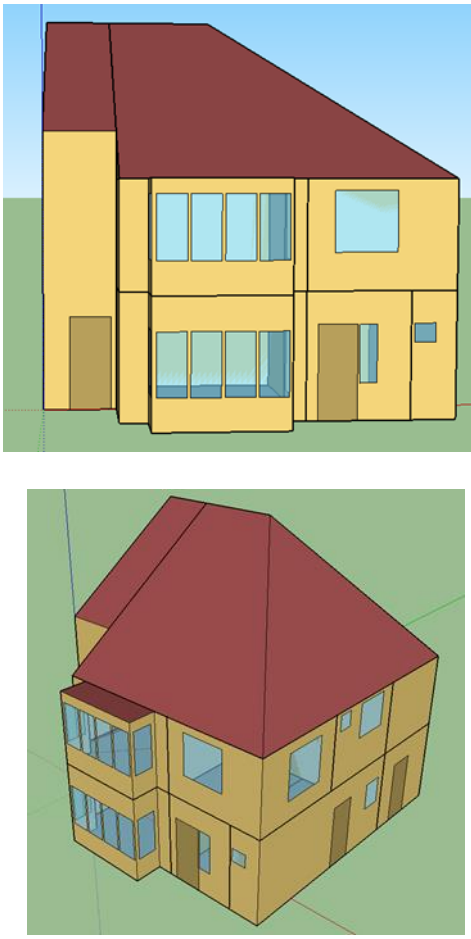


Figure 7-2. The model of E.ON house.

Setting parameters are needed in Energy-plus software, including dates, local weather, the zone of houses, construction materials, the internal condition of each zone and the operating schedule.

7.3.2.1 Calendar

Two design months were selected to represent two seasons, winter and summer. January on behave of winter and July is presented as summer. The simulation will be monitored for a whole year.

7.3.2.2 Nottinghamshire weather and geography

Nottinghamshire is one of the oldest cities in the UK with a significant rainfall. It is always linked to foggy and rainy weather. The average annual temperature is 10.5℃, and the annual

average rainfall is 118.05 mm (average from January 2000 to December 2008). July is the warmest month of summer, with an average temperature of around 17.6 ℃. The coldest month is January, with an average temperature of around 4.2℃. In the UK, 30.4 mm (April) always presents as the driest month of the year, and the maximum precipitation will appear at 207.6 mm (December). The precipitation varies by 177.2 mm between the driest and wettest months. Throughout the year, temperatures vary by 13.4°C. All the detailed information is presented in Figure 7-3. Due to the weather in Nottingham, there are no air cooler in most Nottingham families. So it is assumed that cooling will not be included in the simulation.

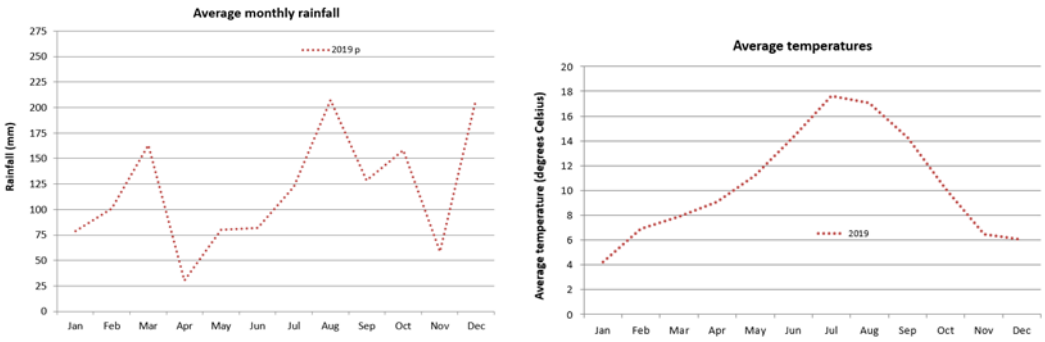


Figure 7-3. The average monthly rainfall and average air temperature in the UK.

7.3.2.3 Zoning distribution

Figure 7-4 shows E.ON house zone setting on the ground floor and 1st floor with the available floor area of 110 m^2 including a living room, a kitchen and store on the ground floor and three bedrooms, a toilet which contains a bathroom and a separate toilet on the first floor. The detailed area distribution is presented in Table 7-2.

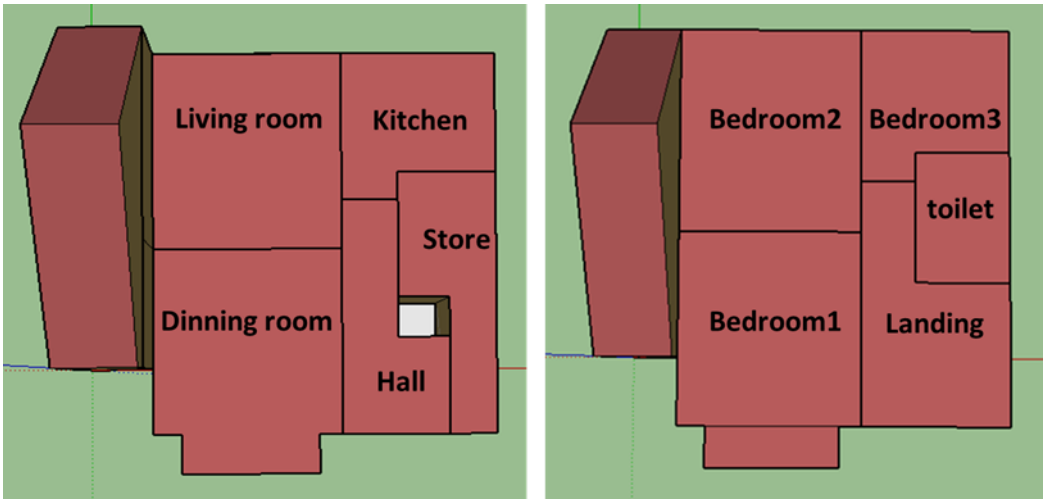


Figure 7-4. Schematic of zoning on the ground floor (left) and 1st floor (right).

Table 7-2 Dimensions of zones of E.ON research house.

	Area [m^2]
Plant zone	11.86
Dining room	19.53
Hall	9.76
Living room	17.92
Kitchen	9.66
Store	9.04
1^{st} bedroom 1	19.53
1^{st} Landing	11.87
1^{st} Toilet	5.94
1^{st} bedroom 2	17.92
1^{st} bedroom 3	9.66
2^{nd} floor	63.29
Total	205.97

7.3.2.4 The existing energy system of E.ON house

In this section, the detailed information of resident numbers, appliances, natural gas, people and zone infiltration are listed in Table 7-3. In this research, it is assumed that there are three researchers of the University of Nottingham residents in this house, they share living room, kitchen, and bathroom as the common area. Furthermore, it is also assumed that this three people need to go out to work during the workdays and are not at home. The first floor is the main area for leisure and public activities. The energy source of the building is divided into two parts, including gas and electricity. A second-hand 15-year-old non-condensing gas fired boiler is used to supply the space heating for the living room, kitchen, dining room, toilet and three bedrooms. The electricity is consumed by the living equipment. The electricity and gas are based on the resident occupancy schedules sorted by the weekdays and weekends. In addition, the electricity consumption by the refrigerator and freezer is estimated based on their annual energy consumption as refrigerator and freezer are working intermittently.

Table 7-3 Detailed information about appliances, natural gas, people and zone infiltration.

	Categories	Item	Value
Appliances	Light		8-12 Wm^{-2} (watts per zone floor area)
	Kettle	Kitchen	500 W
	Microwave	Kitchen	600 W
	TV	Living room	150 W
	Laptop	Living room	125 W
	Fridge	Kitchen	61.4kWh/yr
	Freezer	Kitchen	52.9kWh/yr

	Oven	Kitchen	293 W
	Heater	Plant zone	800 W
Natural gas	Cooker	Kitchen	Max 1.5 kW
	Shower	Toilet	7.5kW
People	Residents	Main in the bedrooms and living room	3
Zone infiltration (Air Changes/Hour)			0.26-0.5/per hour

From the perspective of indoor comfort, the constant heating setpoint is set as 22-26°C, supplied by the heating gas. However, the cooling machine is not considered in this research.

7.4 SIMULATION RESULTS OF THE ORIGINAL E.ON HOUSE

As the baseline, the original E.ON house shows the primary energy consumption has 18916.67 kWh of natural gas and 3361.11 kWh of electricity equipment, with a total of 24947.22 kWh of annual primary energy consumption. The total energy consumption is divided into four parts, including space heating (76%), lighting electricity (9%), equipment electricity (13%) and pump electricity (2%), as shown in Figure 7-5. Space heating accounts for more than 70% of the energy consumption, with the most contribution to energy consumption, which needs thermal insulation in priority to reduce natural gas consumption.

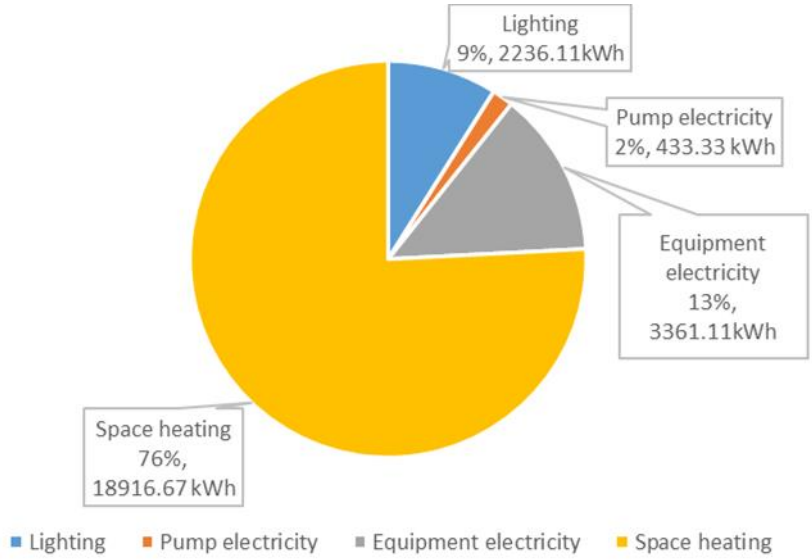


Figure 7-5. Specification of the overall energy consumption of the original E.ON house.

7.5 EXTERIOR WALL RETROFIT MEASURES AND SIMULATION MODELLING RESULTS OF E.ON HOUSE WITH A WALL INSULATION

The E.ON house represents the majority of British homes with low energy efficiency. In this research, the currently responsible for retrofitting the E.ON house is to improve the thermal insulation performance of the exterior wall. Different from the construction of a new house, thermal insulation renovation of the existing house should be transformed based on not destroying the original structure and changing the original functions to the greatest extent. At the same time, the construction method should be as simple as possible and easy to operate. Therefore, the experiments were carried out with the internal retrofit of insulation in this house.

In this research, the main aim is to reduce the heat loss from building exterior walls. The original E.ON house wall was retrofitted with the combination of biomass aerogel insulation (thickness of 15 mm) to improve thermal insulation property. The new exterior wall is mainly based on a 50 mm uninsulated cavity, 100 mm solid block with lath and plaster finish and 15 mm biomass aerogel, the overall U-value is 0.84 $Wm^{-2}K^{-1}$ as shown in Table 7-4. The 1.5 cm insulation materials are generally required to retrofit a cavity wall to decrease the U value from

1.29 $Wm^{-2}K^{-1}$ to 0.84 $Wm^{-2}K^{-1}$. Other building construction materials and room setting parameters (constant heating setpoint) will keep the same as the original house.

Table 7-4 The new exterior wall construction materials of E.ON research house with wall insulation.

	Materials	Thickness (mm)	Conductivity ($Wm^{-1}K^{-1}$)	Specific heat capacity (J/kg·K)
Exterior wall	100 mm brick	100	0.24	800
	50mm uninsulated cavity	50	0.27	-
	100 mm solid block with lath and plaster finish	100	0.56	1000
	Biomass aerogel	15	0.037	2260

After the retrofit of the exterior wall, the E.ON house with wall insulation shows the primary energy consumption has 16222.22 kWh of heating natural gas and 3361.11 kWh of electricity equipment, with a totally 22188.89 kWh of annual primary energy consumption. Figure 7-6 shows the monthly heating gas demand of E.ON house with wall insulation, in which the natural heating gas for January and December is 3.94E+03 (24.31% of whole year heating gas demand) and 4E+03 (24.65% of whole year heating gas demand), respectively. The total energy consumption is divided into four parts, including space heating (73%), lighting electricity (10%), equipment electricity (15%) and pump electricity (2%), as shown in Figure

7-7. With the 15 mm biomass aerogel combination, the space heating demand has been reduced to 16222.22 kWh (save gas: 2694.44 kWh). As shown in Figure 7-5, 7-6, 7-7, it could be found that the post-retrofit E.ON house with biomass aerogel wall insulation could reduce the primary heating gas consumption. Compared with the heating gas demand of the original E.ON house, the space heating energy consumption reduced from 18916.67 kWh to 16222.22 kWh (14.24% of the primary heating gas reduction) after adding biomass aerogel as the wall insulation. Especially in winter, the reduction of heating gas demand is more obvious. In January, February and December, the post-retrofit can bring the reduction of gas demand by 11.80%, 11.90% and 14.29%, respectively. According to the gas tariff of the company E.ON in January 2023, the daily standing charge is 28.48 penny/day, and all units fee is 10.24 penny/kWh. The annual heating gas fee saving is about £ 275.91 after the exterior wall is retrofitted with a biomass aerogel panel.

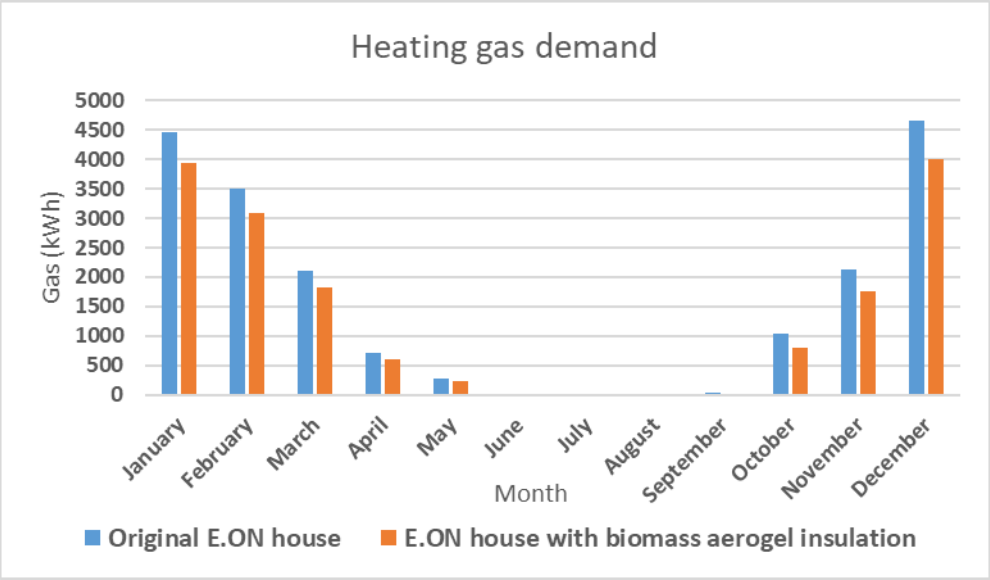


Figure 7-6. Heating gas demand of the E.ON house comparison between original E.ON house and the E.ON house with biomass aerogel wall insulation.

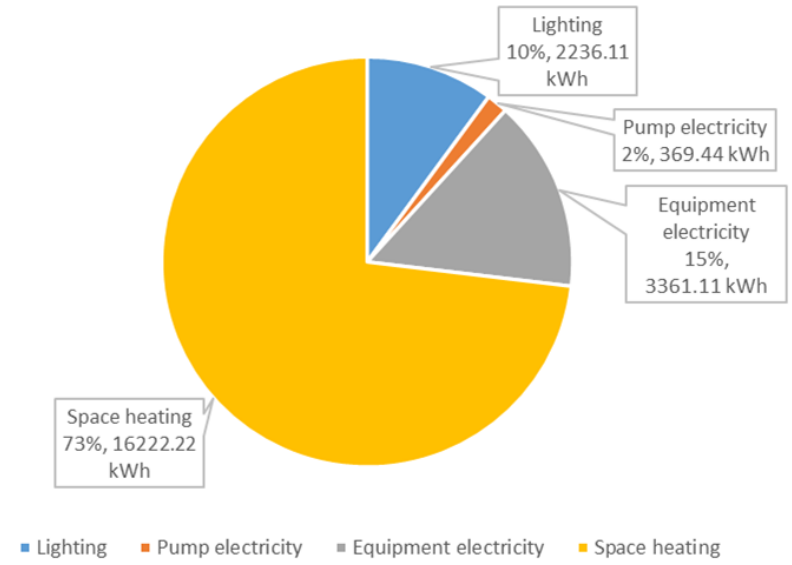


Figure 7-7. Specification of the overall energy consumption of the E.ON house with wall insulation.

7.6 CONCLUSION

In this section, a computer simulation of heating energy demand has been stated. Energy plus software was used for modelling the heating gas energy consumption in a typical semi-detached house. Compared with the space heating gas demand of the original E.ON (base-case), the post-retrofit E.ON house with a biomass aerogel wall insulation achieved the goal with 14.24% of the primary heating gas reduction (gas saving: 2694.44 kWh/year). To be more specific, the E.ON house with wall insulation shows 16222.22 kWh of heating natural gas, 3361.11 kWh of electricity equipment, and a total 22188.89 kWh of annual primary energy consumption.

8 ECONOMIC AND ENVIRONMENTAL ANALYSIS

8.1 INTRODUCTION

Recent research indicates that global energy demand is expected to rise from 524 quadrillions BTUs (2010) to 820 quadrillion BTUs (2040) [244]. The building sector contributes significantly to total energy consumption. For example, in the UK, building energy consumption accounts for 39% of total energy consumption [245]. Therefore, energy-saving and protection of the environment have become a major global concern. With the industrial and other sectors paying greater attention to environmental protection and management, the eco-environment coordination of new biomass aerogels has laid a foundation for controlling pollution from the source. Globally environment-friendly materials are being promoted regarding their chemical and physical properties and environmental efficiency indicators, which has proven to be another important feature. This chapter uses various methodologies and modelling tools to assess the cost and environmental viability of these novel developed materials [246]. One effective tool is the life cycle assessment (LCA) method, which is extensively used to evaluate the economic and environmental impact of materials during their life cycle providing the desired direction for improvement in materials and their processing technology. The economic and environmental analysis indicates the sustainability and great future market potential of these novel biomass aerogels based on the type of raw materials utilized and the manufacturing process.

8.2 ECONOMIC ANALYSIS

An economic analysis is presented in this section. Cost and relative contribution during the aerogel life cycle (from cradle to gate) were evaluated. This study aims to identify and reveal the main aspects that influence the final cost of the production stages. In this study, both the laboratory scale and larger batches have been analyzed. The results based on the lab-scale can

be regarded as a conservative estimate. However, an estimation of the industrial manufacturing process cost referred to the data of Licheng Biological Technology Co., Ltd (Wuhan, China). These large batches' results are closer to the actual situation, which could be used as a reference for the industrial investment of biomass aerogels to achieve efficiency gains.

8.2.1 Declared unit

The main objective of the declared unit is to provide a common base and a reference to describe the performance of a product (1 m^2·cm) when it fulfils its function (inputs and outputs of the system).

8.2.2 System boundaries

The main objective of the system boundaries is to define the unit processes to be included in this study [247]. The system boundary drawn for this study focuses on the manufacturing stage of biomass aerogels, i.e., from 'gate to gate' consisting of three major substages: gel preparation, ageing and freeze drying. As presented in Figure 8-1, the inputs (raw materials and electricity usage) and outputs (biomass aerogel and emissions) have been listed. The transportation process has not been included currently.

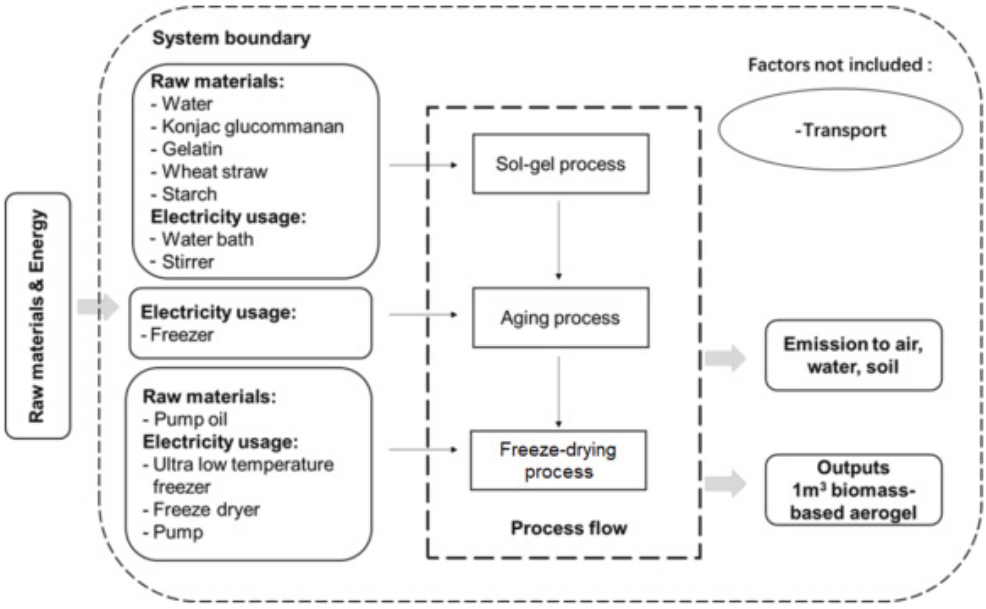


Figure 8-1. System boundary of biomass aerogel production process (gate to gate).

8.2.3 Cost of energy and Cumulative Net Present Value (NPV) Calculation

(1) Energy saved

The energy demand was compared between the existing original E.ON house (baseline) and E.ON house with wall insulation (post-retrofit) to calculate the energy saving based on the computer simulation results in Chapter 7.

(2) Energy Cost Saving

The annual energy cost saving is calculated based on the domestic energy tariff of the E.ON company in the calculated year. Based on the average annual domestic gas bill of the gas consumption 150000 kWh/per year from 1999 to 2019 in the UK (statistic data from GOV. UK), the natural gas increase rate (r_1) is obtained from the literature [248] as shown in Table 8-1. The cost of energy saved (£) per year is calculated by the following equation (8-1):

$$\text{Cost of gas saving fee } (i^{th} \text{ year}) = \text{gas saved (kWh)} \times \text{unit price of gas (£/kWh)} \times (1 + r1)^i \quad (8\text{-}1)$$

Where ri is the natural gas increase rate; i is the perios to which the cash inflow relates.

(3) Cumulative NPV of the cost of energy saved and the discounted payback period

According to the Association of British Insurers, the real discounted rate (r_2) over 15 years is 2.5% to allow the flow of cash happening over an extended period to be considered at an equivalent value in comparison to energy prices of today. According to Ibn-Mohammed, the discounted cash flow and Cumulative NPV of the gas saving cost were calculated by the following equations (8-2) and (8-3). Ibn-Mohammed et al. [249] estimated by discounting all future savings to their corresponding present value.

$$\text{Discounted cash flow} = \frac{CFi}{(1+r2)^i} \quad (8\text{-}2)$$

$$\text{Cumulative NPV} = -I + \sum_1^n \frac{CFi}{(1+r2)^i} \quad (8\text{-}3)$$

where Cumulative NPV is the cumulative net present value; I is the initial investment cost; CFi is the cost of gas saving fee; r_2 is the real discount rate, which depends on the market interest R and the inflation rate R_i. The market values of inflation and interest rate and energy price & their increasing rate for Lisbon, Venice, Nottingham and Helsinki are shown in the following Table 8-1. r_2 could be calculated by using equations (8-4):

$$Rr=(R-Ri)/(1+Ri) \quad (8\text{-}4)$$

Table 8-1 Economic indicators and natural gas increase rate

	Market interest rate (R) %	Inflation rate Ri (%)	Natural gas increase rate (%)
UK-Nottingham	0.57 [248]	0.7 [248]	12.99 [248]

The discounted payback period is the length of time when the cumulative net present value of a project becomes positive to pay back the initial cost. The initial cost of investment must equal the discounted value of expected cash flows. Different from the simple payback period, the discounted payback period takes into account the principle of the time value of money.

$$\text{Discounted Payback Period} = (n\text{-}1) + \frac{\text{Cumulative NPV}^{(n-1)}}{\text{Discounted cash flow}^{n}} \quad (8\text{-}5)$$

where n is the year when the negative cumulative NPV becomes positive;

8.2.4 Economic assessment results

This section aims to evaluate the economic assessment of biomass aerogel on a laboratory scale and in large batches. According to the analysis of biomass aerogel production on a laboratory scale, it should be considered that biomass aerogel is produced by a small water bath and freeze dryer in the lab. All the steps should be repeated several times, contributing to inaccurate data. For the industrial manufacture, 1 m^2·cm biomass aerogel could be produced in one cycle process. The of all unit stages will be calculated and shown as follows.

8.2.4.1 Cost from the gate to the site

For lab scale, the transportation fee of raw materials, which is the supplier's responsibility, has been included in the cost (£/m^2·cm of biomass aerogel) of raw materials and VAT is also included in the cost of raw materials. The water is shared in this lab, so the actual cost of water cannot be estimated, which will not be considered. There is no sub product generated as waste in the production processes. In addition, all equipment is shared by all the researchers in the lab and is only part of an initial investment since they are subsequently reused. Therefore, these equipment costs will not be considered in the economic evaluation of the production process. It should be noted that the water baths and refrigerators are not working continuously on full power but working intermittently. The actual working situation will be analyzed to calculate the authentic energy consumption. For example, according to the technical data of the refrigerator and ultra-low temperature freezer, the electricity power of two freezers is 0.014 kW (122 kWh/annual) and 0.094 kW (2.256 kWh/24 h), respectively. The total actual energy consumption of refrigerator and ultra-low temperature freezer to produce 1 m^2·cm biomass aerogel are 0.014 kW × 0. 5 h × 5.14 (0.04 kWh) and 0.094 kW × 10 h × 2.36 (2.22 kWh), respectively. Finally, the waste should be considered during the gel and biomass aerogel production in which the total waste ratio is estimated by the lab experience to be 3%. This means that when producing 1 m^2·cm biomass aerogel, only 0.97 m^2·cm biomass aerogels will be finally obtained to be packaged and will be sent to the site at the end of the laboratory.

Table 8-2 Cost of the raw materials for the production in a lab scale.

	Item	Amount/m^2·cm of aerogel	Cost （£）
raw materials acquisition	Konjac glucomannan	64.4 g	1.61 (Alibaba)
	Gelatin	32.2 g	0.48 (Amazon)

	Starch	128.7 g	1.24 (Amazon)
	Wheat straw	128.7 g	-
	Water	64366.6 mL	-
The production process	Pump oil	78.75 mL	1.05 (Fisher)
Raw material cost of package	Packaging plastic bag	10 per m^3 (each plastic bag capacity 100L)	0.05 (Amazon)
Electrical cost of the production	Electrical equipment	Total energy consumption (kWh)	Cost （£）
	Water bath	1.88	0.564 (Grant Instrument)
	Stirrer	1.45	0.435 (Scilogex)
	Freezer	0.04	0.12 (Elecrtrolux)
	Ultra-low temperature freezer	2.22	0.67 (Fisher)
	Freeze dryer	80.24	24.07 (Boyikang)
Cost of production labour costs	An operator	0.1h (add the raw materials and transfer the sample to the next production process)	2.38
Total cost in lab scale (£)	Total cost of production 0.97 m^2·cm biomass aerogel (K1G0.5S2WS1.5) is £ 28.24, which shows the unit cost is		

£ 29.11/m^2·cm.

At the production stage, the energy cost to produce 1 m^2·cm of aerogel (C) is given by the following equation (8-5):

$$C = T \times E \quad (8\text{-}5)$$

Where T is the cost of 1 kWh of electricity in the United Kingdom (January 2023: 0.3 £/kWh), whose average annual usage is > 30,000 kWh and equal to or < 50,000 kWh;

E is the total energy consumption of an instrument.

According to the electricity consumption data in the company, the electricity demand of large batches for production is about 2 kWh for 1 m^2·cm biomass aerogel. In one production cycle, the freeze dryer needs 40 L of pump oil, which could be reused 12 times. In industrial production, the operator will only spend approximately 1 h to deal with the product during the process, which requires £ 0.024. Moreover, the raw materials price will be reduced due to the large batches purchase, which have not been considered. The total cost of production 0.97 m^2·cm biomass aerogel is £ 4.43 (as shown in Table 8-3), which shows the unit cost is £ 4.57/m^2·cm.

Table 8-3 Economic assessment of the biomass aerogel Life Cycle in large batches.

	Raw materials cost	Pump oil cost	Energy consumption cost	Packaging bags cost	Labor cost
Cost (£)	3.32	0.44	0.6	0.05	0.02
Total cost on an	The total cost of production 0.97 m^2·cm biomass aerogel				

industrial scale (£)	(K1G0.5S2WS1.5) is £ 4.43, which shows the unit cost is £ 4.57/m^2·cm.

8.2.4.2 The total estimated cost of the biomass aerogel used in E.ON house renovation

The total wall area of the E.ON house is 205.97 m^2. It is estimated that the total demand for biomass aerogel is about 2.52 m^3 (the house height is about 9 m, and each floor height is 3 m). Based on the unit price of biomass aerogel produced on the lab scale and industrial scale, the total cost is calculated as in Table 8-4.

Table 8-4 Total cost of the biomass aerogel used in E.ON house renovation.

	The unit cost of biomass aerogel (K1G0.5S2WS1.5) (m^2·cm)	Total cost
E.ON house renovation (aerogel produced in lab scale)	£ 29.11	£ 7335.25
E.ON house renovation (aerogel produced in industrial scale)	£ 4.57	£ 1151.64

8.2.4.3 Energy cost-effectiveness of the retrofitting with K1G0.5S2WS1.5 aerogel insulation

Figure 8-2 shows the cost-effectiveness by presenting the capital cost, cost saving and cumulative NPV due to energy saving and net saving for the 10-year service period. For the lab scale, the positive value appears in the 13th year (£847.11) and the NPV value is £3672.50 in the 15th year. For large industrial batches, the positive value appears in the 4th year (£101.94) and the NPV value is £3186.87 in the 10th year.

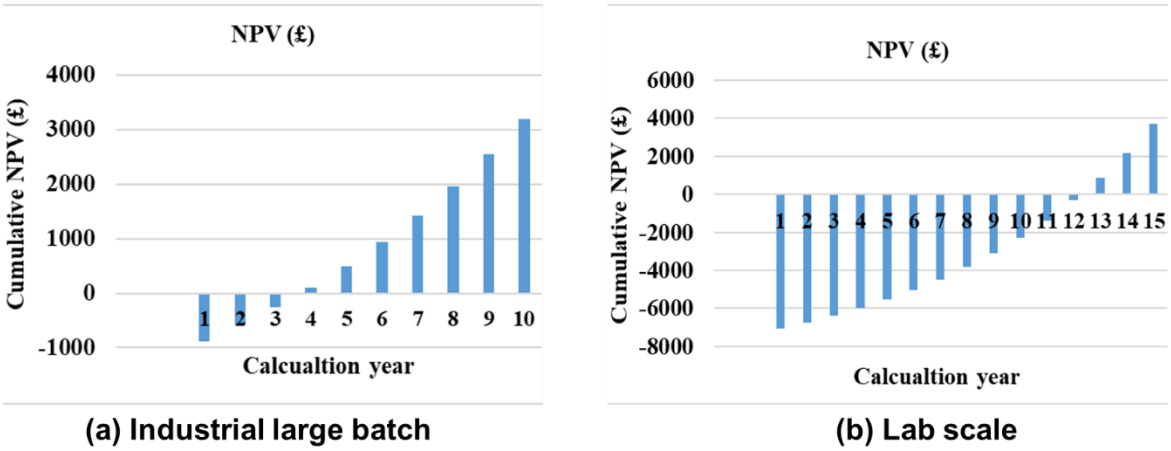


Figure 8-2. The Net Present Value of E.ON house with K1G0.5S2WS1.5 aerogel wall insulation in lab scale and industrial scale.

8.2.5 Comparison between common insulation materials and biomass aerogels in an industrial scale

Compared with other common insulation materials in the market, the unit cost of biomass aerogel produced on the industry scale is more suitable (4.57/m^2·cm). The unit cost comparison is based on the same U value (1 $Wm^{-2}K^{-1}$). All the data is presented in Table 8-5. To obtain the same U value, the cost of biomass aerogel is higher than Kingspan TP10 PIR. And lower than super wool fiber and silica-aerogel.

Table 8-5 The cost of common insulation materials and biomass aerogels.

Item	Unit cost	K value ($Wm^{-1}K^{-1}$)	Cost of materials with same U value (1 W/m^2·K)
Kooltherm K108 Cavity Board	3.46 £/cm·m^2	0.018	£ 6.228
Kooltherm K12 Framing	3.22 £/cm·m^2	0.020	£ 6.44

Board			
Kingspan TP10 PIR	2.6 £/cm·m^2	0.022	£ 5.72
Superwool 607 Fiber	19.62 £/cm·m^2	0.048	£ 94.18
Polyurethane Foam Sheets	4.58 £/cm·m^2	0.030	£ 13.74
Silica-aerogel insulation panels	40.15 £/cm·m^2	0.019	£ 76.29
Biomass aerogel (K1G0.5S2WS1.5)	4.57 £/cm·m^2	0.037	£ 16.91

8.3 ENVIRONMENTAL ANALYSIS

Environmental analysis is presented in this section. First, the environmental benefit (CO_2 emission reductions) of retrofitting E.ON house exterior wall with biomass aerogel was investigated. Secondly, the life cycle environmental impacts of manufacturing biomass aerogel were examined.

Based on the greenhouse gas (GHG) emission conversion factors from the UK government report and the simulation data in Chapter 7, the CO_2 emission reduction data has been calculated using the following equation:

CO_2 $Emission$ Reduction ($kg \cdot CO_2$ per $year$) = $Natural\ gas$ saving (kWh per $year$) × $Emission\ conversion\ factors\ for\ CO_2$ (8-6)

Where, the annual gas saving is 2694.44 kWh/year; CO_2 conversion factor is 0.2049 for natural gas in a typical UK house. The annual CO_2 e$mission$ reduction is calculated as follows:

CO_2 $Emission$ Reduction (kg) = 2694.44 kWh/year × 0.2049 = 552.09 kg

Therefore, the annual CO_2 e*mission* reduction of retrofitting E.ON house exterior wall with biomass aerogel is about 552.09 kg per year.

8.4 CONCLUSION

This section states the economic and environmental analysis of the E. ON house with the combination of biomass aerogel insulation. Based on the simulation results in **Chapter 7**, the investment cost of all stages was calculated, including the fee for raw materials, gel preparation, ageing, freeze-drying and packaging from two different scales, laboratory scale and industrial scale. The total cost of production of 1 m^2·cm biomass aerogel on a laboratory and industrial scale is £ 16.30/m^2·cm and £ 4.16/m^2·cm, respectively. Based on the energy saving fee and the investment cost, the cost of energy cash flow, discounted cash flow, and cumulative NPV have been calculated. On a laboratory scale, the cumulative NPV is in a positive direction towards zero in the 13^{th} year, and the discounted payback period is 12.28 years with wall insulation of biomass aerogel. To have the actual situation, the cumulative NPV of the industrial scale has also been calculated, leading to the shorter payback period. On the industrial scale, the cumulative NPV is in a positive direction towards zero in the 4^{th} year, and the discounted payback period is 3.72 years with wall insulation of biomass aerogel. In the environmental aspect, the retrofitting E.ON house exterior wall with biomass aerogel shows a reduction in CO_2 emissions (552.09 kg/year) compared with the original E.ON House. In comparing the impact values quantified in this study with previous studies focused on conventional aerogel types, including silica aerogels, it has been depicted that aerogel manufactured by biomass raw materials using the freeze-drying method is an environmentally sound and efficient alternative. Once the production and manufacturing process is largely commercialized, the greater product batches or a continuous flow process will further improve the environmental performance of the product and process due to the concept of economies of scale.

9 CONCLUSIONS AND FUTURE WORK

9.1 GENERAL CONCLUSIONS

This research aimed to design, develop and characterize a kind of novel aerogels based on biomass, including polysaccharides and protein. The biomass aerogels were produced through a sol-gel, freeze drying process and were expected to be used in building applications. This research was conducted to produce a new generation of porous materials and investigate the correlations between their morphology and their properties(i.e., sound absorption, thermal insulation, filtration and mechanical performances). This leads to recommendations for future work following the current research.

(1) Chapter 2: a comprehensive literature review was first conducted on the following aspects: the pore structure design, raw materials selection, existing preparation technologies and application fields of the existing biomass aerogels. For the future development and improvement of biomass aerogels, some perspectives were put forward.

(2) Chapter 3: the initial experiments have been carried out to study the characteristics of different binary composite mixtures/gels prepared with konjac glucomannan, starch, gelatin and wheat straw. The characterisation results obtained the optimal process parameters and addition ranges of raw materials for biomass aerogel preparation.

(3) Chapter 4: biomass aerogels with addition of KGM, gelatin and wheat straw were produced. Gelatin addition can significantly improve sound absorption performance and mechanical strength. Little wheat straw addition improves sound absorption property, but it is reduced with more content added. The best result of K1G1.5WS1 is obtained with an average noise reduction coefficient of 0.38, and the coefficient reaches 0.88 at 4500 Hz. A proposed material model is validated to predict the compressive stress–train curves.

(4) Chapter 5: is aimed to further reduce and improve the thermal insulation property of biomass aerogels. With the same density, the K1G05S2WS1.5 aerogel used with wheat straw (sieved through 120 mesh) showed the lowest thermal conductivity (0.0420 $Wm^{-1}K^{-1}$). At pre-freezing temperatures of -15°C, -25°C, -30°C, and -40°C, K1G0.5S2WS1.5 aerogels exhibit thermal conductivity values of 0.0478, 0.0420, 0.0375, and 0.0327 $Wm^{-1}K^{-1}$, respectively. As tested, biomass aerogels show good thermal stability and flame retardant properties.

(5) Chapter 6: biomass aerogels with the addition of KGM, gelatin, starch and wheat straw were produced. Compared with other commercial filtration materials, biomass aerogel K0.9G1.8S3.6WS1.8 shows excellent performance in removing particulate matter 2.5 (PM 2.5) (99.50%) and PM 10 (99.40%) from the environment. The filtration performance of the biomass aerogels has been verified with an actual room test.

(6) Chapter 7: The original E.ON house with poor thermal insulation property was used to analyze the feasibility of biomass aerogel as insulation materials. This typical semi-detached house was simulated with heating natural gas and a load of 16222.22 kWh. Compared to the original E.ON house, the retrofitted house with K1G0.5S2WS1.5 aerogel insulation achieved the goal by reducing primary heating gas by 14.24% (savings: 2694.44 kWh/year).

(7) Chapter 8: the economic and environmental analyses were presented. With the analysis of the cost of the retrofitting of E.ON on lab scale and industrial scale, it shows that the discounted payback period are 3.72 years and 12.28 years with retrofitting biomass aerogel. In the environmental aspect, the retrofitting E.ON house exterior wall with biomass aerogel shows a reduction in CO_2 emissions (552.09 kg/year) compared with the original E.ON House.

9.2 RECOMMENDATION AND FUTURE WORK

Biomass aerogels have many advantages, such as non-toxicity, sustainability and biodegradability. The raw materials are derived from biomass, which is widely available and

has a low environmental impact. However, based on this research, there are some limitations of work that need to be considered in the future:

(1) Further improve the thermal insulation performance. In this research, the thermal conductivity of biomass aerogels needs to be further reduced and bring them close to the silica aerogels with nano-pores. According to these, freezing with liquid nitrogen is a good choice to produce tiny pores, resulting in extremely low thermal conductivity. It should be noted that liquid nitrogen is a hazardous material in the lab, which will lead to frostbite when there is direct skin contact, and there is a risk of cracking and explosion if encountered with high heat. Therefore, operation must be specially trained.

(2) Increase hydrophobicity. In practical applications, the use of biomass aerogels is far from enough. There are some challenges in developing polysaccharide-based aerogel materials, such as hydrophobicity. Generally, polysaccharides are hydrophilic materials. The problem from weather, water and microorganism will follow, contributing to destroying and degrading polysaccharide-based aerogels. So researchers need to pay attention to increasing hydrophobicity. In recent years, some chemical methods have been found to increase hydrophobicity. In the initial experiment, we used the thermal chemical vapour deposition of methyltrichlorosilan to obtain hydrophobic biomass aerogels. Figure 9-1 shows the comparison between before and after treatment. However, most of these hydrophobic treatment methods will harm our environment. We need to balance hydrophilic and hydrophobic, which could refer to bionics, such as lotus leaves with specific non-polar methyl groups. When the balance between hydrophilic and hydrophobic can be adjusted as wanted, the use of scope and shelf life of aerogels will be expanded.

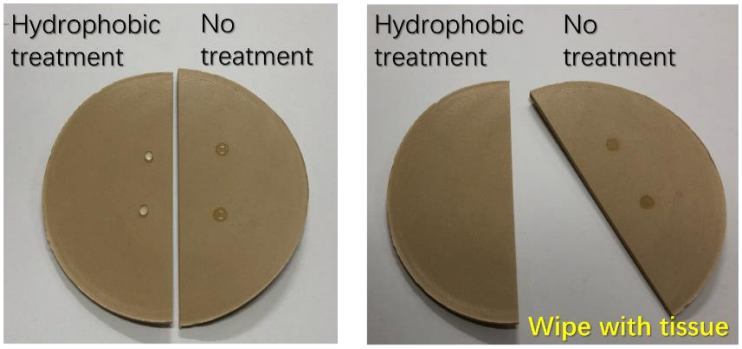


Figure 9-1. The macro images of biomass aerogels with and without hydrophobic treatment.

(3) Product shape design. Biomass aerogels have been used in many fields as new functional materials. To meet the market requirement, biomass aerogel products of different sizes and shapes need to be designed and manufactured. Currently, aerogel shapes are relatively simple, mainly including sheet panels, balls and beads, which all depend on mould shape. However, complex shapes cannot be achieved, so 3D printing technology has a high potential to be used to prepare biomass aerogels.

REFERENCES

[1] Ramírez-Villegas R, Eriksson O, Olofsson T. Assessment of renovation measures for a dwelling area – Impacts on energy efficiency and building certification. Building and Environment. 2016;97:26-33.
[2] Somu N, Raman M R G, Ramamritham K. A deep learning framework for building energy consumption forecast. Renewable and Sustainable Energy Reviews. 2021;137:110591.
[3] Beck A, Heinemann U, Reidinger M, Fricke J. Thermal Transport in Straw Insulation. Journal of Thermal Envelope and Building Science. 2004;27(3):227-34.
[4] Cuce E, Cuce PM, Wood CJ, Riffat SB. Optimizing insulation thickness and analysing environmental impacts of aerogel-based thermal superinsulation in buildings. Energy and Buildings. 2014;77:28-39.
[5] Septevani AA, Evans DAC, Chaleat C, Martin DJ, Annamalai PK. A systematic study substituting polyether polyol with palm kernel oil based polyester polyol in rigid polyurethane foam. Industrial Crops and Products. 2015;66:16-26.
[6] Janik H, Sienkiewicz M, Kucinska-Lipka J. 9 - Polyurethanes. In: Dodiuk H, Goodman SH, editors. Handbook of Thermoset Plastics (Third Edition). Boston: William Andrew Publishing; 2014. p. 253-95.
[7] Bronzaft AL, Hagler L. Noise: The invisible pollutant that cannot be ignored. Emerging Environmental Technologies, Volume II: Springer; 2010. p. 75-96.
[8] Chen DR, Chang XH, Jiao XL. Chapter 22 - Aerogels in the Environment Protection. In: Fanun M, editor. The Role of Colloidal Systems in Environmental Protection. Amsterdam: Elsevier; 2014. p. 573-91.
[9] Schmidt F, Kolle K, Kreuder K, Schnorbus B, Wild P, Hechtner M, et al. Nighttime aircraft noise impairs endothelial function and increases blood pressure in patients with or at high risk for coronary artery disease. Clinical Research in Cardiology. 2015;104(1):23-30.
[10] Seidman MD, Standring RT. Noise and Quality of Life. International Journal of Environmental Research and Public Health. 2010;7(10).
[11] Tzivian L, Winkler A, Dlugaj M, Schikowski T, Vossoughi M, Fuks K, et al. Effect of long-term outdoor air pollution and noise on cognitive and psychological functions in adults. International Journal of Hygiene and Environmental Health. 2015;218(1):1-11.
[12] Stansfeld SA, Matheson MP. Noise pollution: non-auditory effects on health. British Medical Bulletin. 2003;68(1):243-57.
[13] Arenas JP, Crocker MJ. Recent trends in porous sound-absorbing materials. Sound & vibration. 2010;44(7):12-8.
[14] Koruk H, Genc G. Investigation of the acoustic properties of bio luffa fiber and composite materials. Materials Letters. 2015;157:166-8.
[15] Liu Z, Zhan J, Fard M, Davy JL. Acoustic properties of a porous polycarbonate material produced by additive manufacturing. Materials Letters. 2016;181:296-9.
[16] Hung T-C, Huang J-S, Wang Y-W, Lin K-Y. Inorganic polymeric foam as a sound absorbing and insulating material. Construction and Building Materials. 2014;50:328-34.
[17] Wang C-N, Torng J-H. Experimental study of the absorption characteristics of some porous fibrous materials. Applied Acoustics. 2001;62(4):447-59.
[18] Azevedo LJ, Nabuo M. Sound absorption of sisal fiber panels. INTER-NOISE and NOISE-CON Congress and Conference Proceedings: Institute of Noise Control Engineering; 2005. p. 1806-11.
[19] Zhao T, Yang M, Wu H, Guo S, Sun X, Liang W. Preparation of a new foam/film structure poly (ethylene-co-octene) foam materials and its sound absorption properties. Materials Letters. 2015;139:275-8.

[20] Wu G, Li R, Yuan Y, Jiang L, Sun D. Sound absorption properties of ceramic hollow sphere structures with micro-sized open cell. Materials Letters. 2014;134:268-71.
[21] Jamshaid H, Mishra R. A green material from rock: basalt fiber – a review. The Journal of The Textile Institute. 2016;107(7):923-37.
[22] Sgard FC, Olny X, Atalla N, Castel F. On the use of perforations to improve the sound absorption of porous materials. Applied Acoustics. 2005;66(6):625-51.
[23] Rey Rd, Alba J, Arenas JP, Sanchis VJ. An empirical modelling of porous sound absorbing materials made of recycled foam. Applied Acoustics. 2012;73(6):604-9.
[24] Cao L, Fu Q, Si Y, Ding B, Yu J. Porous materials for sound absorption. Composites Communications. 2018;10:25-35.
[25] Meng H, Wen J, Zhao H, Wen X. Optimization of locally resonant acoustic metamaterials on underwater sound absorption characteristics. Journal of Sound and Vibration. 2012;331(20):4406-16.
[26] Merkel A, Theocharis G, Richoux O, Romero-García V, Pagneux V. Control of acoustic absorption in one-dimensional scattering by resonant scatterers. Applied Physics Letters. 2015;107(24):244102.
[27] Wang Y, Su Y, Wang W, Fang Y, Riffat SB, Jiang F. The advances of polysaccharide-based aerogels: Preparation and potential application. Carbohydrate polymers. 2019;226:115242.
[28] Meng X, Zhang Y, Yang K-Q, Yang Y-K, Zhou X-L. Potential Harmful Effects of PM2.5 on Occurrence and Progression of Acute Coronary Syndrome: Epidemiology, Mechanisms, and Prevention Measures. International Journal of Environmental Research and Public Health. 2016;13(8):748.
[29] Zoran MA, Savastru RS, Savastru DM, Tautan MN. Assessing the relationship between surface levels of PM2.5 and PM10 particulate matter impact on COVID-19 in Milan, Italy. Science of The Total Environment. 2020;738:139825.
[30] Zhang S, Sun J, Hu D, Xiao C, Zhuo Q, Wang J, et al. Large-sized graphene oxide/modified tourmaline nanoparticle aerogel with stable honeycomb-like structure for high-efficiency PM2.5 capture. Journal of Materials Chemistry A. 2018;6(33):16139-48.
[31] Mandal SK, Srimani BN. Jute Fiber as a Filter Medium in Microbial Air Filters. Annals of the New York Academy of Sciences. 1987;506(1):682-8.
[32] Zare Shahneh A. Improving aircraft cabin air quality by reducing Tri-Cresylic Phosphate. 2020.
[33] Liu H, Liu L, Yu J, Yin X, Ding B. High-efficiency and super-breathable air filters based on biomimetic ultrathin nanofiber networks. Composites Communications. 2020;22:100493.
[34] Rajak A, Hapidin DA, Iskandar F, Munir MM, Khairurrijal K. Electrospun nanofiber from various source of expanded polystyrene (EPS) waste and their characterization as potential air filter media. Waste Management. 2020;103:76-86.
[35] Jia C, Liu Y, Li L, Song J, Wang H, Liu Z, et al. A Foldable All-Ceramic Air Filter Paper with High Efficiency and High-Temperature Resistance. Nano Letters. 2020;20(7):4993-5000.
[36] Lv S, Zhao X, Shi L, Zhang G, Wang S, Kang W, et al. Preparation and Properties of sc-PLA/PMMA Transparent Nanofiber Air Filter. Polymers. 2018;10(9).
[37] Leung WWF, Sun Q. Electrostatic charged nanofiber filter for filtering airborne novel coronavirus (COVID-19) and nano-aerosols. Separation and purification technology. 2020;250:116886.
[38] El-Naggar ME, Othman SI, Allam AA, Morsy OM. Synthesis, drying process and medical application of polysaccharide-based aerogels. International Journal of Biological Macromolecules. 2020;145:1115-28.
[39] Kistler SS. Coherent expanded aerogels and jellies. Nature. 1931;127(3211):741-.

[40] Buratti C, Belloni E, Merli F, Zinzi M. Aerogel glazing systems for building applications: A review. Energy and Buildings. 2021;231:110587.
[41] Ibrahim M, Nocentini K, Stipetic M, Dantz S, Caiazzo FG, Sayegh H, et al. Multi-field and multi-scale characterization of novel super insulating panels/systems based on silica aerogels: Thermal, hydric, mechanical, acoustic, and fire performance. Building and Environment. 2019;151:30-42.
[42] Jiang Y, Chowdhury S, Balasubramanian R. New insights into the role of nitrogen-bonding configurations in enhancing the photocatalytic activity of nitrogen-doped graphene aerogels. Journal of Colloid and Interface Science. 2019;534:574-85.
[43] Zhang C, Liu S, Qi Y, Cui F, Yang X. Conformal carbon coated TiO2 aerogel as superior anode for lithium-ion batteries. Chemical Engineering Journal. 2018;351:825-31.
[44] Rudaz C, Courson R, Bonnet L, Calas-Etienne S, Sallée H, Budtova T. Aeropectin: Fully Biomass-Based Mechanically Strong and Thermal Superinsulating Aerogel. Biomacromolecules. 2014;15(6):2188-95.
[45] Pan J, Li Y, Chen K, Zhang Y, Zhang H. Enhanced physical and antimicrobial properties of alginate/chitosan composite aerogels based on electrostatic interactions and noncovalent crosslinking. Carbohydrate Polymers. 2021;266:118102.
[46] Wang S, Meng W, Lv H, Wang Z, Pu J. Thermal insulating, light-weight and conductive cellulose/aramid nanofibers composite aerogel for pressure sensing. Carbohydrate Polymers. 2021;270:118414.
[47] Pereira ALS, Feitosa JPA, Morais JPS, Rosa MdF. Bacterial cellulose aerogels: Influence of oxidation and silanization on mechanical and absorption properties. Carbohydrate Polymers. 2020;250:116927.
[48] Sun Y, Chu Y, Wu W, Xiao H. Nanocellulose-based lightweight porous materials: A review. Carbohydrate Polymers. 2021;255:117489.
[49] Chen J, Li H, Ma L, Jiang G, Li D, Wu Y, et al. Chitosan-based recyclable composite aerogels for the photocatalytic degradation of rhodamine B. Carbohydrate Polymers. 2021;273:118559.
[50] Zhao J, Xi X, Ouyang H, Yang J, Wang Y, Yi L, et al. Acidic and alkaline gas sensitive and self-healing chitosan aerogel based on electrostatic interaction. Carbohydrate Polymers. 2021;272:118445.
[51] Wu K, Wu H, Wang R, Yan X, Sun W, Liu Y, et al. The use of cellulose fiber from office waste paper to improve the thermal insulation-related property of konjac glucomannan/starch aerogel. Industrial Crops and Products. 2022;177:114424.
[52] Hernández-Varela JD, Villaseñor-Altamirano SL, Chanona-Pérez JJ, González Victoriano L, Perea Flores MdJ, Cervantes Sodi F, et al. Effect of cellulose nanoparticles from garlic waste on the structural, mechanical, thermal, and dye removal properties of chitosan/alginate aerogels. Journal of Polymer Research. 2022;29(4):133.
[53] Duman O, Diker CÖ, Uğurlu H, Tunç S. Highly hydrophobic and superoleophilic agar/PVA aerogels for selective removal of oily substances from water. Carbohydrate Polymers. 2022;286:119275.
[54] Zhao F, Liu H, Li H, Cao Y, Hua X, Ge S, et al. Cogel Strategy for the Preparation of a "Thorn"-Like Porous Halloysite/Gelatin Composite Aerogel with Excellent Mechanical Properties and Thermal Insulation. ACS Applied Materials & Interfaces. 2022;14(15):17763-73.
[55] Manzocco L, Plazzotta S, Powell J, de Vries A, Rousseau D, Calligaris S. Structural characterisation and sorption capability of whey protein aerogels obtained by freeze-drying or supercritical drying. Food Hydrocolloids. 2022;122:107117.

[56] Nair SB, Jyothi AN, Sajeev MS, Misra R. Rheological, mechanical and moisture sorption characteristics of cassava starch-konjac glucomannan blend films. Starch - Stärke. 2011;63(11):728-39.
[57] Williams PA, Phillips GO, Crosby G. Managing healthy levels of Blood glucose and cholesterol with konjac flour. 2002.
[58] Qiao D, Shi W, Luo M, Jiang F, Zhang B. Polyvinyl alcohol inclusion can optimize the sol-gel, mechanical and hydrophobic features of agar/konjac glucomannan system. Carbohydrate Polymers. 2022;277:118879.
[59] Wang Y, Wu K, Xiao M, Riffat SB, Su Y, Jiang F. Thermal conductivity, structure and mechanical properties of konjac glucomannan/starch based aerogel strengthened by wheat straw. Carbohydrate Polymers. 2018;197:284-91.
[60] Wu K, Fang Y, Wu H, Wan Y, Qian H, Jiang F, et al. Improving konjac glucomannan-based aerogels filtration properties by combining aerogel pieces in series with different pore size distributions. International Journal of Biological Macromolecules. 2021;166:1499-507.
[61] Khan S, Anwar N. Gelatin/carboxymethyl cellulose based stimuli-responsive hydrogels for controlled delivery of 5-fluorouracil, development, in vitro characterization, in vivo safety and bioavailability evaluation. Carbohydrate Polymers. 2021;257:117617.
[62] Wahlström N, Steinhagen S, Toth G, Pavia H, Edlund U. Ulvan dialdehyde-gelatin hydrogels for removal of heavy metals and methylene blue from aqueous solution. Carbohydrate Polymers. 2020;249:116841.
[63] Kenar JA, Eller FJ, Felker FC, Jackson MA, Fanta GF. Starch aerogel beads obtained from inclusion complexes prepared from high amylose starch and sodium palmitate. Green Chemistry. 2014;16(4):1921-30.
[64] Zou Y, Huda S, Yang Y. Lightweight composites from long wheat straw and polypropylene web. Bioresource Technology. 2010;101(6):2026-33.
[65] Saadatnia M, Ebrahimi G, Tajvidi M. Comparing sound absorption characteristic of acoustic boards made of Aspen particles and different percentage of Wheat and Barely straws. 17th world Conference on Non-destructive Testing2008.
[66] Liu Q, He W-Q, Aguedo M, Xia X, Bai W-B, Dong Y-Y, et al. Microwave-assisted alkali hydrolysis for cellulose isolation from wheat straw: Influence of reaction conditions and non-thermal effects of microwave. Carbohydrate Polymers. 2021;253:117170.
[67] Nishinari K, Williams P, Phillips G. Review of the physico-chemical characteristics and properties of konjac mannan. Food hydrocolloids. 1992;6(2):199-222.
[68] Teixeira BS, Garcia RH, Takinami PY, del Mastro NL. Comparison of gamma radiation effects on natural corn and potato starches and modified cassava starch. Radiation Physics and Chemistry. 2018;142:44-9.
[69] Martins M, Barros AA, Quraishi S, Gurikov P, Raman SP, Smirnova I, et al. Preparation of macroporous alginate-based aerogels for biomedical applications. The Journal of Supercritical Fluids. 2015;106:152-9.
[70] Ziegler C, Wolf A, Liu W, Herrmann A-K, Gaponik N, Eychmüller A. Modern Inorganic Aerogels. Angewandte Chemie International Edition. 2017;56(43):13200-21.
[71] Vareda JP, Lamy-Mendes A, Durães L. A reconsideration on the definition of the term aerogel based on current drying trends. Microporous and Mesoporous Materials. 2018;258:211-6.
[72] Yue R, An C, Ye Z, Owens E, Taylor E, Zhao S. Green biomass-derived materials for oil spill response: recent advancements and future perspectives. Current Opinion in Chemical Engineering. 2022;36:100767.
[73] Sen S, Singh A, Bera C, Roy S, Kailasam K. Recent developments in biomass derived cellulose aerogel materials for thermal insulation application: a review. Cellulose. 2022.

[74] Smirnova I, Gurikov P. Aerogel production: Current status, research directions, and future opportunities. The Journal of Supercritical Fluids. 2018;134:228-33.
[75] Bauli CR, Rocha DB, de Oliveira SA, Rosa DS. Cellulose nanostructures from wood waste with low input consumption. Journal of Cleaner Production. 2019;211:408-16.
[76] Sheng K, Zhang S, Qian S, Fontanillo Lopez CA. High-toughness PLA/Bamboo cellulose nanowhiskers bionanocomposite strengthened with silylated ultrafine bamboo-char. Composites Part B: Engineering. 2019;165:174-82.
[77] Cheng H, Gu B, Pennefather MP, Nguyen TX, Phan-Thien N, Duong HM. Cotton aerogels and cotton-cellulose aerogels from environmental waste for oil spillage cleanup. Materials & Design. 2017;130:452-8.
[78] Harini K, Ramya K, Sukumar M. Extraction of nano cellulose fibers from the banana peel and bract for production of acetyl and lauroyl cellulose. Carbohydrate Polymers. 2018;201:329-39.
[79] Rosa MF, Medeiros ES, Malmonge JA, Gregorski KS, Wood DF, Mattoso LHC, et al. Cellulose nanowhiskers from coconut husk fibers: Effect of preparation conditions on their thermal and morphological behavior. Carbohydrate Polymers. 2010;81(1):83-92.
[80] Hüsing N, Schubert U. Aerogels—Airy Materials: Chemistry, Structure, and Properties. Angewandte Chemie International Edition. 1998;37(1-2):22-45.
[81] Rouquerol J, Avnir D, Fairbridge CW, Everett DH, Haynes JM, Pernicone N, et al. Recommendations for the characterization of porous solids (Technical Report). Pure and Applied Chemistry. 1994;66(8):1739-58.
[82] De Marco I, Baldino L, Cardea S, Reverchon E. Supercritical gel drying for the production of starch aerogels for delivery systems. Chemical Engineering Transactions. 2015;43:307-12.
[83] Cuadros TR, Erices AA, Aguilera JM. Porous matrix of calcium alginate/gelatin with enhanced properties as scaffold for cell culture. Journal of the Mechanical Behavior of Biomedical Materials. 2015;46:331-42.
[84] Pircher N, Fischhuber D, Carbajal L, Strauß C, Nedelec J-M, Kasper C, et al. Preparation and Reinforcement of Dual-Porous Biocompatible Cellulose Scaffolds for Tissue Engineering. Macromolecular Materials and Engineering. 2015;300(9):911-24.
[85] Wang C-S, Virgilio N, Wood-Adams PM, Heuzey M-C. A gelation mechanism for gelatin/polysaccharide aqueous mixtures. Food Hydrocolloids. 2018;79:462-72.
[86] Groult S, Budtova T. Tuning structure and properties of pectin aerogels. European Polymer Journal. 2018;108:250-61.
[87] Somerville C. Cellulose Synthesis in Higher Plants. Annual Review of Cell and Developmental Biology. 2006;22(1):53-78.
[88] Moon RJ, Martini A, Nairn J, Simonsen J, Youngblood J. Cellulose nanomaterials review: structure, properties and nanocomposites. Chemical Society Reviews. 2011;40(7):3941-94.
[89] Wan C, Jiao Y, Wei S, Zhang L, Wu Y, Li J. Functional nanocomposites from sustainable regenerated cellulose aerogels: a review. Chemical Engineering Journal. 2019;359:459-75.
[90] Khalil H, Davoudpour Y, Aprilia NS, Mustapha A, Hossain S, Islam N, et al. Nanocellulose-based polymer nanocomposite: isolation, characterization and applications. Nanocellulose polymer nanocomposites. 2014:273-309.
[91] Cherian J, Paulose J, Vysakh P. Harnessing nature's hidden material: Nano-Cellulose. Materials Today: Proceedings. 2018;5(5):12609-14.
[92] Xiao S, Gao R, Lu Y, Li J, Sun Q. Fabrication and characterization of nanofibrillated cellulose and its aerogels from natural pine needles. Carbohydrate polymers. 2015;119:202-9.
[93] de Oliveira JP, Bruni GP, El Halal SLM, Bertoldi FC, Dias ARG, da Rosa Zavareze E. Cellulose nanocrystals from rice and oat husks and their application in aerogels for food packaging. International journal of biological macromolecules. 2019;124:175-84.

[94] Seabra AB, Bernardes JS, Fávaro WJ, Paula AJ, Durán N. Cellulose nanocrystals as carriers in medicine and their toxicities: A review. Carbohydrate polymers. 2018;181:514-27.
[95] Bodin A, Bäckdahl H. Bacterial cellulose as biomaterial. 2011.
[96] Foresti ML, Vázquez A, Boury B. Applications of bacterial cellulose as precursor of carbon and composites with metal oxide, metal sulfide and metal nanoparticles: A review of recent advances. Carbohydrate polymers. 2017;157:447-67.
[97] Hosseini H, Kokabi M, Mousavi SM. BC/rGO conductive nanocomposite aerogel as a strain sensor. Polymer. 2018;137:82-96.
[98] Picheth GF, Pirich CL, Sierakowski MR, Woehl MA, Sakakibara CN, de Souza CF, et al. Bacterial cellulose in biomedical applications: A review. International journal of biological macromolecules. 2017;104:97-106.
[99] Amnuaikit T, Chusuit T, Raknam P, Boonme P. Effects of a cellulose mask synthesized by a bacterium on facial skin characteristics and user satisfaction. Medical Devices (Auckland, NZ). 2011;4:77.
[100] Keskin Z, Urkmez AS, Hames EE. Novel keratin modified bacterial cellulose nanocomposite production and characterization for skin tissue engineering. Materials Science and Engineering: C. 2017;75:1144-53.
[101] Petersen N, Gatenholm P. Bacterial cellulose-based materials and medical devices: current state and perspectives. Applied microbiology and biotechnology. 2011;91(5):1277-86.
[102] Sheikhi A, Hayashi J, Eichenbaum J, Gutin M, Kuntjoro N, Khorsandi D, et al. Recent advances in nanoengineering cellulose for cargo delivery. Journal of Controlled Release. 2019;294:53-76.
[103] Hu W, Lu L, Li Z, Shao L. A facile slow-gel method for bulk Al-doped carboxymethyl cellulose aerogels with excellent flame retardancy. Carbohydrate Polymers. 2019;207:352-61.
[104] Lin N, Dufresne A. Nanocellulose in biomedicine: Current status and future prospect. European Polymer Journal. 2014;59:302-25.
[105] Maningat CC, Seib PA, Bassi SD, Woo KS, Lasater GD. Wheat starch: production, properties, modification and uses. Starch: Elsevier; 2009. p. 441-510.
[106] Ubeyitogullari A, Ciftci ON. Formation of nanoporous aerogels from wheat starch. Carbohydrate Polymers. 2016;147:125-32.
[107] Druel L, Bardl R, Vorwerg W, Budtova T. Starch aerogels: A member of the family of thermal superinsulating materials. Biomacromolecules. 2017;18(12):4232-9.
[108] Zhu F. Starch based aerogels: Production, properties and applications. Trends in Food Science & Technology. 2019;89:1-10.
[109] Abhari N, Madadlou A, Dini A. Structure of starch aerogel as affected by crosslinking and feasibility assessment of the aerogel for an anti-fungal volatile release. Food chemistry. 2017;221:147-52.
[110] Miao Z, Ding K, Wu T, Liu Z, Han B, An G, et al. Fabrication of 3D-networks of native starch and their application to produce porous inorganic oxide networks through a supercritical route. Microporous and Mesoporous Materials. 2008;111(1-3):104-9.
[111] Ziatabar S, Zepf J, Rich S, Danielson BT, Bollyky PI, Stern R. Chitin, chitinases, and chitin lectins: emerging roles in human pathophysiology. Pathophysiology. 2018;25(4):253-62.
[112] El Knidri H, Belaabed R, Addaou A, Laajeb A, Lahsini A. Extraction, chemical modification and characterization of chitin and chitosan. International journal of biological macromolecules. 2018;120:1181-9.
[113] Hsan N, Dutta P, Kumar S, Bera R, Das N. Chitosan grafted graphene oxide aerogel: Synthesis, characterization and carbon dioxide capture study. International journal of biological macromolecules. 2019;125:300-6.
[114] Takeshita S, Yoda S. Chitosan aerogels: transparent, flexible thermal insulators. Chemistry of Materials. 2015;27(22):7569-72.

[115] Hassan S, Suzuki M, Abd El-Moneim A. Synthesis of MnO2–chitosan nanocomposite by one-step electrodeposition for electrochemical energy storage application. Journal of Power Sources. 2014;246:68-73.
[116] Ji C-C, Xu M-W, Bao S-J, Cai C-J, Lu Z-J, Chai H, et al. Self-assembly of three-dimensional interconnected graphene-based aerogels and its application in supercapacitors. Journal of colloid and interface science. 2013;407:416-24.
[117] Jin W, Xu W, Ge H, Li J, Li B. Coupling process of phase separation and gelation in konjac glucomannan and gelatin system. Food Hydrocolloids. 2015;51:188-92.
[118] Li C, Wu K, Su Y, Riffat SB, Ni X, Jiang F. Effect of drying temperature on structural and thermomechanical properties of konjac glucomannan-zein blend films. International journal of biological macromolecules. 2019;138:135-43.
[119] Zhu J, Hu J, Jiang C, Liu S, Li Y. Ultralight, hydrophobic, monolithic konjac glucomannan-silica composite aerogel with thermal insulation and mechanical properties. Carbohydrate polymers. 2019;207:246-55.
[120] Xin C, Chen J, Liang H, Wan J, Li J, Li B. Confirmation and measurement of hydrophobic interaction in sol-gel system of konjac glucomannan with different degree of deacetylation. Carbohydrate Polymers. 2017;174:337-42.
[121] Wu J, Deng X, Lin X. Swelling characteristics of konjac glucomannan superabsobent synthesized by radiation-induced graft copolymerization. Radiation Physics and Chemistry. 2013;83:90-7.
[122] Xia B, Ha W, Meng X-W, Govender T, Peng S-L, Ding L-S, et al. Preparation and characterization of a poly(ethylene glycol) grafted carboxymethyl konjac glucomannan copolymer. Carbohydrate Polymers. 2010;79(3):648-54.
[123] Ratcliffe I, Williams PA, English RJ, Meadows J. Small strain deformation measurements of konjac glucomannan solutions and the influence of borate cross-linking. Carbohydrate polymers. 2013;95(1):272-81.
[124] Luo P, Nie M, Wen H, Xu W, Fan L, Cao Q. Preparation and characterization of carboxymethyl chitosan sulfate/oxidized konjac glucomannan hydrogels. International journal of biological macromolecules. 2018;113:1024-31.
[125] Dekamin MG, Karimi Z, Latifidoost Z, Ilkhanizadeh S, Daemi H, Naimi-Jamal MR, et al. Alginic acid: A mild and renewable bifunctional heterogeneous biopolymeric organocatalyst for efficient and facile synthesis of polyhydroquinolines. International journal of biological macromolecules. 2018;108:1273-80.
[126] Shao L, Cao Y, Li Z, Hu W, Li S, Lu L. Dual responsive aerogel made from thermo/pH sensitive graft copolymer alginate-gP (NIPAM-co-NHMAM) for drug controlled release. International journal of biological macromolecules. 2018;114:1338-44.
[127] Anderson NS, Dolan TC, Rees DA. Carrageenans. Part VII. Polysaccharides from Eucheuma spinosum and Eucheuma cottonii. The covalent structure of ι-carrageenan. Journal of the Chemical Society, Perkin Transactions 1. 1973:2173-6.
[128] Derkach S, Voron'Ko N, Kuchina YA, Kolotova D, Gordeeva A, Faizullin D, et al. Molecular structure and properties of κ-carrageenan-gelatin gels. Carbohydrate polymers. 2018;197:66-74.
[129] Zamora-Sequeira R, Ardao I, Starbird R, García-González CA. Conductive nanostructured materials based on poly-(3,4-ethylenedioxythiophene) (PEDOT) and starch/κ-carrageenan for biomedical applications. Carbohydrate Polymers. 2018;189:304-12.
[130] Leong KH, Chung LY, Noordin MI, Mohamad K, Nishikawa M, Onuki Y, et al. Carboxymethylation of kappa-carrageenan for intestinal-targeted delivery of bioactive macromolecules. Carbohydrate Polymers. 2011;83(4):1507-15.
[131] Groult S, Budtova T. Thermal conductivity/structure correlations in thermal super-insulating pectin aerogels. Carbohydrate polymers. 2018;196:73-81.

[132] Mørch ÝA, Donati I, Strand BL, Skjak-Braek G. Effect of Ca2+, Ba2+, and Sr2+ on alginate microbeads. Biomacromolecules. 2006;7(5):1471-80.
[133] Gupta B, Tummalapalli M, Deopura B, Alam MS. Functionalization of pectin by periodate oxidation. Carbohydrate polymers. 2013;98(1):1160-5.
[134] Işıklan N, Tokmak Ş. Microwave based synthesis and spectral characterization of thermo-sensitive poly (N, N-diethylacrylamide) grafted pectin copolymer. International journal of biological macromolecules. 2018;113:669-80.
[135] Muthukumaran C, Kanmani B, Sharmila G, Kumar M, Shanmugaprakash M. Carboxymethylation of pectin: optimization, characterization and in-vitro drug release studies. Carbohydrate polymers. 2018;194:311-8.
[136] Duconseille A, Wien F, Audonnet F, Traore A, Refregiers M, Astruc T, et al. The effect of origin of the gelatine and ageing on the secondary structure and water dissolution. Food Hydrocolloids. 2017;66:378-88.
[137] Madkhali O, Mekhail G, Wettig SD. Modified gelatin nanoparticles for gene delivery. International Journal of Pharmaceutics. 2019;554:224-34.
[138] Abdelhedi O, Nasri R, Mora L, Toldrá F, Nasri M, Jridi M. Collagenous proteins from black-barred halfbeak skin as a source of gelatin and bioactive peptides. Food Hydrocolloids. 2017;70:123-33.
[139] Huang Z, Gao C, Huang Y, Zhang X, Deng X, Cai Q, et al. Injectable polyphosphazene/gelatin hybrid hydrogel for biomedical applications. Materials & Design. 2018;160:1137-47.
[140] Veres P, Kéri M, Bányai I, Lázár I, Fábián I, Domingo C, et al. Mechanism of drug release from silica-gelatin aerogel—Relationship between matrix structure and release kinetics. Colloids and Surfaces B: Biointerfaces. 2017;152:229-37.
[141] Buggy AK, McManus JJ, Brodkorb A, Hogan SA, Fenelon MA. Pilot-scale formation of whey protein aggregates determine the stability of heat-treated whey protein solutions—Effect of pH and protein concentration. Journal of dairy science. 2018;101(12):10819-30.
[142] Verheul M, Roefs SP, de Kruif KG. Kinetics of heat-induced aggregation of β-lactoglobulin. Journal of Agricultural and Food Chemistry. 1998;46(3):896-903.
[143] Roefs SP, De Kruif KG. A model for the denaturation and aggregation of β-lactoglobulin. European Journal of Biochemistry. 1994;226(3):883-9.
[144] Anema SG. Chapter 9 - The Whey Proteins in Milk: Thermal Denaturation, Physical Interactions, and Effects on the Functional Properties of Milk. In: Singh H, Boland M, Thompson A, editors. Milk Proteins (Second Edition). San Diego: Academic Press; 2014. p. 269-318.
[145] Vuocolo T, Haddad R, Edwards GA, Lyons RE, Liyou NE, Werkmeister JA, et al. A highly elastic and adhesive gelatin tissue sealant for gastrointestinal surgery and colon anastomosis. Journal of Gastrointestinal Surgery. 2012;16(4):744-52.
[146] Blanco A, Monte MC, Campano C, Balea A, Merayo N, Negro C. Nanocellulose for industrial use: cellulose nanofibers (CNF), cellulose nanocrystals (CNC), and bacterial cellulose (BC). Handbook of nanomaterials for industrial applications: Elsevier; 2018. p. 74-126.
[147] Bhat A, Khan I, Usmani MA, Umapathi R, Al-Kindy SM. Cellulose an ageless renewable green nanomaterial for medical applications: An overview of ionic liquids in extraction, separation and dissolution of cellulose. International journal of biological macromolecules. 2019;129:750-77.
[148] Torres F, Arroyo J, Troncoso O. Bacterial cellulose nanocomposites: An all-nano type of material. Materials Science and Engineering: C. 2019;98:1277-93.
[149] Liu S, Yao F, Oderinde O, Zhang Z, Fu G. Green synthesis of oriented xanthan gum–graphene oxide hybrid aerogels for water purification. Carbohydrate polymers. 2017;174:392-9.

[150] Ciftci D, Ubeyitogullari A, Huerta RR, Ciftci ON, Flores RA, Saldaña MD. Lupin hull cellulose nanofiber aerogel preparation by supercritical CO2 and freeze drying. The Journal of Supercritical Fluids. 2017;127:137-45.
[151] Nešić A, Gordić M, Davidović S, Radovanović Ž, Nedeljković J, Smirnova I, et al. Pectin-based nanocomposite aerogels for potential insulated food packaging application. Carbohydrate polymers. 2018;195:128-35.
[152] Salgado M, Santos F, Rodríguez-Rojo S, Reis RL, Duarte ARC, Cocero MJ. Development of barley and yeast β-glucan aerogels for drug delivery by supercritical fluids. Journal of CO2 Utilization. 2017;22:262-9.
[153] Tkalec G, Kranvogl R, Uzunalić AP, Knez Ž, Novak Z. Optimisation of critical parameters during alginate aerogels' production. Journal of Non-Crystalline Solids. 2016;443:112-7.
[154] Matsuyama K, Morotomi K, Inoue S, Nakashima M, Nakashima H, Okuyama T, et al. Antibacterial and antifungal properties of Ag nanoparticle-loaded cellulose nanofiber aerogels prepared by supercritical CO2 drying. The Journal of Supercritical Fluids. 2019;143:1-7.
[155] Wang X, Zhang Y, Jiang H, Song Y, Zhou Z, Zhao H. Fabrication and characterization of nano-cellulose aerogels via supercritical CO2 drying technology. Materials Letters. 2016;183:179-82.
[156] Goimil L, Braga ME, Dias AM, Gomez-Amoza JL, Concheiro A, Alvarez-Lorenzo C, et al. Supercritical processing of starch aerogels and aerogel-loaded poly (ε-caprolactone) scaffolds for sustained release of ketoprofen for bone regeneration. Journal of CO2 Utilization. 2017;18:237-49.
[157] López-Iglesias C, Barros J, Ardao I, Monteiro FJ, Alvarez-Lorenzo C, Gómez-Amoza JL, et al. Vancomycin-loaded chitosan aerogel particles for chronic wound applications. Carbohydrate polymers. 2019;204:223-31.
[158] Paraskevopoulou P, Gurikov P, Raptopoulos G, Chriti D, Papastergiou M, Kypritidou Z, et al. Strategies toward catalytic biopolymers: Incorporation of tungsten in alginate aerogels. Polyhedron. 2018;154:209-16.
[159] Lin L, Li Z, Song X, Jiao Y, Zhou C. Preparation of chitosan/lanthanum hydroxide composite aerogel beads for higher phosphorus adsorption. Materials Letters. 2018;218:201-4.
[160] Ni X, Ke F, Xiao M, Wu K, Kuang Y, Corke H, et al. The control of ice crystal growth and effect on porous structure of konjac glucomannan-based aerogels. International journal of biological macromolecules. 2016;92:1130-5.
[161] Wang Y, Chen X, Kuang Y, Xiao M, Su Y, Jiang F. Microstructure and filtration performance of konjac glucomannan-based aerogels strengthened by wheat straw. International Journal of Low-Carbon Technologies. 2019;14(3):335-43.
[162] Zaragotas D, Liolios NT, Anastassopoulos E. Supercooling, ice nucleation and crystal growth: A systematic study in plant samples. Cryobiology. 2016;72(3):239-43.
[163] Searles JA, Carpenter JF, Randolph TW. The ice nucleation temperature determines the primary drying rate of lyophilization for samples frozen on a temperature-controlled shelf. Journal of pharmaceutical sciences. 2001;90(7):860-71.
[164] Lorenzo A, Müller A. Estimation of the nucleation and crystal growth contributions to the overall crystallization energy barrier. Journal of Polymer Science Part B: Polymer Physics. 2008;46(14):1478-87.
[165] Chen H, Ma Y, Lin X, Yang D, Chen Z, Li X, et al. Preparation of aligned porous niobium scaffold and the optimal control of freeze-drying process. Ceramics International. 2018;44(14):17174-9.
[166] Zhu S, Ramaswamy HS, Le Bail A. Ice-crystal formation in gelatin gel during pressure shift versus conventional freezing. Journal of Food Engineering. 2005;66(1):69-76.

[167] Zhang X, Sun P, Yan T, Huang Y, Ma Z, Zou B, et al. Water's phase diagram: from the notion of thermodynamics to hydrogen-bond cooperativity. Progress in Solid State Chemistry. 2015;43(3):71-81.
[168] Kalichevsky-Dong MT, Ablett S, Lillford PJ, Knorr D. Effects of pressure-shift freezing and conventional freezing on model food gels. International journal of food science & technology. 2000;35(2):163-72.
[169] Martino MN, Otero L, Sanz P, Zaritzky N. Size and location of ice crystals in pork frozen by high-pressure-assisted freezing as compared to classical methods. Meat science. 1998;50(3):303-13.
[170] Sequeira-Munoz A, Chevalier D, Simpson B, Le Bail A, Ramaswamy H. Effect of pressure-shift freezing versus air-blast freezing of carp (Cyprinus carpio) fillets: a storage study. Journal of Food Biochemistry. 2005;29(5):504-16.
[171] Van der Sman R. Phase field simulations of ice crystal growth in sugar solutions. International Journal of Heat and Mass Transfer. 2016;95:153-61.
[172] Shimada W, Furukawa S. Rapid growth of ice crystal dendrite tips in dilute solution of trehalose. Journal of Crystal Growth. 2018;493:25-9.
[173] Fernández PP, Martino MN, Zaritzky N, Guignon B, Sanz P. Effects of locust bean, xanthan and guar gums on the ice crystals of a sucrose solution frozen at high pressure. Food Hydrocolloids. 2007;21(4):507-15.
[174] Gupta P, Singh B, Agrawal AK, Maji PK. Low density and high strength nanofibrillated cellulose aerogel for thermal insulation application. Materials & Design. 2018;158:224-36.
[175] Geng H. A facile approach to light weight, high porosity cellulose aerogels. International journal of biological macromolecules. 2018;118:921-31.
[176] Li J, Cheng R, Xiu H, Zhang M, Liu Q, Song T, et al. Pore structure and pertinent physical properties of nanofibrillated cellulose (NFC)-based foam materials. Carbohydrate polymers. 2018;201:141-50.
[177] Jung I-K, Gurav JL, Ha T-J, Choi SG, Baek S, Park H-H. The properties of silica aerogels hybridized with SiO2 nanoparticles by ambient pressure drying. Ceramics International. 2012;38:S105-S8.
[178] Scherer GW. Aging and drying of gels. Journal of Non-Crystalline Solids. 1988;100(1-3):77-92.
[179] Yang H, Kong X, Zhang Y, Wu C, Cao E. Mechanical properties of polymer-modified silica aerogels dried under ambient pressure. Journal of non-crystalline solids. 2011;357(19-20):3447-53.
[180] Zannin PHT, Diniz FB, Barbosa WA. Environmental noise pollution in the city of Curitiba, Brazil. Applied Acoustics. 2002;63(4):351-8.
[181] Chen D, Chang X, Jiao X. Aerogels in the environment protection. The Role of Colloidal Systems in Environmental Protection. 2014:573-91.
[182] Seidman MD, Standring RT. Noise and quality of life. International journal of environmental research and public health. 2010;7(10):3730-8.
[183] Smirnova OM, Menéndez Pidal de Navascués I, Mikhailevskii VR, Kolosov OI, Skolota NS. Sound-absorbing composites with rubber crumb from used tires. Applied Sciences. 2021;11(16):7347.
[184] Zhang D, Zhou X, Gao Y, Lyu L. Structural Characteristics and Sound Absorption Properties of Waste Hemp Fiber. Coatings. 2022;12(12):1907.
[185] Zhang Y, Li H, Abdelhady A, Du H. Laboratorial investigation on sound absorption property of porous concrete with different mixtures. Construction and Building Materials. 2020;259:120414.

[186] Ma B, Jin Z, Su Y, Lu W, Qi H, Hu P. Utilization of hemihydrate phosphogypsum for the preparation of porous sound absorbing material. Construction and Building Materials. 2020;234:117346.
[187] Gao H, Liu H, Liao L, Mei L, Zhang F, Zhang L, et al. A bifunctional hierarchical porous kaolinite geopolymer with good performance in thermal and sound insulation. Construction and Building Materials. 2020;251:118888.
[188] Mahmud MZH, Hassan NA, Hainin MR, Ismail CR, Jaya RP, Warid MNM, et al. Characterisation of microstructural and sound absorption properties of porous asphalt subjected to progressive clogging. Construction and Building Materials. 2021;283:122654.
[189] Yoon J, Kim H, Koh T, Pyo S. Microstructural characteristics of sound absorbable porous cement-based materials by incorporating natural fibers and aluminum powder. Construction and Building Materials. 2020;243:118167.
[190] Wang J, Du B. Experimental studies of thermal and acoustic properties of recycled aggregate crumb rubber concrete. Journal of Building Engineering. 2020;32:101836.
[191] Wu H, Zhang T, Pan R, Chun Y, Zhou H, Zhu W, et al. Sintering-free preparation of porous ceramsite using low-temperature decomposing pore former and its sound-absorbing performance. Construction and Building Materials. 2018;171:367-76.
[192] Feng J, Le D, Nguyen ST, Nien VTC, Jewell D, Duong HM. Silica cellulose hybrid aerogels for thermal and acoustic insulation applications. Colloids and Surfaces A: Physicochemical and Engineering Aspects. 2016;506:298-305.
[193] Septevani AA, Evans DA, Chaleat C, Martin DJ, Annamalai PK. A systematic study substituting polyether polyol with palm kernel oil based polyester polyol in rigid polyurethane foam. Industrial Crops and Products. 2015;66:16-26.
[194] Janik H, Sienkiewicz M, Kucinska-Lipka J. Polyurethanes. Handbook of thermoset plastics: Elsevier; 2014. p. 253-95.
[195] Fesmire JE. Aerogel insulation systems for space launch applications. Cryogenics. 2006;46(2):111-7.
[196] Zhao Y-W, Tian M-Z, Huang P. Starch/clay aerogel reinforced by cellulose nanofibrils for thermal insulation. Cellulose. 2021;28(6):3505-13.
[197] Guerrero-Alburquerque N, Zhao S, Adilien N, Koebel MM, Lattuada M, Malfait WJ. Strong, Machinable, and Insulating Chitosan–Urea Aerogels: Toward Ambient Pressure Drying of Biopolymer Aerogel Monoliths. ACS Applied Materials & Interfaces. 2020;12(19):22037-49.
[198] Wang L, Sánchez-Soto M, Abt T. Properties of bio-based gum Arabic/clay aerogels. Industrial Crops and Products. 2016;91:15-21.
[199] Chen H-B, Li X-L, Chen M-J, He Y-R, Zhao H-B. Self-cross-linked melamine-formaldehyde-pectin aerogel with excellent water resistance and flame retardancy. Carbohydrate polymers. 2019;206:609-15.
[200] Mandal S, Srimani B. Jute fiber as a filter medium in microbial air filters. Annals of the New York Academy of Sciences. 1987;506:682-8.
[201] Lv S, Zhao X, Shi L, Zhang G, Wang S, Kang W, et al. Preparation and properties of sc-PLA/PMMA transparent nanofiber air filter. Polymers. 2018;10(9):996.
[202] Xie X, Zheng Z, Wang X, Lee Kaplan D. Low-Density Silk Nanofibrous Aerogels: Fabrication and Applications in Air Filtration and Oil/Water Purification. ACS nano. 2021;15(1):1048-58.
[203] Zeng Z, Ma XYD, Zhang Y, Wang Z, Ng BF, Wan MP, et al. Robust Lignin-Based Aerogel Filters: High-Efficiency Capture of Ultrafine Airborne Particulates and the Mechanism. ACS Sustainable Chemistry & Engineering. 2019;7(7):6959-68.
[204] Ma S, Zhu P, Wang M. Effects of konjac glucomannan on pasting and rheological properties of corn starch. Food Hydrocolloids. 2019;89:234-40.

[205] Corobea MC, Muhulet O, Miculescu F, Antoniac IV, Vuluga Z, Florea D, et al. Novel nanocomposite membranes from cellulose acetate and clay-silica nanowires. Polymers for Advanced Technologies. 2016;27(12):1586-95.
[206] Guo J, Wang C, Liu C, Wang P. Effect of Konjac Glucomannan on Gelatinization, Retrogradation, and Gelling Properties of Frozen Wheat Starch. Starch - Stärke. 2021;73(1-2):2000025.
[207] Tao K, Li C, Yu W, Gilbert RG, Li E. How amylose molecular fine structure of rice starch affects functional properties. Carbohydrate Polymers. 2019;204:24-31.
[208] Yoshimura M, Takaya T, Nishinari K. Effects of Konjac-Glucomannan on the Gelatinization and Retrogradation of Corn Starch As Determined by Rheology and Differential Scanning Calorimetry. Journal of Agricultural and Food Chemistry. 1996;44(10):2970-6.
[209] Nishinari K. Rheological and DSC study of sol-gel transition in aqueous dispersions of industrially important polymers and colloids. Colloid and Polymer Science. 1997;275(12):1093-107.
[210] Ni X, Wang K, Wu K, Corke H, Nishinari K, Jiang F. Stability, microstructure and rheological behavior of konjac glucomannan-zein mixed systems. Carbohydrate Polymers. 2018;188:260-7.
[211] Doi M, Takimoto J-i. Molecular modelling of entanglement. Philosophical Transactions of the Royal Society of London Series A: Mathematical, Physical and Engineering Sciences. 2003;361(1805):641-52.
[212] Iqbal S, Wu P, Kirk TV, Chen XD. Amylose content modulates maize starch hydrolysis, rheology, and microstructure during simulated gastrointestinal digestion. Food Hydrocolloids. 2021;110:106171.
[213] Li J, Yang Y, Su Y, Gu L, Chang C, Yang Y. Phase separation in ternary composite cold-set gel of egg yolk/κ-carrageenan/xanthan: Study on rheological and proton mobility properties. LWT. 2019;116:108497.
[214] Acar H, Kurt A. Purified salep glucomannan synergistically interacted with xanthan gum: Rheological and textural studies on a novel pH-/thermo-sensitive hydrogel. Food Hydrocolloids. 2020;101:105463.
[215] Casas-Forero N, Moreno-Osorio L, Orellana-Palma P, Petzold G. Effects of cryoconcentrate blueberry juice incorporation on gelatin gel: A rheological, textural and bioactive properties study. LWT. 2021;138:110674.
[216] Cao L, Yu X, Yin X, Si Y, Yu J, Ding B. Hierarchically maze-like structured nanofiber aerogels for effective low-frequency sound absorption. Journal of Colloid and Interface Science. 2021;597:21-8.
[217] Tang G, Zhang H, Zhao Y, Zhang Y, Li X, Yuan X. Preparation of PLGA scaffolds with graded pores by using a gelatin-microsphere template as porogen. Journal of Biomaterials Science, Polymer Edition. 2012;23(17):2241-57.
[218] Su K, Wang C. Recent advances in the use of gelatin in biomedical research. Biotechnology Letters. 2015;37(11):2139-45.
[219] Liu X, Ma PX. Phase separation, pore structure, and properties of nanofibrous gelatin scaffolds. Biomaterials. 2009;30(25):4094-103.
[220] Jin H, Nishiyama Y, Wada M, Kuga S. Nanofibrillar cellulose aerogels. Colloids and Surfaces A: Physicochemical and Engineering Aspects. 2004;240(1-3):63-7.
[221] Kiani H, Sun D-W. Water crystallization and its importance to freezing of foods: A review. Trends in Food Science & Technology. 2011;22(8):407-26.
[222] Dunne R, Desai D, Sadiku R. A Review of the Factors that Influence Sound Absorption and the Available Empirical Models for Fibrous Materials. Acoustics Australia. 2017;45(2):453-69.

[223] Mamtaz H, Fouladi MH, Al-Atabi M, Narayana Namasivayam S. Acoustic absorption of natural fiber composites. Journal of Engineering. 2016;2016.
[224] Zhang XH, Qu ZG, He XC, Lu DL. Experimental study on the sound absorption characteristics of continuously graded phononic crystals. AIP Advances. 2016;6(10):105205.
[225] Wang Y, Chen X, Kuang Y, Xiao M, Su Y, Jiang F. Microstructure and filtration performance of konjac glucomannan-based aerogels strengthened by wheat straw. International Journal of Low-Carbon Technologies. 2017;14(3):335-43.
[226] Li Z, Zhang L, Mao C, Song Z, Li X, Liu C. Preparation and characterization of konjac glucomannan and gum arabic composite gel. International Journal of Biological Macromolecules. 2021;183:2121-30.
[227] Qiao D, Wang Z, Cai C, Yin S, Qian H, Zhang B, et al. Tailoring Multi-Level Structural and Practical Features of Gelatin Films by Varying Konjac Glucomannan Content and Drying Temperature. Polymers. 2020;12(2):385.
[228] Ghaffar SH, Fan M. Revealing the morphology and chemical distribution of nodes in wheat straw. Biomass and Bioenergy. 2015;77:123-34.
[229] Pu H, Ding X, Chen H, Dai R, Shan Z. Functional aerogels with sound absorption and thermal insulation derived from semi-liquefied waste bamboo and gelatin. Environmental Technology & Innovation. 2021;24:101874.
[230] Wang W, Wang H, Zhou J, Fan H, Liu X. Machine learning prediction of mechanical properties of braided-textile reinforced tubular structures. Materials & Design. 2021;212:110181-.
[231] Rivlin RS, Saunders DW, Andrade ENDC. Large elastic deformations of isotropic materials VII. Experiments on the deformation of rubber. Philosophical Transactions of the Royal Society of London Series A, Mathematical and Physical Sciences. 1951;243(865):251-88.
[232] Ogden RW, Hill R. Large deformation isotropic elasticity – on the correlation of theory and experiment for incompressible rubberlike solids. Proceedings of the Royal Society of London A Mathematical and Physical Sciences. 1972;326(1567):565-84.
[233] Yeoh OH. Some Forms of the Strain Energy Function for Rubber. Rubber Chemistry and Technology. 1993;66(5):754-71.
[234] Tabernero A, Baldino L, Cardea S, Martín del Valle E, Reverchon E. A Phenomenological Approach to Study Mechanical Properties of Polymeric Porous Structures Processed Using Supercritical CO2. Polymers. 2019;11(3).
[235] Treloar LRG. The elasticity and related properties of rubbers. Reports on Progress in Physics. 1973;36(7):755-826.
[236] Lu X, Caps R, Fricke J, Alviso C, Pekala R. Correlation between structure and thermal conductivity of organic aerogels. Journal of Non-Crystalline Solids. 1995;188(3):226-34.
[237] Lee O-J, Lee K-H, Yim TJ, Kim SY, Yoo K-P. Determination of mesopore size of aerogels from thermal conductivity measurements. Journal of Non-Crystalline Solids. 2002;298(2-3):287-92.
[238] Wang X, Zhong J, Wang Y, Yu M. A study of the properties of carbon foam reinforced by clay. Carbon. 2006;44(8):1560-4.
[239] Shi Z, Zhao G, Zhang L, Wang G. Lightweight, strong, flame-retardant PVDF/PMMA microcellular foams for thermal insulation fabricated by supercritical CO2 foaming. Composites Part B: Engineering. 2022;230:109554.
[240] Kuang Y, Chen L, Zhai J, Zhao S, Xiao Q, Wu K, et al. Microstructure, thermal conductivity, and flame retardancy of konjac glucomannan based aerogels. Polymers. 2021;13(2):258.

[241] Kuang Y, Chen L, Zhai J, Zhao S, Xiao Q, Wu K, et al. Microstructure, Thermal Conductivity, and Flame Retardancy of Konjac Glucomannan Based Aerogels. Polymers. 2021;13(2).
[242] Wang Y, Chen X, Kuang Y, Xiao M, Su Y, Jiang F. Microstructure and filtration performance of konjac glucomannan-based aerogels strengthened by wheat straw. International Journal of Low-Carbon Technologies. 2018;13(1):67-75.
[243] Gillott M, Loveday DL, White J, Wood C, Chmutina K, Vadodaria K. Improving the airtightness in an existing UK dwelling: The challenges, the measures and their effectiveness. Building and Environment. 2016;95:227-39.
[244] Jiang T, Zhang Y, Olayiwola S, Lau C, Fan M, Ng K, et al. Biomass-derived porous carbons support in phase change materials for building energy efficiency: a review. Materials Today Energy. 2022;23:100905.
[245] Ding Y, Zhang D, Lv J. Comparison of the applicability of city-level building energy consumption quota methods. Energy and Buildings. 2022;261:111933.
[246] Janetti MB, Wagner P. Analytical model for the moisture absorption in capillary active building materials. Building and Environment. 2017;126:98-106.
[247] Garrido R, Silvestre JD, Flores-Colen I, de Fátima Júlio M, Pedroso M. Economic assessment of the production of subcritically dried silica-based aerogels. Journal of Non-Crystalline Solids. 2019;516:26-34.
[248] Wang Y, Qu K, Chen X, Gan G, Riffat S. An innovative retrofit Motivation-Objective-Criteria (MOC) approach integrating homeowners' engagement to unlocking low-energy retrofit in residential buildings. Energy and Buildings. 2022;259:111834.
[249] Ibn-Mohammed T, Randall C, Mustapha K, Guo J, Walker J, Berbano S, et al. Decarbonising ceramic manufacturing: A techno-economic analysis of energy efficient sintering technologies in the functional materials sector. Journal of the European Ceramic Society. 2019;39(16):5213-35.